



A University of Sussex DPhil thesis

Available online via Sussex Research Online:

<http://sro.sussex.ac.uk/>

This thesis is protected by copyright which belongs to the author.

This thesis cannot be reproduced or quoted extensively from without first obtaining permission in writing from the Author

The content must not be changed in any way or sold commercially in any format or medium without the formal permission of the Author

When referring to this work, full bibliographic details including the author, title, awarding institution and date of the thesis must be given

Please visit Sussex Research Online for more information and further details



**Particle Physics Methodologies Applied
to Time-Of-Flight Positron Emission
Tomography with
Silicon-Photomultipliers and Inorganic
Scintillators**

Edward J. Leming

Submitted for the degree of PhD

University of Sussex

July 2014

Declaration

I hereby declare that this thesis has not been and will not be submitted in whole or in part to another University for the award of any other degree.

All of the work henceforth presented is the original work of the author, Edward J. Leming. Experimental measurements presented in Chapters 5 and 6.1 were designed in collaboration with Prof. Boris Vojnovic at the University of Oxford. For these measurements data acquisition was performed by both the author and Dr. Mahfuza Ahmed. Experimental measurements presented in Chapter 6.2 were taken at the University of Surrey where all experimental design and data acquisition was the work the author. All simulation and analysis code was designed and written from scratch by the author.

Signature:

Edward J. Leming

UNIVERSITY OF SUSSEX

EDWARD J. LEMING, DOCTOR OF PHILOSOPHY

Particle Physics Methodologies Applied to Time-Of-Flight Positron
Emission Tomography with Silicon-Photomultipliers and Inorganic Scintillators

ABSTRACT

Positron emission tomography, or PET, is a medical imaging technique which has been used in clinical environments for over two decades. With the advent of fast timing detectors and scintillating crystals, it is possible to envisage improvements to the technique with the inclusion of time-of-flight capabilities. In this context, silicon photomultipliers coupled to fast inorganic LYSO crystals are investigated as a possible technology choice. As part of the ENVISION collaboration a range of photon detectors were investigated experimentally, leading to the selection of specific devices for use in a first prototype detector, currently being commissioned at the Rutherford Appleton Laboratory. In order to characterise the design of the prototype a GEANT4 simulation has been developed describing coupled systems of silicon photomultipliers and LYSO scintillators. Very good agreement is seen between the timing response of the experimental and simulated systems. Results of the simulation for a range of detector array arrangements are presented and a number of optimisations proposed for the final prototype design. Without the results provided here a detector system including only $3 \times 3 \times 5 \text{ mm}^3$ crystals would have been adopted. A $3 \times 3 \times 5 \text{ mm}^3$ crystal geometry is shown to provide little-to-no timing advantage over an identical system with $3 \times 3 \times 10 \text{ mm}^3$ crystals, where detection efficiency is improved by approximately a factor of three. Additionally an investigation is presented which explores the impact of using events where gamma-ray photons are scattered internally within the detector array. It is shown that including such events could increase the signal achievable with one-to-one coupled detector arrays systems for PET by approximately 60%, with only minor reductions in coincidence timing resolution.

Acknowledgements

There are a number of people who have had a significant influence on me over the course of my academic career, only a fraction of whom can be mentioned here.

Of the many thanks I would like to extend, the first and foremost go to my primary supervisor, Professor Antonella De Santo, who has provided an unwavering clarity of thought which has frequently inspired and continuously motivated the work I present here. Without Antonella's support this thesis surely would not have been written, I cannot thank her enough for the time, but especially the thought, which she has tirelessly set-aside for me over the last four years.

Additionally, this work would not have been possible without the extended network of academic and industrial supervisors with whom I have worked. Dr. Fabrizio Salvatore has been an immeasurable source of academic perspective when it has been needed most and has provided energy and enthusiasm for the project throughout. Dr. Barbara Camanzi, who first proposed this project and therefore without whom I would never have continued my academic carrier. Finally, Dr. Annika Lostroh who has been unfailingly supportive and accommodating at every step.

During the four years of this project, ten months were spent working directly with the advanced technology group in the department of oncology, at the University of Oxford. This group is lead by Prof. Boris Vojnovic, with whom I spent numerous late nights in the lab learning a trade in instrumentation. I cannot thank Boris enough for the time he put aside for me. Throughout these months both Dr. Ian Tullis and Dr. Anthony Kavanagh provided me with the sharp analysis, advice and, at times, the light relief that made my time in Oxford memorable.

As well as the number of supervisors and advisers, there are a number of professional scientists with whom I have worked directly or have provided intermittent advice during this project. Primarily I was like to thank Dr. Mahfuza Ahmed with whom I worked closely for two years. Dr. Paola Avella must also be mentioned separately, whose guidance was

invaluable, particularly in the first few months when I was at my most naive. Additionally, Dr. Mike Partridge, Dr. Mark Sutton, Emyr James, Dr. Tina Potter, Dr. Valeria Bartsch and Dr. John Matheson have all provided invaluable input.

However, I have found the drive to continue through the day-to-day toils of a studentship have come from my direct peer group and those working around me. For this purpose I would like to thank: Dr. Anthony Rose, Dr. Stewart Martin-Haugh, James Sinclair, Nicky Santoyo, Zara Grout, Yusufu Shehu, James Waterfield, Davide Volpi, Dan Gibbon, Luke Vinton, Ashley Back. Without you all this would have been a much duller affair.

Stepping back a moment from the academic environment, I would be nowhere without my family whom I love. They are the foundation through which I have been given the confidence to take on challenges such as this and I owe everything to them. In fact, of the academic abilities I have acquired, it is critical thinking which I value the most. This ability was grown and nurtured through the freedom to question and explore everything through my formative years. I could not have got to this point without my mother's immovable support and belief and my father's encouragement and stoic sacrifice, for which I am eternally grateful. This work is dedicated to you. Additionally, my siblings Alex, Quinten, Sophie and Isabel have all contributed immeasurably to who I am today and can consider this work as much theirs as it is mine.

Finally, through all the ups and downs that have come with this process, Sofie has provided the joy, relief, patience, care and encouragement which has kept me sane and positive throughout. I can only hope to be given the opportunity to reciprocate the levels of love and support she has provided for me through the course of this work.

List of abbreviations

ADC	Analogue-to-Digital Converter
APD	Avalanche Photodiode
CTR	Coincidence Timing Resolution
DAQ	Data Acquisition
DCR	Dark Count Rate
DOI	Depth of Interaction
e-h	electron-hole
EM	Expectation Maximisation
ENVISION	European Novel Imaging Systems for Ion therapy
FIR	Finite Impulse Response
FOV	Field Of View
FWHM	Full Width at Half Maximum
FWTM	Full Width at Tenth Maximum
GM	Geiger Mode
IIR	Infinite Impulse Response
LOR	Line of Response
MLEM	Maximum-Likelihood Expectation Maximum
NECR	Noise Equivalent Count Rate
OSEM	Ordered-Subset Expectation Maximisation
p.e.	Photoelectrons
PET	Positron Emission Tomography
PDE	Photon Detection Efficiency
PMT	Photomultiplier Tube
QE	Quantum Efficiency
RAL	Rutherford Appleton Laboratory

SiPM	Silicon photomultiplier
SNR	Signal-to-Noise Ratio
STE	Self Trapped Exciton
TOF	Time-of-Flight

Contents

List of Tables	xiv
List of Figures	xxv
1 Introduction	1
2 Positron Emission Tomography	3
2.1 Technique overview	3
2.2 Positron emission and radioisotopes	6
2.3 Interactions of high energy photons with matter	7
2.3.1 Photoelectric absorption	9
2.3.2 Compton Scattering	11
2.3.3 Pair production	12
2.4 Detection of coincident photons	13
2.4.1 Block detectors	15
2.4.2 Spatial resolution	16
2.4.3 Noise contributions	19
2.4.4 Noise Equivalent Count Rate	20
2.5 Time-of-Flight PET	21
2.6 Reconstruction	24

3	Inorganic scintillators	29
3.1	Scintillators and their properties	29
3.1.1	The scintillation mechanism	31
3.1.2	Stokes shift	33
3.1.3	Scintillation time	35
3.1.4	Energy resolution	36
3.2	Scintillators for PET	38
3.2.1	Attenuation length	39
3.2.2	Photoelectric fraction	39
3.2.3	Decay time	40
3.2.4	Light yield and Energy Resolution	40
3.3	Contributions to timing resolution	41
3.3.1	Statistical considerations	41
3.3.2	Propagation time	43
4	Photodetectors for PET	47
4.1	The photomultiplier tube	47
4.2	Solid-state detectors	49
4.2.1	The p-n junction	49
4.2.2	PIN diodes	50
4.2.3	Avalanche photodiodes	51
4.3	The Silicon Photomultiplier	53
4.3.1	Principles of operation and electronic characteristics	56
4.4	Characteristics properties of SiPMs	60
4.4.1	Gain	60
4.4.2	Photon detection efficiency	61
4.4.3	Noise	64

4.4.4	Dynamic range and linearity	67
4.4.5	Timing resolution	68
4.4.6	Temperature effects	69
4.5	Signal processing	70
4.5.1	Discrete-time signals	70
4.5.2	Digital filters	72
4.5.3	Up-sampling	77
5	Selection of a candidate SiPM device for TOF-PET	79
5.1	The ENVISION project	80
5.2	Experimental setup	80
5.3	Measurement techniques	84
5.3.1	Signal-to-noise	85
5.3.2	Rise time	85
5.3.3	Fall time	86
5.3.4	Timing jitter	87
5.4	Results	88
5.4.1	Signal-to-noise	88
5.4.2	Rise time	90
5.4.3	Fall time	92
5.4.4	Timing jitter	94
5.5	Device selection	97
6	Characterisation of a coupled SiPM and LYSO detector system	100
6.1	Coincident detector systems	101
6.1.1	Experimental arrangement	101
6.1.2	Energy results	103

6.1.3	Coincident timing results	105
6.2	Depth-of-interaction measurement	107
6.2.1	Experimental arrangement	108
6.2.2	Energy results	110
6.2.3	Coincidence timing results	114
7	Implementation of coupled LYSO and SiPM detector system into a GEANT4 simulation	116
7.1	Some considerations on timing	116
7.2	GEANT4	119
7.2.1	General properties of GEANT4	119
7.2.2	Detector construction and materials	120
7.2.3	Primary generator action	121
7.2.4	Electromagnetic physics	122
7.2.5	LYSO simulation and optical models	122
7.3	SiPM device simulation	127
7.3.1	Simulation framework	129
8	Simulation results of a coupled SiPM and LYSO detector system	132
8.1	Photon statistics	132
8.2	Coincident detector systems	134
8.2.1	Energy results	135
8.2.2	Timing results	138
8.3	Systematic uncertainties on the timing response	140
8.3.1	Dead time	140
8.3.2	Photon detection efficiency	141
8.3.3	Surface roughness	145

8.4	Depth-of-interaction	147
8.4.1	Energy results	147
8.4.2	Timing results	150
8.5	Comparison of experimental and simulated CTR	151
9	Simulation of prototype PET detector systems	155
9.1	Detector simulations for a TOF-PET prototype	156
9.1.1	Array geometries and experimental arrangement	156
9.1.2	Energy resolution	159
9.1.3	Coincidence timing resolution	162
9.1.4	Detection efficiency	166
9.1.5	First design recommendations	168
9.2	Crystal length studies	170
9.2.1	Energy resolution	170
9.2.2	Coincidence timing resolution	173
9.2.3	Detection efficiency	173
9.3	Three-detector events	177
9.3.1	Energy resolution and response	178
9.3.2	Coincidence timing resolution	180
9.3.3	Angular resolution	180
9.3.4	Efficiency	186
9.3.5	Summary and outlook	187
10	Conclusions	191
	Bibliography	194

List of Tables

2.1	List of PET radioisotopes and their key parameters. R_e refers to the maximum extrapolated positron range in water and R_{rms} the root mean square range.	7
2.2	Time resolution, spatial uncertainty and estimated TOF NECR gain for two different source diameters.	24
3.1	Selected inorganic scintillators proposed for PET [59]	39
3.2	List of photon emission angles and their interactions at optical boundaries. R = reflected, T = transmitted.	46
4.1	Comparative table of three photodetectors considered for use in PET: PMT, APD and SiPM [22].	56
4.2	Table listing the Geometric efficiencies for a range of pixel sizes [86] [87]	64
5.1	List of SiPM models used in LED measurements	81
5.2	Characteristics of SiPM devices investigated for model selection.	96
7.1	Properties of materials used in the simulation.	121
7.2	List of characteristic parameters of LYSO scintillation response, including the Rayleigh scattering length and the reflectivity of the TiO_2 painted covering.	124
7.3	List of characteristic parameters of SiPM response.	130
9.1	Weighted mean energy resolutions as calculated from full range of crystal arrangement measurements given in Figure 9.3b. Uncertainties are the standard deviation on the weighted mean.	160

9.2 Coincident timing resolution as measured at the 2% trigger threshold for
each crystal arrangement. 163

List of Figures

2.1	A diagram outlining the basic principles of PET including: annihilation of a positron in patient, emission of co-linear photons, detection and storage of electronic coincidence and reconstruction of detected LORs.	4
2.2	A diagram outlining the standard 2D coordinates system used in PET data acquisition. The intensity distribution $p(s, \phi)$ develops over the duration of a scan and is passed to reconstruction algorithms, to be discussed in section 2.6.	5
2.3	Mass attenuation coefficients for some materials of interest for the analysis discussed later in this document. A vertical dashed line indicates a photon energy of 511 keV.	10
2.4	Illustration of a Compton scatter event. The diagram shows the incident photon of energy $h\nu$ interacting with a electron which is considered at rest. The scattered photon with energy $h\nu'$ scatters at an angle θ relative to the original momentum vector.	11
2.5	Schematic view of a PET detector arrangement. (a) Cross sectional view as seen from the front. The ring diameter S is shown along with a ‘fan’ illustrating the range of detector modules which are considered in coincidence relative, in this case, to the central right module. (b) A view from above showing the total field of view (FOV) and the axial detector length (L) given by five separate detector rings.	13
2.6	(a) Diagram of a block detector composed of a scored scintillator block coupled to a 2×2 array of PMTs. (b) An example light distribution produced by the cut scintillator block in an interaction.	16

2.7	Fundamental limits of PET. (a) Range effect results in the reconstructed line of response (LOR) passing through the annihilation point which is some finite distance away from the emission point. (b) non-collinearity of emitted photons results in the reconstructed LOR not passing through the annihilation point.	17
2.8	(a) The angle of approach of an electron towards a positron which is at rest. (b) The deviation from collinearity due to the momentum vector P.	17
2.9	Illustration of the parallax effect increasing as a function of the radial position of an annihilation event. The solid blue and red lines represent the real LOR associated with the annihilations. The dashed lines represent the uncertainties on the measured LOR due to the parallax effect.	18
2.10	Noise effects introduced by interactions with a patient's body. (a) Compton scatter in the body causes a false LOR. (b) It is possible that only single events are recorded from single annihilation.	20
2.11	Diagram showing the principle of TOF-PET. The offset, Δx , is calculated using the difference in arrival times of the photons at detector elements A and B.	22
2.12	Diagram shown the probability distributions of the photon annihilation position along the LOR in the case of (a) Conventional PET (b) TOF-PET. Here a voxelisation of the LOR is considered with an element length, d.	23
2.13	A projection, $p(s,\phi)$, is formed from integration along all parallel LORs at an angle ϕ . The projections are organized into a sinogram such that each complete projection fills a single row of ϕ in the sinogram. In this format, a single point in $f(x,y)$ traces a sinusoid in the sinogram.	25
2.14	Illustration showing the projection of a two-dimensional data set into a one-dimensional slice via the Radon transform, and the two-dimensional Fourier-slice theorem. The right hand illustration represents the equivalence between the one-dimensional Fourier transform of a projection at angle ϕ and the central-section at the same angle though the two-dimensional Fourier transform of the object.	26

3.1	Basic scheme of three major stages involved in scintillation.	32
3.2	Types of luminescent centres in inorganic crystals. Left: A STE luminescence. Right: A doped luminescence.	33
3.3	(a) Absorption and emission spectra of LSO crystal. (b) Configuration coordinate diagram of an inorganic crystal. The curves g and e represent the ground and excited states respectively.	35
3.4	Definition of detector energy resolution. For peaks whose shape is Gaussian with standard deviation σ , the FWHM is given by 2.35σ	37
3.5	Probability distributions relating to the production of the n^{th} photoelectron at the detector for (a) Single exponential scintillator response model and (b) Bi-exponential scintillator response model.	42
3.6	Diagram of the propagation of a scintillation photon in a LYSO crystal, with θ the initial axial angle of propagation. L is the total length of the crystal, while x_0 is the distance of the photon emission point to the face of the crystal. LYSO has a refractive index $n_{LYSO} = 1.81$, the optical grease has $n_{grease} = 1.4$	44
3.7	Reflection and refraction at the scintillator / air interface.	45
4.1	Schematic diagram of a typical PMT. All major physical components are labelled.	48
4.2	Schematic representation of a p-n junction.	50
4.3	Schematic diagram of a reverse biased semiconductor photodiode. Shorter wavelengths will be absorbed closer to the surface, creating more complicated conditions for the achievement of high quantum efficiency.	51
4.4	Schematic diagram of the internal structure of an APD including the corresponding electronic field distribution and net carrier concentration as a function of depth.	52
4.5	Operational principle of an APD showing the three specific gain regions. . .	53
4.6	(a) A photograph of a Hamamatsu SiPM of 1 mm^2 active area with 400 APD microcells. (b) Topology of a GM-APD showing surface connections and junction structure.	54

4.7	(a) A schematic representation of the electrical circuit of a SiPM. Here five microcells are represented by a diode in series with a quenching resistor, activated pixels are shown with lightning symbols. The response of each active pixel is summed to produce the full SiPM response. (b) An illustration of a SiPM response to a temporally spread incident photo-flux, similar to that from a scintillator crystal.	56
4.8	A diagram showing a example circuit for (a) A SiPM diode array and (b) an avalanche microcell.	57
4.9	Shape of GM-APD current response to an avalanche event.	58
4.10	Equivalent SiPM circuit with additional bias circuit as recommended by Hamamatsu, as described in text.	59
4.11	Shape of SiPM current response to an avalanche event.	60
4.12	Avalanche triggering probability as a function of photogeneration position.	63
4.13	Schematic view of tunnel excitation. Left: Energy bands in the presence of an electric field. An electron can tunnel through the forbidden band from the p-layer to the n-layer resulting in a free electron-hole pair. Right: The potential barrier between the valence band of the p-layer and the conduction band of the n-layer can be approximated by a triangular shape.	65
4.14	An illustration showing some possible signals due to a single photon activation in the SiPM. The second pulse is double the amplitude of a single cell activation and is a result of optical cross-talk. An after pulse is shown on the falling edge of the third pulse which shows a reduced gain due to recharging effects.	66
4.15	Non-linear response to a 40 ps laser light signal for SiPMs with different numbers of GM-APD cells.	68
4.16	(a) Photon arrival time of a 830 nm photon emitted from a 20 ps pulse width as measured by a GM-APD. (b) Sketch of the avalanche generation by a photon absorbed in the depletion layer and by a photon absorbed in a neutral region nearby.	69

4.17 (a) Reverse bias as a function of device temperature for a constant gain for Hamamatsu S10362-11-050C (b) Gain as a function of device temperature for a constant reverse bias for Hamamatsu S10362-11-050C.	70
4.18 Signal types: (a) continuous (b) discrete-time signals.	71
4.19 An example of frequency aliasing. The continuous signal being sampled is shown in black, an alias deriving from the under-sampling of the original signal is given in grey.	72
4.20 Comparison between a 3 bit and 16 bit ADC resolution.	73
4.21 Diagram detailing the gain and frequency response of a typical lowpass filter.	75
4.22 Filter characteristics of digital filter designs used in Chapters 5 and 6. (a) Frequency specifications (b) Filter response to step change.	76
4.23 Schematic representation of the upsampling process. (a) The initial discrete time signal to be acted on. (b) The original signal is padded with L-1 sample points. (c) The padded signal is filtered with a low pass filter to give an estimate of the underlying continuous signal.	77
5.1 Mechanical arrangement used for characteristic measurements with fast LED signal, not to scale.	82
5.2 Schematics of the bias circuit for fast timing. The values of the components are $R_1 = 3.3 \text{ k}\Omega$, $R_2 = 10 \text{ k}\Omega$, $R_3 = 51 \text{ }\Omega$, $R_s = 50 \text{ }\Omega$, $C_1 = 100 \text{ nF}$, $C_2 = 470 \text{ nF}$, $C_3 = 100 \text{ nF}$	83
5.3 Schematics Photonique AMP_0611 amplifier. The values of the components are $R_1 = 1 \text{ k}\Omega$, $R_2 = 1 \text{ k}\Omega$, $C_1 = 10 \text{ nF}$, $C_2 = 10 \text{ nF}$	84
5.4 Response of Hamamatsu S10362-33-050C to fast LED signal (a) Unfiltered pulse used to calculate the σ_{noise}^{rms} . (b) Filtered pulses used to calculate pulse height, V_{pulse}	86
5.5 (a) Example filtered pulses measured with Photonique 0710G9MM-PCB device with a bi-exponential fit. (b) Example filtered pulses measured with Hamamatsu S10362-33-050C with a single-exponential fit.	87
5.6 Example trigger and SiPM pulse pair used to calculate the intrinsic timing jitter. Linear fits to the leading edges are shown in red.	88

5.7	Signal-to-noise ratio plotted as a function of pixel size. The different colour and marker symbol series differentiate the device manufacturer.	90
5.8	Rise time plotted as a function of pixel size. The different colour series and marker symbols differentiate the device manufacturer.	91
5.9	Fall time plotted as a function of pixel size. The different colour series differentiate the device manufacturer.	93
5.10	Timing jitter plotted as a function of pixel size. The different colour series differentiate the device manufacturer.	95
6.1	Photograph of the mechanical arrangement designed for coupling a S10362-33-050C SiPM to a scintillator crystal. An example SiPM device is shown on the far left. In the centre two identical SiPM holders are positioned to show both the front and back faces where the SiPM and LYSO crystal arrangement are respectively coupled. Finally a $3\times 3\times 5$ mm ³ LYSO crystal, painted in TiO ₂ paint, is shown in the plastic casing used to both centre and secure the crystal in the holder.	102
6.2	Example gamma spectra measured in electronic coincidence for (a) crystals wrapped in PTFE tape (b) crystals painted with TiO ₂ paint. Gaussian fits to the measured photopeak are shown as thick green or blue coloured lines.	104
6.3	An example pulse from within the photopeak FWHM is plotted as recorded and after applying both a 5 th order equiripple filter ($f_c = 500$ MHz) and a 2 nd order Butterworth filter ($f_c = 350$ MHz). The zoomed image in the top right hand corner compares the response of the raw and processed signals to the highest gradient signal change.	105
6.4	A plot of the timing resolution as a function of leading edge discriminator position for a coincident system of $3\times 3\times 5$ mm LYSO crystals, painted with a reflective TiO ₂ paint and read out by Hamamatsu S10362-33-050C SiPMs. The three colour distributions define the processing techniques applied to the recorded pulses before triggers were applied.	106
6.5	Schematic diagram showing the experimental arrangement applied for DOI measurements.	108

6.6	Photographs showing a $4 \times 4 \times 20$ mm ³ LYSO crystal painted with TiO ₂ paint connected to coupling tools used to DOI experiment (a) side view (b) top view	110
6.7	Example pulse height spectra as measured at a number of beam positions along the crystal length (a) -10 mm relative to the crystal's centre (b) +10 mm relative to the crystal centre (c) -8 mm relative to the crystal centre (d) +8 mm relative to the crystal centre (e) -2 mm relative to the crystal centre (f) +2 mm relative to the crystal centre. Fits are shown as thick coloured lines: blue = Channel 1; green = Channel 2. Channel 1 and Channel 2 are positioned at -10 mm and 10 mm respectively.	112
6.8	Distributions of the energy characteristics as measured by fits to gamma spectra produced at step points along the length of a $4 \times 4 \times 20$ mm crystal. (a) Photopeak energy distribution (b) FWHM of the measured photopeak	113
6.9	Distribution of CTR as a function of DOI measured at step points along the length of a $4 \times 4 \times 20$ mm crystal. A range of distributions are given relating to different trigger threshold position on the leading edge between 3-10 % of the photopeak equivalence energy.	114
7.1	Diagram of a coincident detector elements.	118
7.2	Schematic diagram showing the simulated geometry of a coupled LYSO and SiPM PET detector system. The diagram is not to scale.	122
7.3	Diagrams outlining (a) The four reflection types which can be assigned probability weightings in the UNIFIED model (b) The micro-facet distribution which produce a Gaussian distributed range of reflections with respect to the average surface normal.	125
7.4	Diagram showing ground back painted surface type.	126
7.5	A simulated single pixel current response as defined by equation 7.3.2 ($t_a = 10$ ns) and the parameter set given in Table 7.3.	130
8.1	Comparative plots of normalised theoretical and simulated photon arrival distributions (a) Single exponential model (b) Bi-exponential model. The parameters applied to the theoretical considerations are quoted on the plots.	134

8.2	Illustration of a coincident detector system about a point source.	135
8.3	Comparison of example photopeak pulse pairs from simulation and experimental measurements. (a) Example raw, unprocessed experimental and simulated pulses pairs (b) Pulse height spectra as measured from digitally filtered pulse pairs.	136
8.4	Timing resolution as a function of leading edge discriminator position for a coincident system of 3×3×5 mm LYSO crystals, painted with a reflective TiO ₂ paint and read out by Hamamatsu S10362-33-050C SiPMs. The three colour distributions define the processing techniques applied to the recorded pulses before triggers were applied. (a) Simulated system response (b) Experimentally measured system response.	139
8.5	Selected simulation response parameters plotted as a function of single pixel dead time (a) Coincidence timing resolution (b) Energy resolution.	142
8.6	Comparison plot showing simulated photopeak pulses with three separate dead times.	143
8.7	Selected simulation response parameters plotted as a function of PDE (a) Coincidence timing resolution (b) Energy resolution.	144
8.8	Selected simulation response parameters plotted as a function of surface roughness (σ_α) (a) Coincidence timing resolution (b) Energy resolution.	146
8.9	Example pulse height spectra ($\alpha = 1.3$) as measured at a number of beam positions along the crystal length (a) -10 mm relative to the crystals centre (b) +10 mm relative to the crystal centre (c) -8 mm relative to the crystal centre (d) +8 mm relative to the crystal centre (e) -2 mm relative to the crystal centre (f) +2 mm relative to the crystal centre. Fits are shown as thick lines coloured relative to the distribution represented.	149
8.10	Comparison of experimental and simulated photopeak energy. Values of each trace have been normalised relative to the 8 mm beam position for comparison.	150

8.11	Coincidence timing resolution as a function of absolute position along x-axis (a) Experimental CTR results (b) Simulated CTR ($\sigma_\alpha = 1.3$) (c) Result measured at 4% trigger levels for each simulated surface roughness compared to the equivalent experimental distribution.	152
8.12	Comparison of simulated and experimental CTR distributions as a function of leading edge discriminator position. Coincident pulse pairs for both data sets were filtered with a 2^{nd} order Butterworth filter, $f_c = 350$ MHz. Uncertainties quoted on the simulated result are the propagation of statistical and fitting uncertainties with $FWHM_{PDE}$ and $FWHM_{SR}$	153
9.1	GEANT4 visualizations of the geometric crystal arrangements considered for the prototype detector arrays. In these 5 mm and 10 mm crystal are shown in yellow and blue respectively. (a) Full 5 mm (b) Full 10 mm (c) Blocks (d) Mixed (e) Columns (f) Rows.	157
9.2	Diagram showing the overhead view of a coincident array simulation. A point source with an angular emission distribution restricted to the blue cones is shown at the central position, 15 cm from each array. The crystal arrangement in the coincident arrays is equivalent to Columns as shown in Figure 9.1.	159
9.3	Energy results measured using the crystal length channels (a) Example gamma spectra as measured with the mixed array arrangement, fits to the two data sets are shown as a continuous line. (b) Energy resolution of 5 mm and 10 mm detector elements as measured for each crystal arrangement.	161
9.4	Coincidence timing resolution plots (a) Coincidence timing resolution as a function of trigger position on the leading edge. Coloured traces represent the different crystal arrangements. (b) Results measured at the 2% threshold for each of the crystal arrangements.	164
9.5	Coincident event pulse height correlations for pulse pairs passing initial energy cuts. (a) Full 5 mm (b) Full 10 mm (c) Heads (d) Mixed arrays.	165
9.6	Coincident detection efficiency as a function of number of activated detector elements in a full energy deposition.	167

9.7	Energy results plotted as a function of crystal length (a) Mean photopeak energy. Linear fits are applied to the 7-50 mm range (b) Photopeak FWHM. (c) Energy resolution. For both (b) and (c) lines are plotted connecting the points in each data series as a guide for the eye.	171
9.8	Coincidence timing resolution plots (a) CTR distributions as a function of trigger position on the leading edge for each crystal arrangement. (b) Results as measured at the 2% threshold for each of the crystal arrangements. Here error bars are given relating to the uncertainty associated with the measurement and the additional convolution of uncertainties related to the simulation input parameters.	174
9.9	Coincident detection efficiency plots (a) Coincidence detection efficiency as a function of number of activated detector elements for each crystal length (b) Efficiency gains associated with application of the three-detector event as a function of crystal length.	175
9.10	(a) Diagram of a typical Compton scatter event (b) Example distribution of absolute energy deposits as recorded in simulated three-detector events with 10 mm crystal arrays.	177
9.11	(a) Pulse height spectra for three-detector events including fit results to the photopeak and the summed scatter peak. (b) Linearity response of the simulated 10 mm crystal length detector system.	179
9.12	Coincidence timing resolution plots (a) CTR as a function of trigger position on the leading edge for each crystal arrangement. (b) Results as measured at the 2% threshold for each of the crystal arrangements. Here error bars are given relating to the uncertainty associated with the measurement and the additional convolution of uncertainties related to the simulation in put parameters.	181
9.13	Diagram showing the parallax uncertainty introduced by the finite detector dimensions.	182
9.14	(a) Diagram showing reconstructed angles in ϕ as a result of a three-detector event. To calculate ϕ_{avg} , the central y-coordinate between the two activated pixels is considered. (b) Rings of detector elements projected about a scatter event. In this case the scatter has been contained within ring 1.	183

9.15	Histograms showing residuals of real and reconstructed emission angles (a) Angular resolution in both θ and ϕ for two-detector events for a system populated with 10 mm crystals. This defines the ultimate angular resolution of the system for this crystal length. (b) Angular resolution in θ and ϕ for a system populated with 10 mm crystals. One ring spatial acceptance window. (c) Angular resolution in θ and ϕ for a system populated with 10 mm crystals. Two ring spatial acceptance window. (d) Angular resolution in θ and ϕ for a system populated with 10 mm crystals. Three ring spatial acceptance window.	185
9.16	(a) FWTM resolution in θ as a function of crystal length. (b) FWTM resolution in ϕ as a function of crystal length.	186
9.17	FWTM efficiency plots. (a) Absolute FWTM detection efficiency after both energy and spatial cuts. (b) Efficiency gains associated with the application of three-detector events as a function of crystal length.	188

Chapter 1

Introduction

Since the late 1890's, when the very first clinical X-ray image was produced to diagnose a broken wrist in a man who had fallen over ice-skating [1], photons with energies in the keV-MeV range have been used to image human anatomy. In these early scans photographic plates were applied to measure the intensity distribution of the X-rays passing through a patient. This method would require the patient to be almost completely motionless for an hour or more while exposed to an extremely high flux of X-ray photons, a situation which was both uncomfortable and unhealthy. With advances in X-ray detector technology, first with improved photographic plates and then with semiconductor technologies, patient dose rate and exposure times have been reduced by orders of magnitude, with equivalent improvements in the image contrast and spatial resolution.

In this work we investigate the application of a relatively new photodetector technology, the silicon photomultiplier (SiPM), for use in the nuclear imaging modality, positron emission tomography (PET). These sensors are solid-state devices consisting of an array of pixel elements, each of which can be activated independently by an impinging optical photon. One of the key characteristics of the silicon photomultiplier is the high electric field which is established within the active volume of each pixel. By applying an increased field strength relative to other solid state detector technologies, an *avalanche* of charge carriers can be created in response to a photon interaction in the active volume. The avalanche mechanism can typically result in gains of the order of 10^6 and is developed in a time-scale estimated to be of order 20 ps [2]. By applying fast detector systems, a modality of PET known as time-of-flight (TOF) can be exploited. This mode can improve the quality of a reconstructed image without increasing the dose to the patient.

The work presented in this thesis applies detector system simulations, validated against experimental measurements, to investigate the use of SiPM detectors in a prototype TOF-PET detector system. There are a number of steps which are considered in this process. Firstly, characteristic measurements performed on a number of SiPM devices are presented and a candidate device for use in the prototype system selected. Secondly, a simulation framework has been developed which can predict the timing response of a coupled SiPM and scintillator detector system. Finally, this simulation framework is applied to provide design recommendations which have been used to optimise the performance of the prototype detector system, to be built at the Rutherford Appleton Laboratory (RAL), UK. The object of this prototype system is to improve on the coincidence timing resolution of current generation TOF-PET clinical machines, where a performance of ≈ 500 ps is typical [3].

Chapter 2

Positron Emission Tomography

Positron Emission Tomography (PET) is a functional medical imaging technique which is widely applied to investigate the metabolic activity of a patient. The properties of positron emission, occurring through β^+ nuclear decay, are used to produce accurate images of the distribution of positron-emitting radiopharmaceuticals (or ‘tracers’) within a patient’s body. There are a number of tracers available clinically, the choice of which depends on the metabolism of the tissue or process of interest. To date, PET has been used in a broad scope to characterise brain diseases such as Alzheimer’s [4] and epilepsy [5], and for cardiac diseases such as coronary artery disease [6]. However, the major application of PET is in oncology, where tumours can be imaged for use in both treatment planning and disease detection [7]. In this chapter an overview of PET as a technique is given, including a discussion of: the physical principles on which it is based, β^+ decay and radioisotopes, interactions of gamma-ray photons with matter, methods and limitations for detecting coincident annihilation photons, and an overview of two major reconstruction techniques. A section is then dedicated to describing the time-of-flight (TOF) modality of PET. Designing a prototype TOF-PET detector system is one of the main goals of the work presented in this thesis and as such details of the quantitative signal gains associated with the technique are discussed. Finally a brief overview discussion is presented on standard reconstruction techniques for PET data sets.

2.1 Technique overview

PET is a molecular imaging technique which provides images of functional processes within a patient. The basic principle of operation is different to transmission technologies where

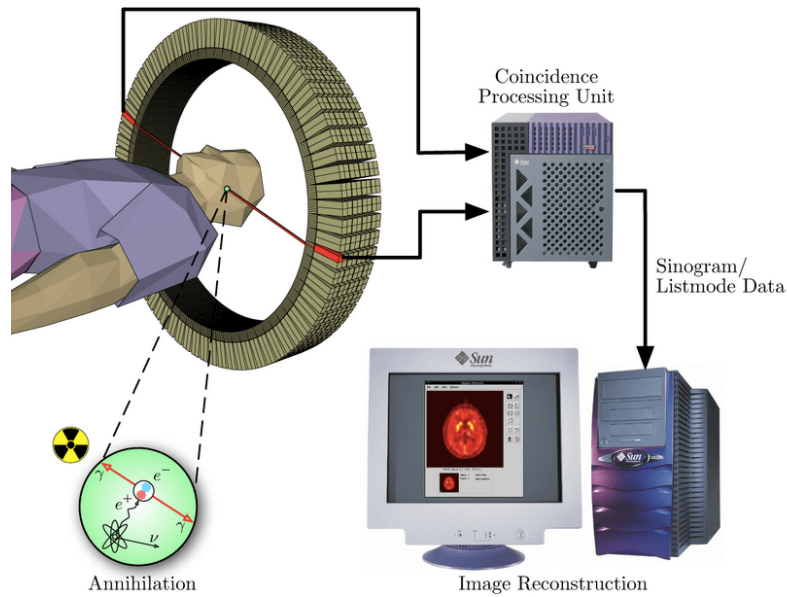


Figure 2.1: A diagram outlining the basic principles of PET including: annihilation of a positron in patient, emission of co-linear photons, detection and storage of electronic coincidence and reconstruction of detected LORs [8].

an image is reconstructed from a beam of radiation transmitted through a patient. With transmission techniques the image represents the three dimensional attenuation properties of biological tissue. Conversely, in PET, a positron-emitting radiopharmaceutical is injected into the patient and spreads physiologically in the body. The key steps associated with the PET process are presented in Figure 2.1. Here the tracer has been given time to spread though the body and has amassed in a region of interest, in this case in the patient’s head. Positrons emitted through β^+ decays of the radiopharmaceuticals radioactive isotope annihilate with electrons in the surrounding tissue, resulting in a pair of 511 keV gamma photons, emitted collinearly so as to conserve total momentum. These photons are then detected by a ring of detector elements centred about the patient, the signals passed to a processing unit and the energy and timing characteristics are analysed in order to establish a correlation between coincident events and a single annihilation event. If the selection criteria (or *cuts*) are satisfied then a line-of-response (LOR) can be inferred between the coincident detector elements described by 2D polar coordinates; s and ϕ , as defined in Figure 2.2. A tomographic image is then reconstructed using the data set recorded in a scan through either analytic or statistical techniques.

In the history of commercial PET scanners, several configurations of detector arrays have been used, including detectors mounted on a rotating gantry, in a circular ring or a polygonal ring. Modern scanners apply a circular ring configuration where typically 16 to 32 independent rings form a cylindrical detector volume which monitors the annihilation pho-

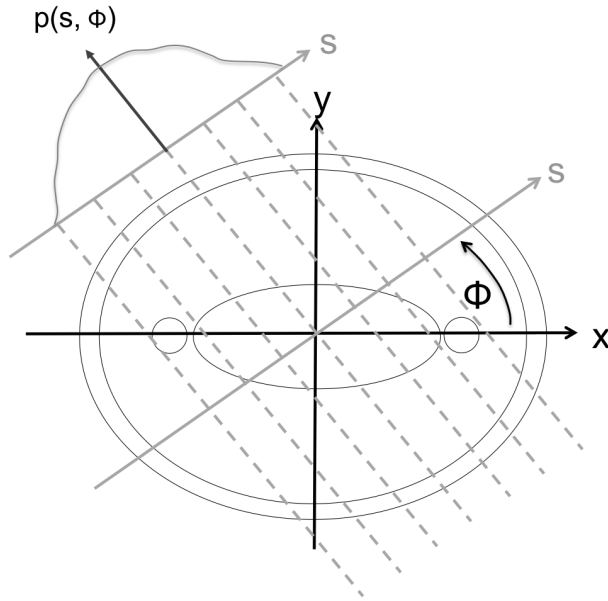


Figure 2.2: A diagram outlining the standard 2D coordinates system used in PET data acquisition. The intensity distribution, $p(s, \phi)$, develops over the duration of a scan and is passed to reconstruction algorithms, to be discussed in section 2.6.

tons emerging from the patient, or ‘source’. Due to the effects of high-energy radiation on the patient, the maximum source activity available for a scan is restricted. A circular ring structure provides the maximum angular coverage of the source volume, maximising the detection efficiency of the system. Applying a number of independent rings then increases the total field of view (FOV) of the system, allowing for a larger volume to be imaged simultaneously and adding a third dimension to the data set.

With a limited source activity available one of the most significant limitations of PET detector systems is the total signal statistics acquired during a scan. Signal statistics can be improved in a number of ways, most obviously by applying more efficient detector materials. However, this method tends to be expensive, requiring an increase in either volume or density. The focus of the work presented in this thesis is to apply a fast timing detector system where the time-of-flight (TOF) can be used to improve the signal-to-noise of the statistical signal, resulting in an improved image quality for an equivalent level of statistics. This modality is known as TOF-PET and is available in current generation clinical PET systems with a coincidence timing resolution of 527.5 ± 4.9 ps [3]. A key objective of the work presented here has been to provide design recommendations for a prototype system which can improve on the coincidence timing resolution of current generation clinical PET detector systems.

2.2 Positron emission and radioisotopes

In view of the considerations just discussed, the first step in the PET process is the selection and production of a suitable molecular probe. In general, low atomic number nuclei are chosen to label the biological molecule of interest due to the ease with which they are absorbed by the body. Positron emitters are neutron-deficient isotopes that achieve stability through the conversion of a proton into a neutron. This process involves the weak process emission of a positive electron, or positron (e^+) and an electron neutrino (ν_e) from a parent nucleus with mass and atomic number A and Z respectively:



There are two physical parameters of fundamental importance when selecting a candidate radioisotope for PET: the range of the emitted positron in tissue (typically considered to be equivalent to water) and the half-life associated with the radioactive decay.

The range of a positron emitted in the patient, often referred to as the *range effect*, is typically quoted as either the upper limit of the travel distance prior to annihilation (R_e) or the root mean squared of all possible paths (R_{rms}). The effect itself derives from the finite kinetic energy associated with positron emission in the β^+ process. The cross section of electron-positron annihilation is inversely proportional to the momentum of the combined electron-positron system [9], hence the kinetic energy must be reduced, possibly to zero, before annihilation will occur. Emitted positrons will therefore travel some distance through the surrounding media before their associated kinetic energy is lost and annihilation is most probable. This effect introduces a fundamental limitation to the spatial resolution of the system as a detector system will reconstruct the annihilation position of the positron, not the emission position.

The half-life of the isotope must also be considered. A scan conducted in a current generation clinical PET machine will typically take of the order of ten minutes. The source should therefore decay rapidly on an equivalent timescale to avoid a prolonged patient exposure. The key characteristics of some of the commonly used isotopes are given in Table 2.1, where half-lives between one and more than a hundred minutes are shown.

It is, however, the chemistry and the difficulty of synthesising a suitable molecular probe

which most often drives the final candidate radioisotope selection. The most widely used molecular probe in clinical PET is Fluorodeoxyglucose (^{18}F -FDG), which is predominantly applied in oncology to study tumours where characteristically high metabolic rates lead to glucose accumulating in high concentrations [10]. Although ^{18}F has a low electron range in water, and so is not significantly limited by the range effect, the half-life is long compared to other candidate isotopes. The selection of ^{18}F in this case has been made due to the ease with which FDG can be synthesised using the ^{18}F isotope. This process is both fast, which is key due to half-life considerations of all candidate radioisotopes, and inexpensive. The extensive application of ^{18}F -FDG is ultimately due to the ease and cost of synthesis, not detailed considerations of the comparative characteristic parameters.

Table 2.1: List of PET radioisotopes and their key parameters. R_e refers to the maximum extrapolated positron range in water and R_{rms} the root mean square range. Selected values taken from [11].

Radioisotope	Half-life [mins]	Max β^+ Energy [MeV]	β^+ range in water [mm]	
			R_e	R_{rms}
^{11}C	20.4	0.96	3.9	0.4
^{13}N	9.96	1.2	5.1	0.6
^{15}O	2.05	1.7	8.0	0.9
^{18}F	109.7	0.64	2.3	0.2
^{62}Cu	9.74	2.9	15	1.6
^{68}Ga	68.4	1.9	9	1.2
^{82}Ru	1.3	3.4	18	2.6

2.3 Interactions of high energy photons with matter

In order to develop a detector system for the photons pair produced in an electron-positron annihilation event, it is important to understand how these photons interact with matter. The first concept to consider is the attenuation of a beam of photons traversing some material. This can be effectively described by an exponential decay law, where the rate at which photons are removed from the initial count through either scatter or absorption processes, is defined by the linear attenuation coefficient ($\mu_{att,l}$), typically expressed in units of cm^{-1} . The intensity profile of a beam of photons after interaction with a medium

of thickness x , will hence follow:

$$I = I_0 e^{-(\mu_{att,l}x)}, \quad (2.3.1)$$

where I_0 is the initial beam intensity and $\mu_{att,l}$ is the characteristic linear attenuation coefficient of the material. For a given thickness, the probability of interaction is dependent on the number of atoms per unit volume. This dependency can be overcome by normalizing the linear attenuation coefficient for the density of the material. The linear attenuation coefficient, normalized to unit density, is called the *mass attenuation coefficient* which is in turn related to the cross section for all possible scattering or absorption processes (σ_{tot}) via:

$$\mu_{att,m} = \frac{n_A}{\rho} \sigma_{tot} [cm^2 g^{-1}], \quad (2.3.2)$$

where ρ is the density of the material being traversed and n_A is the number of atoms per volume. The most probable processes contributing to the total linear attenuation at energies of 10 keV and above are:

- Photoelectric effect;
- Compton scattering;
- Pair production (at energies above 1.022 MeV).

The total attenuation cross section for photons of 10 keV and above can then be approximated as the linear combination of the contributions from each of these three effects:

$$\sigma_{tot} = \tau_{p.e.} + \mu_{Compton} + \kappa_{pair}, \quad (2.3.3)$$

where $\tau_{p.e.}$, $\mu_{Compton}$ and κ_{pair} refer to the interaction probabilities of the photoelectric effect, Compton scatter and pair production respectively. These three processes are described in detail below.

For completeness, it should be noted that, at energies below the 10 keV limit considered here, both Thomson scattering (where photons scatter through direct interaction with electrons) and Rayleigh scattering (where the scatter occurs through interaction with an atom) become increasingly probable and must be considered in σ_{tot} . Both processes are

typically referred to as coherent scatter as they result in a change of direction of the original photon, but with no energy exchange between the incident photon and matter. The cross sections associated with these processes at 511 keV are extremely small compared to $\tau_{p.e.}$, $\mu_{Compton}$ and κ_{pair} and so are discussed in no further detail in what follows.

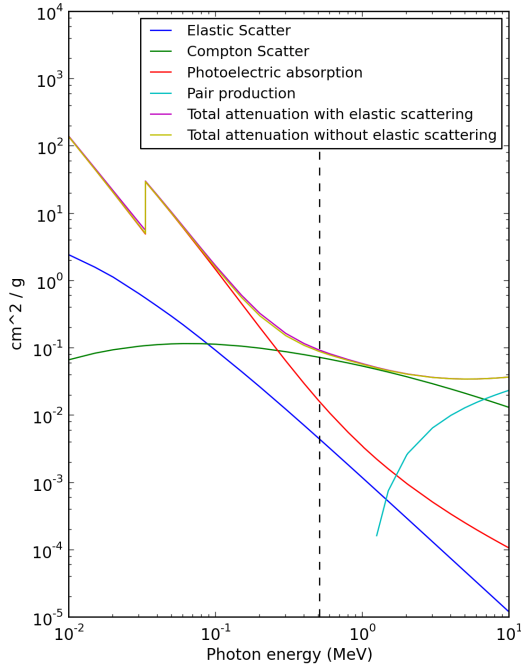
2.3.1 Photoelectric absorption

In photoelectric absorption a photon interacts with an atom and in the process is completely absorbed. The energy of the absorbed photon, $h\nu$, is then transferred to an electron bound to one of the atomic shells of the absorber atoms, which is in turn ejected from the atom. This process is possible whenever the energy of the incident photon is greater than the binding energy of the atomic electrons, E_b . In general electrons liberated from bound shells through interactions with photon are referred to as photoelectrons (p.e.). Through conservation of energy and momentum, the kinetic energy (E_{e^-}) of a photoelectron produced via photoelectric absorption is then:

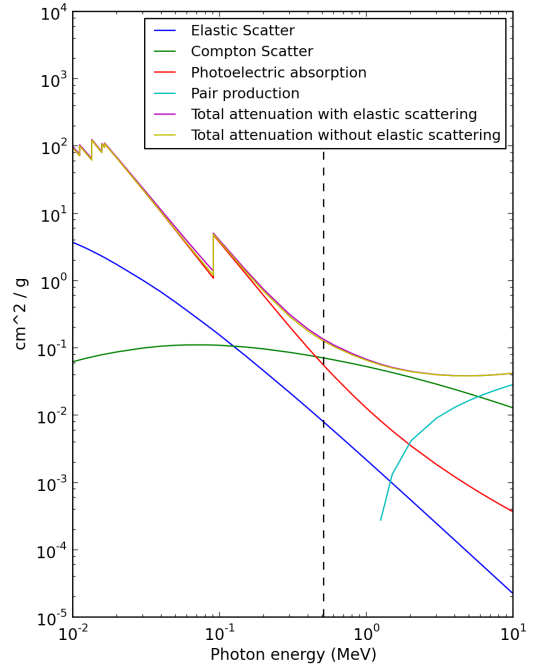
$$E_{e^-} = h\nu - E_b. \quad (2.3.4)$$

In this process, a small recoil energy is absorbed by the atom so as to conserve momentum. As a result, photoelectric absorption cannot act on a free electron and the cross section scales with the binding energy of an electron. When the energy of the incident photon coincides with the ionisation energy of specific atomic electron shell the probability of photoelectric absorption can be strongly influenced. An observation of this effect is given in the mass attenuation plots in Figure 2.3 where *absorption edges* seen in the Photoelectric absorption coefficient can be used to identify the binding energies of the different electron shells and sub-shells in a specific material. In the case of the 511 keV photons of interest in PET, the energy of the incident photon is well above that of the atomic shell structure of most materials. Photoelectric absorption interactions are therefore likely to occur with electrons in the most tightly bound K-shell of an atom [9].

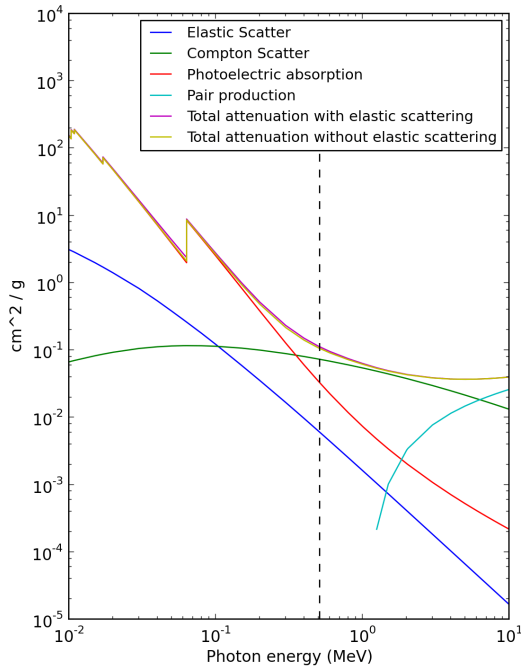
In addition to photoelectron emission, the interaction also creates an ionized atom which rapidly fills the vacancy in one of its bound shells. An electron is then captured into the vacant K-shell either from a free electron available in the surrounding material or by rearranging the remaining bound atomic electrons to a more energetically favourable state. As a result one or more X-rays will be produced with energies characteristic to the specific



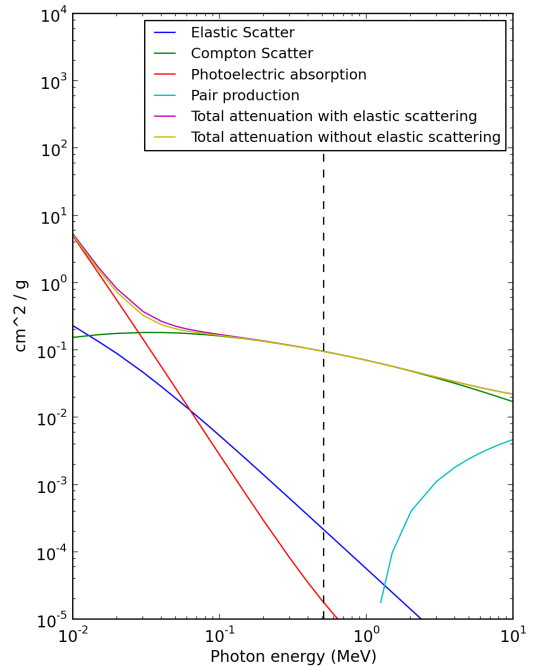
(a) NaI ($Z = 50$)



(b) $\text{Bi}_4\text{Ge}_3\text{O}_{12}$ ($Z = 75$)



(c) $\text{Lu}_{1.8}\text{Y}_{0.5}\text{SiO}_5$ ($Z = 66$)



(d) H_2O ($Z = 6$)

Figure 2.3: Mass attenuation coefficients for some materials of interest for the analysis discussed later in this document. A vertical dashed line indicates a photon energy of 511 keV. Data sets were obtained from [12].

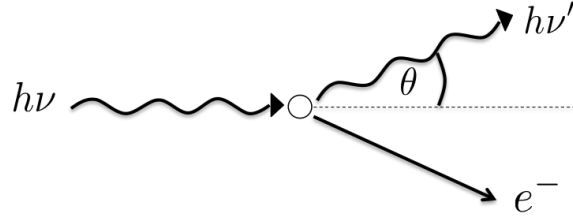


Figure 2.4: Illustration of a Compton scatter event. The diagram shows the incident photon of energy $h\nu$ interacting with a electron which is considered at rest. The scattered photon with energy $h\nu'$ scatters at an angle θ relative to the original momentum vector.

atom's excited state. These secondary emissions are by nature of lower energy than the original interaction, often in the range 10-50 keV [9], and are re-absorbed close to the emission site.

The binding energies of atomic electrons are known to range from 13.6 eV for ^1H to >100 keV for ^{92}U [13]. With binding energies varying over five order of magnitude over a range of atomic numbers (Z) defined by the periodic table (1-92 for natural elements), there is no definitive analytic expression to describe the photoelectric interaction probability, τ . However an approximation can be given as [9]:

$$\tau \propto \frac{Z^n}{E_\gamma^{3.5}}, \quad (2.3.5)$$

where n varies between 4 and 5 over the E_γ range of interest. The strong dependence of photoelectric absorption on the atomic number correlates with an increased range of binding energies associated with a large number of electron shells [13]. Materials with a high atomic number Z therefore maximise the probability of interactions through the photoelectric effect.

2.3.2 Compton Scattering

Compton scattering is the predominant interaction of 511 keV gamma-ray photons in soft tissue. Due to its high water content, tissue is often simply modelled as H_2O . The mass attenuation coefficients given in Figure 2.3d can therefore be considered an approximation of the attenuation characteristics of a patient's body and it is clear that Compton scattering is the overwhelmingly dominant interaction process.

Unlike photoelectric absorption, where a photon interacts with an atom as a whole, Compton scatter interactions can conserve momentum without a recoil off an additional body

and therefore are most likely to occur between photons and weakly bound *valence shell* electrons. In a Compton scatter event the incoming photon is deflected through an angle (θ) with respect to its original path. The photon transfers a portion of its energy to the electron, which recoils conserving the total momentum of the system. In such an interaction all scattering angles are possible and hence the energy transferred to electron can vary from approximately zero to a large fraction of the photon energy, $h\nu$. A schematic diagram of this interaction is given in Figure 2.4. The energy of the scattered photon can be calculated from the energy of the incident photon and the angle of the scattered photon, as follows [9]:

$$h\nu' = \frac{h\nu}{1 + \frac{h\nu}{m_0c^2}(1 - \cos\theta)}, \quad (2.3.6)$$

where m_0c^2 is the rest-mass energy of the electron (511 keV). Hence energy transfer is maximal at $\theta = \pi$ and minimal at $\theta = 0$. However, it should be noted that even in the extreme $\theta = \pi$ case not all energy is transferred to the scattered electron. Through conservation of energy, the energy transferred to the electron is given by:

$$E_{e^-} = h\nu - h\nu' = h\nu \left(\frac{(h\nu/m_0c^2)(1 - \cos\theta)}{1 + (h\nu/m_0c^2)(1 - \cos\theta)} \right). \quad (2.3.7)$$

The probability of Compton scatter depends on the number of electrons available to the photon to scatter off, and therefore increases linearly with Z . The differential cross section of photons scattered from a single electron is predicted in full by the Klein-Nishina formula [9]. However, this can be simplified to approximate a dependence of the Compton scatter probability in terms on Z and E_γ :

$$\sigma_{Compton} \propto \frac{Z}{E_\gamma}. \quad (2.3.8)$$

2.3.3 Pair production

While the process is below threshold at photon energies of 511 keV, a description of pair production is included here for completeness. Pair production is the conversion in matter of a high energy photon into an electron-positron pair. The rest mass of both electrons and positrons (m_0c^2) is 511 keV and the threshold energy for pair production is then $2 \times 511 \text{ keV} = 1.022 \text{ MeV}$. However, as shown in Figure 2.3, the probability of the process remains

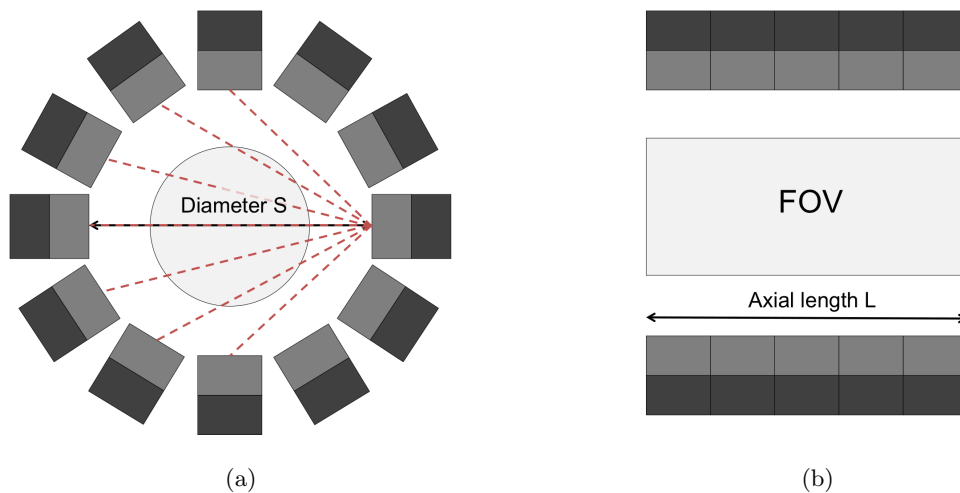


Figure 2.5: Schematic view of a PET detector arrangement. (a) Cross sectional view as seen from the front. The ring diameter S is shown along with a ‘fan’ illustrating the range of detector modules which are considered in coincidence relative, in this case, to the central right module. (b) A view from above showing the total field of view (FOV) and the axial detector length (L) given by five separate detector rings.

low until photon energies reach several MeV. Similarly to the photoelectric effect, pair production requires the presence of another charged, massive object in order to conserve the momentum of the system through recoil interactions and can therefore only occur in matter. No simple expression exists for the probability of pair production per nucleus, but its magnitude varies approximately as [9]:

$$\kappa_{pair} \propto Z^2 E_\gamma. \quad (2.3.9)$$

2.4 Detection of coincident photons

As discussed briefly in the technique overview, clinical PET detector systems consist of a ring structure, typically comprising of 16 to 32 independent detector rings in a cylindrical detector volume. An illustration of a typical ring and an extended detector volume including five rings is given in Figure 3.3 where the two projections (lateral and frontal) of the setup are shown. In a ring configuration, each module of detector elements is typically operated in coincidence with approximately half of the total modules on the opposing side of the detector, creating a ‘fan’ of lines-of-response (LOR) as shown Figure 2.5a. LORs lying outside the fan do not bisect the source volume and so are not considered.

As shown in Figure 2.5a, each module within the ring is a system of scintillating crystals

coupled to photodetectors. During the early developments of PET, NaI was the scintillator material of choice due a high characteristic light yield, relatively cheap production costs and extensive characterisation in literature. However, as a result of a low density and effective atomic number ($Z_{NaI} = 50$), the detection efficiency of NaI is poor, limiting the quality of reconstructed images through the signal statistics acquired in a scan. In the late 1970's, during to a resurgence in scintillator materials research, the scintillation properties of BGO ($Bi_3Ge_4O_{12}$) were fully characterised and it was identified as a good candidate for PET [14]. Although the light yeild of BGO is only $\approx 15\%$ of NaI and the decay time is 25% longer (300 ns), it is very dense with high effective atomic number ($Z_{BGO} = 75$). As a result the mass attenuation coefficient of the photoelectric effect, and therefore the detection efficiency of BGO, represents an improvement of approximately a factor of five on NaI. This effect can be observed by comparing the 511 keV line in Figures 2.3a & 2.3b. Only since the 1990's have scintillator materials such as LSO (Lu_2SiO_5), and its cheaper variant LYSO ($Lu_{2(1-x)}Y_{2x}SiO_5$), been developed and offered an interesting alternative. LSO and LYSO combine an increased light output with a high effective atomic number and short decay constants. These scintillating materials are described in more depth in Chapter 3.

The photodetector of choice for PET has, for a long time, been the photomultiplier tube (PMT). Since their inception, PMTs have been applied in a range of detector applications [15] and, as such, have an extremely well characterised response. However, with the improvement of manufacturing technologies for high gain silicon photodetectors, avalanche photodiodes (APDs) and silicon photomultipliers [16] [17] [18] [19] have been increasingly investigated for use, particularly in fast timing applications [20] [21] [22] [23].

The most basic PET detector modules couple single scintillator crystals directly to the face of a PMT in an arrangement known as *one-to-one coupling*. This arrangement results in optimum performance in terms of both energy and timing resolution, however the cross section dimension of individual detector elements is limited to approximately 1 cm^2 due to the practically achievable miniaturisation of PMTs. This limits the spatial resolution of the system as the gamma interaction position within each detector element is unknown, creating a parallax uncertainty on the projected LOR. In order to continue to improve the spatial resolution, it is thus necessary to determine the gamma interaction position with an accuracy that was a fraction of the PMT size. Such a technique requires the scintillation light to be shared over multiple PMTs, whereby the position can be calculated based on the detected light level at each PMT. A mechanism for reading out multiple scintillator

crystals with a reduced number of photodetector channels was developed in the *Block detector* [24].

2.4.1 Block detectors

Block detectors [24] allow the use of a small number of PMTs reading out an array of small crystal elements, whereby the ratio of scintillator elements to PMTs can be 16:1 or higher. Typically a block detector consists of four PMTs in a matrix arrangement, reading out an 8×8 array of crystal elements, shown in Figure 2.6a. The crystal array is typically not made of individual crystals, but rather a monolithic crystal with partial saw cuts used to define the array elements. The cuts are filled with a reflective material to channel the light with a well defined spatial spread into a coupled PMT detector block, minimising cross talk between crystal elements. The depth of the saw cuts is such that a well defined light response function is produced at the PMTs and a simple algorithm using superposition of signals from the four PMTs can be used to identify the crystal section where the interaction took place. In general, to calculate the average position, the best estimate of the true value \vec{x} is given by the weighted average given by the following equation [25]:

$$\vec{x} = \frac{\sum_i S_i x_i}{\sum_i S_i}, \quad (2.4.1)$$

where \vec{x} indicates the position (x, y) of the event, S_i are the weights and x_i are the positions of the elements in question. In the case presented in Figure 2.6, this equation can be used to estimate the position of interaction in the x and y planes:

$$X_{interaction} = \frac{x_1(S_A + S_C) + x_2(S_B + S_D)}{S_A + S_B + S_C + S_D}, \quad (2.4.2)$$

$$Y_{interaction} = \frac{y_1(S_C + S_D) + y_2(S_A + S_B)}{S_A + S_B + S_C + S_D}, \quad (2.4.3)$$

where S_A-S_D are the integrated charge signals produced by each of the four PMTs and (x_1, y_2) , (x_2, y_2) , (x_1, y_1) , (x_2, y_1) are the positions at which the signals are measured. This technique is often referred to as *Anger logic*, or *Anger weighting* [21]. An example light pattern from an interaction close to the centre of a block detector module is shown in Figure 2.6b. This technique reduces the number of PMTs required to readout a given

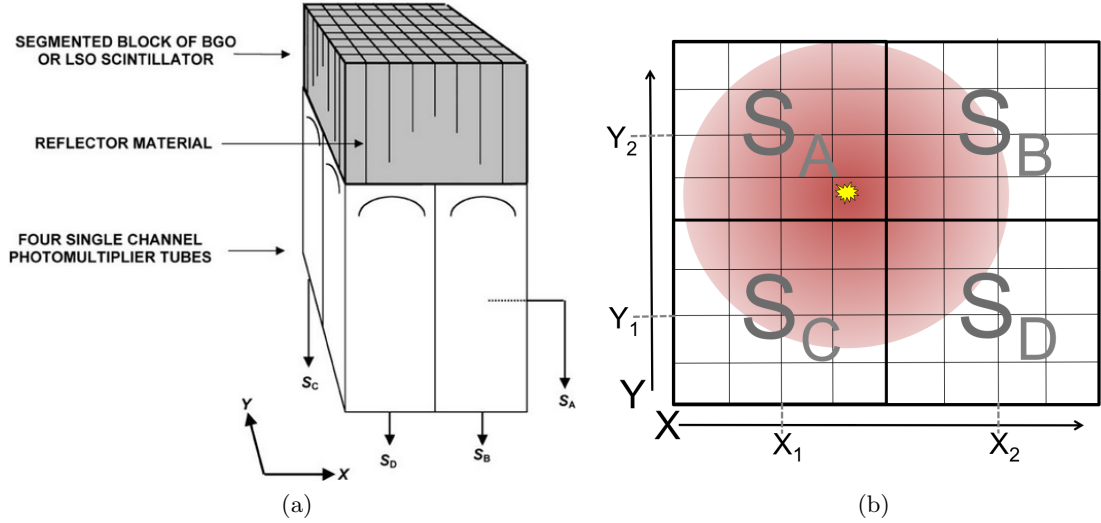


Figure 2.6: (a) Diagram of a block detector composed of a scored scintillator block coupled to a 2×2 array of PMTs [21]. (b) An example light distribution produced by the cut scintillator block in an interaction.

detector volume, providing improved spatial resolution and lowering cost.

2.4.2 Spatial resolution

As well as noise effects, which degrade the signal-to-noise and therefore the contrast of a reconstructed image, the underlying spatial resolution of the image is constrained by a number of physics and detector resolution effects.

It has been described previously that the probability of electron-positron annihilation is inversely proportional to the centre of mass momentum of the two, leading to the *range effect* shown in Figure 2.7a. In the case where this momentum is not exactly zero, some deviations from collinearity will occur, known as the *non-collinearity effect*. By considering the two photons to be nominally emitted at a relative angle $\theta = 180^\circ$, then the uncertainty on this emission angle is described by [26]:

$$\Delta\theta \approx \frac{p \cdot \sin\phi}{m_0 c}, \quad (2.4.4)$$

where p is the incident particle momentum and ϕ is the angle of approach between the electron and positron. A diagram of this configuration is given in Figure 2.8. An average $\Delta\theta$ due to this process has been calculated in literature to be 0.25° [27]. As a result, much like in a scatter coincidence event, the LOR reconstructed between activated detector elements may not directly bisect the annihilation position (see Figure 2.7b). In order to

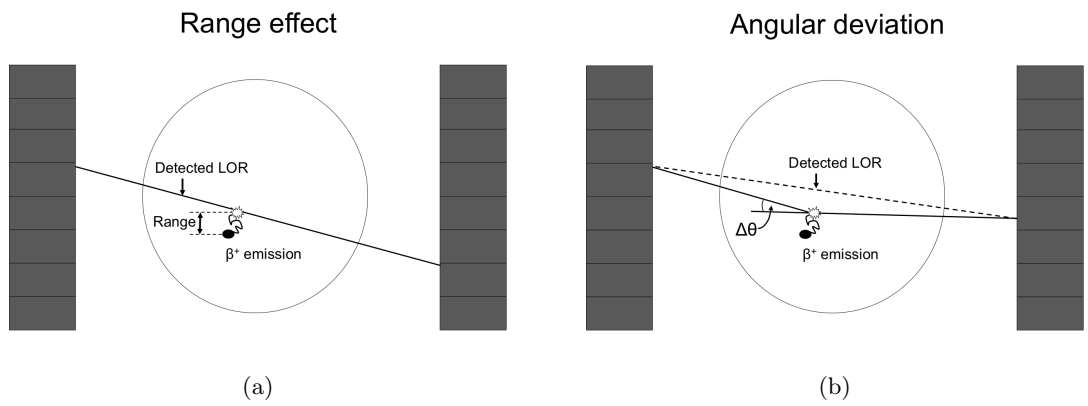


Figure 2.7: Fundamental limits of PET. (a) Range effect results in the reconstructed line of response (LOR) passing through the annihilation point which is some finite distance away from the emission point. (b) non-collinearity of emitted photons results in the reconstructed LOR not passing through the annihilation point.

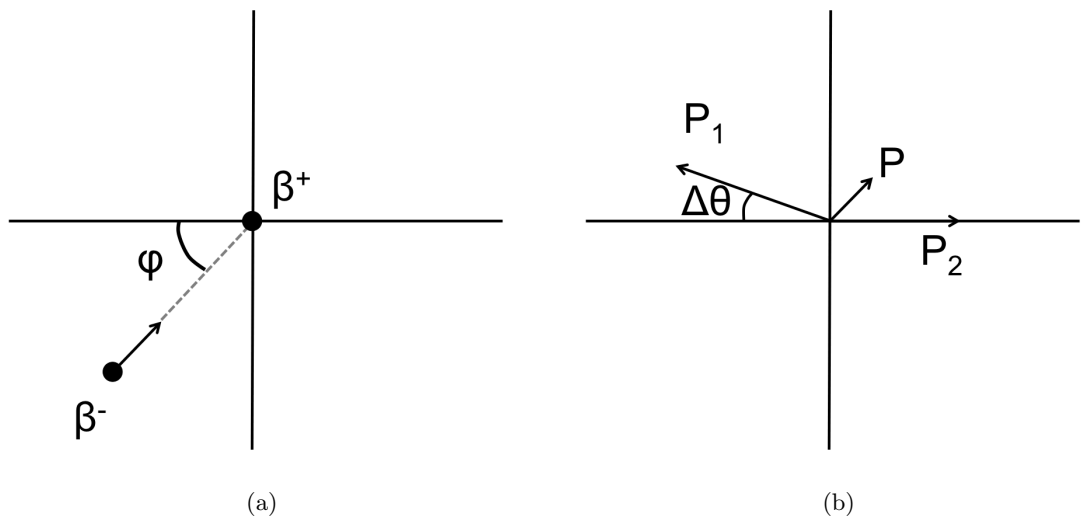


Figure 2.8: (a) The angle of approach of an electron towards a positron which is at rest. (b) The deviation from collinearity due to the momentum vector P.

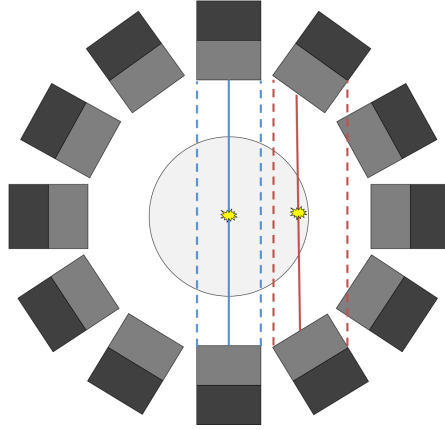


Figure 2.9: Illustration of the parallax effect increasing as a function of the radial position of an annihilation event. The solid blue and red lines represent the real LOR associated with the annihilations. The dashed lines represent the uncertainties on the measured LOR due to the parallax effect.

convert this angular uncertainty into a spatial uncertainty (C) in the reconstructed image, the diameter of the detector ring (S) must also be considered. By applying a small angle approximation to the geometric system given in Figure 2.7b, the spatial uncertainty can then be calculated as:

$$C \approx \Delta\theta \times S/4 = 0.0022 \times S. \quad (2.4.5)$$

If we use the assumption, as given in [26], the distribution of $\Delta\theta$ is Gaussian, then $\Delta\theta_{FWHM}$ can be considered $\approx 0.5^\circ$. By applying equation 2.4.5, C can be estimated to be in the range 1.5 to 2.0 mm for standard 80 to 90 cm diameter PET rings. Scanners with smaller ports therefore have an advantage over a full body PET system and have been suggest for use for specific applications, for example targeted brain scans [28].

A less fundamental, but often limiting, effect is the spatial uncertainty on the gamma interaction position within the activated crystal volume. This effect leads to an uncertainty on the projected LOR called the *parallax effect* as mentioned previously in the context of the block detector. The contribution of the parallax effect is a function of the radial position of the annihilation within the ring diameter, equivalent to half the detector element width at the central position and degrading towards the edge of the field of view. This effect is illustrated in Figure 2.9 where it is shown that the crystal orientation at increased radial positions increases the field of view, and hence the parallax uncertainty of a detector element.

If a block detector arrangement is considered, the *block effect* must also be taken into account. This describes the uncertainty on the interaction position due to mis-positioning of events through: statistical fluctuations in the photodetector response, scatter within the detector or uncertainties on the block decoding scheme. Considering all these effects, an estimation of the spatial resolution of the system is given by:

$$FWHM = k_R \cdot \sqrt{R^2 + C^2 + P^2 + B^2}, \quad (2.4.6)$$

where R is the range effect, C is the photon non-collinearity, P is the parallax error due to crystal dimensions and B is the block effect. Here k_R is a scaling constant representing the contribution from the specific reconstruction algorithm applied to the data set and typically has a value between 1 and 1.5.

2.4.3 Noise contributions

In a perfect system both photons emitted in an annihilation would activate opposing detector elements without the possibility of interaction along the traversed path. A LOR would then be drawn between the two activated elements, for which the response would then be saved to file for use in offline reconstruction after the scan. However, in a clinical setting, gamma-ray photons produced in an annihilation event have a finite probability of interacting in a patient's body before reaching the detector volume, giving rise to effects at reconstruction level.

By applying the mass attenuation coefficients used to produce the plot in Figure 2.3d, and considering the density of water as $\rho = 1 \text{ g/cm}^{-3}$, the linear attenuation coefficient of a 511 keV photon in water is calculated to be $\approx 0.1 \text{ cm}^{-1}$. If, for the sake of argument, we assume the human head and chest to be circular with diameters of 10 cm and 20 cm respectively, by applying equation 2.3.1 we can calculate that only 36% of the photon pairs will reach the detector arrangement without undergoing one or more Compton scatter interactions in a head / brain scan. This reducing to 15% in the case of a body scan. As previously discussed, photons which undergo Compton scattering are deflected from their original path through an angle θ . In the context of PET this will likely result in a LOR projection which does not intersect the point where the annihilation took place (see Figure 2.10a). These events are often referred to as *scatter coincidences*. These,

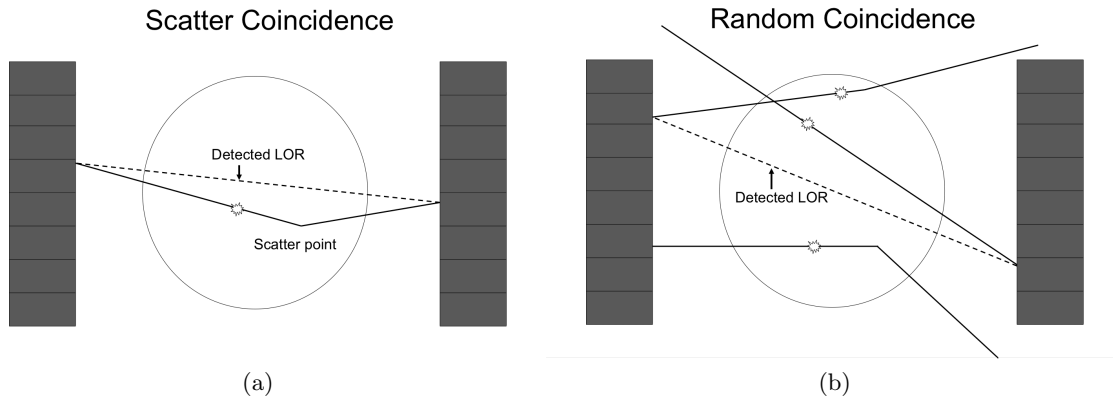


Figure 2.10: Noise effects introduced by interactions with a patient’s body. (a) Compton scatter in the body causes a false LOR. (b) It is possible that only single events are recorded from single annihilation.

if not rejected prior to image reconstruction, contribute to the signal noise of the final data set. Another feature of Compton scatters is the reduced energy associated with the scattered photons. Energy selection criteria are therefore applied to each coincidence pair to reject events where either or both of the coincident detector activations are measured to have an energy less than 511 keV. In view of this, it becomes clear how the energy resolution is an important parameter in a PET detection system. A system with a good energy resolution will reject a higher proportion of scatter events, ultimately leading to an increase in signal-to-noise for the system.

Additional sources of noise in the reconstruction will be events in which photons from unrelated annihilation events happen to trigger coincident elements, therefore mimicking a true coincidence. These events are called *random coincidences*, and an example is illustrated in Figure 2.10b. The random coincidence rate increases linearly with the width of the time window used to define a coincident event. Hence the smaller the time window, the better the noise rejection of the system. In commercial scanners this time window is typically in the range 3 to 12 ns [29], depending on the coincidence timing resolution (CTR) of the specific detector system.

2.4.4 Noise Equivalent Count Rate

In order to describe the quality of a data set acquired by PET detector systems over the course of a scan, a parameter called the *noise equivalent count rate* (NECR) is frequently applied [30] [31]. Here the signal of interest is given by the number of true counts (T) recorded in some unit time, while noise is identified as the count rate of the scatter (S)

and random (R) coincidences as described above. The NECR is then defined as:

$$NECR = \frac{T^2}{T + S + R}. \quad (2.4.7)$$

The NECR is often given as a function of source activity in the scanner and hence the maximum NECR can indicate the optimum source activity with which to operate a system.

2.5 Time-of-Flight PET

In the context of PET, the time-of-flight (TOF) parameter describes the difference in arrival times of the two photons emitted in an annihilation event. In classical PET, timing information is used to determine if two photons are in coincidence and therefore can be correlated to the same annihilation event. A time coincidence window is set (typically 3-12 ns) and if the detection time of two coincident photons is within the time window, the two events are considered to be in coincidence. The measured difference in detection time is related to the actual time-of-flight of the photons, but with a systematic uncertainty or *coincidence timing resolution* defined by the detection system.

Conventional PET uses TOF to select LORs to be used in the reconstruction, but does not extract any information indicating where along the LOR the annihilation occurred. TOF-PET uses an improved system timing resolution in order to locate the annihilation position along the LOR using the time difference between the two signals. It is shown in Figure 2.11 that a difference in path length ($\Delta x = \frac{x_a - x_b}{2}$) is created when the annihilation position is offset from centre of the LOR. The associated difference in arrival times of the two photons at coincident detector elements ($\Delta t = t_a - t_b$) can then be used to calculate the offset spatial offset: $\Delta x = \frac{c \cdot \Delta t}{2}$.

If the system could measure Δt to infinite precision, the above relation could locate the exact position of the annihilation event along the LOR. In this case, statistical reconstruction algorithms would no longer be necessary and the resolution of the reconstructed images would be limited only by the fundamental spatial uncertainty contributions outlined previously in this chapter. However, systematic uncertainties on the timing resolution are introduced by both the physics of the detection mechanism and the subsequent processing of electronic signals, resulting in a finite coincidence timing resolution (σ_t). This leads

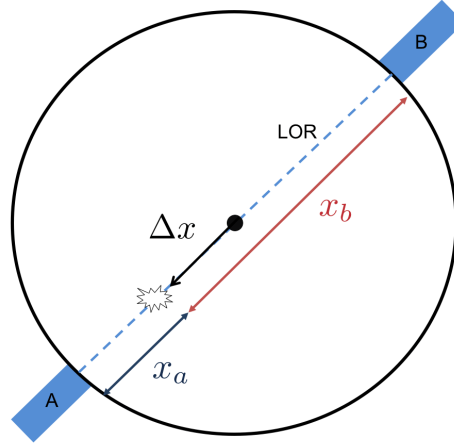


Figure 2.11: Diagram showing the principle of TOF-PET. The offset, Δx , is calculated using the difference in arrival times of the photons at detector elements A and B.

to an uncertainty on the measurement of the annihilation position ($\sigma_x = \frac{c \cdot \sigma_t}{2}$), which is considered as a projected probability distribution centred about Δx . Generally this distribution is considered to be Gaussian, but is ultimately defined by the characteristic system response. As a result, in TOF-PET, the emission position along the LOR is known as $x \pm \sigma_x$. Conversely, in PET, where no knowledge of where the annihilation occurred along the LOR, a uniform probability distribution must be assumed. An illustration of both is given in Figure 2.12.

As a result of this additional parametrisation, improvements in the signal quality, as described by the NECR, can be achieved. To quantify this effect, it is useful to first consider that a reconstructed PET image describes the intensity distribution of a source within a known active volume. The resulting active volume is typically modelled as a matrix of discrete 3-D pixels (or voxels), which are used to quantise the signal. Let us consider the simple case shown in Figure 2.12 where a uniform, cylindrical source with diameter D is described by voxels of dimension d . In the case of classical PET, due to the flat probability distribution of the annihilation position along the LOR, the emission could have occurred in any of the shown voxels, meaning a contribution will have to be considered for $n_{conv.} = D/d$ voxels, as shown in Figure 2.12. Conversely, in TOF-PET, after projecting the probability distribution with width σ_x , the corresponding number of voxels from which the emission could have occurred is $n_{TOF} = \sigma_x / d$. By taking the ratio of these values, it has been shown that the gain in NECR when using TOF information is given by [32] [33]:

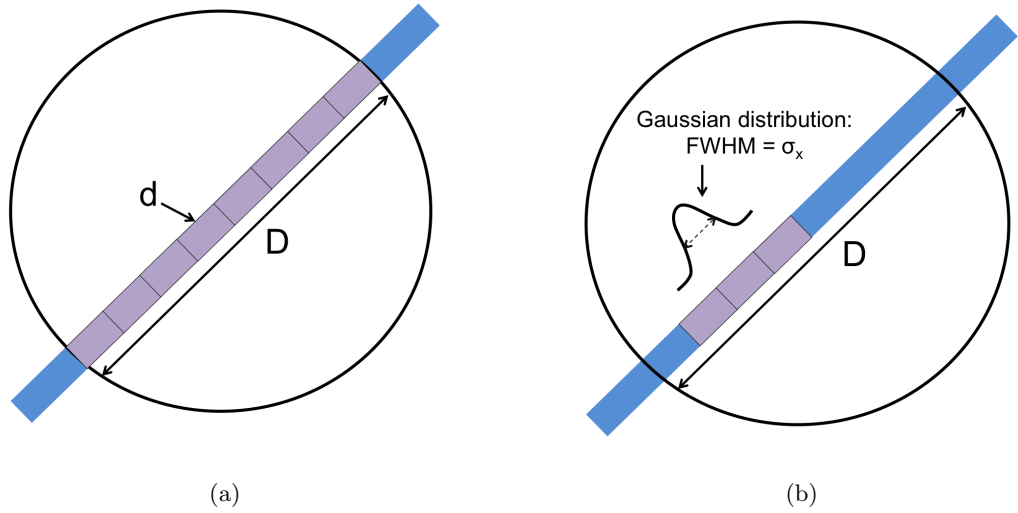


Figure 2.12: Diagram shown the probability distributions of the photon annihilation position along the LOR in the case of (a) Conventional PET (b) TOF-PET. Here a voxelisation of the LOR is considered with an element length, d .

$$NECR_{TOF} = \frac{D}{\sigma_x} NECR_{conv.}. \quad (2.5.1)$$

By using this simple relation one can estimate that the sensitivity of a system, as described by the NECR, scales with the factor D / σ_x , often referred to as the gain [32]. Values of the gain achieved by adding TOF functionality for a range of timing resolutions and two different source dimensions are given in Table 2.2. It is clear then that, as well as scaling linearly with the system timing resolution, additional gains are also seen when imaging large sources, such as larger-than-average (overweight or even obese) patients [21] [34].

The work in this thesis focuses on the development of a simulation to describe the timing properties of a PET detection system based on a one-to-one coupled system of a scintillator plus a photomultiplier. As mentioned above, limitations are introduced by the physics of the detection system, particularly the properties of the scintillator material chosen, and additional electronic and signal processing processes. Detailed explanation of those factors are described in the chapters which follow.

Table 2.2: Time resolution, spatial uncertainty and estimated TOF NECR gain for two different source diameters.

Δt (ns)	σ_x (cm)	Gain (D = 20 cm)	Gain (D = 40 cm)
0.05	1.5	13.3	26.7
0.1	3	6.7	13.3
0.3	9	2.2	4.4
0.5	15	1.3	2.6
1.0	30	-	1.3

2.6 Reconstruction

The formation of quantitative PET images requires the following data sets: an emission data file to be reconstructed; a normalisation file to compensate for non-uniform system response; and a transmission data file for attenuation correction. Understanding the basic concepts of reconstruction allows for conclusions to be drawn in later chapters.

PET reconstruction creates a tomographic image by sequentially stacking the reconstructed images from a set of planes, defined by the detector rings. If a PET scanner is operating in a modality whereby cross-ring activations can pass coincidence acceptance cuts, known as 3D PET [35], 2D planes are no longer well defined within the data set and reconstruction becomes much more complex. In what follows reconstruction is considered in terms of 2D data sets only, so as to avoid detailed discussions not directly applicable to this work. A 2D data set consists of uniform angular sampling around the active volume, stored in polar coordinates as an angle (ϕ) relative to axial field of view, and the shortest distance (s) between the LOR and centre of the gantry. An illustration of such a projection is given in Figure 2.13. The full set of projection data points $p(s, \phi)$ are typically stored as a *sinogram*, which orders the data into a 2D histogram by the s and ϕ values. A point source within an active volume will be observed in a sinogram as a sinusoidal wave (as shown in Figure 2.13), giving the distribution its name. A final data set, containing sinograms as recorded at each active plane, is then passed to a reconstruction algorithm to generate a tomographic image of the patient.

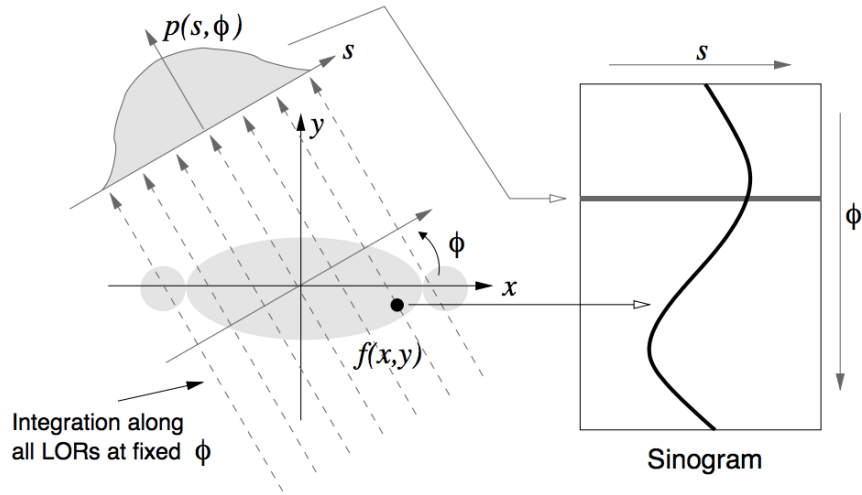


Figure 2.13: A projection, $p(s, \phi)$, is formed from integration along all parallel LORs at an angle ϕ . The projections are organized into a sinogram such that each complete projection fills a single row of ϕ in the sinogram. In this format, a single point in $f(x, y)$ traces a sinusoid in the sinogram [36].

Filtered back projection

The first reconstruction algorithm widely used in PET was the *filtered back projection*. This method provides an accurate reconstruction of an intensity distribution when the projection data set is noise free. It is a fast algorithm to implement and requires only a small amount of computing power.

An essential first step in all PET image reconstruction is back projection, which projects all values of $p(s, \phi)$ back into an image array along the relevant LOR. To do this both the Radon transform and the Fourier-slice theorem are applied. The Radon transform integrates the 2D data along a number of straight lines, or *slices*, to generate a 1D projection of the data set from a given projection direction. A schematic diagram showing a transform from a specified projection direction is given in Figure 2.14. Secondly the Fourier-slice theorem is applied. This states that the Fourier transform of a 1D projection is equivalent to a section, or profile, at the same angle through the centre of the two-dimensional Fourier transform of the object [37]. Figure 2.14 gives an illustration of the Fourier-slice theorem where $\mathcal{F}_1\{p(s, \phi)\}$ is the one dimensional Fourier transform of a projection, $\mathcal{F}_2\{f(x, y)\}$ is the two dimensional Fourier transform of the image, and v_x is then the Fourier space conjugate of x . The theorem then states that by knowing all values of $p(s, \phi)$ from $0 \leq \phi < \pi$, all values of $F(v_x, v_y)$ can be calculated. Finally, the inverse two-dimensional Fourier transform of $F(v_x, v_y)$ will return the original image, $f(x, y)$.

The back projection of four separate LORs in the space domain is illustrated in Figure 2.15.

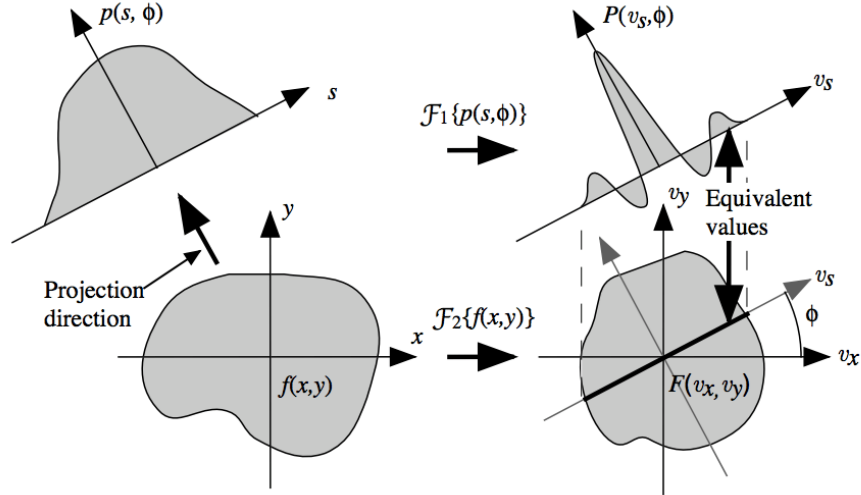


Figure 2.14: Illustration showing the projection of a two-dimensional data set into a one-dimensional slice via the Radon transform, and the two-dimensional Fourier-slice theorem. The right hand illustration represents the equivalence between the one-dimensional Fourier transform of a projection at angle ϕ and the central-section at the same angle though the two-dimensional Fourier transform of the object [36].

By simply back projecting each LOR a blurring, shown as the star-like artefact, will occur in parts of the reconstructed image, degrading the spatial resolution of the image. The oversampling then needs to be re-weighted, or filtered, to correct for this. As such, a digital filter is applied in the frequency domain and the inverse transform performed on the filtered Fourier response to return the data to the space domain as $f(x, y)$. This process is known as *filtered back projection*.

The filter back projection method is simple to implement and can be processed quickly. However, by applying a digital filter to remove the blurring on the edge of emission centres, noise components elsewhere on the LOR can be amplified. Additional low pass ‘smoothing’ filters are often applied to compensate for this effect which in turn degrade the final spatial resolution.

Iterative Algorithms

In contrast to analytical algorithms, iterative algorithms attempt to progressively refine estimates of the activity distribution, rather than directly calculate the distribution, by maximising or minimising some *target function*. The solution is said to converge when the difference of the target function, as calculated between successive estimates (iterations) of the activity distribution, is less than some pre-specified value. A major advantage of this type of algorithm is the possibility of incorporating a number of priori information

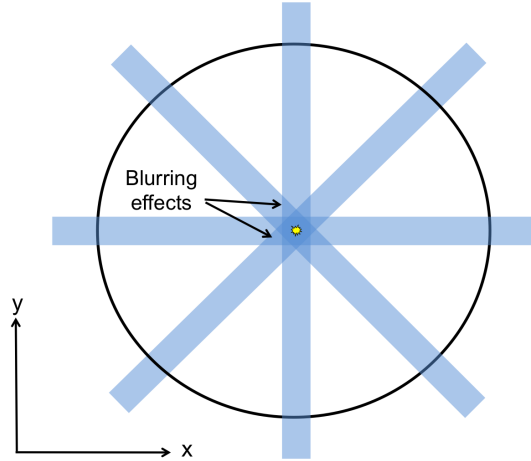


Figure 2.15: Back projection of four recorded LORs. A star-like artefact (or blurring) can be observed at the crossing point of the back-projected LORs, degrading the spatial resolution of the projected image.

such as characteristic detector non-uniformity, attenuation considerations and modelling of statistical noise. The major drawback is the increase in processing time, which is proportional to the number of additional parameters and the number of iterations required to adequately resolve the image. Additionally, depending on the method, the number of iterations can vary and must be well characterised in order to obtain the best image quality [38].

To best describe the process of iterative algorithms we will consider the expectation maximisation (EM) algorithm as proposed by [39]. When the EM algorithm is applied to PET image reconstruction it leads to a simple iterative equation:

$$\hat{f}_j^{(n+1)} = \frac{\hat{f}_j^n}{\sum_{i'} H_{i'j}} \sum_i H_{ij} \frac{p_i}{\sum_k H_{ik} \hat{f}_k^{(n)}}, \quad (2.6.1)$$

where $\hat{f}_j^{(n+1)}$ is the next estimate of the imaging voxel j based on the current estimate \hat{f}_j^n . The multiplicative factor \mathbf{H} describes the *system model* which relates the image to the data. An element, H_{ij} of the system model, \mathbf{H} , characterizes the imaging system and represents the probability that an emission from voxel j is detected in projection i . An illustration of elements within the system model are given in Figure 2.16a. The EM algorithm can be described qualitatively with the help of Figure 2.16b, starting with an initial image guess, $\hat{f}^{(0)}$, shown in the upper left of the figure and present in the denominator of equation 2.6.1. The initial guess usually sets the entire image to a constant value. The first step (i) forward projects this image into the projection domain. These projections are then (ii) compared

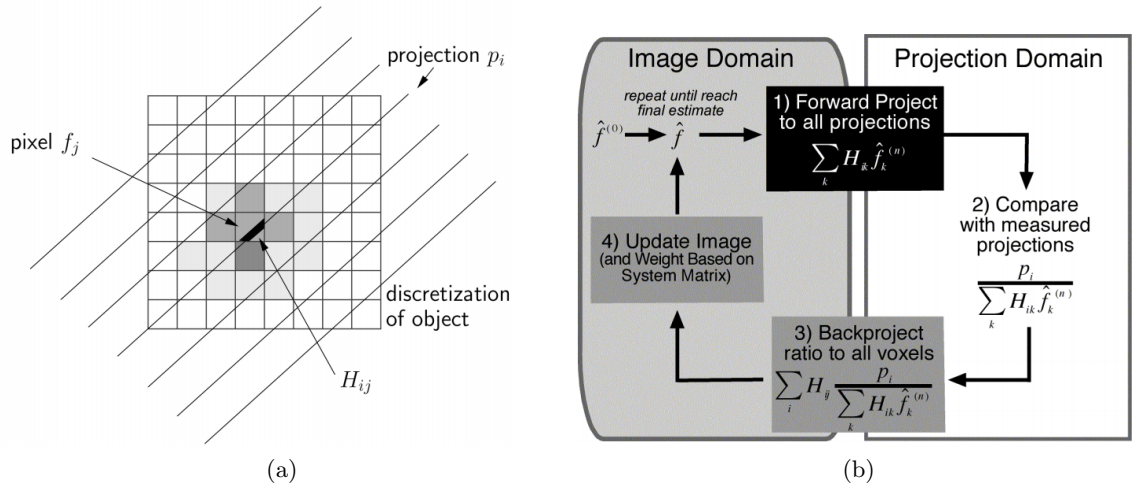


Figure 2.16: (a) Illustration of a single element of the system model, H_{ij} . (b) Flow diagram of the maximum likelihood-expectation maximization algorithm. Starting with an initial image guess ($\hat{f}^{(0)}$) in the upper left, the algorithm iteratively chooses new image estimates based on the measured projections, p [40].

with the measured projections, p . This forms a multiplicative correction factor for each projection, which is (iii) backprojected into image domain to obtain a correction factor for the initial image estimate. This image domain correction factor is multiplied (iv) by the current image estimate and divided by a weighting term based on the system model to apply the desired strength of each image correction factor. The new image estimate is now re-entered in the algorithm as the next image; the algorithm repeats itself while the estimate approaches the maximum likelihood solution.

Different iterative algorithms have been developed and are available in literature based on both linear algebra and statistical considerations. The most widely implemented are statistical, known as the maximum-likelihood expectation maximum (MLEM) [41] and an accelerated version, ordered-subset expectation maximisation (OSEM) [42]. MLEM is based on the maximisation of the logarithm of a Poisson-likelihood target, and works as described above. This method is characterised by very low noise amplification without loss of spatial resolution. In order to improve on the convergence rate, the OSEM algorithm was developed, in which projections are grouped into subsets uniformly distributed around the volume to be imaged. In each iteration the target function is then updated as many times as the number of subsets, proportionally accelerating convergence.

Chapter 3

Inorganic scintillators

As described in Chapter 2, scintillating materials are used in PET detector systems to convert the gamma-ray photons created in an annihilation event into a flux of optical photons. Scintillators can be classified into two major categories: plastic scintillators and inorganic scintillators. Of the two, inorganic scintillating materials are widely used in applications ranging from high energy physics to astrophysics and, as in the context of this thesis, medical physics. These applications often require the detection of radiation with energies of the keV scale and above, where a number of characteristics including: high atomic number Z (implying a very high photoelectric absorption cross section: $\tau \propto Z^5$, equation 2.3.5), timing response of order 10-100 ns and a high light yield ($\geq 25,000$ photons per MeV) [43] make inorganic materials prime candidates. It should be noted that organic scintillators can show timing response up to an order of magnitude faster than their inorganic counterparts, but also show a comparable reduction in light yield, a key parameter in scintillators for PET. In what follows, the mechanism of light production in inorganic scintillators and the main characteristic parameters relevant to PET applications are reviewed. This is followed by a discussion of specific scintillating materials identified in literature as good candidates for PET. The chapter closes with an extensive discussion on the timing uncertainties associated with scintillator detector systems which must be considered in the fast timing TOF-PET modality.

3.1 Scintillators and their properties

The process of scintillation is initiated by the interaction of ionising radiation within a scintillating crystal which, in turn, leads to many electronic excitations. As the crystal

is in a non-equilibrium state after irradiation, the excited states will relax, bringing the crystal to a new state of equilibrium. This basic process is true for the interaction of ionising radiation in all condensed materials. However, in the case of scintillators, the process of relaxation will result in the emission of a number of (typically) optical photons, the total flux of which is proportional to the interaction energy. The production of light in a substance deriving from non-thermal excitations is known as *luminescence*. The emission of light in a scintillator can therefore be described in terms of *luminescence centres*, which decay after excitation to generate individual photons.

In general, an ideal scintillator material should fulfil a number of characteristic properties, including:

- It should convert the kinetic energy of interacting radiation into optical light with high efficiency.
- The energy conversion should yield a number of photons and provide a linear response over as wide a range as possible.
- The decay time of the induced luminescence should be short in order to best define the instant of interaction.
- The material should be transparent to its own scintillation light.
- The material should be capable of being manufactured in volumes required by experimental designs.
- The index of refraction of a material should be close to the refractive index of glass ($n_{glass} \approx 1.5$) so as to permit efficient optical coupling into a photodetector.

In reality no material meets all of these criteria. Choosing an appropriate scintillating material is then a trade off, where properties of highest influence for the application of interest must be prioritised. In the case of PET, the detection efficiency and energy resolution of a crystal are of high importance, influencing the total signal achievable in a scan and the noise rejection respectively. For TOF-PET, additional timing information is required. For timing applications the decay time should be as short as possible so as to best define the instant of interaction and hence reduce the uncertainty on timing measurements. The physics processes influencing these three parameters are discussed in detail in what follows.

3.1.1 The scintillation mechanism

As briefly described above, the process of scintillation can be broken down into quantifiable stages describing both the interaction and response mechanisms. A common method is to consider the process in three stages [44]:

1. Absorption of the ionising energy and development of electronic excitations.
2. Migration of electronic excitations through the crystal lattice to luminescent centres.
3. Relaxation of excited states and photon emission.

A diagram outlining these stages is given in Figure 3.1.

In order to describe the nature of the electronic excitations, it is useful to consider the band structure of a generic scintillating material, as shown in Figure 3.1. Within the electronic band structure it is possible to distinguish a core band with top energy E_c , a valence band with top energy E_v and a conduction band with bottom energy E_g . The valence band and conduction band are separated by a forbidden gap, called the *band gap*, with an energy: $E_{gap} = E_g - E_v$. The main crystal lattice can have no electronic state which lies in this energy range.

In the first of the aforementioned stages of scintillation, ionising radiation incident on the material will liberate an energetic electron into the conduction band, leaving a deep-lying hole in the core band known as an electron-hole (*e-h*) pair. These initial, highly energetic, e-h pairs¹ go on to produce further charge carriers. In the case of electrons this occurs through inelastic electron-electron (e-e) scattering [45], whereby kinetic energy is transferred between the two charged particles through Coulomb interactions. In the case of holes, secondary emission can occur by Auger emission [9], whereby the inner shell vacancy (or hole) is filled by an electron in a less tightly bound shell, resulting in either the emission of a characteristic x-ray, or an electron from the outer shell with a well defined energy. Generation of charge carrying pairs will continue until the energy of the daughter electrons is below the e-e scattering threshold, $\approx 2.5 \cdot E_{gap}$. When both charge carriers lie below the respective threshold energy of the e-e scattering and Auger processes, the charge carriers created in the event will thermalise, losing energy to the surrounding media primarily through phonons. This whole process takes of the order of a few picoseconds, after which almost all secondary electrons will lie at the bottom of the conduction band and holes at the top of the valence band.

¹Often called δ -rays to distinguish them from the less energetic secondary electronic excitations

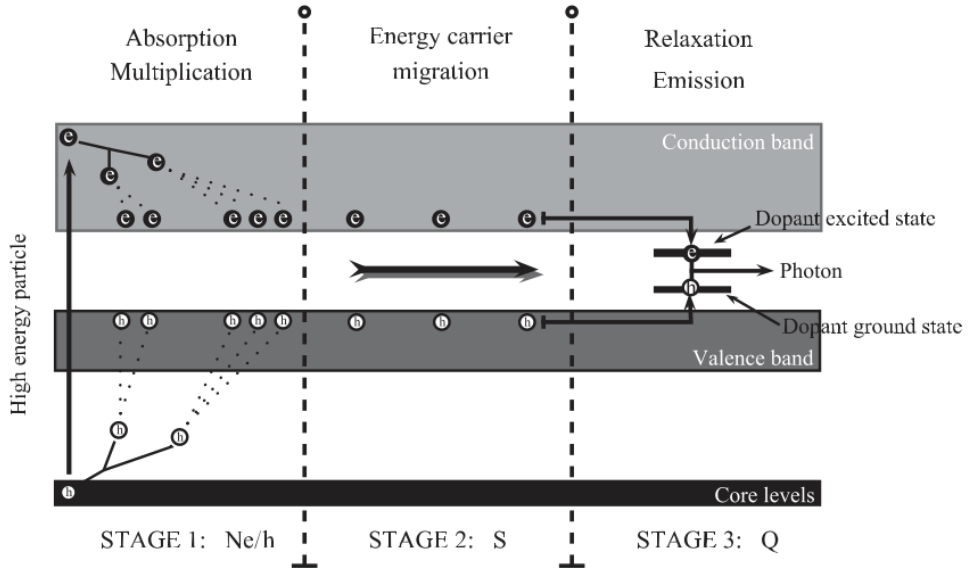


Figure 3.1: Basic scheme of three major stages involved in scintillation [44].

In the second stage, charge carriers migrate through the material and localise at luminescence centres. During this process it is possible that electrons and holes can be captured by trapping centres [46] which derive from defects in the crystal structure, completely removing carriers from the luminescence process. The number of trapping centres in a crystal is typically associated with the quality of the manufacturing processes and should be minimised to keep the efficiency of the energy conversion high.

The final stage involves the interaction and recombination of excitations localised at luminescent centres. This can happen through a number of processes, largely dependent on the type of luminescence centre. There are two major types of luminescence associated with inorganic crystals: self trapped exciton (STE) luminescence and dopant (or *activator*) luminescence. In a STE event, e-h pairs become bound during the migration stage, occupying an energy level just below the conduction band and creating a state called an exciton. Excitons become localised at impurities and defects in the crystal and can decay to a lower energy state, emitting a photon through radiative recombination, see Figure 3.2. In a dopant induced luminescence, specific luminescence centres are defined by a small fraction of activator atoms which are implanted in the crystal structure. Activator atoms then define luminescence centres where the electronic structure of the crystal is modified, allowing electronic states within the previously forbidden band gap. During the migration stage, charge carriers are localised at activator atoms where e-h pairs can radiatively recombine through the modified electronic levels, as shown in Figure 3.2.

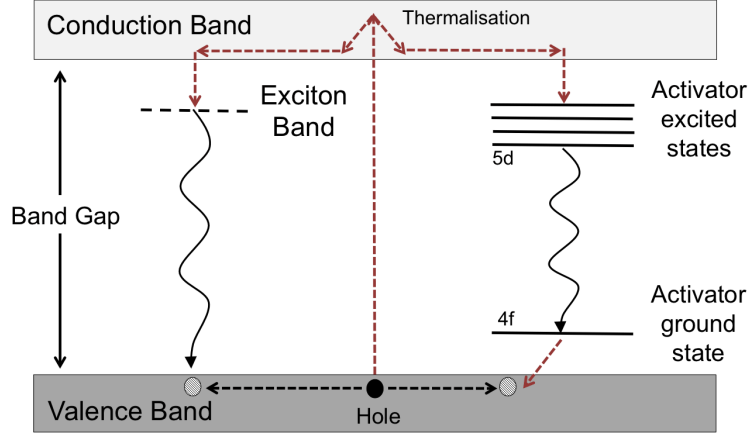


Figure 3.2: Types of luminescent centres in inorganic crystals. Left: A STE luminescence. Right: A doped luminescence.

A number of processes affect the luminescence efficiency, including: (i) Electron phonon coupling; (ii) re-absorption process where the luminescence travelling through the scintillating material can be reabsorbed by identical luminescence centres; and (iii) photo-ionization and thermal-ionization quenching processes, whereby luminescence centres relax through non-radiated processes [47] [48].

The contributions of each stage can be quantified with regard to the total scintillation efficiency (η), as: the number of electron-hole pairs produced by an ionising event (N_{eh}); the efficiency of charge carrier to luminescent centre production during the migration stage (S); and the quantum efficiency of the luminescent centres (ϵ), defined as the ratio between the emitted and the absorbed quanta. These three contributions lead to the efficiency relation:

$$\eta = N_{eh}S\epsilon = \frac{E_{incident}}{E_{eh}}S\epsilon = \frac{E_{incident}}{\beta E_{gap}}S\epsilon, \quad (3.1.1)$$

where E_{eh} is the energy required to create an electron-hole pair, also expressed in terms of the bandgap energy E_{gap} and a proportional constant β typically ranging between 2 and 5 [49] [44], where $E_{incident}$ is the energy deposited in the material by an ionising event.

3.1.2 Stokes shift

A key property for scintillator materials is their transparency to photons emitted through internal luminescence processes, optimising the ϵ value given in equation 3.1.1. For this

property to be met, scintillators must absorb and emit photons of different energies, so as to avoid emitted photons being instantly re-absorbed within the material. In fact, it is often the case that, compared with the absorption spectrum, the emission spectrum is displaced to longer wavelengths. This phenomenon is known as *Stokes shift*, and is seen in the difference between the absorption and emission spectra of LYSO in Figure 3.3a.

To describe this effect let us consider the excitation and relaxation of an electron at an luminescence centre. The electronic charge distribution at the luminescence centre is changed when it is excited from the ground into an excited state. The bonding of the nearest neighbours in the crystal lattice will therefore be influenced. The equilibrium configuration of the neighbouring atoms becomes unstable and the ions take up new equilibrium positions. Part of the excitation energy is thus transferred to the lattice and the electronic transition back to the ground state takes place under a new lattice configuration. Since energy has been given up to the lattice, the electron recombination energy is less than the excitation energy, resulting in the Stokes shift.

The concept of *configuration coordinates* is often used to describe this effect. If one combines the changes in all the lattice coordinates between both lattice configurations into a configuration coordinate (Q), the potential energy of the system (i.e. the sum of the defect electron and the surrounding lattice) can be represented as in Figure 3.3b. In both ground and excited states potential energy is a quadratic function of the configuration coordinate, with a minimum at the equilibrium coordinates; Q_g and Q_e respectively.

An interesting artefact of Figure 3.3b is the intersection of the two curves. If the temperature of the system is high enough to increase the potential energy to the intersection, a non-radiative transition from excited to ground state is allowed. This effect is known as temperature *quenching*, where quenching is used to describe any non-radiative recombination of luminescence centres.

In an ideal scintillator material the Stokes shift should be large so as to maximise the transmission and therefore the efficiency of scintillation. However, a large Stokes shift will often lead to a large temperature dependence as the g curve in Figure 3.3b intersects the e curve closer to the minimum, increasing the probability of temperature quenching. In applications where temperature effects are significant, materials with a small ΔQ (as shown in Figure 3.3b) may be preferable.

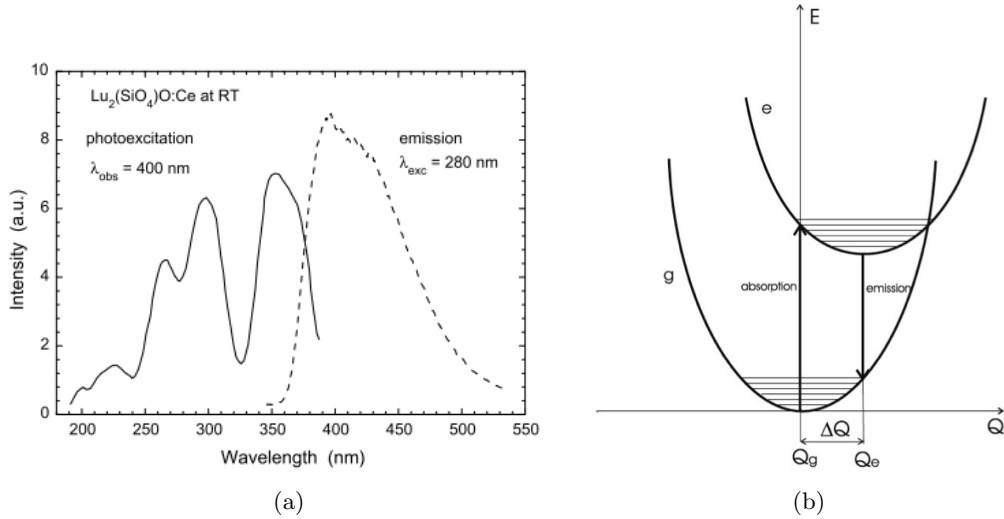


Figure 3.3: (a) Absorption and emission spectra of LSO crystal [50]. (b) Configuration coordinate diagram of an inorganic crystal. The curves g and e represent the ground and excited states respectively. [51].

3.1.3 Scintillation time

If it can be assumed that the luminescent centres in a given material are formed instantly, then the time profile of a scintillation light pulse can be described by an infinitely fast leading edge followed by an exponential decay:

$$I(t) = I_0 \int_0^t e^{-t/\tau} dt, \quad (3.1.2)$$

where $I(t)$ is the mean or expected number of photons produced between $t=0$ and some later time t , τ is the time constant of the characteristic luminescence and I_0 is a scaling constant. Integrating equation 3.1.2, one gets:

$$I(t) = N_{phot} [1 - e^{-t/\tau}], \quad (3.1.3)$$

where the total number of photons produced in an event is then, $N_{phot} = I_0\tau$. This basic model was first proposed in the 1950's [52] [53], when the two major scintillating materials available were CsI:Tl ($\tau = 1000$ ns) and NaI:Tl ($\tau = 230$ ns). In the years since, scintillating materials with decay constants an order of magnitude faster have been identified, for example: LYSO:Ce ($\tau = 41$ ns), LaBr₃:Ce ($\tau = 30$ ns). For these modern, fast-timing scintillators, the rise time defines a non-negligible signal region and the assumption that luminescent centres are formed instantly no longer provides accurate results. The rise time

itself is typically of order 10-100 ps [54] deriving from the finite migration times of e-h pairs to luminescent centres after an ionising interaction. Considering this new condition we can define a bi-exponential timing model:

$$I(t) = I_0 \int_0^t e^{-t/\tau} (1 - e^{-t/\tau_R}) dt, \quad (3.1.4)$$

where τ_R is the characteristic rise time of the specific scintillator material, describing the population of the optical levels, and τ is the time constant describing their decay [55]. Integrating equation 3.1.4 we have:

$$I(t) = N_{phot} \left[1 - \frac{\tau_R + \tau}{\tau} e^{-t/\tau} + \frac{\tau_R}{\tau} e^{-t/(\frac{\tau_R \tau}{\tau_R + \tau})} \right], \quad (3.1.5)$$

where $N_{phot} = I_0 \frac{\tau^2}{\tau_R + \tau}$. By comparing the two models, it can be observed that:

- If $\tau_R = 0$, equation 3.1.5 is equivalent to equation 3.1.3.
- If $\tau_R \neq 0$ but τ_R/τ is very small equation 3.1.5 again approaches equation 3.1.3. Equation 3.1.3 is therefore an appropriate model for a scintillator material characterised by a slow decay of luminescent centres.
- In the case that neither of the above are true, τ_R becomes important in understanding the time response of the scintillation flux. The specifics of the timing considerations are discussed in Section 3.3.1.

The bi-exponential model given by equation 3.1.5 should be applied for the most accurate estimation of the timing response of a scintillating material.

3.1.4 Energy resolution

The energy resolution (R) of a detector system defines its ability to resolve small changes in energy. In the case of a scintillator, the light signal provided by the characteristic luminescence is converted to an electrical one through the application of a photodetector. An illustration of the response of a coupled scintillator-photodetector detection system is given in Figure 3.4. It is shown that the system response to a mono-energetic signal is not infinitely precise, but is defined by a distribution about a mean measurement. The energy resolution can be expressed in terms of the width (FWHM, see Figure 3.4) and the mean (E_0) of this distribution:

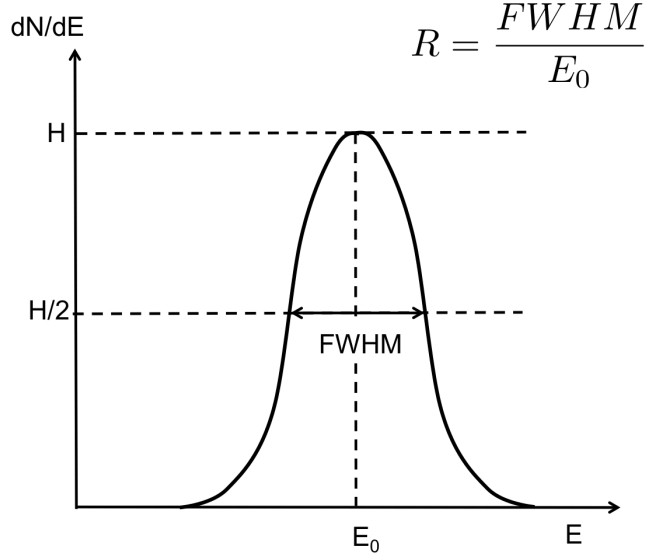


Figure 3.4: Definition of detector energy resolution. For peaks whose shape is Gaussian with standard deviation σ , the FWHM is given by 2.35σ .

$$R = \left(\frac{FWHM}{E_0} \right). \quad (3.1.6)$$

To better understand the energy resolution measured by a coupled scintillator and photodetector system, it can be useful to consider the individual contributions to the total response:

$$R^2 = R_{np}^2 + R_{inh}^2 + R_{trans}^2 + R_{det}^2. \quad (3.1.7)$$

Here R_{np} represents the contribution to the total energy resolution given by non-proportionality effects in the scintillation, mainly due to trapping centres in the crystal lattice. However it is difficult to generalise a description of this effect, which has been shown to be highly dependent on both the material being studied and the energy of the incident radiation [56]. The quantity R_{inh} describes the effects of inhomogeneities in the crystals which can lead to local variations in the scintillation light output. This is typically due to fluctuations in the concentration of luminescence centres, which is highly dependent on the specific manufacturing techniques. As a result, the number of scintillation photons generated in activating events can be dependent on the interaction position, producing a higher yield in areas with high concentrations of luminescence centres. The combination of the first two contributions in equation 3.1.7 can be defined as the intrinsic resolution of the scintillator, R_i . The transfer resolution R_{trans} represents the contribution due to the transfer

efficiency of photons to the photodetectors. This parameter can be broken into two smaller contributions: the probability of detection at a photodetector, due to the characteristic scintillation wavelength, and the path of the optical photons in the crystal. To minimise the contribution of R_{trans} , a photodetector should be chosen with high sensitivity to the specific characteristic wavelength of the scintillator material being investigated, as well as a crystal geometry that minimises losses through both an increased total path length to detection and the number of reflections at optical boundaries.

For an ideal scintillation detector, R_{np} , R_{inh} , R_{trans} will be zero. In this case the resolution will then be given simply by the resolution of the photodetector. Generically this can be described by the variance on the gain of the detector $v(\text{Gain})$, the mean number of photons created in a scintillation event (\bar{N}) and the average transfer efficiency (\bar{p}), which, as $R_{trans} = 0$ is considered to have a variance of zero [51]:

$$R = R_{det} = 2\sqrt{2\ln 2} \cdot \sqrt{\frac{v(\text{Gain})}{\bar{N}\bar{p}}}. \quad (3.1.8)$$

As the resolution has been previously defined using the FWHM, the factor $2\sqrt{2\ln 2}$ is included to give a result again in terms of the FWHM and not the standard deviation σ . For commonly used inorganic scintillator crystals the energy resolution at an energy of 511 keV tends to be in the range 3-12 % [56].

3.2 Scintillators for PET

In general, detector systems must be tailored to the specific application in which they are to be used. This is equally true for scintillator detectors where characteristics such as the decay time and absolute light yield can vary over as much as an order of magnitude. For applications involving detection of gamma-ray photons the atomic number is equally important. In fact, it has been shown in equation 2.3.4 that the interaction probability is proportional to Z^{3-4} , small changes in atomic number can therefore yield large changes in response characteristics.

The requirements for scintillators used in PET detectors have been described previously by [57] [58]. In order of priority these have been given as: (i) short attenuation length (<1.5 cm); (ii) high photoelectric fraction; (iii) short scintillation decay time (<500 ns);

(iv) low cost (<20 \$/cm³²); (v) high light output (>8 photons/keV). Adding a requirement for TOF-PET, the scintillation time should also be short (<50 ns) to allow for a total system timing resolution of <500 ps. A list of candidate scintillator materials which have been identified for use in both conventional PET and TOF-PET are given in Table 3.1.

3.2.1 Attenuation length

With any PET detector design a high efficiency is necessary, implying a detector depth corresponding to at least two attenuation lengths (X_0). While this criterion can be met with a scintillator of any attenuation length, a short attenuation length is desired to minimise degradations in the system's spatial resolution through the parallax effect as discussed in Chapter 2. It has been shown previously (in equations 2.3.4, 2.3.8 and 2.3.9) that the probability a gamma-ray photon will interact with a given medium, and therefore the linear attenuation, is dependent on the atomic number (Z_{eff}) of a given material. Values for both of these parameters are also given in Table 3.1.

Table 3.1: Selected inorganic scintillators proposed for PET [59]

Scintillator	ρ [g/cm ²]	Z_{eff}	X_0 [cm ⁻¹]	τ_p/σ_c	Light yield [ph/keV]	Decay time [ns]
NaI:Tl	3.67	50.8	2.56	0.22	32	230
BGO	7.13	75.2	1.12	0.65	8.2	300
LSO	7.4	66	1.15	0.52	27	40
LYSO	7.1	63.5	1.2	0.49	32	40
LuAP	8.34	65	1.1	0.47	11	17 + 120
LuYAP	7.1-7.4	57-60	1.2-1.25	0.37-0.42	15	20 + 250
Lu ₂ Si ₂ O ₇ :Ce	6.2	64.4	1.39	0.45	30	24
LaBr ₃	5.29	46.9	1.64	0.16	52	30

3.2.2 Photoelectric fraction

Events involving interactions via the photoelectric effect are a preferred detection mode compared to those which Compton scatter. This is because Compton scatter events deposit energy in two (or more) locations in the detector ring and thus reduce the spatial

²At the time of writing.

resolution of the detector module. It is again shown in equations 2.3.4 and 2.3.8 that, although the probability of Compton scatter scales proportionally with Z , the probability of photoelectric interactions scales with Z^{3-4} . The relative fraction (τ_p/σ_c) of the two therefore rapidly increases with the atomic number Z_{eff} . The value for Z_{eff} should therefore be maximised in a candidate scintillator for PET in order to maximise the fraction of events which interact via the photoelectric effect.

3.2.3 Decay time

The decay time of the scintillator applied to conventional PET detector systems affects both the timing resolution and the dead time of the system. While the exact relationship between the decay time and the dead timing is hard to quantify, most PET cameras trigger at the 1-10 photoelectron level so the dead time can be defined as the time that it takes for the scintillation intensity to drop to the level of 1-10 photons/MeV/ns. The dead time is a particularly significant effect for systems that apply block detectors as described in Chapter 2. In this case an interaction in one of the pixels will render the whole block insensitive (*dead*) until the photon flux has fallen below the previously stated level.

As discussed in Chapter 2, the timing information is used in conventional PET to reject noise events, specifically random coincidences. The random coincidence rate is given by $2S^2\Delta t$ [58] where S is the rate of single, full energy detections and Δt is the width of the coincidence window. Better timing resolution will allow shorter coincidence windows to be used to reduce the random fraction. Moreover, the decay time of even modern, fast scintillating crystals defines the lower bound on the timing resolution measurable with a scintillator based detector system [60]. The gains associated with the application of TOF-PET are therefore limited by the decay time of the scintillator, which should be minimised to optimise detector performance.

3.2.4 Light yield and Energy Resolution

The light yield affects both the timing resolution and the energy resolution. The effect on timing is simple for a given decay time: a higher light yield gives a higher initial intensity, reducing the statistical fluctuations. The improvement in energy resolution can be considered in terms of equation 3.1.8, where it is shown that the contribution of the detector decreases as a function of $1/\sqrt{\bar{N}}$, where \bar{N} is the average number of photons interacting with the detector system.

In the case of block detectors, the light yield has an additional influence on the accuracy of the decoding scheme which is based on the ratios of light detected over a block of four PMTs. An increase in light therefore reduces the statistical uncertainties on detected signals, improving the resolution of the technique.

3.3 Contributions to timing resolution

The coincident timing resolution (CTR) is a critical parameter which, to a large extent, defines the system performance of a TOF-PET detector. With modern, fast timing, photodetectors the limiting factor of the CTR in a gamma detection system is most often the response of the scintillator, where the physics processes involved define the finite time distribution of the resulting light pulse. The timing contributions associated with the detection of this light pulse can be separated into two distinct parameters: the statistical fluctuations in the emission of scintillation photons (σ_{stat}), and the variance in the path length of photons en-route to detection (σ_{trans}). Hence the total timing contribution of a single scintillator can be defined as:

$$\sigma_{scint} = \sqrt{\sigma_{stat}^2 + \sigma_{trans}^2}. \quad (3.3.1)$$

3.3.1 Statistical considerations

For the work described in this thesis, scintillator detectors are read out with an optically coupled photodetector. Considering this system, the statistical contribution to the timing resolution is defined as the timing resolution associated with the generation of primary photoelectrons at the detector, prior to amplification. This represents the theoretical limit of timing resolution that a practical scintillator detector can achieve. It is often useful to calculate this contribution to the first order, so to make a first judgement on the feasibility of a system.

The effect derives from the uncertainty on the decay time of individual luminescence centres, each of which contributes to the total photon flux measured by the photodetector. On the level of the individual photon, the probability of N photoelectrons being detected between the initial time 0 and $t > 0$, is described by a Poisson distribution [52]:

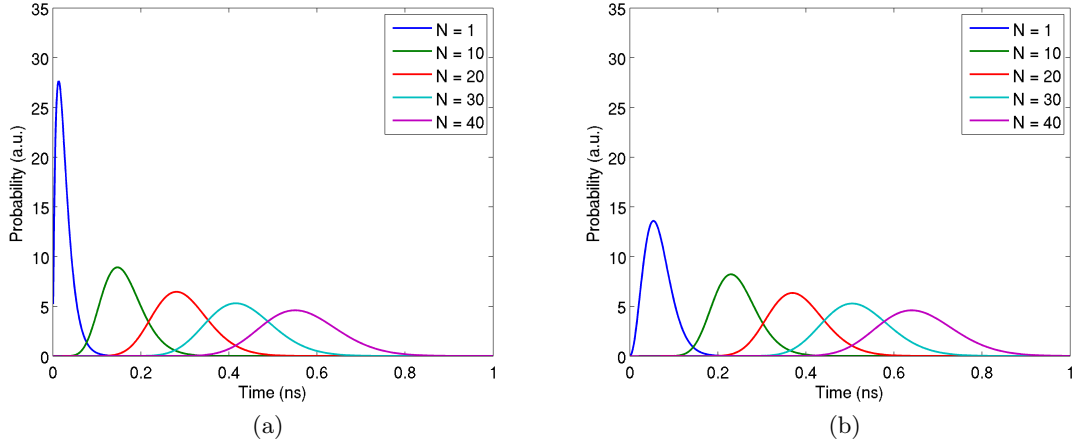


Figure 3.5: Probability distributions relating to the production of the n^{th} photoelectron at the detector for (a) Single exponential scintillator response model [53] and (b) Bi-exponential scintillator response model [55].

$$P(t)_N = \frac{f(t)^N e^{-f(t)}}{N!}, \quad (3.3.2)$$

where $f(t)$ is the predicted number of photons between time 0 and t . Substituting $f(t)$ in equations 3.1.3 and 3.1.5 and assuming a number N_{pe} of photoelectrons created at the detector between times 0 and t , a rise time τ_R and a fall time τ , it is possible to calculate the statistical probabilities of detecting the N^{th} photoelectron for both models. One such example is shown in Figure 3.5 where values $N_{pe} = 3000$, $\tau_R = 0.09$ ns [54] and $\tau = 41$ ns [61] have been used.

The single exponential model describes the statistical contributions of timing resolution based on two parameters: the fall time τ and the total photoelectron yield at the photodetector. The bi-exponential model uses the same parameter set, but with the additional inclusion of the scintillator rise time τ_R , assumed to be zero in the single exponential model. It can be seen in Figure 3.5 that in both models the probability distributions describing photoelectron production span a narrower time interval at lower values of N . Therefore, in order to extract the optimum timing resolution from the detector system, measurements should be made on the lowest possible photoelectron statistic, corresponding to the earliest part of the electrical signal produced by the photodetector.

The difference in response seen between two models can be understood quantitatively by considering that, in the case of a zero rise time, the probability of interaction of the

first photo-electron at the detector is better defined in time than when the probability is convoluted with an additional exponential. The reduced timing resolution due to the rise time can be seen in comparing the N=1 trace of Figures 3.5a and 3.5b. As predicted by considerations in section 3.1.3, at higher order statistics both models tend from a Poisson to a Gaussian response and become equivalent in width as the decay time becomes the dominant contribution to the signal shape.

3.3.2 Propagation time

The propagation time of a scintillator describes the spread on the arrival time of detected photons, which can in turn be attributed to the photon path through the crystal. By considering the refractive index of both the crystal and the medium to which it is coupled, and assuming perfect specular reflection at the optical boundaries, it is possible to estimate the photon travel paths through a scintillating volume with a simple 2D model. A schematic of the generation of optical photons in a LYSO crystal with a rectangular cross section of length L is given in Figure 3.6. The depth of interaction is defined by x_0 and the emission angle with respect to the x-axis is indicated by θ . The LYSO crystal is coupled to the photodetector with optical grease with a refractive index chosen to match the refractive indices of both the scintillating material and the photodetector. The application of index matching grease helps to maximise the transmittance of light from the crystal to the photodetector.

In general, the propagation time t_{prop} of a photon through a crystal, emitted at some position x_0 , is given by the ratio of the total path length to the photon's velocity. The speed of light propagating through a medium is given by c/n_{medium} , where n_{medium} is the refractive index of the relevant medium and c is the speed of light in a vacuum. The propagation path length is the ratio of the axial length to the cosine of the emission angle [62], where the axial length is considered as the path length along the x-axis between the point of emission and the photocathode. Figure 3.6 presents an example photon path through the crystal in which the axial length is defined as the projection of the photon path along the x axis. These considerations are combined to give:

$$t_{prop} = \frac{\text{axial length}}{\cos \theta} \frac{n_{medium}}{c}. \quad (3.3.3)$$

From this equation two cases appear:

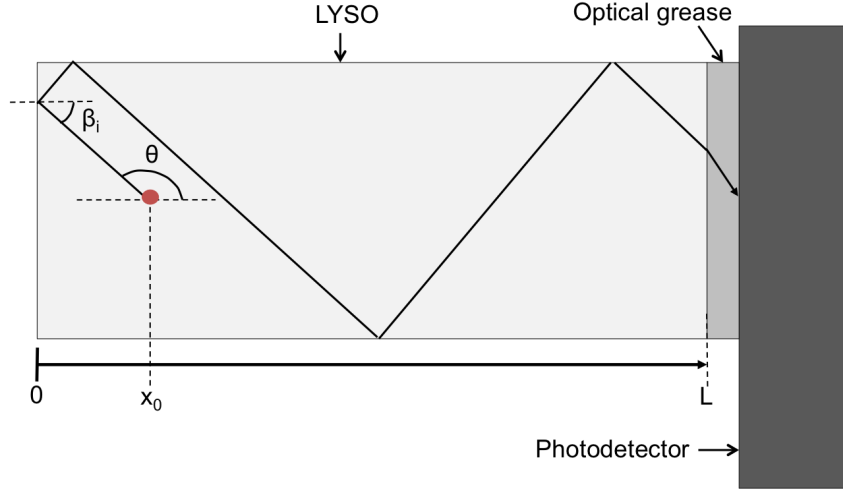


Figure 3.6: Diagram of the propagation of a scintillation photon in a LYSO crystal, with θ the initial axial angle of propagation. L is the total length of the crystal, while x_0 is the distance of the photon emission point to the face of the crystal. LYSO has a refractive index $n_{LYSO} = 1.81$, the optical grease has $n_{grease} = 1.4$.

$$t_{prop} = \frac{n_{medium}(L - x_0)}{c \cdot \cos \theta}, \quad \text{if } 0 \leq \theta \leq \frac{\pi}{2} \quad (3.3.4)$$

$$t_{prop} = \frac{n_{medium}(L + x_0)}{c \cdot \cos \theta}. \quad \text{if } \frac{\pi}{2} \leq \theta \leq \pi \quad (3.3.5)$$

The limit on the propagation time becomes infinite for $\theta \rightarrow \frac{\pi}{2}$. However, as shown in Figure 3.7, light interacting at the LYSO-air interface can either internally reflect at an angle equivalent to the incident angle β_i , or transmit to the air via a refraction at an angle β_t . If the fraction of reflected photons from a total flux of number N is defined as R , the number of refracted photons is the given by $N(1-R)$. Then, according to the Snell-Descartes law, one can calculate:

$$n_1 \sin(\beta_i) = n_2 \sin(\beta_t), \quad (3.3.6)$$

$$\beta_t = \arcsin\left(\frac{n_1}{n_2} \sin(\beta_i)\right). \quad (3.3.7)$$

In the case where $n_1 \neq n_2$ there is a critical angle β_c beyond which the light is totally internally reflected. As shown in Figure 3.7, for the case presented here $n_1 = n_{LYSO} = 1.81$ and $n_2 = n_{air} = 1$, however to estimate the transmittance to the photodetector a

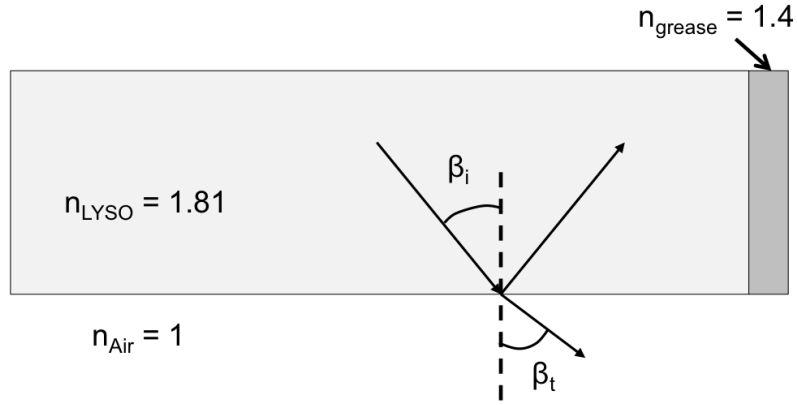


Figure 3.7: Reflection and refraction at the scintillator / air interface.

third index, $n_{grease} = 1.4$ must be considered. $n_{grease} = 1.4$ is typical of industry standard detector assembly materials [63]. Due to the different index of refraction of air and grease, the critical angle is different for each interface:

$$\beta_c^{LYSO/Air} = 33.5^\circ, \quad (3.3.8)$$

$$\beta_c^{LYSO/Grease} = 50.7^\circ. \quad (3.3.9)$$

We can then consider the approximation that at the LYSO-air interface any photon is totally internally reflected for $\beta_i > 33.5^\circ$ and transmitted for $\beta_i < 33.5^\circ$. Additionally, at the LYSO-grease interface, any photon is totally internally reflected for $\beta_i > 45.6^\circ$ and transmitted for $\beta_i < 50.7^\circ$. A list of each of the possible situations arising due to these reflection and transmission angles is given in Table 3.2.

Table 3.2: List of photon emission angles and their interactions at optical boundaries. R = reflected, T = transmitted.

β_i range	LYSO-air interface	LYSO-grease interface	Possible detection?
0 - 50.7°	R	T	Yes
50.7° - 56.7°	R	R	No
56.7° - 123.5°	T	-	No
123.5° - 129.3°	R	R	No
129.3° - 146.5°	R	T	Yes
145.5° - 180°	T	-	No

By considering the extreme cases of optical transmission in the crystal an estimate may be made of the timing contribution due to the *propagation time* of photons in the crystal. For photons traversing the shortest path, the emission point is at $x_0 = L$ with an angle $\theta = 0^\circ$, so that $t_{prop}^{min} = 0$. Instead, the maximum propagation time is obtained for $x_0 = L$ and $\theta = 129.3^\circ$, as per the above calculation. An estimate of the maximum time interval between two events is:

$$\Delta t_{max} = t_{prop}^{max} - t_{prop}^{min} = \frac{2Ln}{c \cdot |\cos(129.3)|}. \quad (3.3.10)$$

For a 5 mm crystal, $\Delta t_{max} = 95$ ps. This value then represents the largest possible variation for a crystal equivalent to those applied in ultra-precise timing measurements [64]. Assuming the full distribution of Δt values are Gaussian distributed [65], one can predict that 99.7% of events will be contained within $\pm 3\sigma$. We can therefore assume that: $\Delta t_{max} = 6\sigma$. As such we can then define the $\sigma_{prop} = 16$ ps or $FWHM = 38$ ps.

In order to increase the measurable light yield scintillators are often wrapped or painted with a reflective material of which the most common are PTFE and TiO₂ paint [66]. In this case it can be assumed that $\sim 95\%$ of the photons which escape the crystal through transmittance are scattered back into the crystal with a cosine distribution. This additional parametrisation complicates the process making further analytical prediction difficult. The effect of both reflective coatings and the surface roughness on the detector system's timing resolution are investigated with Monte-Carlo simulation in Chapter 8 to follow.

Chapter 4

Photodetectors for PET

Traditionally, the photodetector of choice for PET has been the photomultiplier tube (PMT). In fact, not confined to use in PET, the PMT has been the dominant photodetector within the high energy and astro-particle physics communities since the 1930's [15]. However, with the development of engineering and production techniques for microelectronics over the past ~ 30 years, detector quality silicon substrate can now be produced cheaply and in large quantities. As a result, solid state detectors have been increasingly investigated as an alternative to the PMT in PET detector systems. Of all the solid state detector designs, including p-i-n (PIN) diodes and avalanche photodiodes (APDs), particular interest has been given to the Silicon Photomultiplier (SiPM). With its high gains and equivalent or better photon detection efficiencies, the SiPM can be considered the solid state alternative to the PMT. Moreover, SiPM's promising timing properties have led to significant interest for use as a candidate photodetector in time-of-flight PET, and its insensitivity to magnetic fields have provoked interest for application in a combined PET-MR machine. In this section an overview is given of the major photodetector technologies applicable to PET, including: the PMT, PIN diodes, APDs and an extended description of the SiPM. Additionally a section is dedicated to outlining and describing the digital signal processing techniques applied to the response of an SiPM in the following chapters.

4.1 The photomultiplier tube

The widespread use of scintillator materials in radiation detection relies heavily on the availability of devices which can convert the optical signal resulting from an interacting

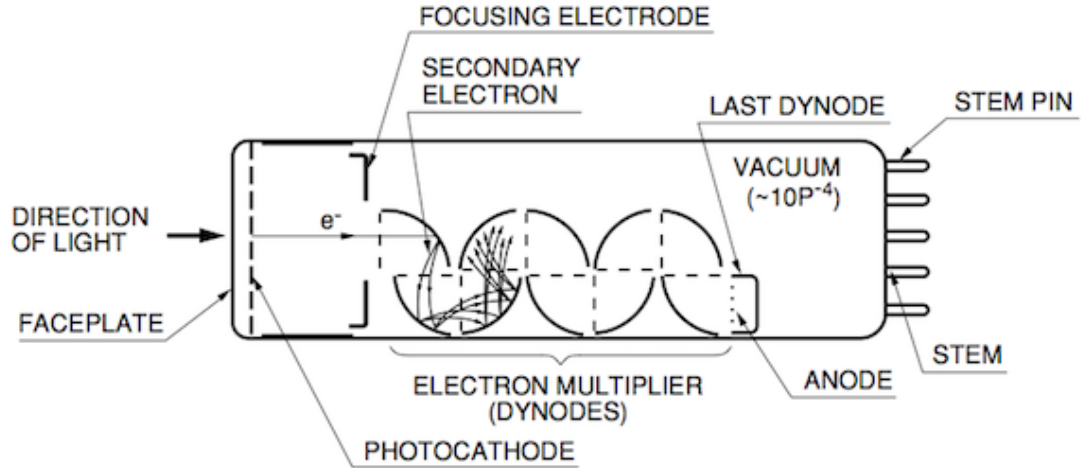


Figure 4.1: Schematic diagram of a typical PMT. All major physical components are labelled.

event into a corresponding electrical one. For this purpose, the PMT has conventionally been the photodetector of choice. The basic structure of a PMT is a glass vacuum tube containing a photo-cathode, an anode and several dynodes. A schematic outlining a typical PMT design is given in Figure 4.1.

The operational flow of a PMT begins with incident photons traversing a transparent window at the front face of the vacuum tube. Photons then interact with the photocathode, which is a photo-sensitive electrode placed on the front face of the device, emitting charge in the form of individual electrons when excited by incident photons. The efficiency of this conversion process is known as the *quantum efficiency* (QE) of the PMT and can be considered the ratio of the number of emitted photoelectrons to the number of incident photons. Photoelectrons from all parts of the photocathode surface are then accelerated via a static electric field onto the first stage of the dynode chain. On impact with the first dynode, the photoelectron signal is amplified by *secondary emission*, whereby a number of electrons are emitted from the dynode. Producing secondary particles requires bound electrons to be freed, requiring energies equal to or greater than the specific work function of the dynode material (typically of order 2-3 eV). Electrons emitted from the photocathode have kinetic energies of order 1 eV or less [9], resulting in 3-4 secondary electrons emitted for every 100 V of potential applied to the electric field. In order then to yield a total electron gain of order 10^6 , which is typical, all PMTs employ multiple stage amplification as represented by dynodes 1-12 in Figure 4.1. Secondary electrons emitted from each dynode stage are accelerated onto the next via a step potential of ~ 100 V applied between the two. The voltage supply needed to operate a PMT depends linearly

on the number of dynode stages. In the case of Figure 4.1, this gives a voltage of $100 \times 12 \text{ V} = 1.2 \text{ kV}$.

The requirement for power supplies which can provide thousands of volts, combined with the relatively bulky physical size of PMTs can be limiting characteristics in applications where high packing fractions and channel densities are required. In PET, where detector systems can have more than 18,000 detector elements (e.g. 288 block detectors each with 8×8 crystals per block) [29] these limitations can be significant.

4.2 Solid-state detectors

The typical FWHM spatial resolution of a PMT-based PET cameras tends to be in the range 3-10mm and is limited by the scintillator block detector design and the low QE of PMTs. To achieve higher spatial resolution a finer segmentation of scintillators is required with, ideally, the ability to read out each segment individually, eliminating positional uncertainties of the block detector and reducing the system dead time. In contrast to PMTs, solid state photodetectors have small package requirements, operate at lower voltages and exhibit significantly improved QE, often increasing by a factor of two or more, making them strong candidates for such detector systems. The key devices and mechanisms of solid state detectors applicable to PET are overviewed in this section.

4.2.1 The p-n junction

All solid state photodetectors devices are based on a semiconductor structure called a *p-n junction*. A p-n junction is created by doping two separate substrates, one with acceptor ions giving a net positive charge and one with donor ions yielding a net negative charge. When the substrates are brought into contact a concentration gradient forms causing holes from the n-side to diffuse into the p-side and vice versa with electrons from the p-side. This process creates a neutral region, called the *depletion region*, centred about the physical junction which is depleted of mobile charge carriers. A schematic diagram showing the basic representation of a p-n junction is given in Figure 4.2. As a result of the established depletion region, an electrostatic potential is also established across the junction, restricting further diffusion of electrons and holes.

If we now consider the junction as a component with some external circuitry, it will behave as a diode restricting the flow of electric current in the n to p direction. By applying a

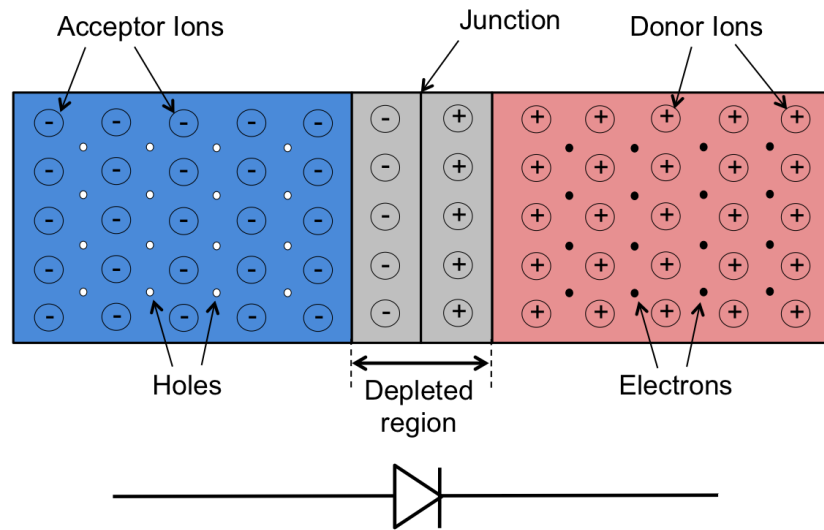


Figure 4.2: Schematic representation of a p-n junction.

voltage (referred to as either *forward biased*, if the positive and negative terminal are connected to the p and n sides respectively, or *reverse biased*, if the terminal connections are switched) it is possible to modify the nature of the depletion region. If the device is forward-biased, the electrostatic potential across the depletion region is reduced and current flow is less restricted. This observed behaviour is ohmic in nature and as such follows the $V = IR$ relation between potential difference V , current I and resistance R . However, if the device is reverse biased the junction potential is increased, extending the depletion region and accentuating the diode behaviour.

4.2.2 PIN diodes

A PIN diode uses the basic principle of the p-n junction but with an additional, lightly doped layer used to control the shape and depth of the internal electric field. A typical diode structure is given in Figure 4.3 where the depletion layer is shown to be formed between the p and n doped layers. An electric field is induced across the depletion layer, which decreases linearly from a maximum near the p region to zero at the edge of the depletion region. Typically, for a substrate with thickness 0.35 mm, an operating voltage of approximately 50 V is required to form the manufacturer recommended static electric field in the device [29].

In the case where optical photons are incident on the device, providing the photon energy is higher than the band gap energy of the semiconductor material, there is a probability

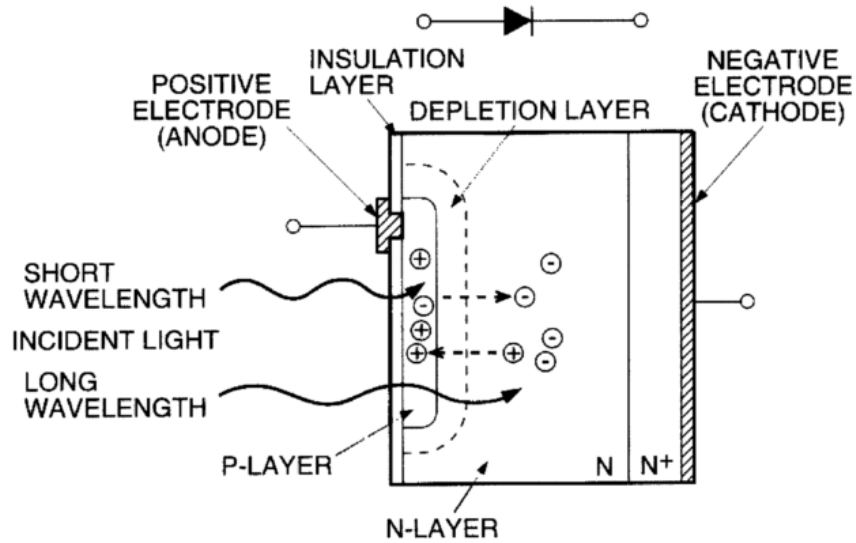


Figure 4.3: Schematic diagram of a reverse biased semiconductor photodiode. Shorter wavelengths will be absorbed closer to the surface, creating more complicated conditions for the achievement of high quantum efficiency [29].

an e-h pair will be produced in the depletion region. For silicon devices this energy is about 1.1 eV, corresponding to a wavelength less than 1000 nm. Any e-h pairs generated in the depletion region will be influenced by the static electric field and will be accelerated towards the electrodes, inducing a current. Typically, this charge signal will be seen at the input of an ultralow noise pre-amplifier which produces a proportional response representative of the activating flux of scintillation photons.

PIN diodes are robust, inexpensive devices, which operate at voltages of ≈ 50 V, are insensitive to magnetic fields and have QE up to three times that of PMT devices. However, they tend to exhibit high levels of electronic noise due to the intrinsic capacitance of the silicon substrate. They also have a slow signal response time and show internal gain of order one. As such the pre-amplifiers used in conjunction with PIN diodes must be extremely low noise, adding to the cost of the readout electronics.

4.2.3 Avalanche photodiodes

A technological advance on the PIN diode is the avalanche photodiode (APD). The APD has the advantage to display both improved gain of the order 10^2 - 10^3 and faster timing (of order of 1 ns), making it a more eligible candidate for use in PET applications.

In an APD device, an internal gain mechanism is generated by increasing the reverse bias applied across the p-n junction, which creates a high field region in the internal electronic

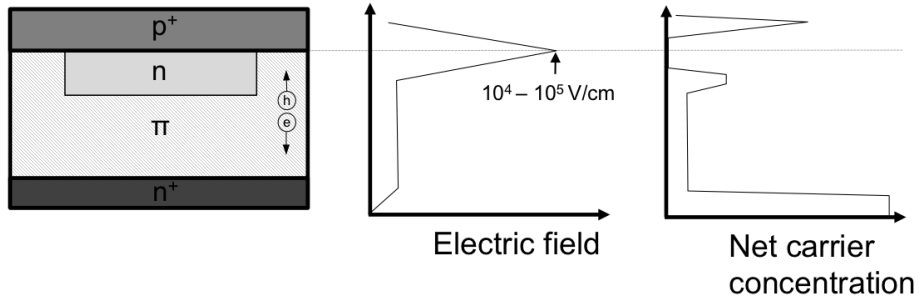


Figure 4.4: Schematic diagram of the internal structure of an APD including the corresponding electronic field distribution and net carrier concentration as a function of depth.

field structure close to the device surface, known as the *avalanche region*. Charge carriers entering this region are accelerated to high enough energies that secondary e-h pairs can be generated through impact ionisation along the drift path, increasing the charge signal. The gain returned by this process depends exponentially on the reverse bias, which can be in the range 200-1000 V depending on the device's final application. A schematic showing a typical electronic field distribution through the cross section of an APD is given in Figure 4.4.

One of the major complications associated with APDs is their susceptibility to temperature changes. The APD gain is reduced as free electrons interact with phonons, causing gain changes of $\approx -3 \%/^{\circ}C$ at gain values of 10^2 , and gain changes as high as $-15 \%/^{\circ}C$ at gain values of 10^3 [67]. They therefore require extremely stable, high voltage bias supplies and must be either accurately temperature controlled or be instrumented with temperature compensating feedback electronics. Additionally, the gain in APD devices, although a significant improvement on the PIN diode, is still not high enough to negate the need for pre-amplification. Low noise amplifiers are therefore still required with APD devices, which adds to the cost and complexity of the necessary electronic readout systems.

However, APDs exhibit two possible modes of operation, *linear-mode* (as considered above) and *Geiger-mode*. The two modes derive from the magnitude of the bias voltage applied across the APD. If the bias is high enough to create electronic conduction, the device is considered to be in *breakdown*. The minimum reverse voltage required to meet this criterion is called the breakdown voltage (V_{BR}). When the bias voltage applied across an APD is below V_{BR} , the number of secondary carriers generated in the avalanche region is proportional to the number of primary charge carriers generated in an activating event. In this regime devices are operated in linear-mode. Conversely, in Geiger-mode both the

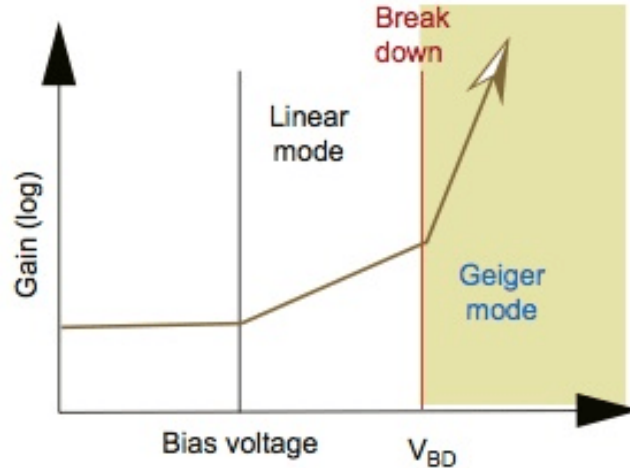


Figure 4.5: Operational principle of an APD showing the three specific gain regions [69].

electrons and the holes entering the avalanche region cause further impact ionisations, and an avalanche of charge develops. The distinction between linear- and Geiger-mode is illustrated in Figure 4.5. The response signal of the device in Geiger-mode is then independent of the number of charge carriers generated in the active area by the photon flux of an event, imitating the Geiger discharge process which gives it its name [68]. When operating in Geiger-mode, the output is effectively binary and the device can either be inactive or can be activated to create a standard response.

Although the gain associated with the Geiger-modality can be as high as 10^6 , equivalent to the PMT, the binary nature of the response makes it impossible to distinguish between different energy signals. The SiPM provides a solution to the energy resolution problem while retaining the high gain and extremely fast signals of Geiger-mode APDs (GM-APDs).

4.3 The Silicon Photomultiplier

The SiPM is a relatively new photodetector, with the first patents being filed in the late 1990's [70] [71]. They consist of an array of miniature GM-APDs connected in parallel on a common substrate, introduced to address the shortcomings of both APDs and PMTs. A comparison of some typical characteristics of the three photodetector types are given in Table 4.1.

Figure 4.6 shows both a photograph of the sensitive area of a typical SiPM and a schematic of the underlying topology. As we have seen previously in the APD structure a n-p junction

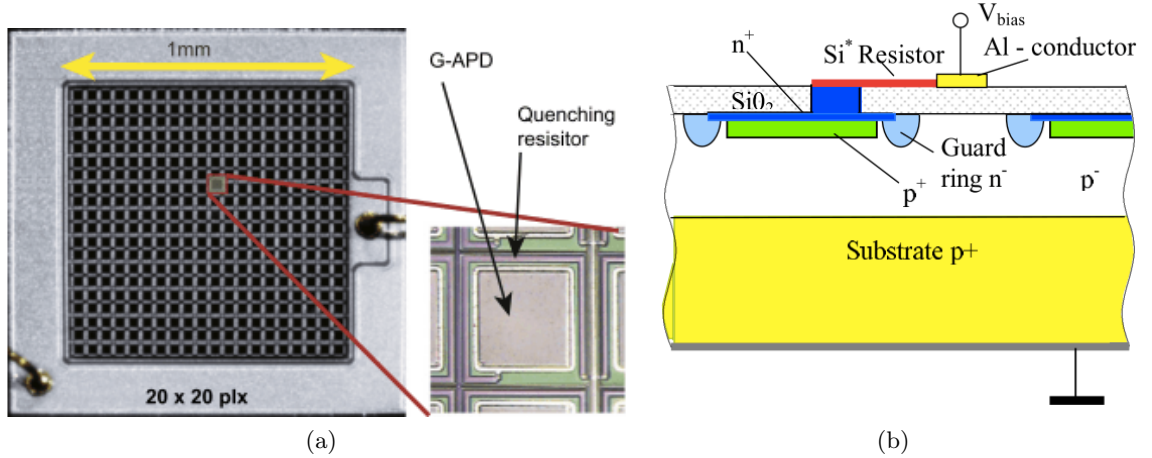


Figure 4.6: (a) A photograph of a Hamamatsu SiPM of 1 mm^2 active area with 400 APD microcells [69]. (b) Topology of a GM-APD pixel [16] showing surface connections and junction structure.

is formed between the thin n^+ layer and the p^+ close to the surface of the device. A lightly doped p^+ layer below the junction is employed to help shape the electronic field, which peaks close to the n-p junction creating the *avalanche region*, dropping off quickly to a uniform, low field strength through the p^+ layer, known as the *drift region*. This extended electronic structure increases the active volume of the detector, improving the photon detection efficiency (PDE) of the device (a full description, along with the factors influencing the PDE are explored in depth in section 4.4.2). Charge carriers created in the drift region will drift towards the corresponding electronic terminals. As in the case of APDs described previously, electrons drifting into the avalanche region then have a probability of triggering a Geiger avalanche. Above the doped silicon junction is a thin, protective layer of SiO_2 which is covered in an anti reflective coating in order to maximise photon transport into the active area. The microcell is then connected in series with a contact resistor through which the device is biased.

The detection principle of the SiPM cells is identical to the APD, whereby e-h pairs entering the high field region trigger an avalanche of charge. This process involves a large number of charge carriers and, as a result, the output signal is negligibly affected by statistical fluctuations. This yields a well known, repeatable response at each pixel. In order to operate in this mode it is necessary to protect the diode from being damaged by the large currents with an appropriate quenching circuit. In current-generation SiPM devices, this is done using a large quenching resistor (R_Q) in series with each APD cell, typically of several hundred $k\Omega$. This resistor is shown in both Figures 4.6a and 4.6b.

Every time a large current flows through this resistor a voltage drop will occur across the terminals of the micro-cell. The voltage drop is large enough for the voltage to fall below V_{BR} , resulting in an interruption of the avalanche process. The quenching resistor is built directly onto each APD pixel, typically in the form of high resistivity poly-silicon material, as shown in Figure 4.6a. Due to the inherent capacitance which exists in each microcell, as well as the parasitic capacitance of the overall summing network, each micro-cell will take a characteristic time to recover before the bias voltage is restored to the pre-set value above breakdown. This characteristic time is known as the recovery or *fall time*. During the recovery phase, the cell is insensitive to external activation. Cells are physically isolated from each other via guard rings that reach into the silicon substrate.

The major advantage the SiPM holds above the standard GM-APD is the ability to respond proportionally to a incident flux of optical photons. This is achieved by summing the response of each of the individual micro-cells through a common readout line, as shown in Figure 4.7a. Here each pixel in the parallel array is modelled as a diode in series with the associated quenching resistor, details of the electronic characteristics are explored further in section 4.3.1. As a result, the response of a SiPM is linear, provided that the incident photon flux is low enough for each micro-cell to respond to a single visible photon. An illustration of the total SiPM response pulse, formed of the individual micro-cell activations is given in Figure 4.7b.

The rest of this section is dedicated to the detailed description of principles of operation of SiPM devices including the electronic representation of both the single APD cell and the extended considerations of the full SiPM matrix.

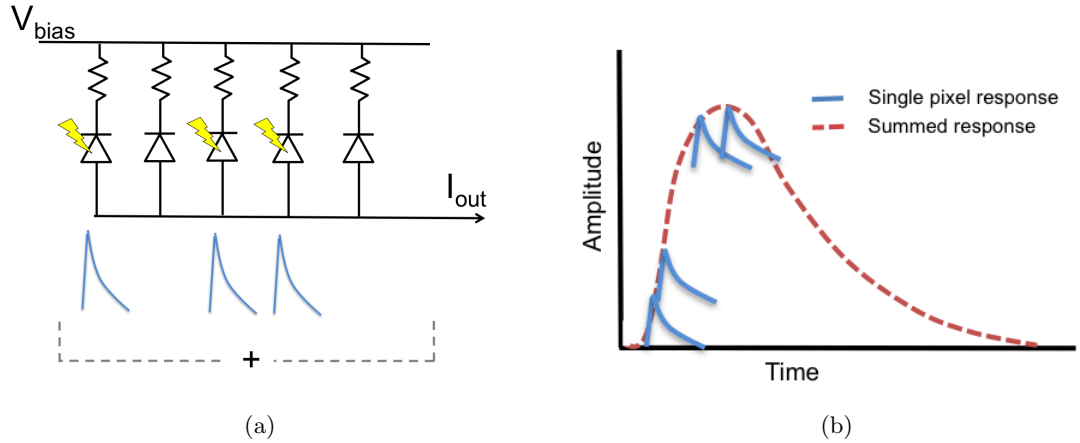


Figure 4.7: (a) A schematic representation of the electrical circuit of a SiPM. Here five microcells are represented by a diode in series with a quenching resistor, activated pixels are shown with lightning symbols. The response of each active pixel is summed to produce the full SiPM response. (b) An illustration of a SiPM response to a temporally spread incident photo-flux, similar to that from a scintillator crystal.

Table 4.1: Comparative table of three photodetectors considered for use in PET: PMT, APD and SiPM [22].

	PMT	APD	SiPM
Gain	10^6	10^2 - 10^3	10^6
Rise time (ns)	~ 0.6	~ 5	~ 1
QE @ 420 nm (%)	~ 25	~ 70	25-75 (PDE)
Bias (V)	>1000	200-1000	30-80
Temperature-Gain Sensitivity ($\frac{\%}{^\circ C}$)	<1	~ 3	1-8
Magnetic Field sensitivity	Yes	No	No
Sensitive area	mm^2 - cm^2	mm^2	mm^2
Price / channel (\$)*	>200	~ 100	~ 50

* Prices accurate as of 2014.

4.3.1 Principles of operation and electronic characteristics

Independent of the specific APD cell structure all SiPMs operate as an array of APDs connected in parallel. Considering the basic principle of a photodetector, whereby an optical signal is converted to an electric one, it is important that the electrical characteristics of the system are well understood. One of the main reasons why, in a field where technology progresses so quickly, the PMT has been ubiquitous for a number of decades is because it

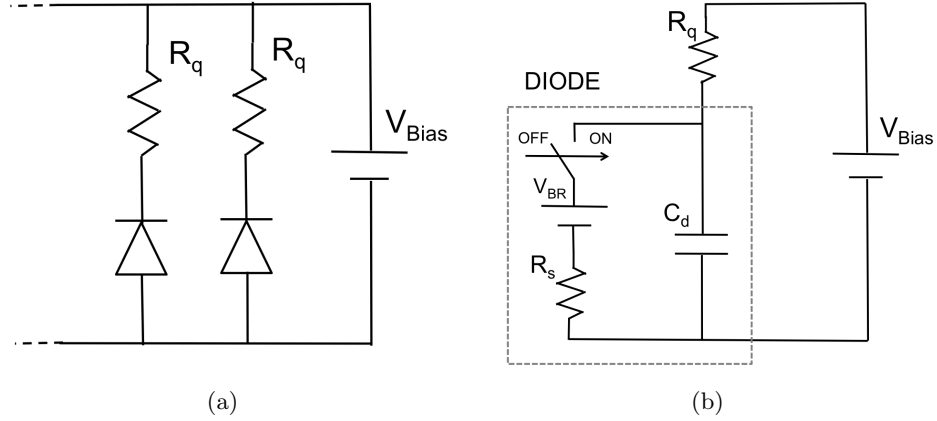


Figure 4.8: A diagram showing a example circuit for (a) A SiPM diode array and (b) an avalanche microcell [72].

behaves as a near perfect current source, significantly reducing need to design additional signal processing electronics. Although the SiPM has similar gain characteristics to the PMT, and can improve on the performance of a number of parameters (see section Table 4.1), the SiPM is a more complicated case. In order to understand the operation of the full device first the response of the individual photodiodes must be considered.

Avalanche photodiodes

When inactive the p-n junction of an APD acts as a diode. The system can be simply represented as a parallel array of diodes in series with their respective quenching resistors (R_Q), see Figure 4.8a. Each cell is then biased between the quenching resistor and a metal contact on the bottom of the microcell, as was shown previously in Figure 4.6b.

The full circuit model for the electrical response of an GM-APD, shown in Figure 4.8b, derives from a model developed in the 1960's to describe the micro-plasma instability in silicon [73] [74]. In this model the system has two possible states: pre-breakdown and breakdown (corresponding to switch on and switch off in Figure 4.8b). The pre-breakdown state can be represented as a capacitance in series with a the quenching resistor. When an event occurs in the photocell, there is a probability that the cell will initiate an avalanche discharge, called the *triggering probability* (see also section 4.4.2). If an avalanche is triggered, the new state of the system can be modelled by adding a voltage source, equivalent to the breakdown voltage of the GM-APD cell (V_{BR}), in series with a resistor (R_S) to the system. The component R_S represents the internal resistance of the bulk silicon, including contributions from both the neutral regions and the space charge

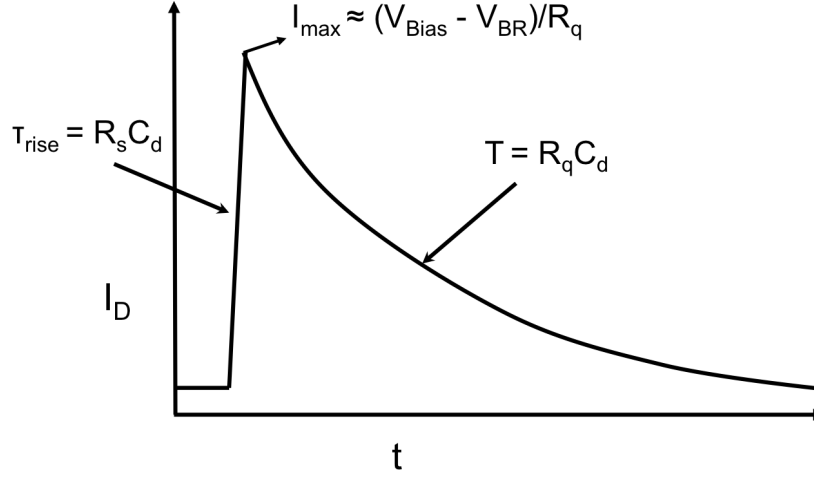


Figure 4.9: Shape of GM-APD current response to an avalanche event.

resistance. At this point, the diode capacitance (C_D), which had been charged to V_{Bias} (where $V_{Bias} > V_{BR}$) pre-breakdown, then discharges through R_S until the voltage across it drops to V_{BR} . This process defines the lower bound of the rise time of a single APD microcell signal, given by:

$$\tau_{rise} = R_S \cdot C_d. \quad (4.3.1)$$

Considering some typical values for C_d and R_S ($C_d = 15.4$ fF and $R_S = 1$ k Ω [75]), one gets $\tau_{rise} = 15.4$ ps. However, it should be noted that the avalanche development process can be of order hundreds of ps, therefore τ_{rise} is not necessarily the dominant contribution to the GM-APD rise time.

As the voltage on C_D decreases the current flowing through the quenching resistance, and hence the diode, approaches a maximum of $I_{max} \approx (V_{Bias} - V_{BR})/(R_q - R_S)$. Once the process is passively quenched by R_q , the switch is again considered open and the cell capacitance C_D is recharged to V_{Bias} with a time constant; $\tau_{Re} = R_q C_d$. In order to effectively quench the internal avalanche, R_q must be high and is typically of order of 100 k Ω (measured in the range 100-400 k Ω for Hamamatsu devices [75]). This results in a recharge time of the order of 10 ns. While the cell is recharging, the internal electric field is reduced and hence the probability of a photo-generated e-h pair in the depletion region is less likely to produce an avalanche. A diagram illustrating the response time of GM-APD to an avalanche event is given in Figure 4.9.

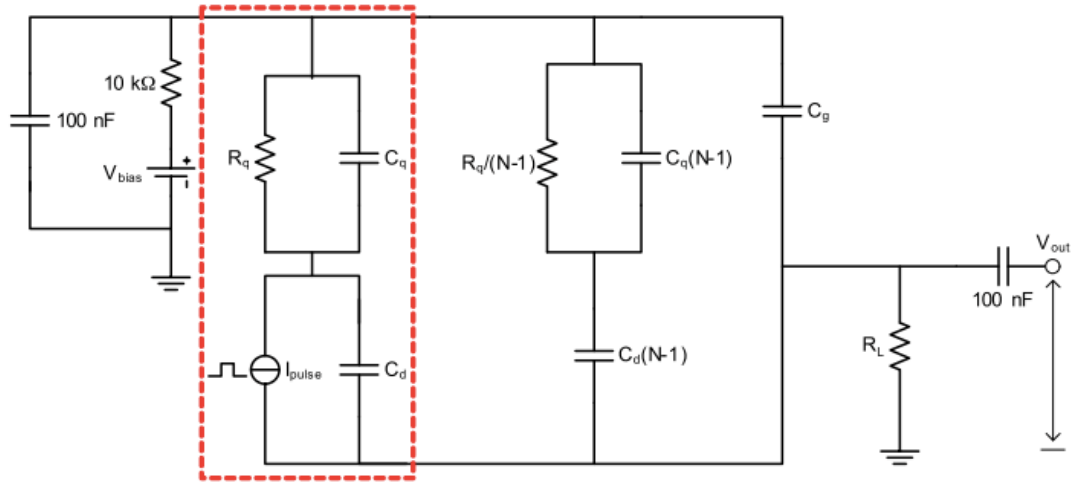


Figure 4.10: Equivalent SiPM circuit with additional bias circuit as recommended by Hamamatsu [75] [78], as described in text.

The Silicon Photomultiplier

Although the response of a SiPM is similar to that of the single GM-APD, some higher order effects are introduced due to the contribution of non-active microcells linked in parallel. A full equivalent circuit for a SiPM, as proposed by [76], is given in Figure 4.10. The diagram includes a simple bias circuit of a source with a RC low-pass filter (as suggested by Hamamatsu [77]) and a load resistor R_L and AC coupling capacitor to represent external circuitry. The representation of a single GM-APD microcell is circled in red. In parallel with the APD cell, all the non-active pixels are considered as the lumped contributions of the pixel capacitance C_d and the quenching resistor R_q , with its associated capacitance C_q , for $N-1$ pixels where N is the total number of GM-APD pixels in the SiPM device. An additional capacitance C_g is included in parallel to represent the parasitic contributions of the non-ideal electrical contacts and conductors in the device.

The diagram in Figure 4.10 shows equivalent circuit in the case of a single pixel firing. The additional contributions of the passive pixels have little effect on the electronic modelling of the rise time, which is still described by the current pulse I_{pulse} charging the diode capacitance C_d . If we model the current pulse as in Figure 4.8b with a voltage source (V_{BR}) in series with a resistor (R_s), the rise time is given by: $\tau_d = R_s C_d$. However, the fall time of the signal, where the capacitance is being recharged, is now defined by two decay constants, a fast constant τ_{fast} and a slow constant τ_{slow} . The slow component tends to dominate the signal and is attributed to the re-charging of the pixel capacitance after

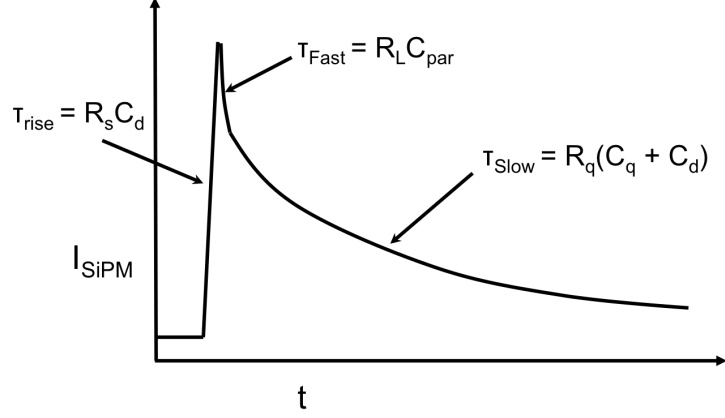


Figure 4.11: Shape of SiPM current response to an avalanche event.

an activating event. It can be approximated by considering the quenching resistance (R_q), its associated capacitance (C_q), and the diode capacitance (C_d). The fast component is due to the current flowing in the external load and is given by the product of the resistive load and the parasitic capacitance due to any non-firing pixels (C_g). The expressions for both are then:

$$\tau_{slow} = R_q(C_q + C_d), \quad (4.3.2)$$

$$\tau_{fast} = R_L \cdot C_g, \quad (4.3.3)$$

The resulting pulse shape is given in Figure 4.11 where the different parts of the time response are also identified and labelled with the corresponding time constants.

4.4 Characteristics properties of SiPMs

4.4.1 Gain

As mentioned above, GM-APD signals produce a fixed signal for any active micro-cell. The gain of each microcell is determined by the total charge Q_{total} generated during the Geiger discharge [79] [80] and is typically in the range $\sim 10^5 - 10^7$:

$$G_{pixel} = \frac{Q_{total}}{e} = \frac{C_D(V_{Bias} - V_{BR})}{e}. \quad (4.4.1)$$

Equation 4.4.1 defines the gain as the number of charge carriers produced during an

avalanche, dependent upon the *over-voltage* ($V_{Bias} - V_{BR}$) and the diode capacitance. The charge response of a SiPM device is this the sum of the charge produced at each activated pixel in an event.

4.4.2 Photon detection efficiency

The photon detection efficiency (PDE) of a SiPM is the product of three variables: The quantum efficiency QE of the active area, the probability P_t that an incoming photon triggers an avalanche breakdown, which is dependent on the incoming photon wavelength, and the ratio of active area and total area in the APD matrix know as the *geometrical fill factor* G_f [81]. Overall:

$$PDE(\lambda, V_{Bias}) = QE(\lambda) \times P_t \times G_f, \quad (4.4.2)$$

where the wavelength and V_{Bias} have been made explicit. An additional correction can also be included in equation 4.4.2 by considering the number of cells which maybe recovering from a previous event and may therefore be inactive. However, this parameter is highly dependent on the spatial and temporal distribution of the activating source and will not be considered further in the discussion here.

Quantum efficiency

The QE gives the probability that an incident photon will create an e-h pair inside the device. The QE of a SiPM is dependent on two main variables:

- the *transmittance* of the dielectric layer on the surface of the device
- the internal QE of the device.

For a SiPM, the internal QE can be as high as 80-90% [82], but is heavily dependent on wavelength - peaking in specific ranges for different micro-cell designs. Specifically, it describes the probability that a photon that has penetrated the surface creates an e-h pair in the active layer. The optimisation of both the transmittance and internal QE depends on technological improvements of the fabrication process. To minimise the reflection of photons on the silicon surface it is possible to implement suitable anti-reflective coatings. Whereas, depending on the wavelength of the incident light, the internal quantum efficiency for radiation with high λ is maximised by increasing the thickness of the depletion

layer, and for short wavelength by using a shallow junction.

Triggering probability

Once an e-h pair is generated in the depletion region, the charge carriers are accelerated at a rate proportional to the electric field strength, in turn generating secondary daughter e-h pairs through impact ionisation with a given probability. In order to create a self-sustaining avalanche at least one daughter ionisation must be created and, in turn, go on to create further ionisations. The probability that an e-h pair generated in the depletion region of the device will go on to trigger a full avalanche is then a function of the probabilities of avalanche creation associated with both the electron P_e and the hole P_h separately. If one e-h pair is created at some depth (x) in the junction, then the probability that neither the electron nor the hole causes an avalanche is given by $(1 - P_e) \cdot (1 - P_h)$. Consequently, the probability (P_t) that either the electron or hole initiates an avalanche is given by [83]:

$$P_t = P_e + P_h - P_e P_h. \quad (4.4.3)$$

If one considers a n-on-p device, it is possible to define the boundary conditions of this process. In the case where an e-h pair is generated at the n^+ edge, close to the photon window, the electron is collected almost instantly at the cathode and P_e will tend to zero. Conversely, the hole will transverse the whole high-field region maximizing the contribution of P_h . If photogeneration occurs deep in the active region, the situation is reversed and the drifting electrons will be the dominating contribution to the total probability, P_t .

The probabilities P_e and P_h depend on the impact ionization rates of both electrons (α_e) and holes (α_h). These parameters are not currently well determined, and large discrepancies exist among the values extracted from the various models (as an example see [84] [85]). Despite these discrepancies in absolute values it is well established that (i) both coefficients increase with electric field (ii) the electron ionisation rate is higher for electrons than holes (e.g., at 5×10^5 V/cm, α_e is approximately twice α_h [84]), and (iii) their differences decrease with increasing fields. As a consequence of $\alpha_e > \alpha_h$, the triggering probability is maximized when photo-generation occurs towards the p side of the junction. This effect is shown in Figure 4.12 where the P_e and P_h values are shown as a function of depth of interaction within the active volume.

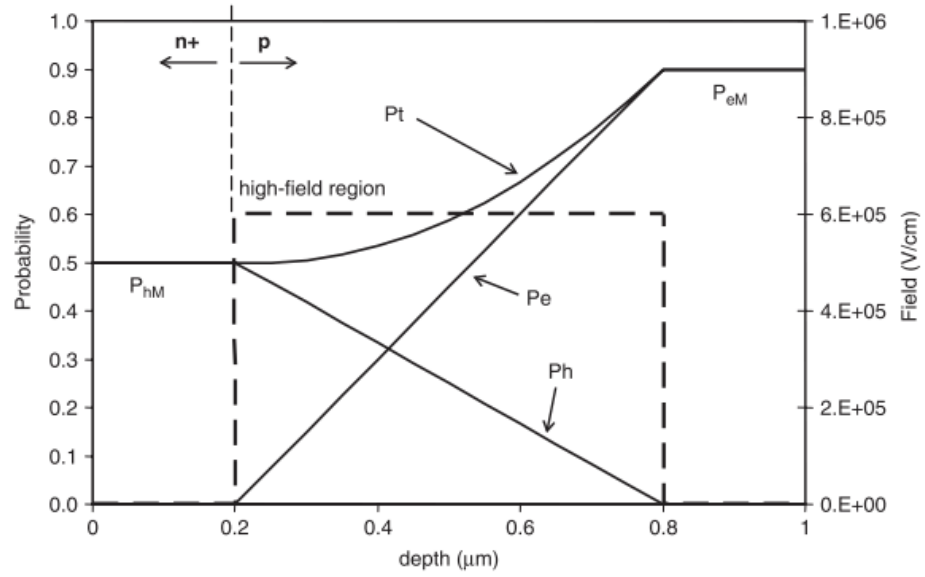


Figure 4.12: Avalanche triggering probability as a function of photogeneration position [72].

Geometric efficiency

The geometric efficiency (G_f) is defined as the ratio of the area of a device which is sensitive to impinging photons to the total area covered by the GM-APD matrix. By convention, manufacturers tend to quote a *sensitive area* referring to the total area covered by the GM-APD matrix along with a *fill factor* to describe G_f .

Often, $G_f < 1$, as each GM-APD is bounded by a dead region of guard rings and trenches (see Figure 4.6a) to reduce optical cross-talk. The quoted fill factor of devices from any given manufacturer ranges widely and is typically between 25-80 %. It is shown in Table 4.2 that the quoted fill factor is often dependent on the area of individual APD pixels. A smaller pixel size results in a higher number of pixels per unit sensitive area and hence a higher number of guard rings and trenches, reducing the overall fill factor. With an internal QE of 80-90 % and a triggering probability > 50 %, the geometric efficiency can therefore often be the limiting factor for an optimal total PDE.

Table 4.2: Table listing the Geometric efficiencies for a range of pixel sizes [86] [87]

Manufacturer	Model	Active area (mm ²)	Pixel Area (μm ²)	N _{pixels}	Fill factor (%)
Hamamatsu	S10362-11-25C	1	25	1600	30.8
	S10362-11-50C	1	50	400	61.5
	S10362-11-100C	1	100	100	78.5
SensL	M-series 10010	1	10	2720	28
	M-series 10020	1	20	1144	48
	M-series 10035	1	35	504	64
	M-series 10050	1	50	282	72

4.4.3 Noise

Dark count rates

The largest source of noise in SiPMs is from the dark count rate (DCR). Due to the small (1.1 eV) valence band gap of silicon, there is a finite probability that an e-h pair will be generated through thermal excitation or electric-field-assisted tunnelling and go on to generate an avalanche. The signal produced in such an event is indistinguishable from a photo-generated event and is called *dark noise* [81] [88]. At room temperature the dark noise is dominated by thermal generation and can typically lead to a single-pixel dark rate of ~ 1 MHz/mm², corresponding to one pixel activation every 1 μs. [89]. The temperature dependence of the number (N_{thermal}) of thermally generated carriers is well understood and is given by:

$$N_{thermal} \propto T^{3/2} \exp(-E_G/2k_B T), \quad (4.4.4)$$

where E_G is the band gap energy of the silicon in the active volume [90], T is the temperature and k_B is Boltzmann's constant.

Another process which contributes to the dark-rate is *tunnel excitation*. Tunnel excitation is due to a quantum mechanical phenomena that allows particles to *tunnel* through a potential barrier with a certain probability. Figure 4.13 shows the energy bands as a

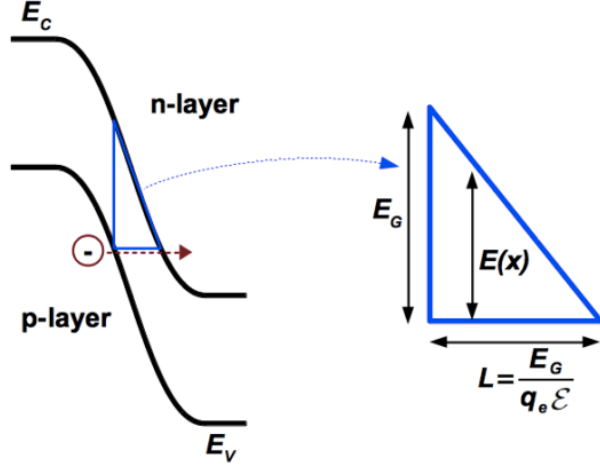


Figure 4.13: Schematic view of tunnel excitation. Left: Energy bands in the presence of an electric field. An electron can tunnel through the forbidden band from the p-layer to the n-layer resulting in a free electron-hole pair. Right: The potential barrier between the valence band of the p-layer and the conduction band of the n-layer can be approximated by a triangular shape.

function of position in the presence of an electric field. The potential barrier between the two energy bands is approximately triangular in shape. The height of the barrier is equivalent to the band gap energy (E_G) and the width is given by: $L = E_G / q_e \mathcal{E}$, where q_e is the charge of an electron and \mathcal{E} is the electric field. Electrons can then tunnel through the band gap to a state with the same energy. The number of carriers (N_{field}) generated from field-assisted tunnelling can be approximated as [91]:

$$N_{field} = \exp\left(\frac{-4\sqrt{2m}E_G^{-3/2}}{3q_e\hbar\epsilon}\right), \quad (4.4.5)$$

The tunnelling probability increases with the electrical field since the width of the potential barrier decreases. For this reason, tunnelling processes play an important role for the dark-rate due to the high electric field in the multiplication region of the SiPM. Unlike thermal pulses, this effect cannot be reduced by cooling of the device [90].

After-pulsing

An avalanche generated in a pixel can trigger further avalanches in either neighbouring pixels (described in the section on optical cross talk section which follows) or in the same pixel at a later time. The latter, referring to secondary avalanches generated in the same pixel, is called *after-pulsing*. After-pulses are believed to be caused by the release of a charge carrier that was produced in a earlier avalanche and trapped by an impurity in the

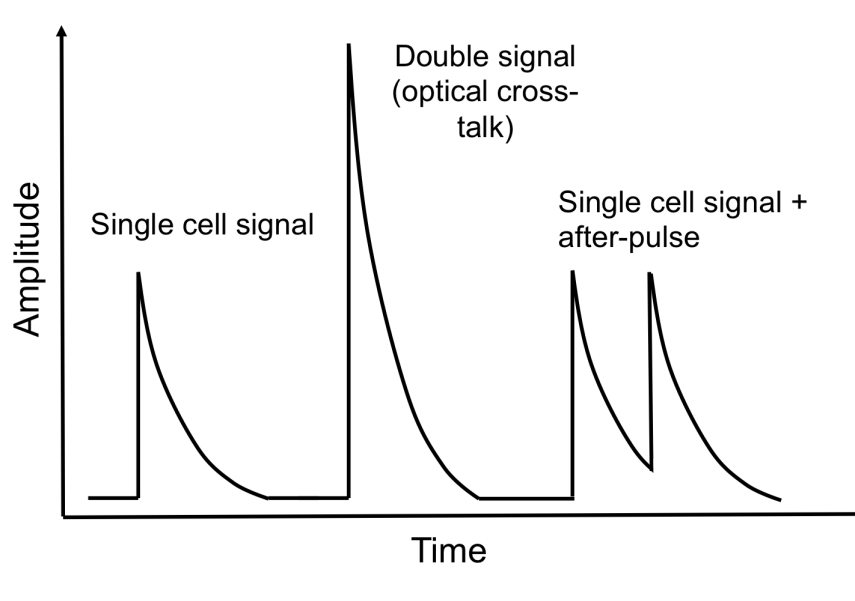


Figure 4.14: An illustration showing some possible signals due to a single photon activation in the SiPM. The second pulse is double the amplitude of a single cell activation and is a result of optical cross-talk. An after pulse is shown on the falling edge of the third pulse which shows a reduced gain due to recharging effects.

silicon [92]. As previously discussed, the probability of a carrier triggering an avalanche is dependent on the field strength in the active area. Therefore the carriers released from traps with lifetimes less than a few ns, when the cell is still recharging from a previous event, have a reduced probability of generating an avalanche. The probability of a trapped carrier generating an after pulse P_{ap} is given by [69]:

$$P_{ap}(t) = N_c P_t \frac{e^{-t/\tau}}{\tau} P_{trigger}, \quad (4.4.6)$$

where N_c is the number of carriers generated in an avalanche, τ is the average lifetime of a trap, P_t is the capture probability and $P_{trigger}$ is the triggering probability. If an after-pulse avalanche is triggered before the cell is fully recharged, the resulting gain will be less than a typical response due to the reduced voltage across the cell, as shown in Figure 4.14.

In principle there can be several types of trapping centres with different characteristics, results from [93] indicate the existence of two types, one with a slow ($\tau_{slow} \approx 50-100$ ns) and one with a fast time constant ($\tau_{fast} \approx 10-20$ ns).

Optical cross talk

As a result of an avalanche breakdown, an average of three photons per 10^5 carriers [94] are emitted with energies greater than the bandgap of silicon (~ 1.1 eV [9]). There is then a finite probability that these photons will go on to initiate an avalanche in a neighbouring pixel. The number of pixels firing from a single charge carrier production is not a constant but follows a Poisson distribution. This is an important limitation of the photon counting capabilities of SiPMs. The optical crosstalk of a device can be reduced by reducing the overall gain of the devices but many manufactures add additional *decoupling trenches* between pixels to minimise the effects without compromising on gain. An example of a cross-talk event is given in Figure 4.14. As a result of two avalanches being formed simultaneously, the resulting signal is twice the amplitude of a single cell activation.

Excess noise factor

The excess noise factor is represented by the multiplication noise due to after-pulses and optical cross-talk for each pixel. The excess noise of a SiPM can be measured from the width of single electron spectra and calculated as [94]:

$$F = 1 + \frac{\sigma^2}{M^2}, \quad (4.4.7)$$

where M is the gain from each GM-APD and σ^2 is the variance on the single photon response spectrum deriving from both optical cross talk and after pulsing. Excess noise factors of between 1.05 and 1.30 were measured for Photonique and Hamamatsu devices by [81].

4.4.4 Dynamic range and linearity

As described above, when an avalanche has been triggered within a GM-APD, the sensitivity of the diode to a further activating event is drastically reduced while the cell is re-charging. This means that the output signal for any pixel will be identical regardless of how many photons are incident upon it during a time interval τ_C . As the detector has a finite number of pixels, the dynamic range (i.e. the maximum number of photons that can be simultaneously detected) is limited. Assuming a uniform photon distribution at the active area and a temporal distribution of less than the effective deadtime of an APD cell,

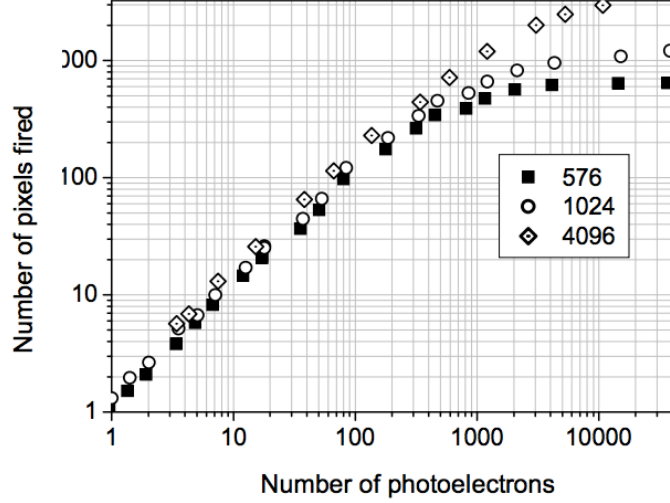


Figure 4.15: Non-linear response to a 40 ps laser light signal for SiPMs with different numbers of GM-APD cells [96].

the saturation of the signal with increasing light intensity can be calculated as [95]:

$$N_{fired} = N_{total} \left[1 - \exp \left(- \epsilon \frac{N_{photon}}{N_{total}} \right) \right], \quad (4.4.8)$$

where N_{fired} is the number of pixels that give an output signal, N_{total} is the total number of pixels across the SiPM, N_{photon} is the number of incident photons and ϵ is the PDE of each GM-APD pixel. When the number of impinging photons times the PDE exceeds 50% of the available cells, the deviation from linearity is more than 20% [96]. This effect for SiPMs with varying numbers of cells is given in Figure 9.11b.

4.4.5 Timing resolution

The GM-APD timing resolution is defined as the time jitter between the creation of an e-h pair and the instant when the output current pulse is recorded. The distribution of counts versus time for a GM-APD has a particular shape, consisting of a narrow peak and a slow tail, as shown in Figure 4.16a. The peak, which contains a significant majority of events, is due to e-h pairs created in the avalanche or drift regions where charge carriers are swiftly generated and then collected. This collection time depends on the drift velocity of the two carriers that in the high field region can be supposed to be equal for both of them and of the order of 10^7 cm/s.

The active layer of silicon in a GM-APD is very thin (2 to 4 μm) and the process of the

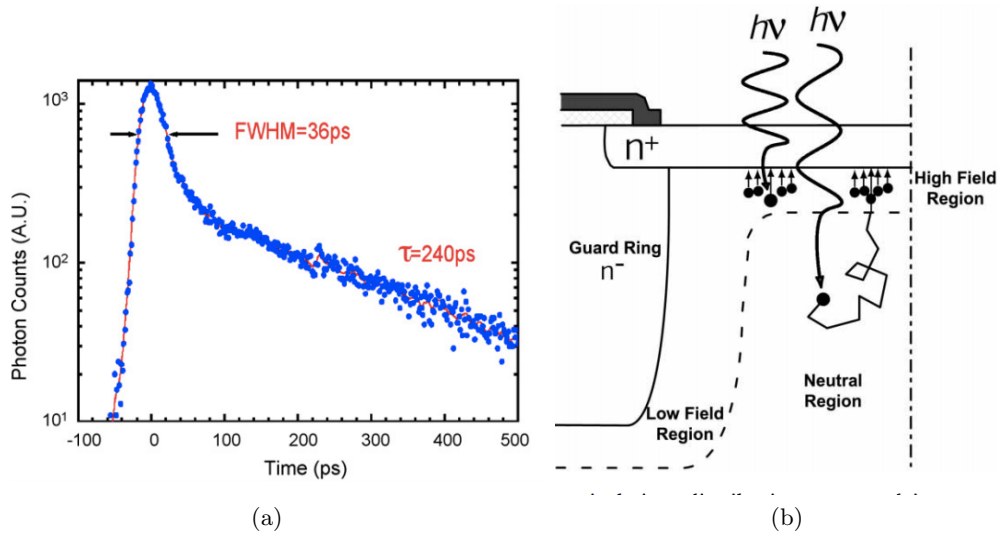


Figure 4.16: (a) Photon arrival time of a 830 nm photon emitted from a 20 ps pulse width as measured by a GM-APD [97]. (b) Sketch of the avalanche generation by a photon absorbed in the depletion layer and by a photon absorbed in a neutral region nearby [98].

breakdown development is fast. In addition, the signal amplitude is big because of the high cell capacitance. Therefore, very good timing properties even for single photons can be expected. In reality the time spread on single photon emission is a high peak followed by a long tail, shown by the logarithmic plot in Figure 4.16a.

The slow tail of the distribution derives from carriers generated in neutral regions where no electric field is present. These carriers must diffuse through the device until they reach a high field region, where they are accelerated and can trigger an avalanche. This process is illustrated in Figure 4.16b. The randomness in the diffusion path then contributes to the shape of the diffusion tail.

4.4.6 Temperature effects

The largest effects of temperature on SiPMs in a laboratory operating range of approximately 273-323 K are on the DCR and gain. As shown in equation 4.4.4, the number of thermal carriers exponentially increases as a function of temperature T . For applications where either low light levels are expected or in timing applications where triggers are often set at the one-photoelectron level, a high DCR can cause significant systematic uncertainties.

As the temperature rises, the lattice vibrations in the crystal become stronger. This increases the probability that carriers may strike the crystal before the accelerated carrier

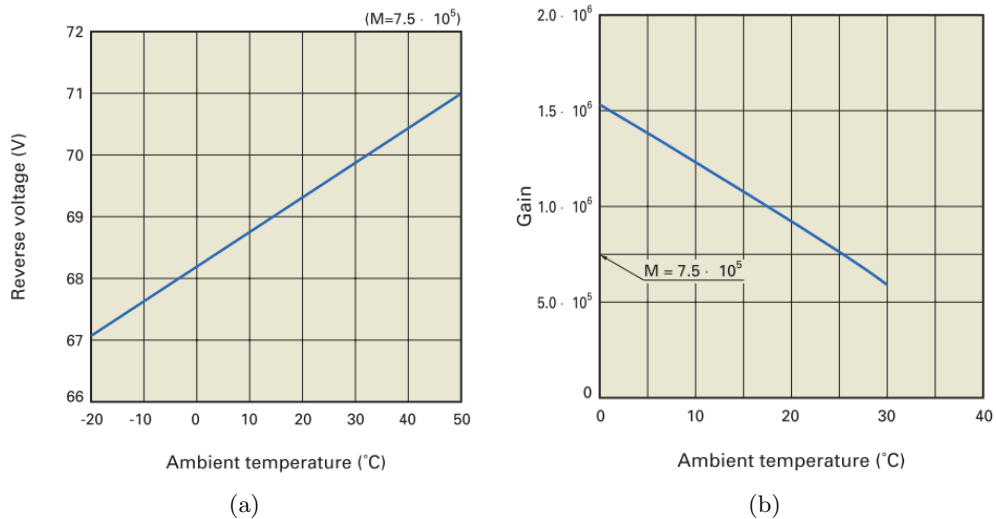


Figure 4.17: (a) Reverse bias as a function of device temperature for a constant gain for Hamamatsu S10362-11-050C (b) Gain as a function of device temperature for a constant reverse bias for Hamamatsu S10362-11-050C [78].

energy has become large enough, and reduces the ionization probability of either carriers. This has the effect of increasing the breakdown voltage of the system. Moreover, as the temperature rises, the gain at a fixed reverse voltage drops. Both of these effects are shown in Figure 4.17. As a result, much like APDs described earlier, SiPMs require a stable bias supply which must be either temperature controlled, or be instrumented with temperature compensating feed-back electronics.

4.5 Signal processing

In this work the response of SiPM devices is characterised through the use of digital techniques. In fact, all measurements made on either experimental or simulated response pulses were performed by digitizing the waveforms, applying digital filters and running analysis algorithms. In this section the digital signal processing techniques applied throughout this work are presented and described.

4.5.1 Discrete-time signals

In signal processing two basic signal types can be defined: *Continuous* and *discrete-time*. A continuous signal is a function (commonly of time) which changes continuously, for example an audio waveform. Alternatively, if a signal only changes in specific instants of time, like a pulsed laser where the signal is either on or off, it can be represented by a

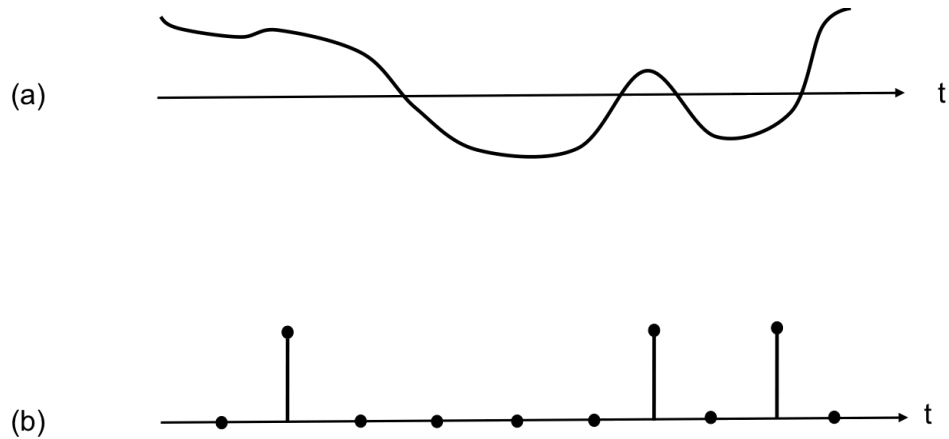


Figure 4.18: Signal types: (a) continuous (b) discrete-time signals.

discrete sequence of numbers, and is called a discrete-time signal. An illustration of these two signals types is given in Figure 4.18.

Analogue-to-digital Conversion

In order to digitally process the analogue response of an electronic system, signals can be converted from continuous to discrete-time by sampling at a given frequency. Changing a continuous-time to a discrete-time signal is commonly referred to as *analogue-to-digital conversion*. In order for the sampled series to be an accurate representation of the underlying continuous distribution, the time interval between samples must be chosen carefully. It is possible to generalise the minimum sampling frequency needed to fully recreate a sampled distribution as:

$$T = \frac{1}{2f_c}, \quad (4.5.1)$$

where T is the sampling interval and f_c is the highest frequency content of the continuous signal. That is, if the sampling interval is chosen to be smaller than the reciprocal of twice the highest frequency ($2f_c$ - known as the Nyquist frequency), no information will be lost through sampling. If, however, a continuous distribution is sampled below the Nyquist rate, *frequency aliasing* can occur, where different frequencies can appear as indistinguishable. An example of frequency aliasing is given in see Figure 4.19.

In an experimental environment there is often a trade off to be made between the minimal sampling rate needed to capture all the information in a given waveform and the technical limitations of the data acquisition (DAQ) system. The limitation will often derive from

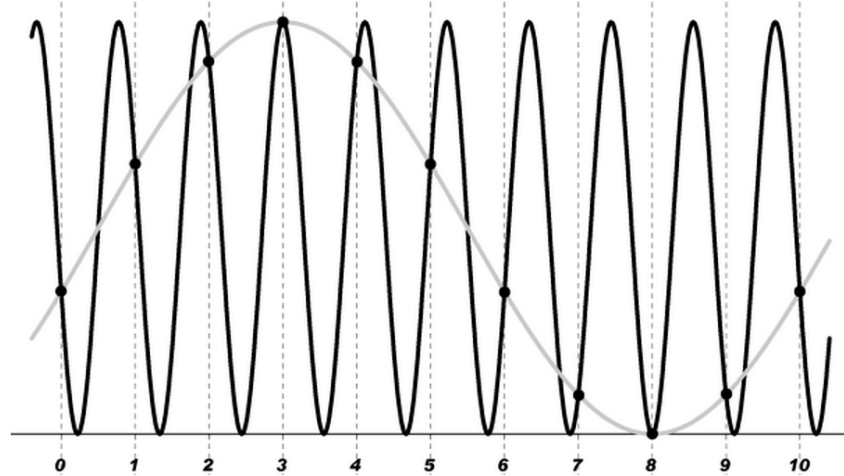


Figure 4.19: An example of frequency aliasing. The continuous signal being sampled is shown in black, an alias deriving from the under-sampling of the original signal is given in grey.

the maximum sample rate of the analogue-to-digital converter (ADC) being used, but memory and storage considerations can also be a problem. The latter can be of particular significance if the distribution being sampled is many orders of magnitude longer than the sample interval T , or if analysis requires storage of a large number of samples.

Another important parameter to consider when digitizing a signal is the ADC resolution. The resolution of an ADC defines the number of quantized levels available to represent the amplitude range of a continuous signal and is quoted in terms of bits (n), where the total number of energy levels is 2^n . A 3-bit ADC will therefore have $2^3 = 8$ amplitude levels available to represent a signal. A comparison of a continuous signal measured with both a 3-bit and a 16-bit ADC is given in Figure 4.20. In the case of a 3 bit system, the poor amplitude resolution will mean increasing the sample rate will have a minimal influence on the reconstruction of the sampled distribution. As such, the resolution of a digitiser is, in general, of fundamental importance for an accurate representation of the underlying continuous signal. In this work signal digitization has been performed both a LeCroy Wavepro and a Tektronix TDS 7254B oscilloscopes, both of which operate 8 bit ADCs resulting in a full scale quantization of $2^8 = 256$ levels. Sampling rates for individual experiments are discussed in Chapters 5 and 6.

4.5.2 Digital filters

A filtering system is a system which can be applied to remove unwanted or redundant information from a data set. In signal processing, the main goal of a filtering system, be

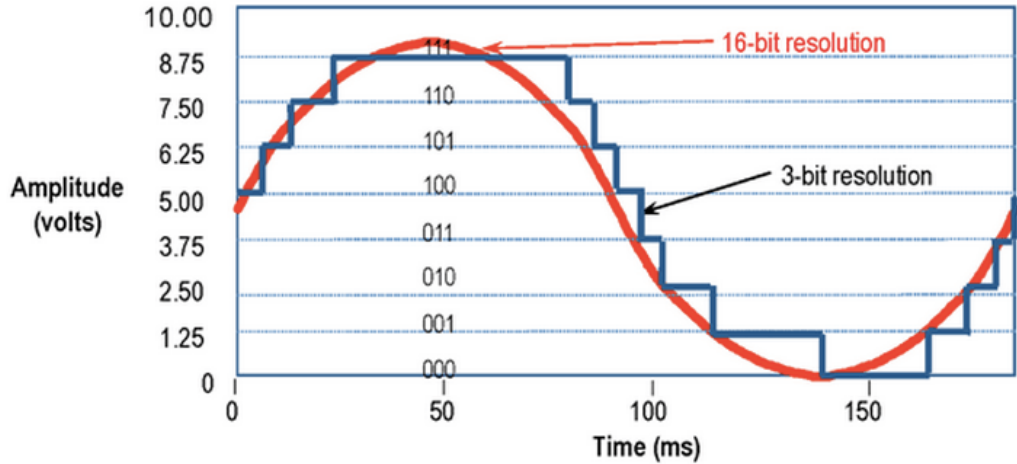


Figure 4.20: Comparison between a 3 bit and 16 bit ADC resolution [99].

it analogue or digital, is to reduce the noise rate of a signal with the aim to improve the quality of the time or frequency component of interest. This is often referred to as improving the signal-to-noise ratio (SNR) of the signal. There are a number of advantages to using digital filters over analogue implementations. Perhaps the most significant is that analogue filters are built of physical components, the characteristics of which have finite tolerances due to the quality of the build materials and the manufacturing techniques used to produce them. Digital filters are not affected by manufacturing tolerances and therefore yield a more predictable response. In this work analogue response signals from SiPMs are digitized without filtering. Stored signals are then digitally filtered during analysis, allowing comparison of processed and un-processed results.

There are two main parameters which define a filter: how it differentiates frequencies and how it scales these frequencies. Frequency selectivity is the most common mode of classification, where often quoted categories of frequency selective filters are: *lowpass*, *highpass*, *bandpass* and *bandstop*. In this work only lowpass filters have been applied. The scaling of frequency components within the original signal is called the *gain*. A filter's gain is simply the ratio of the output signal level to the input signal level. If the filter's gain is greater than 1, then the output signal is larger than the input signal, while if the gain is less than 1, the output is smaller than the input. In most filter applications, the gain response of the suppressed region, known as the *stopband*, is very small and as such gain is often quoted in dB:

$$(gain)_{dB} = 20 \cdot \log(gain), \quad (4.5.2)$$

where gain is the linear gain as described above.

The typical frequency response of a lowpass filter can be seen in Figure 4.21. This plot illustrates a number of characteristic parameters of this filter type, including: passband, stopband, 3 dB attenuation (also known as the *cut-off frequency*), transition band (also known as the *roll-off*) and the stopband attenuation.

The passband defines the frequency range which is unaffected by the filter's gain characteristics. For an ideal filter the linear gain of the passband is one, however in reality there are often small attenuation effects in this region known as *passband ripple*. The stopband is the range of frequencies which are attenuated by the action of the filter. For an ideal filter the value of gain in the stop-band would be zero. In the ideal case the stopband attenuation would be one and the filter response a step function. In reality filters are also characterised by a transition band, which is a region between the passband and stopband where the gain has a continuous value between 0 and 1, where the gain 'rolls-off'. With the introduction of roll-off, a cut-off frequency (f_c) is defined as the point of a -3 dB attenuation. Similarly to the passband ripple, non-uniform gains are often seen in the stopband attenuation. A final parameter, which is not represented in Figure 4.21, is the order N of the filter. In an analogue system the order refers to the number of passive components used in the circuit implementation. The higher the value of N , the steeper the roll-off in the transition band will be and therefore the closer the response is to an ideal filter. In a digital system, the order is the number of coefficients considered in the mathematical representation of the filter [100].

As described above, filter design is based in the frequency domain. However, typically the signals which they act upon are based in the time domain. The response characteristics must therefore be converted from one to the other. In the case of analogue filters continuous-time electronic signals are acted on using resistor and capacitor circuits with resistance R and capacitance C . In this case a *time constant* is defined by the multiplication of the two, $\tau = RC$, which relates to the cut-off frequency, and therefore the frequency domain response, $f_c = 1/2\pi\tau$. Conversely, digital filter design in the frequency domain is given by the *transfer function* where mathematical analysis of the transfer function can describe how it will respond to any input. In order to characterise a filter's response in the time domain the transfer function is converted to a set of coefficients to be applied to the discrete time signal is called the *Linear constant-coefficient difference equation*:

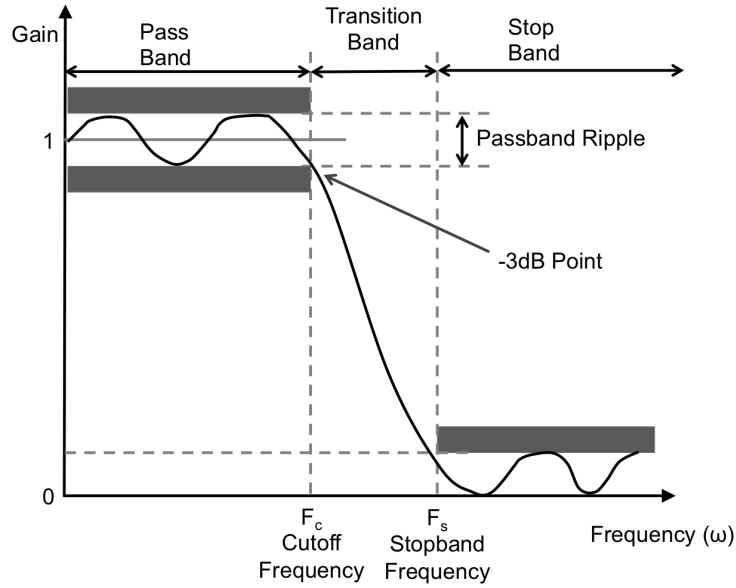


Figure 4.21: Diagram detailing the gain and frequency response of a typical lowpass filter.

$$y(n) = \sum_{i=0}^N a_i x(n-i) - \sum_{i=0}^N b_i y(n-i). \quad (4.5.3)$$

Here n describes an element in the signal passed to the filter to processing, $y(n)$ is the current filter output while $y(n-i)$ and $x(n-i)$ are the previous filter outputs and current or previous inputs respectively. These values are scaled by a_i and b_i which are the filter's *feed-forward* and *feed-backward* coefficients respectively. N defines the number of coefficients considered within the filter's response and, as described above, defines the filter's order. Considering this equation, digital filters can be broken down into two categories: *finite impulse response* (FIR) filters, where only feed-forward coefficients are considered (all values of b_i are set to zero), and *infinite impulse response* (IIR) filters, where one or more feed backwards coefficients are considered. By applying feed-backwards components the filter response, once excited by an impulse, will never completely reach zero, hence infinite response.

In this thesis two specific filter designs were used, both of which were designed and implemented in Matlab with the signal processing toolbox:

- a 5th order Hamming windowed filter of finite impulse response (FIR) with cut-off frequency $f_c=500$ MHz;
- a 2nd order Butterworth filter of infinite impulse response (IIR) with a cut-off fre-

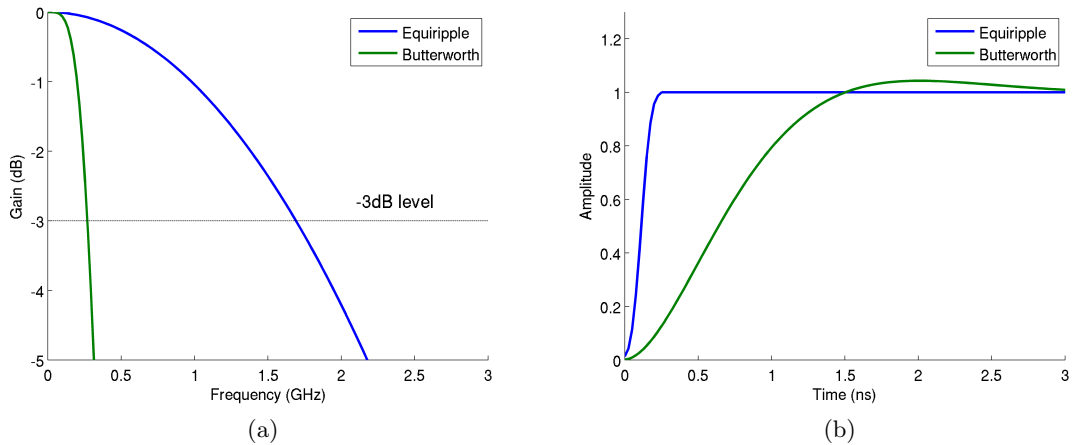


Figure 4.22: Filter characteristics of digital filter designs used in Chapters 5 and 6. (a) Frequency specifications (b) Filter response to step change.

quency $f_c=350$ MHz.

A windowed filter provides extra control of the roll-off and stop band characteristic of a FIR filter design. The Hamming window [101] is the default MATLAB FIR filter implementation and so has been applied here. The response coefficients of the filter are then generated by the Matlab filter design function using *equiripple minimisation* [102]. This filter is henceforth referred to as the *equiripple filter*. A *Butterworth filter* is a standard IIR implementation which does not require any additional coefficient weighting. The specific coefficients of this design were again calculated by the Matlab toolbox.

In this work the equiripple design has been applied to SiPM response signals initiated by a fast-pulsed LED. These measurements, described in Chapter 5, have been used to determine characteristic parameters of a range of SiPM devices. This filter was chosen for its characteristic slow roll-off, as shown in Figure 4.22a, as it is applied to a number of devices with varying response. The Butterworth design is applied to signals recorded with the SiPM coupled directly to a LYSO scintillating crystal. Due to the increased temporal spread of the photon flux, the SiPM response shows a reduced rise time and it is possible to apply a reduced f_c , further constraining the electronic noise. A direct comparison of these signal, filtered with both designs, is given in Chapter 6.

For completeness, in addition to the frequency response shown in Figure 4.22a, the step response plot of these two filters is given in Figure 4.22b. This shows the response of each filter in the time domain. The Butterworth filter shows a much sharper roll-off, restricting the rise time in the step response and creating an overshoot where the frequencies required to model the sharp corner are discriminated. The windowed filter is characterised by a

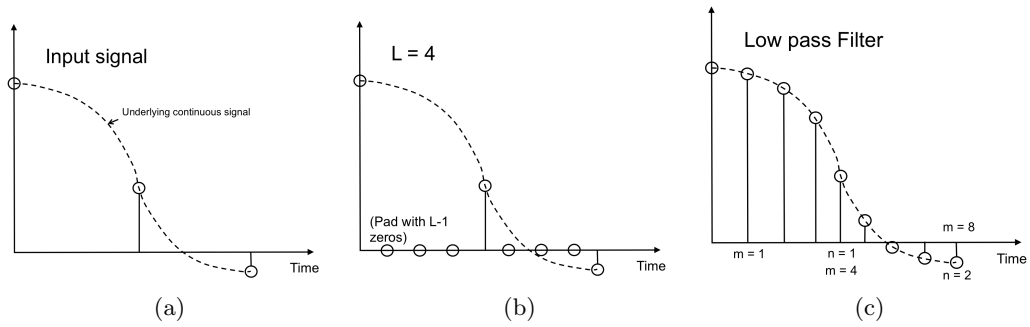


Figure 4.23: Schematic representation of the upsampling process. (a) The initial discrete time signal to be acted on. (b) The original signal is padded with $L-1$ sample points. (c) The padded signal is filtered with a low pass filter to give an estimate of the underlying continuous signal.

gentler roll off, resulting in higher frequencies passing the cut and allowing a faster rise in the step response and better reconstruction of corner effects. The specific of application of each filter are discussed in the results and analysis chapters to follow.

4.5.3 Up-sampling

Another discrete-time signal processing technique used in this work is *up-sampling*. Up-sampling is an interpolation technique often applied in the context of digital signal processing which produces an approximation of the sequence that would have been obtained by sampling the under-lying continuous signal at a higher rate. Specifically, the process increases the sample frequency of a discrete time signal, with sample period T , by an integer factor L .

The first step in the up-sampling procedure is to pad $L-1$ zeros between each sample point in the original signal, increasing the sample rate by L . This creates a new signal with a sampling period $T'=T/L$, an illustration of which is given in Figure 4.23b. The newly generated, up-sampled, array must then be acted on to be made representative of the underlying continuous distribution. To this end a low pass filter is applied to the new array with f_c equivalent to the highest frequency in the original signal. The result is an accurate estimation of the underlying continuous signal, which, if the original sample was recorded at the Nyquist rate, can be an almost perfect approximation [102]. A diagram detailing each of the key steps in this process is given in Figure 4.23.

For the work presented in this thesis up-sampling was performed using the `resample` function of Matlab. This function calculates f_c of the original array which is passed and applies

a 10th order Hanning windowed FIR filter to produce the response [103].

Chapter 5

Selection of a candidate SiPM device for TOF-PET

This chapter describes measurements taken as a contribution to work carried out within the ENVISION (European NoVel Imaging Systems for ION therapy) collaboration [104]. The results of these measurements were presented to the ENVISION collaboration in February 2012 as a recommendation of which SiPM device to use by the collaboration in fast timing measurements applying scintillator detectors. As a result of studies presented here, the selected device has been chosen for use also in a prototype TOF-PET detector system now under construction at the Rutherford Appleton Laboratory (RAL), UK. The characteristic measurements of the selected device have also been used as input parameters for a purpose-built simulation framework which has been developed entirely as a standalone package to predict the performance of systems using coupled SiPM and scintillator detectors. The simulation framework and results simulated with it are described in Chapters 7 and 8 of this thesis.

This chapter is broken into three main parts. The first section describes the experimental arrangement and procedures used to characterise the response of a range of SiPM devices to LED light. Details of the hardware, analysis techniques and related software are given. The second part presents and discusses the results of characteristic parameters measured for each device, including: signal-to-noise ratio (SNR), signal rise and fall times and intrinsic timing jitter. A final part presents an overview of the results, discusses their significance with respect to application in a prototype TOF-PET detector system and identifies a candidate device for further use.

5.1 The ENVISION project

The ENVISION collaboration [104], launched in 2010 and coordinated by CERN, is a four-year project set up by 17 leading European research organisations, including two leading European industrial partners (Siemens and IBA). The goal of the project is to drive research efforts of novel imaging modalities which can be applied for on-line dose monitoring relating to ion therapies. It concentrates on the detection of nuclear reaction products from the interaction of an ion beam with atomic nuclei in a patient’s tissue.

One method of monitoring these products is by applying PET detector systems, operating in a modality known as in-beam PET [105]. Here β^+ emissions occur as a product of the ion beams’ interaction with the patient’s tissue, but are present in much reduced concentrations relative to the activity applied for standard PET techniques. The project is therefore interested in detector systems with superior timing resolution for the development of TOF systems, to be applied for optimal image quality of the low statistics signal generated from these ion interactions. The University of Oxford, in conjunction with RAL, are party to the ENVISION project and are involved in developing a prototype TOF-PET detector system which applies SiPM detector technology. Both of these institutes provided access to the experimental equipment and expertise to aid in the measurements described here.

5.2 Experimental setup

A range of SiPM devices were identified by the ENVISION collaborators at RAL for characterisation. These devices were from three of the leading manufacturers at time of the projects inception: Hamamatsu, SensL and Photonique. Specific models were identified from each manufacturer to provide a sample including a range of active areas and pixel sizes with a finite sensitivity to ~ 420 nm light. The 420 nm wavelength is equivalent to the peak spectral emission of LYSO, which was selected by the RAL group for application in the prototype detector system. A list of the SiPM devices identified for testing from each of the three manufacturers is given in Table 5.1, values of some characteristic parameters are also included. Here *active area* refers to the total area of the device surface covered by the GM-APD pixel matrix, *pixel size* defines the area of an individual pixel and *fill factor* the percentage of the active area sensitive to incident photons. Devices with a range of characteristics were selected in order to study the systematic effects of these parameters

on the device response.

Table 5.1: List of SiPM models used in LED measurements

Manufacturer	Model	Active area [mm ²]	Pixel area [μm ²]	N_{pixels}	Fill factor [%]	PDE at 420 nm [%]
Hamamatsu	S10362-11-25C	1	25 × 25	1600	30.8	24
	S10362-11-50C	1	50 × 50	400	61.5	48
	S10362-11-100C	1	100 × 100	100	78.5	67
	S10362-33-25C	9	25 × 25	14400	30.8	24
	S10362-33-50C	9	50 × 50	3600	61.5	48
	S10362-33-100C	9	100 × 100	900	78.5	65
Photonique	0611B1MM-PCB	1	~44 × 44	~500	>70	22
	0611B4MM-PCB	4.4	~50 × 50	~1700	>70	25
	0710G9MM-PCB	9	~70 × 70	~8100	>60	18
SensL*	MicroSL-10035-X13	1	35 × 35	576	64	10
	MicroSL-30035-X13	9	35 × 35	4774	64	10

*These devices were mounted on Photonique AMP_0611 pre-amplifier boards [106].

All results presented in this chapter were acquired through analysis of the response of each SiPM device to fast pulsed LED light in a temperature controlled lab with a nominal temperature of $20 \pm 2^\circ$. For this purpose a PicoQuant PLS-420 LED was used, defined by a 420 nm peak emission. The LED was driven by a Sepia 808 picosecond pulsed diode laser driver as recommended by the manufacturer. This combination of LED and driver system gives a fast optical pulse with a width of 800 ps [107]. When characterising the electrical response of a system in the time domain, the temporal response of the source should be negligible compared to the induced signal to avoid significant convolution effects of the two. It has been shown in literature that, for a number of pre-amplifiers with bandwidths in the range 0.1-2 GHz, the optimum response of a Hamamatsu SiPM to a picosecond laser pulse is 1.71 ns [75]. For device rise times of this order, a source signal with 800 ps pulse width is negligible to good approximation.

A mechanical arrangement was designed to ensure reproducibility of the LED signal measurement of each device based on standard 1-inch diameter ‘SM1’ threaded optical lens

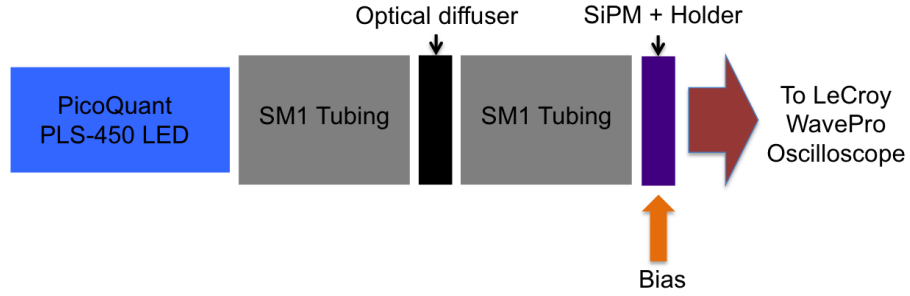


Figure 5.1: Mechanical arrangement used for characteristic measurements with fast LED signal, not to scale.

tubes. A diagram of this arrangement is given in Figure 5.1. The PLS-420 LED was coupled directly into a SM1 tube and a Thorlabs DG10-220-P01 optical diffuser attached to the opposing end. The diffuser is a ground glass surface which randomises the direction of traversing optical photons, producing an approximately uniform intensity distribution of light. The addition of a diffuser was to optimise the uniformity of the photon distribution reaching the SiPM surface. Due to the pixel nature of SiPMs, a non-uniform photon distribution impinging on the active area could lead to saturation effects, which may in turn be difficult to quantify for devices with different pixel sizes and active areas. To enhance this effect a long (~ 15 cm) SM1 tube was used between the diffuser and the SiPM, the tube had been annealed to give a matt black finish to reduce surface reflections. The SiPM under investigation was coupled into the system via a custom-designed mechanical holder, threading directly into a second optical lens tube.

SiPM devices from both Hamamatsu and Photonique were mounted on biasing electronics described by the schematic shown in Figure 5.2. This was designed for purpose by ENVISION collaborators at the University of Oxford [108]. The design applies two simple RC low pass filters on the incoming bias voltage, represented by R_1 , C_1 and R_2 , C_2 in Figure 5.2. The biasing voltage was supplied to the board by pin connectors to a Keithley 2612 dual-channel precision power supply. The SiPM device, represented in Figure 5.2 as a diode, was reproducibly placed into the circuit via a pin socket for the device leg pins. A permanent load (R_3) of 51Ω was used on the output. This, in parallel with the 50Ω termination resistance of the oscilloscope (R_s), yields a system load of 25.2Ω . Although no additional pre-amplifiers were used in this work, a 51Ω load was chosen to match the input impedance of a large range of commercially available pre-amplifiers to be used in series with the bias circuit if desired. The output signal was then AC coupled via a capacitor (C_3) in series with the output connector. Finally, there are protecting diodes

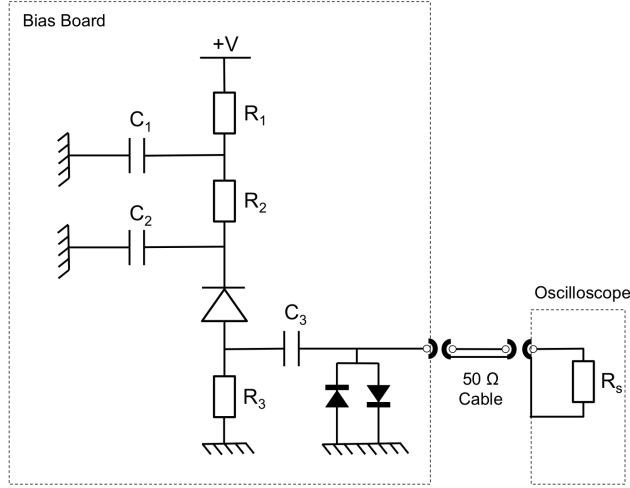


Figure 5.2: Schematics of the bias circuit for fast timing. The values of the components are $R_1 = 3.3 \text{ k}\Omega$, $R_2 = 10 \text{ k}\Omega$, $R_3 = 51 \text{ }\Omega$, $R_s = 50 \text{ }\Omega$, $C_1 = 100 \text{ nF}$, $C_2 = 470 \text{ nF}$, $C_3 = 100 \text{ nF}$ [108].

positioned before the output connector that were introduced to avoid overload and consequent damage of the oscilloscope input when the circuit is used without a pre-amplifier in series. All passive components were surface mounted to minimise stray inductance and capacitance.

It is shown in Table 5.1 that the devices from SensL are less sensitive to 420 nm photons than the other candidates, with a PDE of only 10%. The response signal of these devices, when mounted in the biasing circuit described above, was very close to the noise floor of the oscilloscope and presented a challenge applying the measurement techniques described later in this chapter. The SensL devices were therefore mounted on Photonique AMP_0611 pre-amplifier boards. The schematic for these boards can be seen in Figure 5.3. Similarly to the bias circuit shown in Figure 5.2, a low pass RC filter is applied to the biasing voltage to be held across the SiPM. The drop in voltage caused by an activating event at the SiPM is AC coupled to the input of an operational amplifier. The amplifier was independently biased at +5 V by an ISO-Tech IPS-2303D dual channel power supply to provide approximately a $\times 10$ signal amplification [106].

The analogue signals resulting from activating SiPMs with the fast pulse LED system were transmitted from the bias boards to a 4 GHz WaveMaster Zi-8 oscilloscope via a 50 Ω coaxial cable, terminated with 50 Ω at the oscilloscope input. Signals were digitised at 40 GS/s by the oscilloscope’s internal ADCs. For each device, a data set of 5000 nominally identical response pulses were saved to file for analysis.

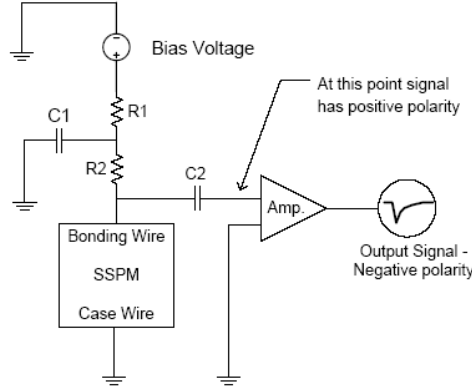


Figure 5.3: Schematics Photonique AMP_0611 amplifier. The values of the components are $R_1 = 1 \text{ k}\Omega$, $R_2 = 1 \text{ k}\Omega$, $C_1 = 10 \text{ nF}$, $C_2 = 10 \text{ nF}$ [106].

5.3 Measurement techniques

For all measurements described in this chapter the recorded pulses were digitally filtered for electronic noise with a finite impulse response (FIR) filter (see Chapter 4). The filter was designed using a function available in MATLAB which creates designs based on a windowed, linear phase FIR implementation characterised by two inputs: the filter order (N) and the cut-off frequency (f_c) to be applied. In our case the default Hanning window [101] was applied with $N = 5$ and $f_c = 500 \text{ MHz}$. Using higher order filters increases the number of weighted values used to calculate a point on the resulting filtered signal and yields a sharper roll off. In the application here, where the response of devices may vary, the ideal cut-off frequency may change for each device. A 5th order design was chosen to apply a shallow roll-off to account for this effect. A 500 MHz cut-off frequency was chosen to artificially reduce the bandwidth of the system, in turn reducing the electronic noise, without affecting the analogue rise time of system (t_r), previously assumed to be 1.71 ns [75]. The constraint put on the rise time due to a 500 MHz bandwidth can be estimated as: $t_r \cong \frac{0.34}{BW} = \frac{0.34}{500 \text{ MHz}} \approx 700 \text{ ps}$, well below the 1.71 ns limit. Comparisons of a typical response pulse from a Hamamatsu S10362-33-050C device both before and after filtering are given in Figure 5.4. The signal shown is the device response to a fast LED optical pulse from the previously described LED system.

For all measurements, a histogram was produced of the parameter values measured as described below from each of the 5000 recorded pulses. With the exception of the timing jitter, which is described separately in section 5.3.4, the result quoted in section 5.4 are the mean value extracted from a Gaussian fit to these histograms. The uncertainties quoted are the standard deviations extracted from the same histogram fits.

5.3.1 Signal-to-noise

The signal-to-noise ratio of a device response voltage can be defined as:

$$V_{SNR} = \frac{V_{pulse}}{\sigma_{noise}^{rms}} \quad (5.3.1)$$

where V_{pulse} is the pulse height (i.e. the maximum voltage measured for each filtered pulse) and σ_{noise}^{rms} is the rms of the noise floor of each pulse, prior to filtering. These parameters are illustrated graphically on example pulses in Figure 5.4.

In order to avoid operating the devices in saturation mode, the LED brightness was calibrated. With a uniform distribution of photons incident at the device active area, the device(s) with the lowest saturation threshold are those with the highest PDE and the largest pixel areas, leading to the smallest number of pixels per unit active area. With this in mind the Hamamatsu S10362-11-100C, which has the fewest pixels and the highest PDE (see Table 5.1), was used to calibrate the LED brightness to be used with all devices. The calibration was run by varying an arbitrary-unit potentiometer on the Sepia 808 driver which varies the maximum amplitude of the current pulse used to activate the LED. By varying this scale from the zero point upwards it was possible to observe a region where the SiPM response signal no longer increases linearly with the current pulse to the LED, a relative potentiometer setting of 10-7. By reducing the setting to 6-4, approximately 60% of the region where non-linear behaviour was first observed, a signal is seen well above the noise floor, below the saturation region. A potentiometer setting of 6-4 was used to measure the SNR of each device.

5.3.2 Rise time

The rise time of each device was measured by digitally up-sampling the recorded pulses to a rate of 50 GS/s using a windowed filter technique as discussed in Chapter 4. In essence the process works by inserting new values in-between the original sample points of the recorded pulse, all of which are set to zero. A digital filter is then applied to this newly formed array to remove any high frequency content resulting in an up-sampled array.

To measure the rise time, amplitude thresholds were individually set at 10 % and then 90 % of the pulse height. The first sample points to cross these thresholds were then identified and their time stamps stored. The 10-90 % rise time of each individual pulse

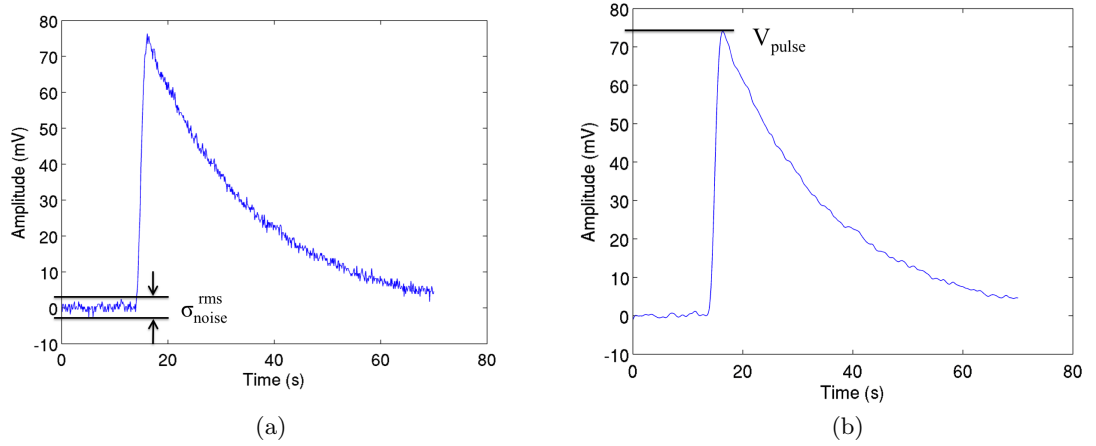


Figure 5.4: Response of Hamamatsu S10362-33-050C to fast LED signal (a) Unfiltered pulse used to calculate the σ_{noise}^{rms} . (b) Filtered pulses used to calculate pulse height, V_{pulse} .

was then recorded as the difference between the timestamps relating to the two threshold crossings.

5.3.3 Fall time

As discussed in Chapter 4, the falling edge of a SiPM devices response pulse is characterised by two decay constants, a fast constant τ_{fast} and a slow constant τ_{slow} . The slow component is attributed to the re-charging of the pixel capacitance after an activating event and the fast component to the current flowing in the external load.

For most of the devices tested the slow fall time dominates the shape of the falling edge with a negligible contribution from the fast response. Only in the case of the Photonique devices the fast time constant was prominent enough to fit. As a result both fast and slow constants were extracted from the response of Photonique devices via the linear sum of two exponential fits, while for all other devices only the slow component was measured by using a single exponential fit to the falling edge. Example fits to Photonique 0611B4MM-PCB and Hamamatsu S10362-11-050C response pulses are given in Figure 5.5. Five pulses are plotted for each device, labelled data 1-5, with the fit to the 5th pulse. The two component behaviour is shown to significantly contribute to the response of Photonique device presented in Figure 5.5a. A fast component is visible in Figure 5.5b however it provides only a minor contribution to the total response shape and so was not fitted explicitly. The τ extracted from the exponential fits were scaled to give the 10-90% fall time in the final results: $t_{fall} = \tau \cdot \ln(9)$.

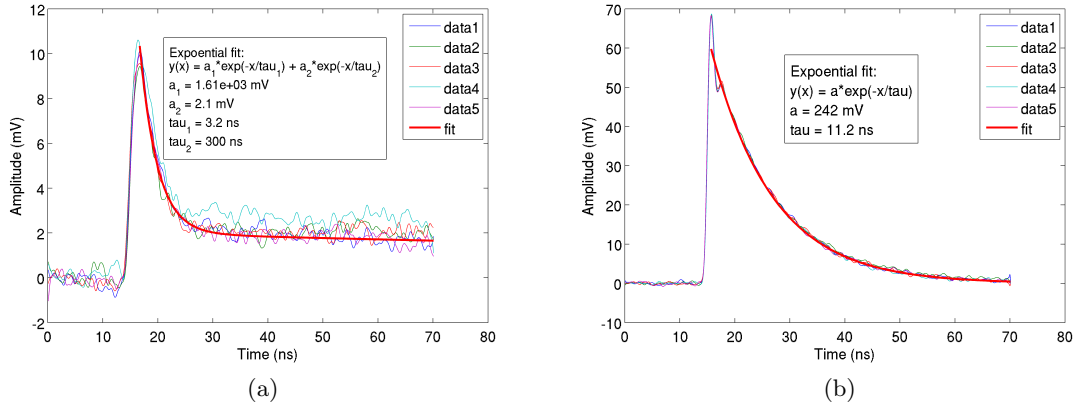


Figure 5.5: (a) Example filtered pulses measured with Photonique 0710G9MM-PCB device with a bi-exponential fit. (b) Example filtered pulses measured with Hamamatsu S10362-33-050C with a single-exponential fit.

5.3.4 Timing jitter

The timing jitter, or transit time spread of the response signal, was measured by calculating the time difference between the current pulse used to drive the LED signal and the SiPM device response. The triggering signal used to define the current pulse to the LED was connected directly to a second channel of the oscilloscope, terminated at 50Ω .

Timing measurements are often taken using simple leading edge discriminators where a time stamp is defined by the first sample point to cross a chosen amplitude threshold (V_T). This technique was used for the rise time measurements already discussed. However, timestamps acquired this way are affected by an additional uncertainty on the position of sample points introduced by the electronic noise of the system, the signal jitter (σ_{Signal}). This uncertainty can be defined as:

$$\sigma_{signal} = \frac{\sigma_{noise}^{rms}}{\frac{dV}{dt} |_{V_T}} \cong \frac{t_{rise}}{SNR}, \quad (5.3.2)$$

where $\frac{dV}{dt} |_{V_T}$ is the signal gradient at threshold and t_{rise} is the 10-90% signal rise time. In order to minimise the effects of this uncertainty recorded pulses were filtered to minimise the σ_{noise}^{rms} and a linear fit was applied to the 25-75% range of the leading edge of both the trigger and signal pulses. By using a fit which considers multiple points on the leading edge the effects of any residual electronic noise are averaged out. The 25-75% range was chosen to avoid non-linear affects at the extremes introduced by the system bandwidth. Timestamps were then defined as the baseline crossing, mathematically extrapolated from each

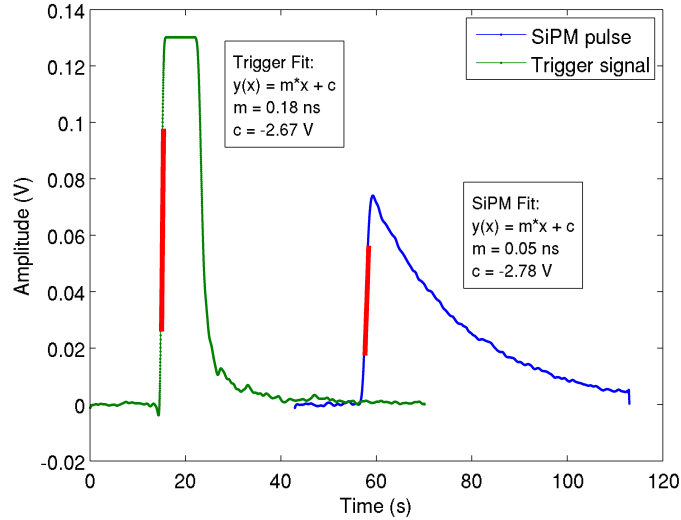


Figure 5.6: Example trigger and SiPM pulse pair used to calculate the intrinsic timing jitter. Linear fits to the leading edges are shown in red.

fit. Example fits to the trigger and SiPM response signals are shown in Figure 5.6.

The timing jitter was calculated by first creating a histogram of the recorded timestamps with a bin width of 25 ps (equivalent to the 40 GS/s sample rate of the recorded traces). A Gaussian fit was applied to the resulting distribution and the FWHM extracted from the fit parameters. The uncertainty on this measurement was then assumed to be the convolution of the statistical uncertainty associated with the data set and the contribution of non-Gaussian tails. Non-Gaussian tails were estimated by refitting the histogram for incremental fit ranges stepping between three to six σ in steps of $\sigma/2$. The range of FWHM values calculated over all fit limits was considered the uncertainty due to non-Gaussian tails.

5.4 Results

5.4.1 Signal-to-noise

As shown in Equation 5.3.1, the V_{SNR} of a detector system is defined as the ratio of the peak response voltage to the rms of the noise floor - the baseline detector signal when no activating event is present. It defines the quality of the system response relative to internal noise limitations. The highest possible SNR is desirable in any detection system.

The noise floor of the system can be considered as the sum of all the noise sources in the experimental apparatus, where noise is defined as any signal other than the one being

measured. In the case of electronic systems the main contributions of the baseline noise are from thermal (Johnson-Nyquist) noise, generated by the random thermal motion of charge carriers in the system, and shot noise which defines random statistical fluctuations in the motion of charge carriers. Both sources are approximately Gaussian about a baseline voltage and are hence proportional to the system bandwidth. Due to the avalanche mode operation of the SiPMs APD array, the gain variation between pixels is small [109]. As a result, the peak signal voltage of a SiPM device, in response to a fast light pulse where temporal effects are negligible, is linearly dependent on both the number of pixels fired in an activating event and the single pixel gain of the device.

Results from SNR measurements for each device are presented in Figure 5.7, where the quoted error bars represent the standard deviation of each measurement. Results are additionally listed explicitly in Table 5.2. The first feature to notice is that, for each device manufacturer, V_{SNR} is shown to degrade as a function of increased pixel dimension¹. Assuming an even photon distribution across the SiPM device surface, the probability of multiple, non-activating, photon hits at each pixel is proportional to the pixel dimension. Although larger pixel areas result in an increased capacitance, and therefore a higher gain (see equation 4.4.1), this trend indicates that the increased number of activated pixels is the dominant effect. Additionally, it should be noted that the devices from the same manufacturer with identical pixel size, but differing total active areas, behave comparably to within one error bar. This effect can be expected as increasing the active area correlates with a proportional increase in total number of pixels, and therefore an extended dynamic range. However, as the light source applied in these measurements was calibrated to be well below the saturation region of all devices tested, no change in response is observed.

The best performing manufacturer is shown to be Hamamatsu where devices with both the $25 \times 25 \mu\text{m}^2$ and $50 \times 50 \mu\text{m}^2$ pixel areas outperformed all other devices. This is attributed partly to the higher PDE of the Hamamatsu devices, shown in Table 5.1. For a pixel area of $50 \times 50 \mu\text{m}^2$ the Hamamatsu and Photonique devices are characterised by a PDE of 48% and 25% respectively. The approximate increase by a factor of nine seen in V_{SNR} is due to a convolution of the PDE reduction and the signal shape from the two devices. It is shown in Figure 5.5 and Table 5.2 that the slow fall time of the Photonique device is an order of magnitude longer than that measured with the Hamamatsu detectors. This is explored in detail in Section 5.4.3. As a result, the total charge generated by the

¹Pixels produced by all device manufacturers are square in shape and are most regularly identified in literature by the single edge dimension, this convention is used here referred to as ‘pixel dimension’.

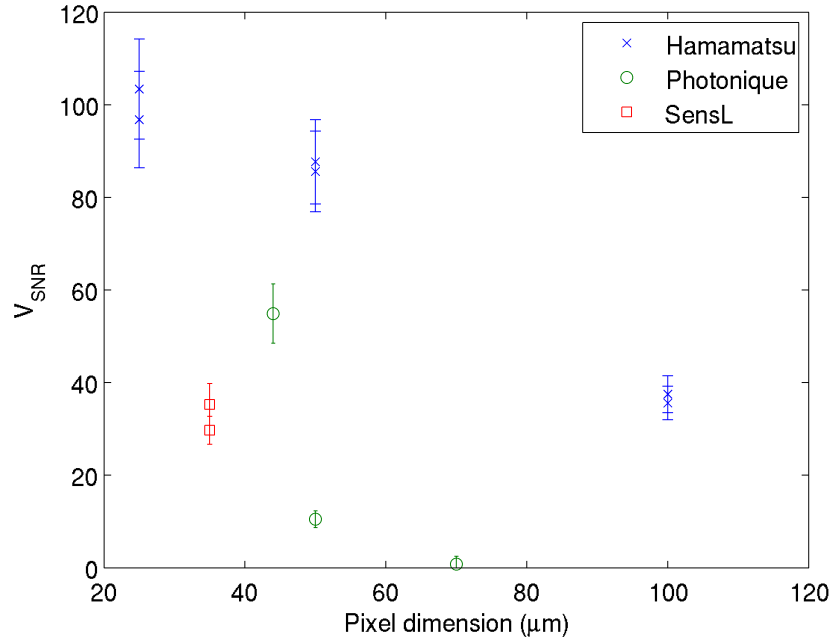


Figure 5.7: Signal-to-noise ratio plotted as a function of pixel size. The different colour and marker symbol series differentiate the device manufacturer.

pixels is distributed over an extended time period, reducing the optimal pulse height (V_{pulse}).

5.4.2 Rise time

The rise time is defined as the time interval in which the rising edge of the pulse reaches two predetermined voltage levels, usually defined as 10% and 90% of the total pulse amplitude. The rise time of a detector system describes how well defined the detector activation is in time. An ideal detector system would show an infinitely sharp rise time so the activation time could be measured with infinite precision.

It was discussed in Chapter 4 that the rise time attributed to the electrical model of a single APD cell is extremely small. By applying equation 4.3.1 and considering the electronic characteristics of a Hamamatsu S10362-33-025C device measured by [75], this contribution was calculated explicitly as 15.4 ps.

The results of rise time measurements are presented in Figure 5.8 where the quoted error bars represent the standard deviation of each measurement. Results are also listed in Table 5.2. Values for measured rise times are of order 1-3 ns across all devices, much higher than the predictions of the electrical model. Rise times of this order are in agreement with the experimental measurements of other groups [75] [110]. As mentioned briefly above,

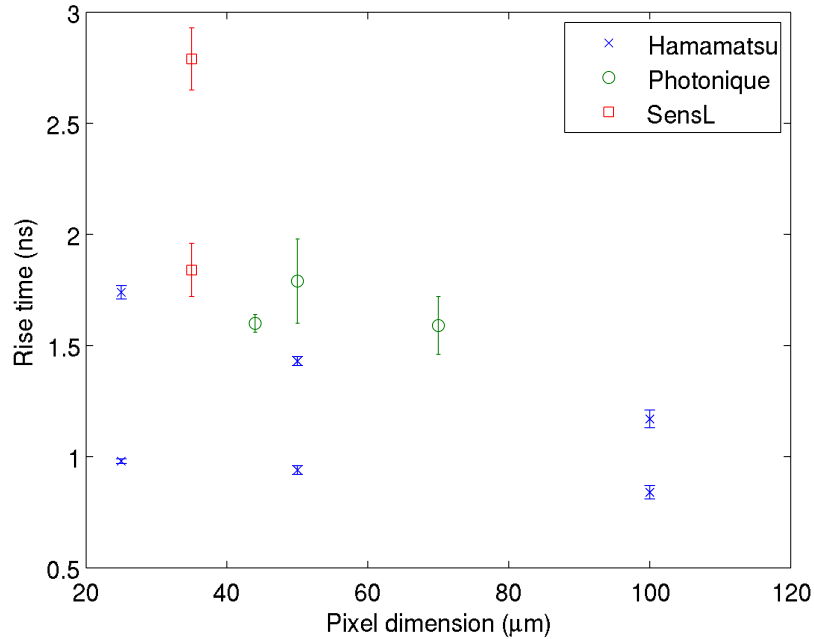


Figure 5.8: Rise time plotted as a function of pixel size. The different colour series and marker symbols differentiate the device manufacturer.

with the experimental arrangement used here a lower limit will be set for the rise time of the system by the temporal spread of photons arriving at the device surface from the LED. The latter is quoted as 800 ps by the LED manufacturer. The general degradation of the rise time of all devices beyond this value must then be described by a number of additional factors not accounted for in the electrical model. One contribution is the influence of an inductance introduced by the bonding wire connecting the pixel array to the SiPM output pins, apparent in each device model. This wire is in series with the signal chain and has an estimated value of a few nH.

However, a significant source of degradation in the device rise time comes from the transient times of signals from individual microcells. This effect can be observed in the data presented in Figure 5.8 where devices with equivalent pixel sizes but differing active areas show consistent offsets in response. The trend is best seen in the Hamamatsu devices where a clear offset is observed for each of the three devices. An increase in active area is correlated with a parabolic increase in the total number of pixels needed to populate that area. In turn, this creates a greater range of paths which the signal could take to reach the terminals of the device, increasing the uncertainty on the time at which the voltage is induced at the terminals. As a result the best performing devices from each manufacturer are those with the smallest active area. Again the best performing manufacturer was Hamamatsu.

5.4.3 Fall time

The purpose of the measurements presented in this section is to select a candidate SiPM to read out the characteristic light distribution from scintillator crystals, specifically LYSO. LYSO is characterised by an exponential scintillation emission time of 41 ns, much longer than the rise time of the device ($\sim 1\text{-}2$ ns). In this scenario the device response signal will not be characterised by a sharp rise, but can be approximated as the convolution of the source signal shape and the single pixel's response function. The dominant component of the single pixel signal shape is the fall time (see Figure 5.5) and, therefore, it is the fall time which will have the largest influence on the signal shape in response to a temporally spread signal. Additionally, the fall time defines the time it takes the electric field across the p-n junction to re-charge after an avalanche event. Whilst the electric field strength is reduced the triggering probability is also significantly reduced, making the pixel insensitive to an impinging photon flux while these conditions persist. This can lead to saturation effects, as, in these conditions, the device response is no longer proportional to the activating flux.

The results of slow fall time measurements, which dominate falling edge signal for all devices, are presented in Figure 5.9, where the quoted error bars represent the standard deviation of each measurement. All fall time measurements, including the fast fall time measurements made on the Photonique devices, which have not been included in Figure 5.9, are listed in Table 5.2.

Photonique devices have been observed to have a significantly degraded fall time compared to the other devices. If we consider equation 4.3.2, this can be attributed to increased values of the quenching resistance (R_q), the capacitance of the quenching resistor (C_q), the pixel capacitance (C_p), or possibly all three factors together. Although no values for these parameters can be found in literature for the specific devices that were tested, it is likely that an increase in the capacitive values is the cause. This educated guess comes from the consideration that the load resistor is a physical component and can be explicitly chosen by the manufacturer to maximise the device performance. There is no operational benefit from increasing the uncertainty on both the signal activation time and the single pixel dead time, so it is unlikely that this characteristic was developed by choice. Considering measurements of the characteristics of Hamamatsu devices [75], it was seen that C_q was typically five times smaller than C_p . Therefore C_p is likely to also be the dominant contribution in this case. Both parameters can be difficult to control. Often C_p will depend on

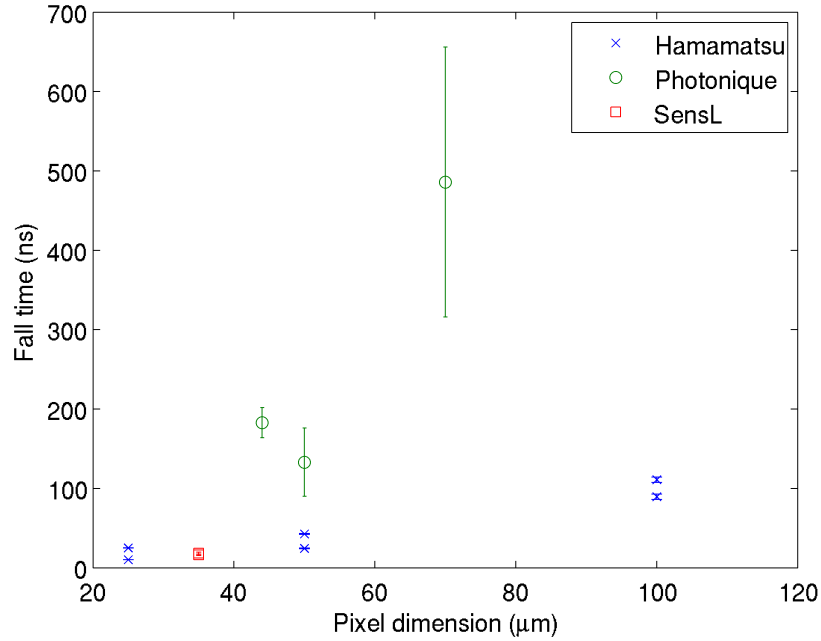


Figure 5.9: Fall time plotted as a function of pixel size. The different colour series differentiate the device manufacturer.

the quality of the silicon wafers and the manufacturing techniques used in the production process [111], hence it is a value that can be expected to vary between manufacturers. The value C_q should be well understood as it will relate to the specific material characteristics of the physical quenching resistor component. However, it is possible that this component could be affected by stray capacitances associated with the metallic grid connecting the pixels. Although all of these effects may provide contributions, without detailed measurements of these electronic characteristics the dominant contribution cannot be known precisely. The large uncertainties on the measured values relative to the Hamamatsu and SensL devices are a result of the characteristic fall time being much longer than the length of the captured pulse (see Figure 5.5a). Hence, only a fraction of the full distribution was used in the fit, leading to significant uncertainties in the fit parameters.

The Hamamatsu devices show two trends. The first is an increase in fall time with pixel area. This is expected as the pixel capacitance is proportional to pixel area and an increased fall time is therefore predicted through equation 4.3.2. The second is the consistent offset measured of 15-20 ns for devices with the same pixel size but an increased active area. A similar effect, although not quoted explicitly by the manufacturer, has been seen previously in [75], where the quenching resistors on the large area devices were measured with a resistance 20-40% higher than the smaller area equivalents. Although the logic of this feature is not understood, it is possible then that a systematic increase in

load resistance was applied by the manufacturer for the larger area devices, degrading the fall time performance. Both the 1 mm² and 9 mm² active area SensL devices, which are both characterised by 35 × 35 μm² pixel areas, performed with consistent uncertainties, suggesting identical quenching resistors were applied to both.

5.4.4 Timing jitter

The timing jitter of a SiPM can be defined as the spread on the time the detector takes to generate a signal in response to a stimulus. This spread is due to statistical and systematic effects which characterise an electron avalanche and its propagation to the terminals of the detector.

The avalanche process itself can be generated by two types of events: a photoelectron creation within the high-field *avalanche region*; or an phototelectron creation in the low field *drift* region. Events occurring in the high field region generate a minor contribution to the time spread as charge carrier can instantly trigger an avalanche. However, when carriers are generated in the drift region, the signal production is slower as charge carriers must drift a finite distance before an avalanche can be triggered. Most SiPM designs are optimised such that the high field region is positioned at a depth of approximately one interaction length of a specific band of optical wavelengths. This way photons of the right wavelength are likely to interact in the high field region of the silicon, optimising both the triggering probability, as charge carriers are less likely to recombine before reaching the high field region, and timing properties of an avalanche process. In addition, it has been shown that the timing jitter is optimum when a photoelectron is generated at the centre of the pixel, and degrades as the interaction position approaches the edges of the pixel [112]. This is correlated with the electric field strength distributions across the pixel area where a high field results in faster avalanche propagation.

Results of the timing jitter measured for all devices are presented in Figure 5.10 where the uncertainties are the convolution of both statistical and estimated fit uncertainties. All values are additionally listed in Table 5.2. In devices from both Hamamatsu and SensL a degradation in timing resolution is observed for devices with identical pixel dimension but increasing active area. This can be attributed to the variation in signal path length associated with single pixel pulse activations scaling proportionally with active area. Additionally, a general trend of timing jitter degrading as a function of increased pixel dimension is observed. It has been shown by [112] that the timing response of each

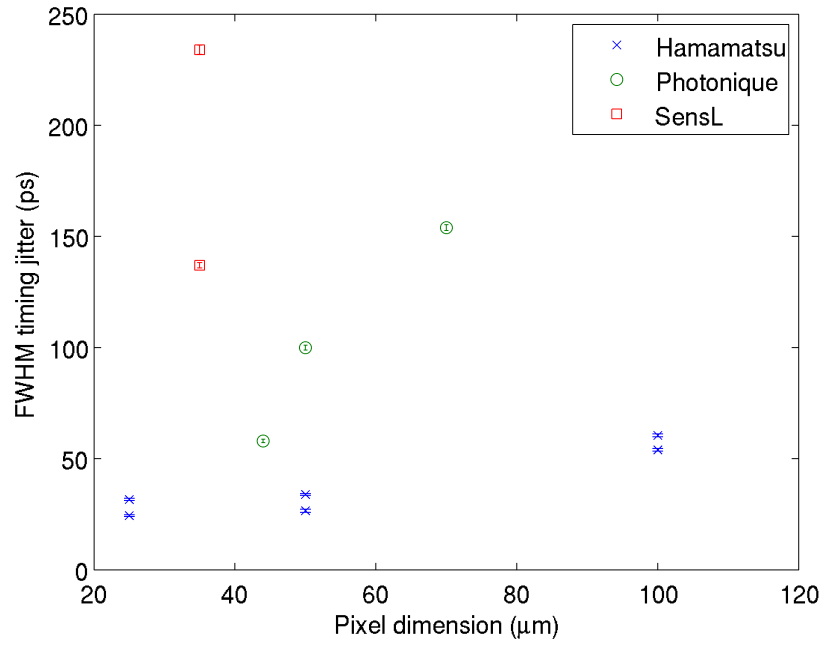


Figure 5.10: Timing jitter plotted as a function of pixel size. The different colour series differentiate the device manufacturer.

APD pixel is position sensitive. Larger pixels exaggerate this effect by increasing the total range of possible interaction positions.

As with all measurements presented in this section, the Hamamatsu devices outperformed those from both SensL and Photonique with the $25 \times 25 \mu\text{m}^2$ and $50 \times 50 \mu\text{m}^2$ showing optimal performance.

Table 5.2: Characteristics of SiPM devices investigated for model selection.

Manufacturer	Active area [mm ²]	Pixel dimension [μm]	N _{pixels}	PDE at 420 nm [%]	SNR	Rise time [ns]	Fast Fall time [ns]	Slow Fall time [ns]	FWHM Timing Jitter [ps]
Hamamatsu	1	25	1600	24	103.4 ± 10.8	0.98 ± 0.01	n/a	10.3 ± 0.1	24.4 ± 0.4
	1	50	400	48	87.7 ± 9.1	0.94 ± 0.02	n/a	24.5 ± 0.4	26.6 ± 0.7
	1	100	100	67	35.6 ± 3.6	0.84 ± 0.03	n/a	89.6 ± 3.4	54.0 ± 0.6
	9	25	14400	24	96.8 ± 10.4	1.74 ± 0.03	n/a	25.1 ± 0.3	31.7 ± 0.5
	9	50	3600	48	85.6 ± 8.7	1.43 ± 0.02	n/a	42.7 ± 0.5	33.9 ± 0.4
	9	100	900	67	37.5 ± 4.0	1.17 ± 0.04	n/a	111.0 ± 3.4	60.5 ± 0.7
	1	~44	~500	22	54.9 ± 6.4	1.60 ± 0.04	6.9 ± 1.1	183 ± 19	58 ± 0.8
	4	~50	~1700	25	10.5 ± 1.8	1.79 ± 0.19	6.8 ± 1.0	133 ± 43	100 ± 1.1
	9	~70	~8100	18	17.5 ± 1.7	1.59 ± 0.13	6.7 ± 0.6	486 ± 170	154 ± 1.3
SensL	1	35	576	10	29.7 ± 3.0	1.84 ± 0.12	n/a	18.4 ± 1.3	137 ± 1.2
	9	35	4774	10	35.3 ± 4.5	2.79 ± 0.14	n/a	16.4 ± 1.0	234 ± 2.1

N.B. n/a is quoted for devices where the fast fall time was not observable, and therefore could not be measured.

5.5 Device selection

As introduced at the start of this chapter, the drive of the measurements presented here has been to identify the best candidate device for application in a prototype TOF-PET detector system. It has been shown that the devices from Hamamatsu outperform the Photonique and SensL devices in all the parameters measured and so should be considered the focus of the final selection process. However, with a range of characteristic measurements performed it is useful to consider the operation conditions associated with the final application in order to identify the best suited device. A logical process of elimination will then follow from these considerations.

The characteristic light yield of LYSO crystals is 32 ph/keV [61], therefore in a 511 keV activation event a total flux of $511 \times 32 \approx 16 \times 10^3$ photons will be produced. These photons will be emitted with an exponential time profile described by the constant, $\tau_{LYSO} = 41$ ns [61]. If we consider the description of light transport in the crystals presented previously in Chapter 3, it was shown through geometric estimations that only photons emitted with a θ angle in the range $0 < \theta < 50.7^\circ$ or $129.3^\circ < \theta < 146.5^\circ$ will reach the active area of the SiPM. This corresponds to $\approx 20\%$ of all emissions. Therefore, we can estimate that the total number of photons impinging the active SiPM surface over the full time profile of an event will be $\approx 3.2 \times 10^3$ photons. If the source signal was well defined in time (i.e. a laser or a fast LED), then the ideal detector would be characterised by a number of pixels much greater than the number of photons in the source signal, so as to avoid saturation effects. However, this is complicated by the increased temporal spread of the light source, as the single pixel dead time (which is proportional to the fall time) will additionally influence the number of source photons which may be detected.

Considering both the source flux described above, and generic timing considerations associated with the detector system, we can identify a number of key parameters.

- The number of pixels in the APD array should be larger than the number of impinging photons. If the number of pixels is equivalent to or less than the source flux then significant saturation effects will be seen. Saturation effects will cause the device response to tend to a single, predictable output, degrading the energy resolution. It was discussed in Chapter 2 that the energy resolution is a key parameter in the noise rejection for a PET detector and hence should be considered.
- The PDE should be as high as possible. It has been shown in Chapter 3 that the

first photons arriving at the active surface of the device have the smallest timing uncertainty. The optimum coincidence timing resolution measurable with the detector system can therefore only be achieved if the probability of detecting these first photons is maximised.

- The fall time should be as short as possible. This has two effects. Firstly, the fall time describes the recovery rate of an APD after an avalanche event has occurred. The time a detector system is insensitive after activation is often called dead time and should be minimised to avoid signal losses. Secondly, for all measured devices, the fall time is an order of magnitude (or more) longer than the rise time and as such describes the largest temporal spread of the signal from an avalanche event. If one considers again that the system's temporal response can be modelled to first order as the convolution of the source emission distribution and the single pixel response, then the single pixel response should approach a Dirac delta function if the source distribution is to be fully recreated. The fall time is therefore directly related to the shape of the response signal where a reduced value of fall time will correspond to an increase in the gradient of the rising edge ($\frac{dV}{dt} |_{V_T}$ from equation 5.3.2), minimising σ_{signal} .
- The timing jitter should be as small as possible. The timing jitter defines the ultimate lower bound of the timing resolution possible with the device and as such should be minimised.

If we consider these parameters in order they are presented above, then the a first round of selection cuts can be made with respect to the number of pixels on each device. There are four devices with $N_{pixels} > 3200$: Hamamatsu S10362-33-025C, Hamamatsu S10362-33-050C, Photonique 0710G9MM-PCB and SensL MicroSL-30035-X13 (see Table 5.1). Of these devices, the SensL MicroSL-30035-X13 and Photonique 0710G9MM-PCB show poor response in the PDE and fall time parameters respectively, and can hence be rejected. This leaves the Hamamatsu S10362-33-025C (9 mm² active area with 25 μ m pixel dimension) and S10362-33-050C (9 mm² active area with 50 μ m pixel dimension) devices.

In order to select between these two devices the three main parameters which must be considered are: the PDE, which affects the statistical uncertainty on the device timing resolution when coupled to a scintillator; the fall time which affects the σ_{signal} uncertainty when coupled to a scintillator; and the timing jitter. The measured value of the timing jitter for the two devices differ by 2 ps and can be considered approximately equivalent.

The 25 μm device then shows a factor of two improvement in fall time and an equivalent factor of two reduction in PDE. It is generally considered that the ultimate limiting factor in the timing resolution of any detector system consisting of a scintillator coupled to a photodetector is the statistical fluctuations [60] [113] [62] [55] [114]. In conclusion, the final device recommended for application in a prototype TOF-PET detector system is the Hamamatsu S10362-33-050C device, which applies a 9 mm² active area with $50 \times 50 \mu\text{m}^2$ pixel area.

A prototype TOF-PET detector system applying the S10362-33-050C device has been in development at RAL since August 2012. Further design optimisations to be applied to this prototype have been investigated by the simulation work presented in the chapters which follow.

Chapter 6

Characterisation of a coupled SiPM and LYSO detector system

With a SiPM device identified, it is key for the work presented in this thesis that the device response is well understood in the context of a detector system applicable to PET. This chapter details the measurements and results of two experimental arrangements, specifically designed to characterise a gamma-ray photon detector system consisting of a Hamamatsu S10362-33-050C SiPM coupled to a LYSO scintillator crystal.

The first experiment presented is aimed at measuring the energy and timing response of a pair of such detector systems operated in electronic coincidence and illuminated by a ^{22}Na positron-emitting radioactive source. The resulting coincident pulse pairs are recorded and used to evaluate both the energy and the coincident timing response of the system.

The second experiment investigates the optical photon transport in the crystals through depth-of-interaction (DOI) measurements taken at different positions along the crystal length. By using a collimated beam of gamma photons it is possible to control the interaction position along the length of the crystal. The resulting optical photon flux, as measured at a number of different longitudinal positions, can then be monitored at opposite ends of the crystal by coincident SiPMs, to measure the energy and timing characteristics.

The results from both experiments described in this chapter were used to both develop and validate the detector system simulation which was developed from scratch and is presented in the following chapter.

6.1 Coincident detector systems

A PET detector system, as discussed in Chapter 2, consists of opposing arrays of detector elements, operated in electronic coincidence. Signals from channels at opposing arrays are then correlated to identify annihilation events using energy and timing constraints. Events are accepted if their properties fall within well chosen intervals which ultimately define the ability of the system to reject noise events from being mistakenly recorded. The contamination from fake signals ultimately degrades the efficiency of the system and limits the quality of the final reconstructed image. This is the reason why an in-depth understanding of the energy and timing characteristic of the system is crucial for reliable and robust conclusions to be drawn on the suitability of a detection system to PET applications.

In this work investigations have focused on the development of an array of detector elements which apply one-to-one coupling between scintillator crystals and SiPMs. This type of arrangement, as discussed previously, has a number of advantages over using block detectors as in conventional PET. Two of the most significant advantages are the improved spatial resolution that one can obtain and the reduced dead time that can be achieved [115] [21] [29] [58]. One-to-one coupling also maximises the statistics measured by a single photodetector. As mentioned in the previous chapter, it is the photon detection statistics which ultimately define the lower bound of timing resolution with scintillator systems [60] [113] and should be maximised where possible for fast timing applications. As a result $3\times 3\times 5$ mm³ scintillator crystals are applied here to enable direct coupling to the 3×3 mm² active area of the Hamamatsu S10362-33-050C SiPM. The crystal length was chosen as 5 mm to keep the aspect ratio (i.e. the ratio of length to cross section) low, as the aspect ratio increases the probability, and as a consequence the average number, of boundary interactions before detection also increases. By using low aspect ratio crystals it is therefore possible to evaluate the system response with a reduced contribution from the effects of boundary interactions - which have been investigated separately with the depth-of-interaction experiment.

6.1.1 Experimental arrangement

As in the LED characterisation measurements described in Chapter 5, SiPMs were mechanically secured with the same custom-designed SiPM holders. These holders included

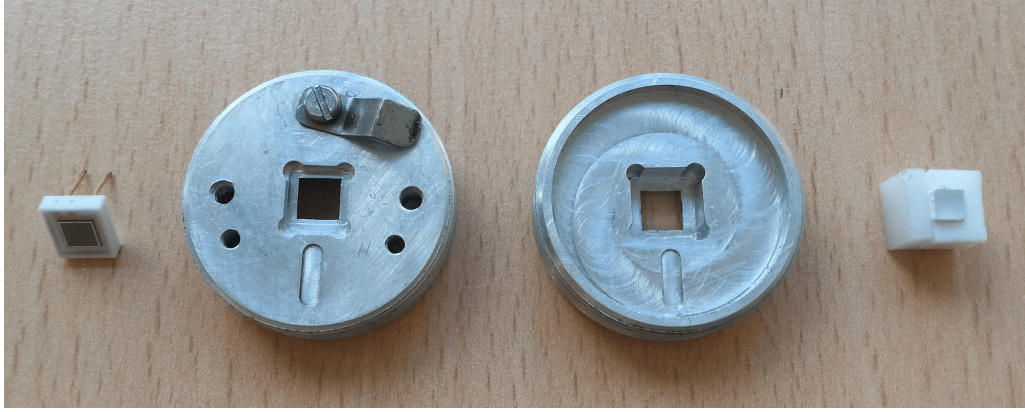


Figure 6.1: Photograph of the mechanical arrangement designed for coupling a S10362-33-050C SiPM to a scintillator crystal. An example SiPM device is shown on the far left. In the centre two identical SiPM holders are positioned to show both the front and back faces where the SiPM and LYSO crystal arrangement are respectively coupled. Finally a $3 \times 3 \times 5 \text{ mm}^3$ LYSO crystal, painted in TiO_2 paint, is shown in the plastic casing used to both centre and secure the crystal in the holder.

a 1 mm deep, $4 \times 4 \text{ mm}^2$ window centred about the active area of the device which was used previously as an opening through which to illuminate the device with an optical LED signal. Here it is used to directly couple a scintillator crystal. The remaining 6 mm thickness of the holder is cut with a wider $7 \times 7 \text{ mm}^2$ opening. The result is that a crystal with a $3 \times 3 \text{ mm}^2$ cross section, with a reflective coating of up to 0.5 mm thickness on each edge, can be reproducibly coupled to the SiPMs active surface centred and protectively held with a plastic casing. A photograph of the arrangement is given in Figure 6.1.

Two such mechanical detector coupling arrangements were screwed into position at either side of a sealed, $1 \mu\text{Cu } ^{22}\text{Na}$ positron source, housed in a custom designed mounting based on 1-inch diameter optical tubes. The distance between the sealed source and the plastic crystal housing during data collection was approximately 1-5 mm. This distance was kept to a minimum in order to maximise the solid angle subtended by the detection system relative to the isotropic emission of collinear 511 keV photons from the source.

The system was optimised for optical performance by applying a layer of optical grease (refractive index: $n_{grease} = 1.61$) at the physical junction between the LYSO crystal and the SiPM. Applying grease reduces the change in refractive index seen by an optical photon approaching the junction, reducing the critical angle as defined by Snell's law and increasing the range of angles in which transmission can occur. Additionally, as briefly mentioned above, reflective coatings were applied to all faces of the crystal, bar the face being read-out by the SiPM. Coating the surface in this way has been shown previously to maximise the light collection at the detector by reflecting light back into

the crystal [116], increasing photon detection efficiency and reducing the statistical limit of the systems energy resolution. For this purpose comparative measurements were made with scintillators wrapped in layers 0.07 mm thick PTFE tape and painted with white TiO₂ paint. These materials were specifically selected as they have been the subject of in-depth investigations into their use as reflector materials for scintillators [66]. With published data available on both, equivalent materials could be more easily developed in simulation.

SiPMs were biased and read-out with the custom designed circuit described in Chapter 5, a schematic of which has been given previously in Figure 5.2. The biasing voltage applied to specific SiPM devices was set to the manufacturer's recommended value (2 V above the breakdown voltage of that device - approximately 70 V), supplied by a Keithely 2612 dual-channel power supply. As before, the output signals were readout through a permanent load of 51 Ω , in parallel with the 50 Ω termination resistance of a LeCroy WaveMaster Zi-8 oscilloscope, yielding a system load of 25.2 Ω . The resulting analogue signals from active SiPMs were digitised for off-line analysis at 40 GS/s using the LeCroy WaveMaster Zi-8 oscilloscope.

6.1.2 Energy results

The system energy response was evaluated via pulse height spectra for both reflective coating materials. For each case, separate spectra were formed for the two coincident channels by filtering 20,000 recorded pulses for electronic noise with a second-order Butterworth filter, $f_c = 350$ MHz. The maximum amplitude of each filtered pulse was measured and the result passed to a histogram with bin width of 1 mV. Uncertainties of $\sqrt{n_i}$, where n_i is the number of bin entries at the i^{th} bins, were applied to each bin and the photopeak fitted with a Gaussian. The energy resolution for each detection system was then calculated as:

$$\frac{\Delta E}{E} = \frac{\sigma_{FWHM}}{\bar{x}}, \quad (6.1.1)$$

where σ_{FWHM} is the FWHM of the Gaussian fit ($\sigma_{FWHM} = 2\sqrt{2\ln 2}\sigma$, where σ is the standard deviation of the distribution) and \bar{x} is the photopeak energy, given by the mean of the same distribution. Uncertainties on each of the fit parameters were assumed to be the propagation of the statistical uncertainties and the uncertainty on the fit. The uncer-

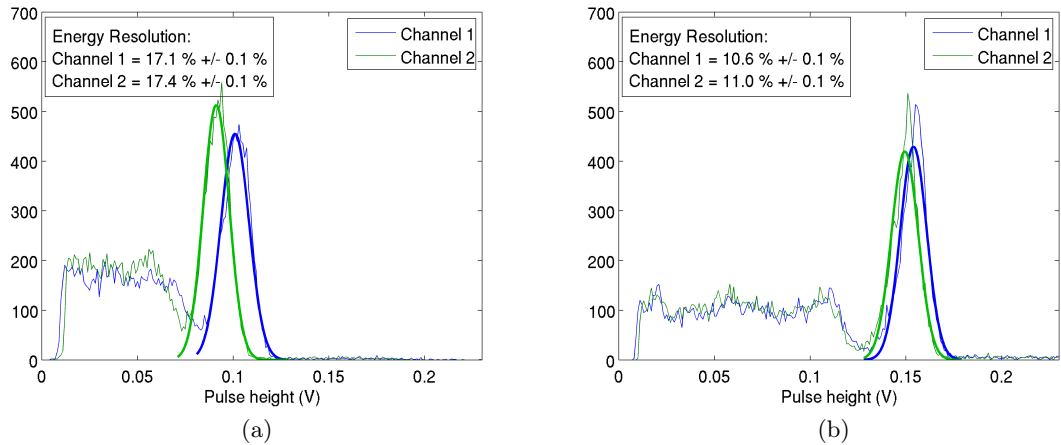


Figure 6.2: Example gamma spectra measured in electronic coincidence for (a) crystals wrapped in PTFE tape (b) crystals painted with TiO_2 paint. Gaussian fits to the measured photopeak are shown as thick green or blue coloured lines.

tainty associated with non-Gaussian tails on the photopeak distributions was estimated by varying the limits of the considered data range and re-fitting. This procedure was repeated in steps of $\sigma/2$ for the data set contained between three to six σ of the original fit. The range of the resulting fit parameters was considered as the contribution due to these tails. Results for both reflector types are given in Figure 6.2.

The resulting pulse height spectra show two key structures: a Compton continuum, where only a fraction of the 511 keV energy was deposited in the crystal, and a full energy photopeak, where an interaction occurred via the photoelectric effect. The first thing to notice in comparing the two measurements is a significant (approximately 50 %) gain in signal for the crystals painted with TiO_2 paint. This result stands in contrast to the relative reflection coefficients given in literature of 0.934 and 0.951 for PTFE and TiO_2 paint [66], which would suggest the materials might perform comparably. In fact, it was found that the photopeak energy could vary by up to 40 % if crystals were re-wrapped and the measurement re-run. Although a recommended procedure was followed for wrapping the crystal [117], the inconsistent results are likely due to non-uniformities which occur through the process of wrapping the crystals by hand. Some small fluctuations of 1-2% were seen in photopeak energy for measurements taken with painted crystal (see Figure 6.2b), however these were attributed to inconsistent optical coupling between runs. It should also be noted that photopeaks measured with the TiO_2 coated crystals are less well described by Gaussian fits. This is due to the increased light levels saturating the device response.

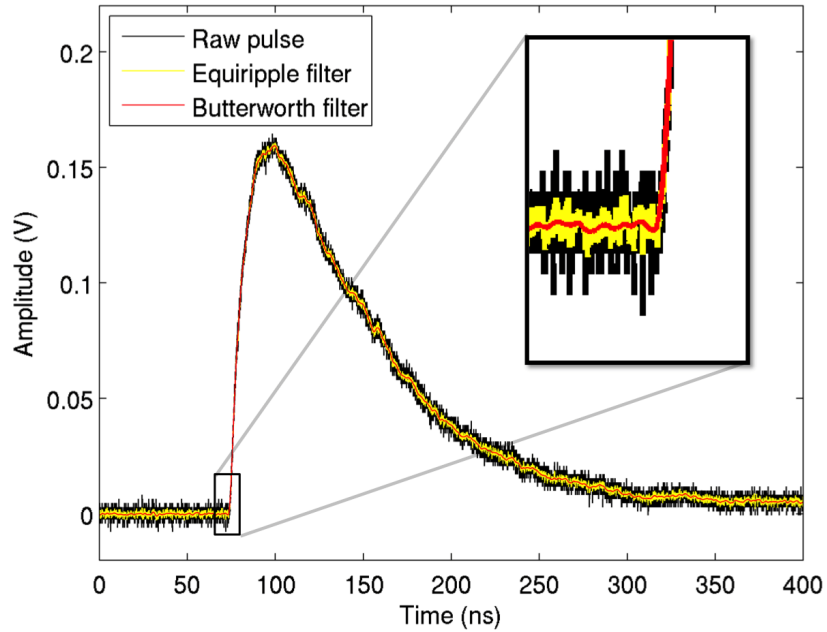


Figure 6.3: An example pulse from within the photopeak FWHM is plotted as recorded and after applying both a 5th order equiripple filter ($f_c = 500$ MHz) and a 2nd order Butterworth filter ($f_c = 350$ MHz). The zoomed image in the top right hand corner compares the response of the raw and processed signals to the highest gradient signal change.

6.1.3 Coincident timing results

For these measurements, due to the large systematic uncertainties seen in the system wrapped in PTFE tape, only data taken with the TiO₂ paint are considered. Here only events which would have passed the initial energy cut are of interest and as such only pulse pairs from within the photopeak FWHM were selected for processing. For a pulse height spectrum including 20,000 events this would typically result in a sample of ~ 1500 pulse pairs.

A set of timestamps were then recorded for each pulse via leading-edge discriminators applied at incremental steps along the leading edge. Trigger levels were applied relative to the mean position of the photopeak pulse height, 0.152 V. At each trigger point the time difference (Δt) between each pulse pair was taken and histogrammed using 25 ps bins (equivalent to the 40 GS/s sample rate of the recorded pulses). The final histograms containing a full sample of Δt values were then fitted with a Gaussian distribution. The mean of this distribution then represents the time delay between the two signals, while the width represents the spread in time. For all coincidence timing resolution (CTR) measurements in this work, the result is given as the FWHM of this Gaussian distribution.

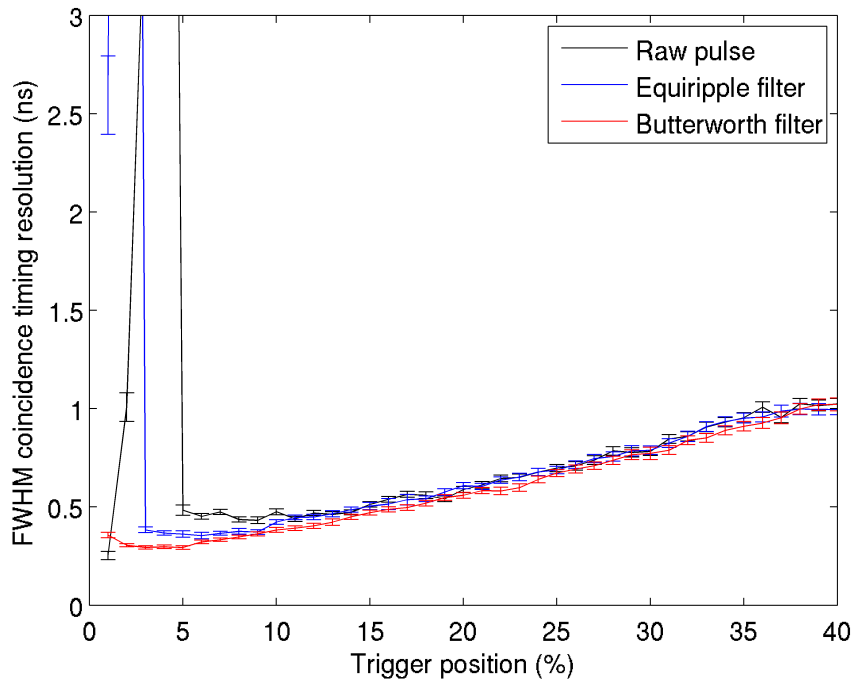


Figure 6.4: A plot of the timing resolution as a function of leading edge discriminator position for a coincident system of $3 \times 3 \times 5$ mm LYSO crystals, painted with a reflective TiO_2 paint and read out by Hamamatsu S10362-33-050C SiPMs. The three colour distributions define the processing techniques applied to the recorded pulses before triggers were applied.

As in the energy measurements, the uncertainty on each FWHM was assumed as the propagation of the statistical uncertainty on the width of the device with the range of values calculated when the fit was re-applied in steps of $\sigma/2$ to the three to six σ range.

This process was repeated for three separate cases:

- The data set received no processing. The leading edge discriminators were applied to the pulses exactly as recorded, or ‘Raw’.
- The data set was filtered using the 5^{th} order, windowed Equiripple filter with $f_c = 500$ MHz.
- The data set was filtered using the 2^{nd} order, Butterworth filter with $f_c = 350$ MHz.

An example photopeak pulse processed with each of the three methods is given in Figure 6.3.

The resulting distribution of CTR as a function of trigger position for each of the three cases is given in Figure 6.4. The Butterworth filtered data set consistently shows the best CTR below a trigger threshold of $\sim 12\%$, with an optimum result of 290 ± 10 ps at a

threshold of 3% of the mean photopeak energy.

As the threshold level increases, more photon interactions are required at the SiPM for the signal amplitude to rise to this level. As described in Chapter 3 the statistical limit on the time spread of detected photons degrades with increasing photon number and the timing resolution degrades as a function of trigger position. In the case of the lower threshold positions, the contribution of photon statistics is reduced and the signal jitter (see equation 5.3.2) becomes a significant contribution. It is clear from Figure 6.3 that the rising gradient ($\frac{dV}{dt}$) of all three signal types are equivalent, but the noise floor (σ_{noise}^{rms}) is significantly reduced for the filtered signals. By filtering the signals for electronic noise, the signal jitter is minimised and the timing resolution improved with the best performance shown by the Butterworth filter.

The sharp increase in the CTR shown by both the Raw and Equiripple filtered signals below the 10 mV level is due to the chosen threshold becoming of comparable size to the electronic noise level. This behaviour establishes the lower bound of the CTR which can be used when applying the leading-edge discriminator technique.

6.2 Depth-of-interaction measurement

In order to re-produce the energy, and, in particular, the timing results presented in section 6.1, it is important to understand the characteristic parameters which contribute towards them. To simulate the scintillator response, an understanding of both the photon emission characteristics and the photon transport through the crystal are required. The emission characteristics include: photon yield, intrinsic energy resolution, rise time and fall time. These are available as either data sheet values or measurements in literature and can be applied with known uncertainties. However, the photon transport in the crystals depends on a range of parameters that are difficult to obtain experimentally or which can often not be characterised by a single value as this in turn depends on other parameters. The addition of a reflective coating surrounding the crystal further complicates the system, making an analytical solution very hard, if not impossible to achieve.

Measurements detailed in this section were designed to attain a set of results from which the depth-of-interaction (DOI) effects of high energy photon interactions in the crystal could be decoupled, allowing an investigation of the optical photon distributions at either end of a crystal at a range of interaction positions. These results can in turn be used to

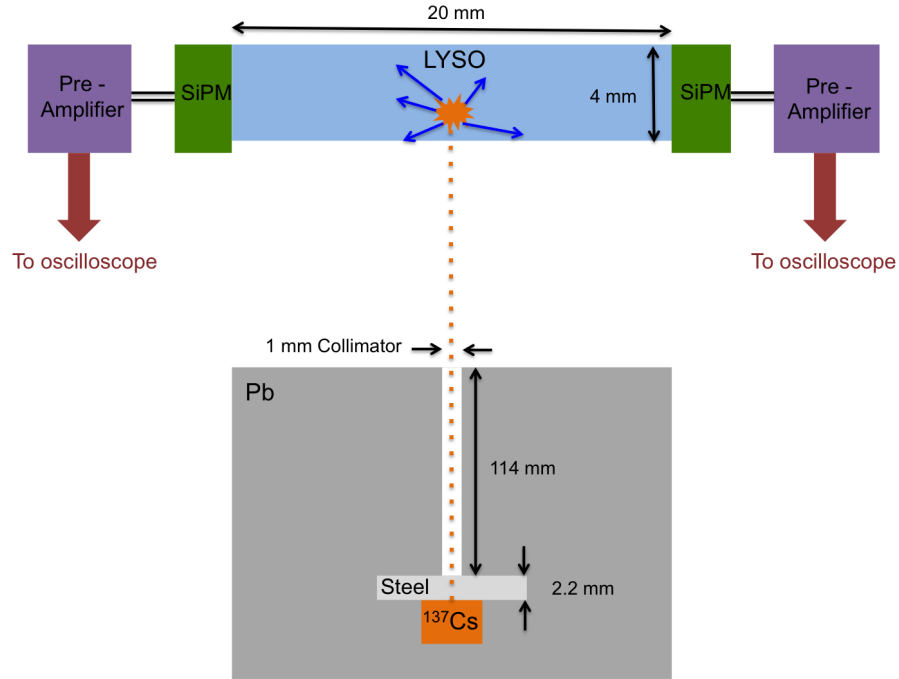


Figure 6.5: Schematic diagram showing the experimental arrangement applied for DOI measurements.

tune a number of simulation parameters relating to the photon transport in the crystal in the simulation environment described in the following chapters.

6.2.1 Experimental arrangement

This experiment was performed at the University of Surrey, where a collimated ^{137}Cs source was available. The ^{137}Cs source, whose main emission components are 32 keV and 662 keV gamma photons [118], was enclosed in a 11.4 cm thick lead container with a 1 mm diameter aperture which provided the collimated signal. A 2.2 mm steel plate was used to secure the source in place and act as attenuation for the low energy 32 keV photon emissions. These were additionally vetoed at the acquisition stage by pulse-height discrimination thresholds. A schematic diagram of the collimator and detector system arrangement is given in Figure 6.5.

The detector system was suspended approximately 10 cm above the aperture of the collimated source in a 5 mm thick, light-tight plastic box mounted on a Parker P25L x-y stage. The stage was fixed to a permanent framework built about the collimated source and was operated with Soloist IDE control software, capable of controlling the motion of the system to a tolerance of 100 μm in both planes. The box itself housed the detector

system and associated electronics, including: a $4 \times 4 \times 20$ mm scintillator crystal, painted with TiO_2 paint; two S10362-33-050C SiPM detectors; and the associated biasing and readout electronics. Both SiPMs were mounted on identical biasing electronics as seen previously in Figure 5.2, however in this case additional amplification was supplied by Minicircuits ZFL-100LN low noise pre-amplifiers as recommended by the Surrey group who had previously found them to perform well with their system [75]. Both amplifiers were biased at +15 V with an Iso-Tech TDS7254B power supply to yield a gain of 20 dB. The SiPMs were biased at the manufacturer recommended operating voltage by a pair of Ortec 659 single channel power supplies. All biasing voltages and SiPM response signals were fed in and out of the box via feed-through BNC connections. The resulting analogue signals were monitored and digitised for off-line analysis at 10 GS/s with a Tektronix TDS 7254B oscilloscope available at Surrey, running a LabVIEW data acquisition script.

This experiment, in contrast to the previous coincident detector system experiments, used a 4×4 mm² cross section LYSO crystal in order to compensate for effects of the higher energy gamma photon signal emitted by ¹³⁷Cs. A 511 keV event will produce $511 \text{ keV} \times 32 \text{ ph/keV} \approx 16 \times 10^3$ photons, whereas a 662 keV photon will produce $\approx 21 \times 10^3$ photons. The latter has been shown to exhibit significant saturation effects when read out by a S01362-33-050C SiPMs [119]. By increasing the crystal cross section to 4×4 mm² the ratio of cross section to SiPM active area is: $16 \text{ mm}^2 / 9 \text{ mm}^2 \approx 60\%$. As a result the fraction of the total photon flux seen by the device is: $0.6 \times 21 \approx 12.6 \times 10^3$ photons, therefore reducing the saturation effects.

Due to both the larger cross section crystals and spatial constraint of the light tight box, the SiPM holders employed for all previous measurements could not be re-used. Small plastic coupling tools were developed to fit over each end of the crystals which could be used to reproducibly couple the SiPMs. This is shown in Figure 6.6. Optical grease (refractive index: $n_{grease} = 1.61$) was applied at the junction between the scintillator and SiPM to optimise photon transport.

A calibration of the crystal's central position in both the x (crystal length) and y (crystal width) planes was run using an ORTEC 661 rate-meter with a lower limit counting threshold of +150 mV. The signal from one SiPM was fed into the rate-meter input and the calibration was run individually in both the x and y planes stepping at 0.5 mm intervals to profile the detector system's count rate response as a function in each 1-D plane. Data sets were recorded at the central crystal position in the y-plane and stepped in 2 mm

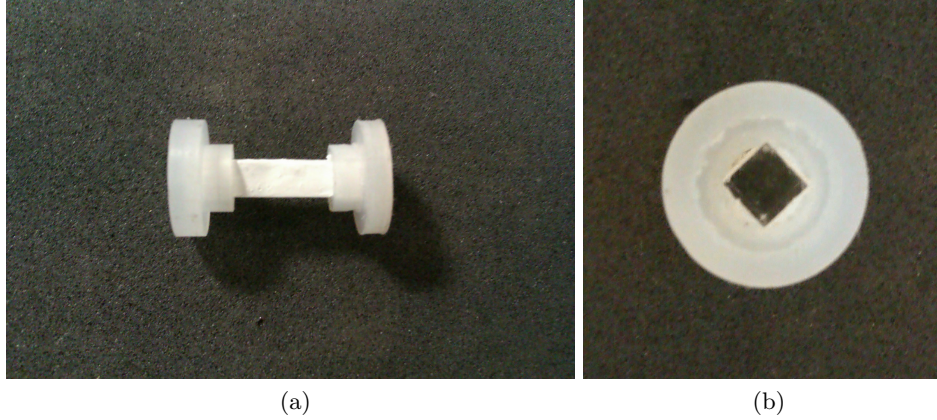


Figure 6.6: Photographs showing a $4 \times 4 \times 20 \text{ mm}^3$ LYSO crystal painted with TiO_2 paint connected to coupling tools used to DOI experiment (a) side view (b) top view

increments along the crystal length (x-plane).

6.2.2 Energy results

The system energy response was evaluated via the pulse height spectra recorded at each step point along the crystal length. Spectra were formed at each point by filtering 5000 pulse pairs for electronic noise with the 2^{nd} order Butterworth filter, $f_c = 350 \text{ MHz}$. The maximum amplitude of each filtered pulse was measured and passed to a histogram with an 8-bit resolution on an arbitrary unit scale. For measurements presented in this section, the pulse heights are considered on an arbitrary unit scale so to avoid direct comparisons with other data-sets where additional amplification was not applied. The specific scaling relates to the raw data as stored in the LabVIEW data file, where the 8 bit amplitude resolution of the scope is represented as floating point numbers between zero and one.

A fit to each distribution was made about the photopeak using a linear sum of a Gaussian distribution and a falling exponential. The additional exponential component was required to account for an exponential feature, prominent in the SiPM response to interactions at the opposing end of the crystal. Gamma spectra recorded at extreme and at central beam positions along the crystal length are given in Figure 6.7. A number of observations can be made from these distributions. Firstly, for the more central beam positions represented by Figures 6.7e and 6.7f, the Compton continuum and photopeak structures are clearly visible, with the energy of the photopeak shown to be measured higher by the channel closest to the interaction position. Secondly, when the interaction position approaches the face of a either of the two detector channels, the energy resolution of the system degrades

to the extent that the features of the distribution are lost and a photopeak is no longer distinguishable. By considering the isotropic emission of scintillation light in the crystal, and assuming an approximately point like source, both behaviours are explained by the increased solid angle subtended by the detector as the interaction position approaches. Similar effects are observed in simulation studies presented in Chapter 8. Due to the inability to distinguish a photopeak at the extreme end positions, these data points have not been included the parameter distributions given in Figure 6.8. The exponential energy distribution, which is shown with an endpoint energy equivalent to the highest energies measured at the extreme positions for each of the two channels, can be attributed to a diffuse source distribution.

The photopeak energy and width were extracted from the fits applied to the gamma spectra as shown in Figure 6.7. Uncertainties on these fits were estimated by re-fitting the distributions over a range of lower limits and convolving the range of resulting parameters with the statistical uncertainties. An initial lower limit on the fit range was selected and the difference (ΔE - measured in a.u.) between this value and the photopeak energy was found. The fit was then reapplied with the lower limit set with ΔE in the range $(0.5-1.5)\Delta E$ in steps of $0.25\Delta E$. The results of these fits are shown in Figure 6.8. The photopeak energy distributions, presented in Figure 6.8a, show a linear dependence on the crystal position. The gradient of the distribution recorded at Channel 2 is lower than Channel 1, likely due to an uncertainty on the method of optical coupling, resulting in a proportional signal drop recorded at Channel 2. However, it is also possible the the SiPM detector applied at Channel 2 was damaged resulting in a number of inactive cells which would result in a similar effect.

A plot of the photopeak FWHM as a function of interaction position in the crystal are given in Figure 6.8b. The trend of the distribution is again shown to be linear but with outlier points, seen in both channels, whereby the width of the peak increases non-proportionally at interaction positions 2 mm from the device surface. In this case, conversely to the photopeak energy measurements, the fit to Channel 2 shows the steeper gradient. These two effects are correlated, as a lower photopeak energy is a consequence of a reduced light signal and therefore reduced photon statistics, widening the photopeak distribution.

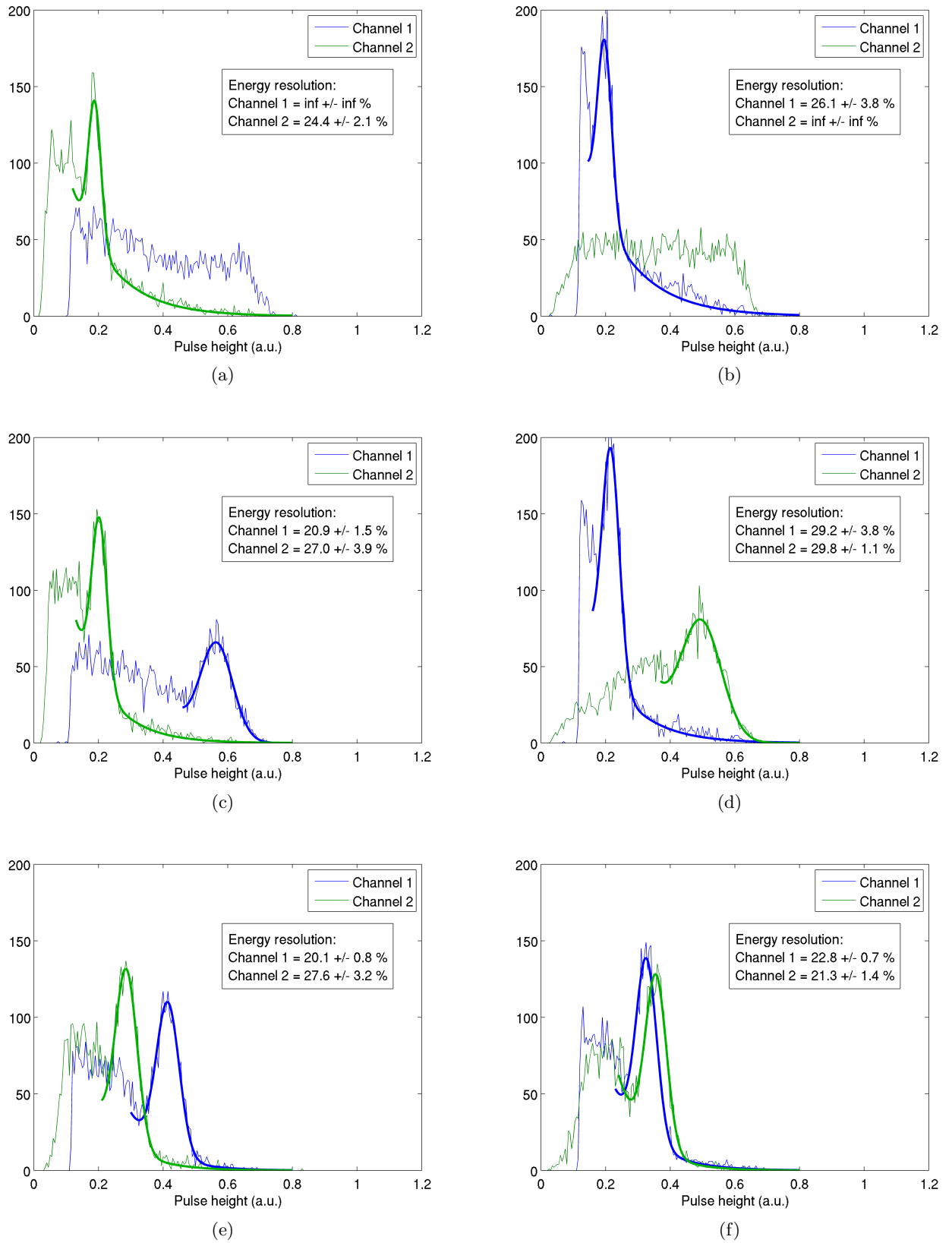
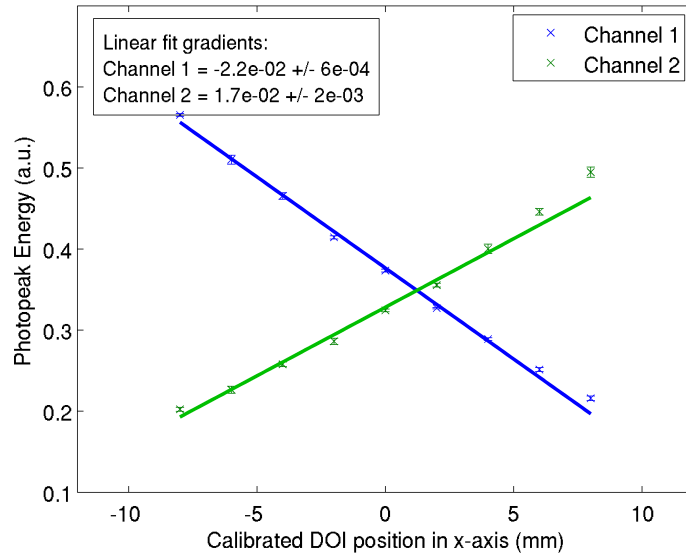
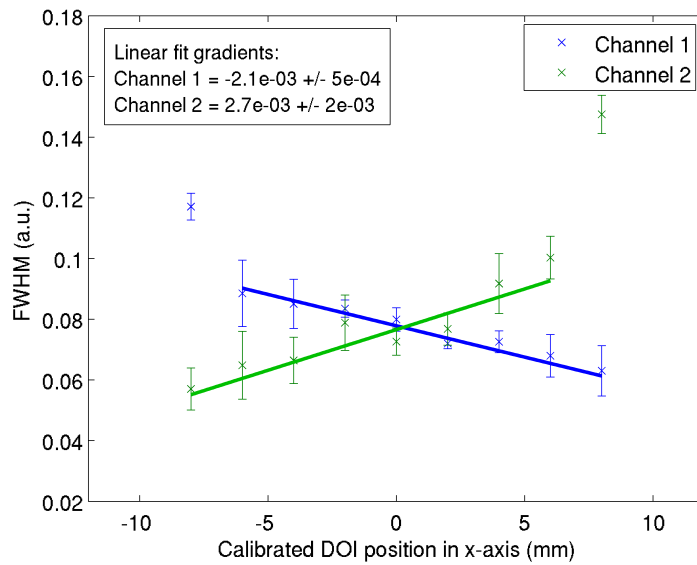


Figure 6.7: Example pulse height spectra as measured at a number of beam positions along the crystal length (a) -10 mm relative to the crystal's centre (b) $+10$ mm relative to the crystal centre (c) -8 mm relative to the crystal centre (d) $+8$ mm relative to the crystal centre (e) -2 mm relative to the crystal centre (f) $+2$ mm relative to the crystal centre. Fits are shown as thick coloured lines: blue = Channel 1; green = Channel 2. Channel 1 and Channel 2 are positioned at -10 mm and 10 mm respectively.



(a)



(b)

Figure 6.8: Distributions of the energy characteristics as measured by fits to gamma spectra produced at step points along the length of a $4 \times 4 \times 20$ mm crystal. (a) Photopeak energy distribution (b) FWHM of the measured photopeak

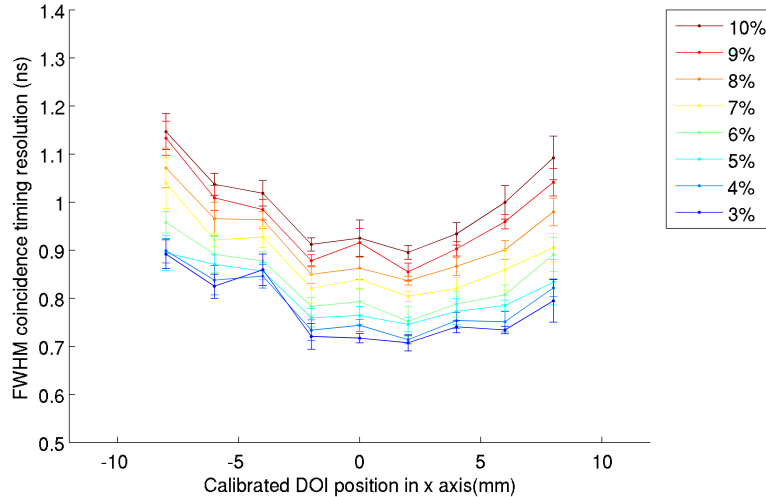


Figure 6.9: Distribution of CTR as a function of DOI measured at step points along the length of a $4 \times 4 \times 20$ mm crystal. A range of distributions are given relating to different trigger threshold position on the leading edge between 3-10 % of the photopeak equivalence energy.

6.2.3 Coincidence timing results

For these measurements pulse pairs where both pulses were within the FWHM of the photopeak of the specific detection channel were selected at each step position. For pulse height spectra including 5,000 events this would typically result in a sample of ~ 1100 pulse pairs.

As described in section 6.1.3, a range of leading edge discriminator trigger thresholds were applied to the leading edge and the resulting time stamps used to calculate Δt . In order for trigger thresholds to be easily comparable to equivalent simulation results where additional amplification is not applied, thresholds were set relative to the crossing point of the photopeak energies shown in Figure 6.8a, in the range 3-10 %. Values of Δt measured at each threshold were histogrammed with 100 ps bins, equivalent to the 10 GS/s sample rate of the oscilloscope. The final distributions were fitted with Gaussian distributions and the standard deviation scaled to give the FWHM. The uncertainty on the FWHM was assumed as the propagation of the statistical uncertainty with a measure of the non-Gaussian tails. As described previously, the tail contribution was estimated as the range of FWHM values found by re-fitting the distributions in steps of $\sigma/2$ between the 3σ and 6σ limits. The results of this measurement are presented in Figure 6.9.

The distribution shows optimum CTR at interaction positions around the centre of the crystal, degrading as the interaction approaches either of the two crystal ends. In agree-

ment with the results shown in Figure 6.4, the timing resolution degrades as the trigger threshold on the leading edge increases. The optimum CTR for this system was measured as 690 ± 10 ps, approximately factor of two degradation on the 320 ± 5 ps measured in the coincident system presented in section 6.1.3. A number of factors can be considered which contribute to this effect. The reduced photon flux resulting from the mismatched crystal cross section and SiPM active area has two separate considerations in that it both significantly reduced photon detection statistics and is non-selective of the time distribution of detected photons. A similar reduction in CTR is presented in simulation studies given in Chapter 8 by applying mis-matched geometries as here. The reduced sample rate of the oscilloscope available for this measurement is also a factor, increasing the bin width, and therefore resolution, of the Δt histogram from 25 ps to 100 ps.

Chapter 7

Implementation of coupled LYSO and SiPM detector system into a GEANT4 simulation

This chapter describes the implementation of a GEANT4 simulation which models the characteristic timing response of a coupled SiPM and LYSO detector system. Similar models have been previously developed, documented in the literature, which reproduce the response of SiPM devices including detailed considerations of a number of noise effects [120] [121] [122] [123]. This work builds on existing results to construct a Monte-Carlo simulation that, based on concrete approximations, is applicable to a specific experimental environment as will be discussed in the chapters which follow. GEANT4 has been selected as the simulation environment of choice due to its scalability [124] [125] [126], and extensively validated in-built physics models [127] [128].

The chapter is split into three main sections. First the theoretical timing considerations which must be reproduced by the final simulation are defined. Secondly, an overview of the GEANT4 environment is given, followed by details of the specific models applied for here. Finally a description of the SiPM response simulation is given.

7.1 Some considerations on timing

The timing precision of a PET detector consisting of a LYSO scintillating crystal directly coupled to a SiPM is defined by a number of uncertainties. These uncertainties derive

from both the characteristic optical photon flux produced by the LYSO crystal and the SiPMs response to that flux. Most of these contributions have been introduced previously but are presented again here for clarity and narrative. The sum in quadrature of each individual contribution gives the total timing uncertainty of the detector:

$$\sigma_{Det} = \sqrt{(\sigma_{Stats}^2 + \sigma_{Trans}^2 + \sigma_{\gamma}^2 + \sigma_{Jitter}^2 + \sigma_{Signal}^2)}, \quad (7.1.1)$$

where the individual components are defined and discussed in detail below.

- σ_{Stats} . The ultimate limiting factor in the CTR of a PET detector system is the *photoelectron statistics*, which have been previously discussed in Chapter 3. A number of works have been produced which describe the single photon variance effects in detail [52] [53] [129] [113], along with additional investigations into the possible gains in CTR if a sample of the total registered photons were instead considered [60]. As a result, the effect of photon detection statistics on the system timing uncertainty is well understood.
- σ_{Trans} . After emission, scintillation photons must propagate through the crystal enroute to detection. The timing uncertainty associated with this process is indicated here as the *photon transport*, or propagation time. A basic estimation of the contribution of the photon transport was given in Chapter 3, where perfect flat surfaces were assumed at the crystal boundaries. This assumption, although useful for a preliminary estimate, is unrealistic in practice as some non-uniformities are bound to have developed both during and after manufacturing. Additionally, the introduction of a reflective coating adds a further effect to account for as photons are reflected back into the system in cases where they would be lost in the ideal case with consequent impact on timing.
- σ_{γ} . The *Gamma transit time spread* derives from the variance of the gamma conversion position in the crystal. A diagram of a standard coincident PET detector system's geometric configuration can be seen in Figure 7.1. Due to the different values of the refractive index of LYSO at gamma and optical photon energies ($n_{LYSO}(E_{\gamma}=511 \text{ keV}) \simeq 1$, $n_{LYSO}(E_{\gamma}=2.8 \text{ keV}) = 1.81$), gamma photons propagate through the crystal at higher speeds. Gamma conversion close to the detector will therefore yield a shorter total transit time than a conversion at the entrance of the crystal. This is a small contribution to the total σ_{Det} and has been estimated

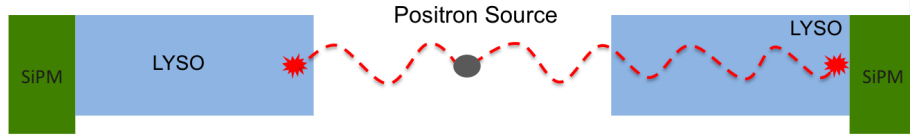


Figure 7.1: Diagram of a coincident detector elements.

as < 10 ps for 15 mm long crystals [65]. Such an effect is accounted for by the electromagnetic and optical physics models available in GEANT4 which consider the refractive index in the propagation velocity of both optical and ‘high energy’ photons.

- σ_{Jitter} . Once a photoelectron has been created in a SiPM pixel, an avalanche develops and a current is induced and seen at the detector’s output pins. A timing uncertainty is then induced in this process from the time spread between e-h hole generation and detected signal at the device output. The value of σ_{Jitter} was measured for the Hamamatsu S10362-33-050C device in Chapter 5 and is applied here to the simulated single pixel response with known uncertainty.
- σ_{Signal} . The *electronic signal jitter* has been introduced previously and can be considered a description of how well any point on the system’s electrical response is defined in time. This uncertainty derives from the electrical noise induced random fluctuation of the response signal about the underlying signal shape. It is defined as:

$$\sigma_{\text{Signal}} = \frac{\sigma_{\text{noise}}^{\text{rms}}}{\frac{dV}{dt} |_{V_T}}, \quad (7.1.2)$$

where $\sigma_{\text{noise}}^{\text{rms}}$ is the root-mean-square of the electronic pedestal (or baseline) noise and $\frac{dV}{dt} |_{V_T}$ is the gradient of the rising edge at a given threshold voltage (V_T). This is a complex parameter as the simulated signal shape, and therefore the gradient at any given point, is dependent on the accurate modelling of both the photon flux arriving at the SiPM surface and the response of the SiPM to this flux. The accuracy of the photon flux is defined by σ_{Stats} , σ_{Trans} and σ_{γ} as described above. The SiPM response depends then on a number of parameters relating to the single pixel response including: PDE, rise time, fall time, gain, dead time and σ_{Jitter} . A full description of both the SiPM and LYSO simulations is given in sections 7.3 and 7.2.5. The second parameter in this equation, $\sigma_{\text{noise}}^{\text{rms}}$, is however well known, measured directly from the response of the coincident detection system presented in Chapter 6.

In a coincident system, the response of both systems used in coincidence must be considered. As such the CTR of a coincident pair of SiPM and LYSO detector systems is given by:

$$\sigma_{Coinc} = \sqrt{2}\sigma_{Det}, \quad (7.1.3)$$

where σ_{Det} is the same as in equation 7.1.1.

7.2 GEANT4

The simulation framework chosen to reproduce the detector systems response is the general purpose, Monte Carlo particle transport toolkit GEANT4 [130] [126]. GEANT4 has applications in particle detection simulation ranging from astrophysics [131] [132] and particle physics [133] [134] [128], to Medical Physics [135] [136] [124]. The object-oriented nature of the framework provides a flexible environment where it is possible to develop 3-D detector geometries, modelling the interaction of traversing particles with constituent atoms in a user-definable range of media. Specific class structures are available to record characteristics of particle interactions with the implemented geometric system, such as energy loss, local or global positioning and time stamps.

For the work described here, the GEANT4 framework is used to model the source emission of collinear 511 keV photons, the interaction of those photons with LYSO crystals, and the subsequent scintillation response to such an event. The paths of all scintillation photons are traced through the detector geometry and the time and position of any photon interactions with the active surface of a SiPM are recorded. Results are processed by a plug-in class, designed from scratch to model the response of a Hamamatsu S10362-33-050C SiPM, which was selected for application in a prototype TOF-PET detector system in Chapter 5.

7.2.1 General properties of GEANT4

The geometry through which particles propagate in GEANT4 is defined within the *DetectorConstruction* class by placing geometric primitives, such as boxes or cylinders, inside an initial ‘world’ volume, which defines the boundaries of the simulated environment. Each volume placed within the ‘world’ is passed material information describing characteristics,

including chemical formula, density and refractive index. By placing multiple volumes, full detector systems can be described.

The specific interaction processes which particles transiting through the user constructed geometric arrangement can undergo are controlled by the *PhysicsList*. Any physics which the user wishes to consider in the simulation must be called explicitly by the *PhysicsList*. This approach allows for multiple models of an interaction to exist within GEANT4, which can be easily replaced in the user code depending on the desired application. The specific GEANT4 physics models applied to this work are described in the sections which follow.

The probabilities of particle interactions with the implemented environment are calculated in terms of ‘steps’. A ‘step’ is a discrete path length which the simulation uses to propagate particles through the simulated geometry. After each step the probabilities of particle interactions are evaluated and, if an interaction has occurred, the particle properties are modified accordingly. The step size applied in the simulations presented here was the system recommended $50 \mu\text{m}$. The smaller the step size, the more evaluations the simulation will attempt per unit length. A balance must therefore be struck between the uncertainty on the interaction position and computation time.

Although the majority of interactions are considered as discrete (and therefore are evaluated in terms of steps), some interactions are classified as ‘continuous’. These processes continuously modify the particle’s energy and are handled separately so as to avoid them imposing considerable slow downs on the computation time. Of those processes applied in this work, only the inelastic scattering of electrons is modelled as continuous.

7.2.2 Detector construction and materials

As discussed above, both the detector system geometry and the associated material definitions are implemented within the *DetectorConstruction* class. In the simulation of a coupled LYSO-SiPM detection system, the geometry directly impacts the σ_{trans} , as it influences the range of optical photon paths available to detected photons. The more exact the real measures and material compositions applied to volumes, the more precisely σ_{trans} will be modelled.

A schematic diagram showing the side view of a simulated detector geometry is given in Figure 7.2. From left to right the Figure shows a LYSO crystal, covered on five of six faces

with 400 μm thick layer of TiO_2 paint. A 100 μm layer of optical grease is assumed between the open face of the LYSO crystal and the SiPM. The SiPM is itself characterised by three separate layers, each implemented according to data sheet dimensions [77], including: a 300 μm thick protective epoxy window, a 100 μm sensitive silicon layer and an outer silicon casing. Any number of identical detector systems may be placed within the ‘world’ volume, which was filled with air to mimic an experimental laboratory environment.

The elementary properties of each material used in the detector geometry are given, with references, in Table 7.1. It is noted that the density and chemical composition of the epoxy and optical grease layers are approximate. The effect of this approximation is negligible on the systems energy and timing response as these parameters do not influence the propagation of scintillation light, which only considers the refractive index.

Table 7.1: Properties of materials used in the simulation.

Material	Chemical composition	Density [g/cm ³]	Refractive index @ 420 nm	Reference
Air	$\text{N}_{0.76} \text{O}_{0.23} \text{Ar}_{0.01}$	1.29×10^{-3}	1.00	[137]
Silicon	Si_1	2.33	3.50	[137]
Epoxy	$\text{C}_1\text{H}_1\text{O}_1$	1.00	1.49	a
Optical Grease	$\text{C}_1\text{H}_1\text{O}_1$	1.00	1.6	a
LYSO	$\text{Lu}_{1.8}\text{Y}_{0.2}\text{SiO}_5$	7.1	1.81	[61]
Paint	TiO_2	1.00	1.61	[138]

^a Refractive index provided by the manufacturer.

7.2.3 Primary generator action

The *PrimaryGeneratorAction* class creates the initial particles at the beginning of each event. For the simulations described here a point source was defined equidistant between the two coincident detector elements. Collinear 511 keV photons were emitted isotropically from the source, with a global time delay of 10 ns. The delay was implemented to give a distinct region with no signal in the SiPMs response, allowing for comparison of the experimental and simulated baseline noise. The non-collinearity of photons described in Chapter 2 is not included as the focus of this work is to investigate the detector systems energy and timing response. Reconstruction studies have not been performed so this effect



Figure 7.2: Schematic diagram showing the simulated geometry of a coupled LYSO and SiPM PET detector system. The diagram is not to scale.

cannot influence results.

7.2.4 Electromagnetic physics

The PhysicsList for the simulations presented in this work makes use of the standard electromagnetic processes of GEANT4 version 10.0, specifically the: `G4PhotoElectricEffect`, `G4ComptonScattering`, `G4eMultipleScattering` and `G4eIonisation` processes [127] [130]. In the context of the detector system simulation, the former two processes determine the interaction of 511 keV photons with LYSO crystals. The latter two processes model the elastic (`G4eMultipleScattering`) and inelastic (`G4eIonisation`) scattering of electrons generated as a result of gamma interaction in the crystals.

Each of these models have been rigorously validated against experimental measurements to insure their accuracy [139] [140] [141] and require no input from the user other than inclusion in the physics list.

7.2.5 LYSO simulation and optical models

The optical physics processes included in the PhysicsList manage both the scintillation model and the propagation of optical photons through the detector system. These two processes are key to reproducing both the σ_{Stats} and σ_{trans} contributions, additionally influencing the σ_{signal} as the gradient of the leading edge is directly correlated with the temporal distribution of the detected photon flux. For this purpose the `G4OpScintillation`, `G4OpBoundaryProcess` and `G4OpRayleigh` optical physics processes were applied to model

scintillation, the reflections of optical photons at boundaries between media and the Rayleigh scattering process respectively.

Scintillation

In the case of scintillating materials a number of additional property inputs are required at the material definition stage, including: scintillation yield, resolution scale, rise time, fall time, absorption length, scattering length, and a emission spectrum. A full list of the parameter set used to define the response of a LYSO is given in Table 7.2.

It was discussed in Chapter 3 that the conversion of ionising radiation to scintillation light can be quantified by the scintillation efficiency. In GEANT4 the efficiency is characterised by the *scintillation yield* (\bar{Y} [photons/keV]), set with a unit-less *resolution scale* (α) which describes the Gaussian distributed fluctuations on the number of photons generated in an event. The resolution scale can be used to describe the combined effects of statistical and systematic contributions to the photon generation in a scintillating material. The average number of photons emitted is:

$$\bar{n}_{ph} = E_{\gamma} \bar{Y}, \quad (7.2.1)$$

where E_{γ} is the energy deposited in the crystal by an incident high energy photon. The variance on \bar{n}_{ph} is then given by $\text{var}(\bar{n}_{ph}) = \alpha^2 \bar{n}_{ph}$. The resolution scale α is a constant describing the degradation of energy resolution. The value of alpha for a given energy resolution ($\Delta E/E$) is given by:

$$\alpha = \frac{\sqrt{\bar{n}_{ph}}}{2.35} \frac{\Delta E}{E}. \quad (7.2.2)$$

In order to reproduce the 8 % energy resolution of LYSO at an energy of 511 keV (see Table 7.2), the resolution scale was set to $\alpha = 4.31$.

The rise and fall times which characterise the time profile of a scintillation event each require a single input parameter¹ as given in Table 7.2. The emission spectrum is more complex, set with a look-up table containing a user-defined number of input values. The wavelength of scintillation emissions is then empirically sampled from within this table.

¹By default the scintillation rise time is not considered by the simulation and, in addition to the material definition, must be activated explicitly with a boolean value within the PhysicsList.

In this work a Poisson like distribution was applied, peaking at 420 nm, to mimic the emission distribution given by Saint-Gobain [61].

After emission, scintillation photons must propagate through the crystal where interactions are split into two categories:

- interaction with bulk materials;
- interactions at optical interfaces.

The former describes the absorption or elastic scatter of photons through interactions with a physical medium. Absorption simply removes the particle track and any influence it has on the surrounding media from the simulated environment. Elastic scatter diverts optical photons from their original path by applying Rayleigh scatter [127] equations. The probability of interaction through either of these processes is set by a user defined interaction length. The scatter length is included in Table 7.2. Based on an approximation presented by [142], it is assumed that the contribution of absorption is negligible due to the Stokes shift which separates LYSOs absorption and emission spectra. As such, the absorption length has not been defined as it is considered to be infinite by the simulation.

Table 7.2: List of characteristic parameters of LYSO scintillation response, including the Rayleigh scattering length and the reflectivity of the TiO₂ painted covering.

Material	Parameter	Value	Reference
LYSO	Light Yield	32 ph/keV	[61]
	Fall time	41 ns	[61]
	Peak emission wavelength	420 nm	[61]
	Energy resolution	8 %	[61]
	Rise time	0.09 ns	[54]
	Scattering length @ 420 nm	55 cm	[143]
TiO ₂	Reflection coeff.	0.95	[144]

Optical interfaces

In order to fully consider the systematic effects related to the optical transport (σ_{Trans}) in the crystal, surface treatments were included at the optical interfaces between media, provided by the UNIFIED model of GEANT4 [145]. Generally in GEANT4, surfaces are

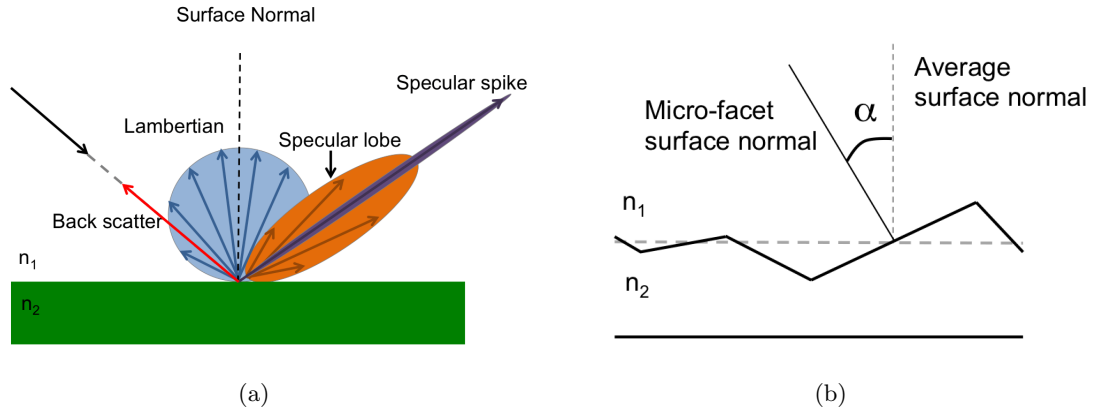


Figure 7.3: Diagrams outlining (a) The four reflection types which can be assigned probability weightings in the UNIFIED model (b) The micro-facet distribution which produce a Gaussian distributed range of reflections with respect to the average surface normal.

defined as either *dielectric-dielectric* or *dielectric-metal*. In the case of a *dielectric-metal* an impinging photon can only be absorbed or reflected by the metal. If the photon is absorbed it is considered detected and characteristics of the interaction are recorded. Conversely, at a *dielectric-dielectric* interface the photon can undergo total internal reflection, refraction or Fresnel reflection. The UNIFIED model allows access to a range of surface effects to describe dielectric-dielectric surfaces based on either a *polished* or a *ground* finish.

In the case of a polished finish, all reflections will be specular (i.e. the angle of incidence is equal to the angle of reflection), assuming a perfectly flat surface. This is the system default for when no surface is specified by the user. Alternatively, a ground surface can be set with user defined probability weightings for four individual types of reflection: *specular spike*, *specular lobe*, *Lambertian* and *back scatter*, see Figure 7.3a.

- *Specular spike* describes a specular reflector on a perfectly flat surface.
- *Specular lobe* is a case of specular type reflection in which the reflective surface is not perfectly smooth but contains micro-facets characterised by a Gaussian distribution of angles (α) about the surface normal, see Figure 7.3b. The standard deviation of this distribution (σ_α) can be defined by the user.
- *Lambertian reflection* is diffuse and results in a cosine probability distribution about the average surface normal, as shown in Figure 7.3b.
- *Backscatter* describes the specific case when the incident photon is reflected back along its incident path.

A further level of detail can be added to polished or ground surfaces by considering the

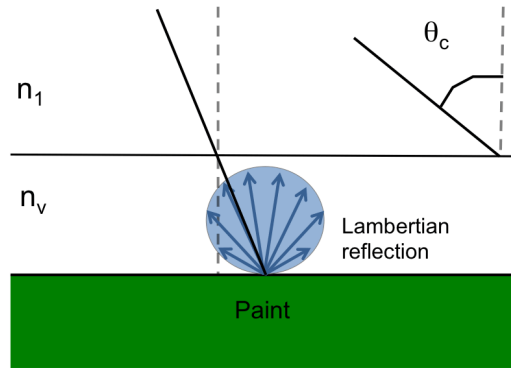


Figure 7.4: Diagram showing ground back painted surface type.

surface as either *front painted* or *back painted*. A front painted surface will not allow refraction from one media to the next, limiting photon interactions to reflection or absorption at the optical boundary. A *polished front painted* surface will consider only specular reflection at the boundary. Similarly, a *ground front painted* surface will consider only lambertian reflections, removing the need for user defined probability weightings of the four reflection types. In both cases the reflectivity of the paint layer is defined by a coefficient in the range 0-1 which must be set by the user.

Back painted surfaces are a complex surface description which are defined with material properties of their own, used to describe a virtual medium between the photon propagation media and the paint, illustrated as n_v in Figure 7.4. This type is useful for modelling higher order effects of painted surfaces as it allows for both user defined reflection type and a surface roughness (σ_α) to be applied at the n_1 - n_v interface. If a photon is refracted through into the n_v medium, it will go on to interact with the paint (or reflector) layer where, similarly to front painted surfaces, the photon is either reflected or absorbed. In the case of a *polished back painted* surface, reflections off the paint layer are specular assuming a perfectly flat surface. In the case of *ground back painted* reflections of the paint are lambertian, see Figure 7.4. Again, in both cases the reflectivity of the paint layer is defined by a coefficient in the range 0-1 which must be set by the user.

A ground back painted surface was used to define the LYSO-paint interface shown in Figure 7.2. The refractive index of the n_v layer was set to 1.61, equivalent to the refractive index of TiO_2 paint given in Table 7.2 and the reflectivity of the paint layer was set to 0.95. A value for the angular distribution of the micro-facets was not available from the crystal manufacturer (Saint-Gobain) and so was set as $\sigma_{\alpha} = 1.3^\circ$, equivalent to the

distribution measured from the surface of a polished BGO crystal by [144].

The only other surface specifically defined was at the epoxy-active surface interface (see Figure 7.2) which was set to dielectric-metal. For this surface type only reflection or detection may occur with probabilities P_{ref} and P_{det} respectively. The probabilities of both parameters can be set by the user with the constraint $P_{ref} + P_{det} \leq 1$. In this simulation $P_{ref} = 0$ and $P_{det} = 0.48$, equivalent to the detection efficiency of the Hamamatsu S10362-33-050C device to 420 nm wavelengths [77]. As a result any photon track which was incident on this surface was simulated no further, independent of detection.

All other optical interfaces shown in Figure 7.2 were set to the default dielectric-dielectric polished type.

7.3 SiPM device simulation

In order to emulate the response of a SiPM device, the pixellated nature of the device must be considered. As discussed in depth in Chapter 4, the combination of high gains and photon counting capability exhibited by the SiPM is achieved through segmentation of the active area into pixels. The number of detected photons and their temporal spread can hence be determined from the number of pixels where an avalanche breakdown occurred, and the shape of the resulting electronic pulse summed from all activated pixels. Besides the photon detection there are a number of other parameters which affect an SiPMs response:

- **Gain.** The gain of a SiPM determines the charge produced in an avalanche event and hence the signal amplitude. The gain depends linearly on the potential difference applied across the device and therefore the static electric field strength through the p-n junction. The value of the single-pixel gain used in this simulation (see Table 7.3) was the data sheet value. The uncertainty on the gain quoted in Table 7.3 defines the gain swing for a temperature change of $\pm 1^\circ\text{C}$.
- **Photon Detection Efficiency (PDE).** A fundamental property of any photodetector device is the PDE. This, as the parameter with the single largest influence on the photon counting resolution, has a significant effect also on the final CTR. A smaller value of PDE will make the probability of detecting the first few photons within the σ_{Stat} statistical distribution smaller, increasing the uncertainty on the signal turn-on. The PDE assumed in this work is the data sheet value as given by

Hamamatsu.

- **Dynamic Range and Pixel Recovery.** The finite number of pixels available to a SiPM intrinsically limits the operational range. Saturation effects can therefore be observed whereby the number of photons in the activating signal is underestimated by the number of avalanche breakdown events. A SiPMs response to an infinitely narrow light pulse can then be described using equation 4.4.8 from Chapter 4. In the case of a SiPM response to a temporally distributed flux, as in scintillator applications, the pixel recovery time can also significantly influence the device response. During an avalanche process, the bias voltage across the p-n junction drops to the characteristic break-down voltage, recovering to the nominal operating voltage at a rate of τ_{fall} :

$$V_{over}(t) = V_{over}(0) \cdot (1 - e^{-t/\tau_{fall}}), \quad (7.3.1)$$

where τ_{fall} is the device fall time as measured in Chapter 5. This process therefore defines how long it takes for the pixel to return to ideal operating conditions, during which time it shows reduced sensitivity to an activating photon flux. In this simulation it is assumed that the single pixel dead time is equivalent to the value as measured by [146]. During dead time the pixel is completely insensitive to any external photon flux. Saturation effects will have little effect on the CTR of the system when measured with a thresholding technique as the early photon detections will not be affected by the saturation effects. However it is possible that a reduced energy resolution caused through pulse height saturation may result in the CTR being overestimated.

- **Cross Talk and After Pulsing.** For each triggered avalanche, there is a finite probability that the process will generate further avalanches through either cross-talk or after-pulse effects, previously discussed in Chapter 4. For $50 \mu\text{m}^2$ Hamamatsu devices, cross-talk has been measured to occur in 4% of pixel activations [147]. After-pulsing is observed in terms of fast τ_{fast} and slow τ_{slow} emission components, both of which have been measured to occur in approximately 13% of pixel activations [93] [109]. However, unlike cross-talk events, the gain distribution of avalanches triggered by after-pulsing is correlated to the state of recharge (given by equation 7.3.1) of the previously activated pixel. Since both cross-talk and after-pulsing events are triggered by avalanche breakdown, they are often referred to as *correlated noise*.

The PDE value as quoted Hamamatsu, and applied to this simulation, is not corrected for correlated noise contributions. However the time window over which the gain was calculated has not been made available through communications with Hamamatsu. Therefore it is not straightforward to make educated guesses on what percentage, if any, of the after pulses are included in the data sheet value [77]. The adopted strategy has been to not simulate correlated noise effects specifically, so to avoid overestimating their effects. Uncertainties on the CTR due to this assumption are considered and discussed in detail in Chapter 8.

- **Thermal noise.** Thermal noise in SiPMs is typically described by the rate of thermally activated pixel avalanches. Hamamatsu quote a thermal noise rate of the S10362-33-050C device as 10 Mcps, measured at the 0.5 p.e photon level. Therefore, in a scintillation event lasting typically 200 ns, 2 thermal noise events are expected. This contribution was considered insignificant and has not been included in the simulation presented here.
- **Electronic noise.** The electronic noise of the system was described previously as σ_{noise}^{rms} and is linearly related to the σ_{signal} timing contribution via equation 7.1.2. This value was measured directly from pulses recorded for the coincident detector system experiments described in Chapter 6.

7.3.1 Simulation framework

A full list of the input parameters describing the SiPM simulation response are listed in Table 7.3. In the first simulation step a list of three dimensional vectors providing the (x,y) coordinate as well as the time t, are read in, generated by the scintillation and optical transport models in response to a γ -photon interaction in the crystal. In this case x and y described the spatial hit coordinate on the SiPMs active surface and t the interaction time. Each three-vector therefore describes the space and time co-ordinates of photons which passed the PDE cut when interacting at epoxy-active silicon surface.

Once loaded into the SiPM response code, the (x,y) coordinates at each hit are assigned to $50 \times 50 \mu\text{m}^2$ pixels, and the list of hits for each pixel are sorted in time. A dead time is next applied at each pixel to discard any hits which occurred during the re-charge cycle, when the pixel is assumed to be inactive. The result is a list of timestamps defining each single pixel activation generated in response to a scintillation event. To account for the transit time spread effects on each activation, time stamps were smeared using a Gaussian

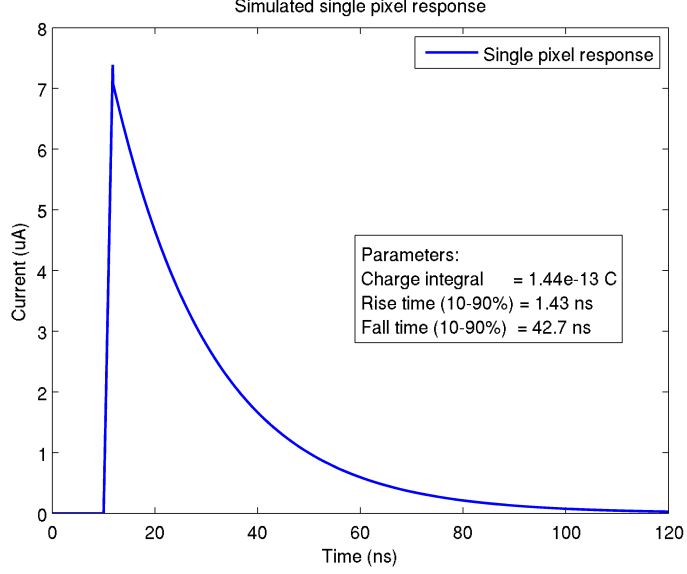


Figure 7.5: A simulated single pixel current response as defined by equation 7.3.2 ($t_a = 10$ ns) and the parameter set given in Table 7.3.

distribution with a FWHM equivalent to $2.35 \cdot \sigma_{Jitter}$. A smeared time stamp was then randomly sampled from within the projected distribution.

Table 7.3: List of characteristic parameters of SiPM response.

Parameter	Value	Unit	Reference
PDE	52 ± 5	%	[77]
Gain	$9 \times 10^5 \pm 3 \times 10^3$	-	[77]
Rise time _{10-90%}	1.43 ± 0.02	ns	see Table 5.2
Fall time _{10-90%}	42.7 ± 0.5	ns	see Table 5.2
Jitter (σ_{Jitter})	33.9 ± 0.4	ns	see Table 5.2
Dead time	50 ± 7	ns	[146]
Electronic noise (σ_{noise}^{rms})	84 ± 5	μA	-
Sample Rate	40	Gs/s	-

A single-pixel response, as defined by the rise time, fall time and gain (see Table 7.3), was produced originating from the calculated smeared time stamps. The shape of this response is mathematically described by a linear rise followed by a single exponential fall, as follows:

$$f(t) = \begin{cases} 0, & t < t_a \\ G \frac{t-t_a}{\delta}, & t_a < t < (t_a + \delta) \\ G e^{-\frac{t-t_a-\delta}{\tau_{fall}}}, & t > (t_a + \delta) \end{cases} \quad (7.3.2)$$

where t_a is the pulse activation time, G a scaling factor used to define the single pixel gain, δ is the time from t_a to the maximum amplitude ($\delta = 1.2 \times \text{rise}_{10-90\%} = 1.71$ ns) and τ_{fall} is the 1/e fall time ($\tau_{fall} = (\ln(0.9) - \ln(0.1)) \text{fall}_{10-90\%} = 19.43$ ns). The resulting pulse shape was scaled so as the integrated charge was equivalent to the charge on a single electron, multiplied by the device gain: $1.6 \times 10^{-19} \text{ C} \times 9 \times 10^5 = 1.44 \times 10^{-13} \text{ C}$. The resulting pulse shape is given in Figure 7.5.

The full device response was formed by sampling each single pixel response at 40 GS/s. The sampled response of each single pixel activation was then summed by recording the values in a histogram with 25 ps bins (equivalent to 40 GS/s). The result is the summed response of all single-pixel activations, mimicking the parallel combination of APD cells in a SiPM device as show in Figure 8.3.

Comparisons of simulated electronic response pulses, produced by the combined GEANT4 and SiPM simulation frameworks described here, and the experimentally measured equivalent are discussed in detail in Chapter 8 which follows.

Chapter 8

Simulation results of a coupled SiPM and LYSO detector system

This chapter characterises the response of the GEANT4 detector simulation model described in Chapter 7, validated against theoretical and experimental results. It has been discussed previously that the limiting contribution to the timing uncertainty of a PET detector system is the photon statistics. As such, validation of the single and bi-exponential photon emission models of the GEANT4 framework are presented first. With confidence in the GEANT4 emission characteristics, initial results of the coincident detector system simulations are presented and discussed. Finally, measurements of the systematic uncertainties associated with CTR of the system are evaluated. Specific parameters which either dominate the systems CTR response, or have been applied with large uncertainties, are identified. The effect of these parameters are measured by varying the parameter values within individually considered limits. By considering the effect of each parameter, a total uncertainty on simulated results is given and comparisons made against experimental results.

8.1 Photon statistics

Theoretical models developed to predict the probability distributions of photon arrival times have been presented previously in Chapter 3, but are additionally included below.

From [52], we can assume the probability that the N^{th} photo-electron is created in a time interval between 0 and t is Poisson-distributed:

$$P_N(t) = \frac{[f(t)]^N e^{-f(t)}}{(N!)}, \quad (8.1.1)$$

where $f(t)$ describes the temporal profile of the characteristic scintillation response. For the single exponential model we then define [53]:

$$f(t) = R \left(1 - e^{-\frac{t}{\tau_{fall}}} \right). \quad (8.1.2)$$

And for the bi-exponential model [55]:

$$f(t) = R \left[1 - \frac{\tau_{rise} + \tau_{fall}}{\tau_{fall}} e^{-\frac{t}{\tau_{fall}}} + \frac{\tau_{rise}}{\tau_{fall}} e^{-t/\frac{\tau_{rise}\tau_{fall}}{\tau_{rise}+\tau_{fall}}} \right]. \quad (8.1.3)$$

In both cases R is the total number of photoelectrons produced at the SiPM in a certain time window (e.g. 200 ns), τ_{rise} and τ_{fall} are the rise time and fall time of the scintillator's characteristic decay.

In order to check the statistical photon emission models of the G4OpScintillation process, simulations were run with input parameters set as Tables 7.2 and 7.3. For these simulations the G4ComptonScattering process was turned off. Gamma-ray photons could therefore only interact via the photoelectric effect. This allowed the mean number of photons associated with photopeak events to be evaluated without correcting for lower energy Compton scatter events. The surface roughness of the LYSO-Paint optical surface was set to $\sigma_\alpha = 1.3^\circ$, equivalent to the distribution of a polished crystal surface as measured by [144]. Time stamps of interacting photon hits at the SiPM active surface were recorded for 5000 independent events. For both coincident detector systems, the average and standard deviation number of photons detected in a photopeak event was $R = 3000 \pm 100$. For the single exponential measurement the SetFiniteRiseTime method of G4OpScintillation was set to false; for the bi-exponential it was set to true.

Comparison of the simulated and theoretical distributions calculated by applying equations 8.1.1, 8.1.2 and 8.1.3 are given in Figure 8.1. The simulation is shown to qualitatively reproduce the single exponential model for a range of photon order statistics when SetFiniteRiseTime is set to false, and likewise the bi-exponential model when set to true. All

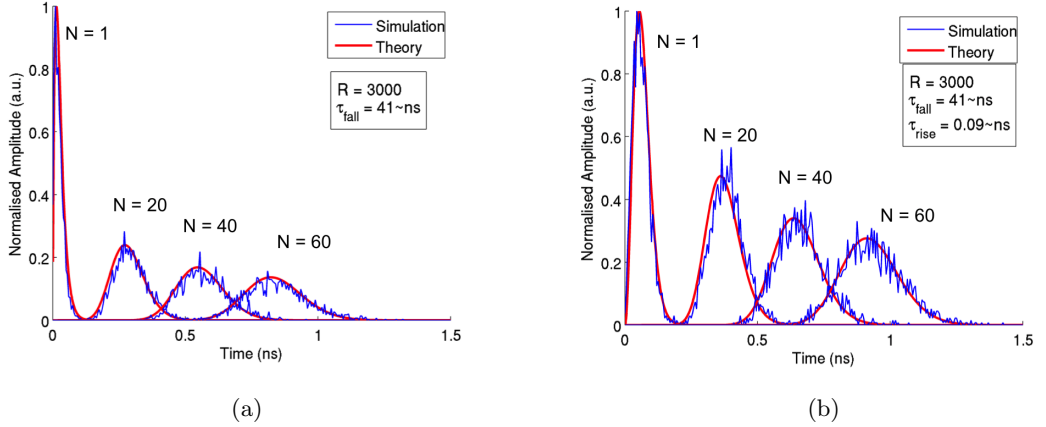


Figure 8.1: Comparative plots of normalised theoretical and simulated photon arrival distributions (a) Single exponential model [53] (b) Bi-exponential model [55]. The parameters applied to the theoretical considerations are quoted on the plots.

simulation results presented in what follows have the SetFiniteRiseTime method set to true in order to consider the more physical bi-exponential model.

8.2 Coincident detector systems

For the coincident detector simulations described in this section, two identical detector systems were placed in the world volume with a spatial separation of 5 cm, see Figure 8.2. As in the photon statistics simulations, only photopeak events are of interest and so the G4ComptonScattering process was turned off, resulting in significantly shorter processing times. A point source was placed at the central position between the two, emitting collinear 511 keV photons isotropically distributed over a spherical surface, but with emission angles restricted to a cone illuminating the detector systems. All response characteristics were applied as in Tables 7.2 and 7.3. The surface roughness of the LYSO-Paint optical surface was set to $\sigma_\alpha = 1.3^\circ$.

Data sets for all measurements presented in this section correspond to 6×10^5 independent γ emission events, yielding approximately 2500 coincident photopeak pulse pairs. For each coincident pair the current response pulses generated by the SiPM simulation were saved to file. It is shown in Figure 7.5 that the simulated single-pixel response is defined in terms of a current response. In order to compare results directly with experimental measurements the simulated current response pulse was scaled by a factor of 25.2, representative of total load resistance of the experimental arrangement to convert the current to a voltage

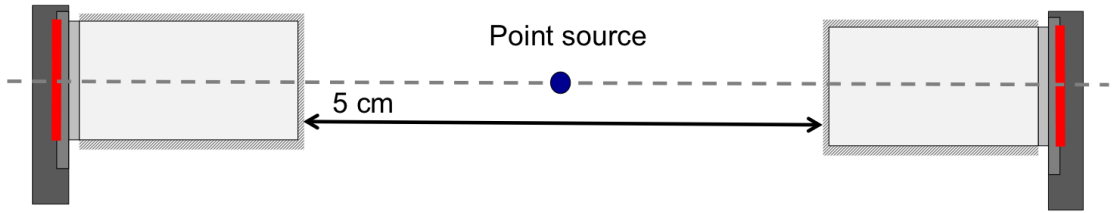


Figure 8.2: Illustration of a coincident detector system about a point source.

response.

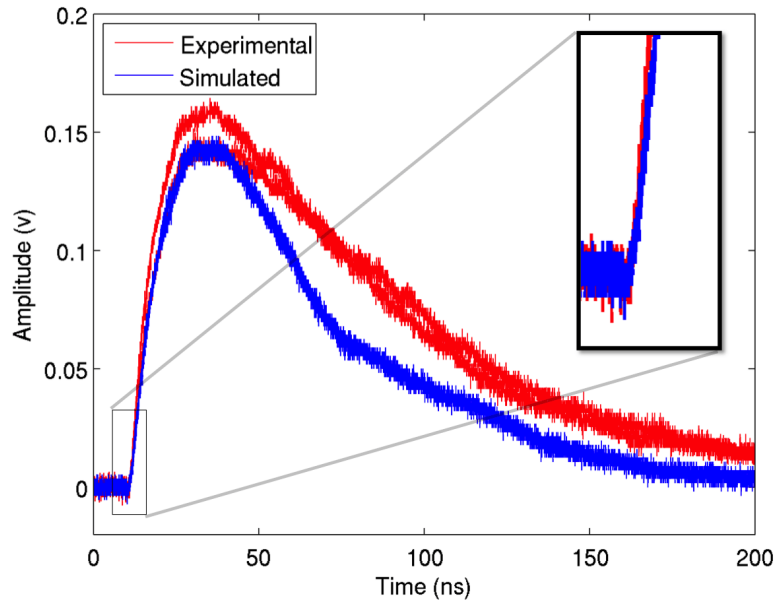
8.2.1 Energy results

Using a method identical to that described in Chapter 6, energy measurements of the simulation response were extracted from a pulse height spectrum formed by filtering the recorded pulses with a second order Butterworth filter, $f_c = 350$ MHz. The maximum amplitude of each filtered pulse was measured and the result passed to a histogram with bin width of 1 mV. The energy resolution was then calculated as described in equation 6.1.1 using the mean and standard deviation as extracted from Gaussian fits to the photopeak. Uncertainties on each of the fit parameters were assumed to be the propagation of the statistical uncertainties and the uncertainty due to non-Gaussian tails. Uncertainties due to non-Gaussian tails on the fitted data set were estimated by varying the limits of the considered photopeak range and re-fitting. This procedure was repeated in steps of $\sigma/2$ for the data set contained between three to six σ of the original fit. The range of the resulting fit parameters was considered as the uncertainty on the fitting routine.

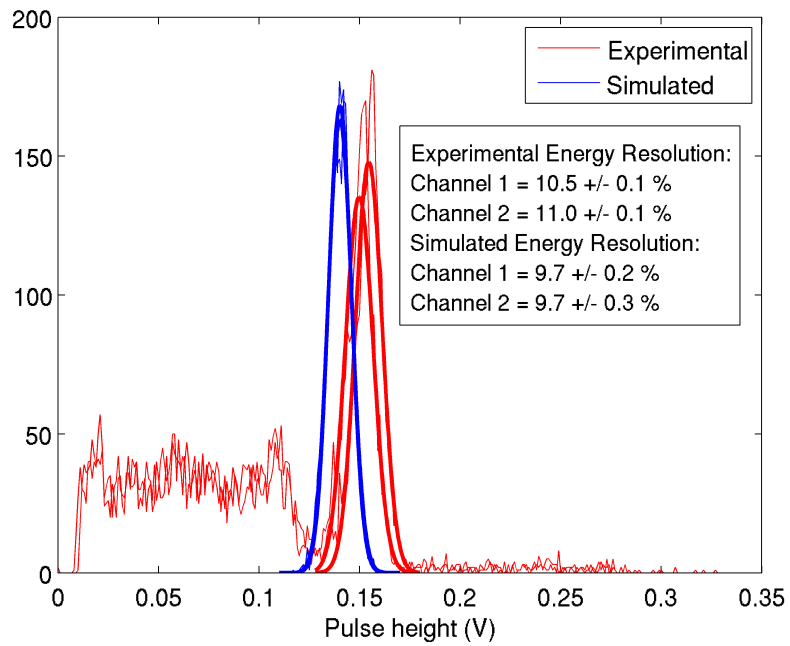
A direct comparison of experimental and simulated electronic pulse pairs are presented in Figure 8.3a with further comparisons of the related photopeak energy results in Figure 8.3b. There are a number of features to note from these distributions.

Firstly, the shape of both simulated and experimentally measured pulses appear comparable in the first few nanoseconds following turn on. This is the signal region which this simulation has specifically been designed to model as it defines the optimum timing performance. Recreating the electronic noise and signal shape in this region equates to matching the σ_{signal} contribution of the systems CTR.

Secondly, the pulse height spectra given in Figure 8.3b shows a reduced photopeak energy and improved energy resolution in the case of the simulated pulses. This effect



(a)



(b)

Figure 8.3: Comparison of example photopulse pairs from simulation and experimental measurements. (a) Example raw, unprocessed experimental and simulated pulse pairs (b) Pulse height spectra as measured from digitally filtered pulse pairs.

can be explained by after-pulse events which are not fully considered by the simulation. As described in Chapter 7, after pulse events have been measured to occur in $\sim 26\%$ of avalanche activations with emission probabilities shared equally between $\tau_{fast} \approx 15 \text{ ns}$ and $\tau_{slow} \approx 80 \text{ ns}$ [93]. As the pulse height is shown to peak approximately 25-30 ns after turn on, it is expected that the signal gain associated with the τ_{fast} emission will contribute to photopeak gain and variation. Due to the gain correlation of after pulses with the associated primary avalanche, and by considering $\tau_{fast} < \tau_{fall} = 19.4 \text{ ns}$, it can be assumed the average gain of a fast emission after pulse event is less than a primary avalanche event. As such the signal gain from these events will be in the range $< 13\%$. The 10% gain offset between simulation and experiment could therefore feasibly be explained by τ_{fast} after pulses.

Finally, differences are observed between the two data sets at the falling edge, where the simulation produces a less than satisfactory approximation. The shape of simulated response pulses is seen to exhibit a two component falling edge either side of approximately 80 ns. This behaviour derives from the 50 ns single pixel dead time which, in combination with the finite size and number of pixels defined within the SiPMs active surface, leads to saturation effects in the device response. At approximately 80 ns one sees the effect from a number of pixels which, having been activated at the beginning of an event, and having since been insensitive to the optical photon flux, are then re-activated. This brings the response closer to a linear regime, thus reducing the gradient of the falling edge. Although S10363-33-050c SiPMs have been shown to saturate when coupled to LYSO crystals, activated with 511 keV γ photons [148], this specific pulse shape behaviour is masked in the experimental measurements by the contribution of the ($\tau_{slow} = 80 \text{ ns}$) after-pulsing events. These events are higher gain than the τ_{fast} events due the gain correlation between the time of the primary avalanche and the initiation of a secondary avalanche. It was calculated previously that $\tau_{fall} = 19.43 \text{ ns}$. It can then be assumed that the approximate relationship $\tau_{slow} \approx 4 \times \tau_{fall}$ is true. As a result the pixels are likely to have completed the re-charge cycle when a τ_{slow} event is initialised. These events can therefore be considered to yield comparable gain characteristics to photon induced activations. In conclusion, a 13% underestimate of the simulated signal gain in approximately 50-150 ns is expected due to τ_{slow} after pulse events which are not included in this simulation model.

8.2.2 Timing results

The CTR of the simulation was measured with the identical method as applied to experimental results in Chapter 6. Only events in which both pulses are within the FWHM of the photopeak were selected for processing. A set of timestamps were recorded for each interesting pulse via leading edge discriminators, applied at incremental steps along the leading edge relative to the mean photopeak pulse height. For each trigger position the time difference (Δt) between each pulse pair was calculated and transferred to a histogram with 25 ps bins (equivalent to the 40 GS/s sample rate of the recorded pulses). The final histograms containing a full sample of Δt values were then fitted with a Gaussian distribution and the FWHM extracted to represent the system CTR. The uncertainty on each FWHM was assumed as the propagation of the statistical uncertainty on the width of the device with the range of values calculated when the fit was re-applied in steps of $\sigma/2$ to the three to six σ range. The process was repeated using: raw, unprocessed pulse pairs, pulse pairs filtered with the 5th order, windowed equiripple filter with $f_c = 500$ MHz and pulses pairs filtered using the 2nd order, Butterworth filter with $f_c = 350$ MHz.

Comparisons of the experimental and simulated CTR are presented in Figure 8.4. The simulation is seen to reproduce all the major features of the three distributions, including the trigger position of the optimum CTR, the divergence of the three distributions below trigger positions of approximately 12%, and linear behaviour of the three distributions at trigger positions above 12%. A feature of note in these two distributions is the abrupt increases in CTR measured in the Raw and Equiripple pulse distributions. This effect derives from the electronic noise (σ_{noise}^{rms}) which has not been fully removed from these distributions. As the threshold approaches the noise floor, there is an increased probability that the noise will cross the threshold, resulting in a time stamp which does not correlate with the detector activation. As a result, the timing distributions are no longer correlated to a detector activation and the timing resolution diverges. This is a limitation of thresholding techniques which must be considered if an accurate measurement is to be made. At the 1% and 2% thresholds, the CTR is seen to improve in both experimental and simulated distributions. This is a *noise saturation* effect where the threshold is so low that only the noise is visible. The timing resolution measured in this case is then correlated only to the σ_{noise}^{rms} distribution.

Finally, one must recall that the purpose of this simulation is to reproduce the timing performance of a coupled LYSO and SiPM detector system. The CTR of the simulated and

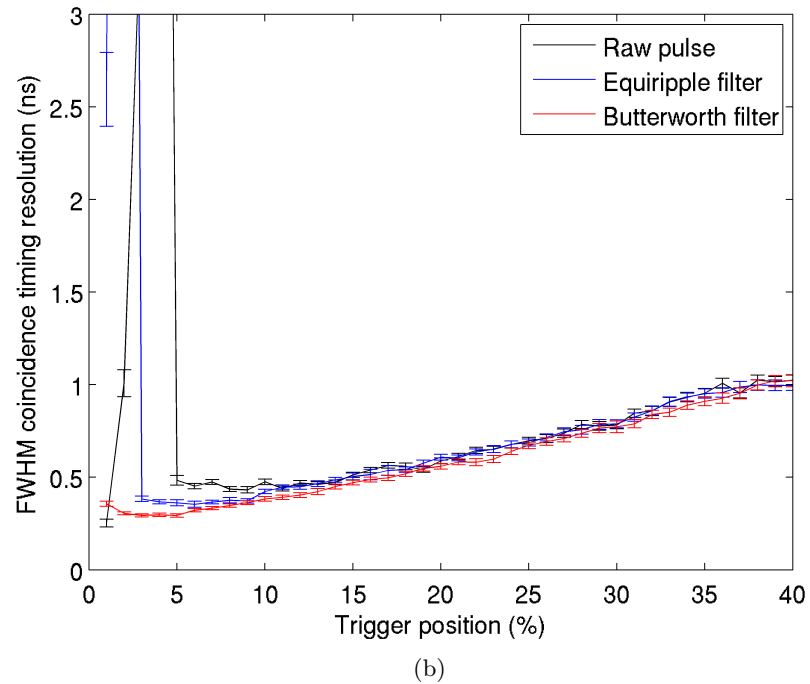
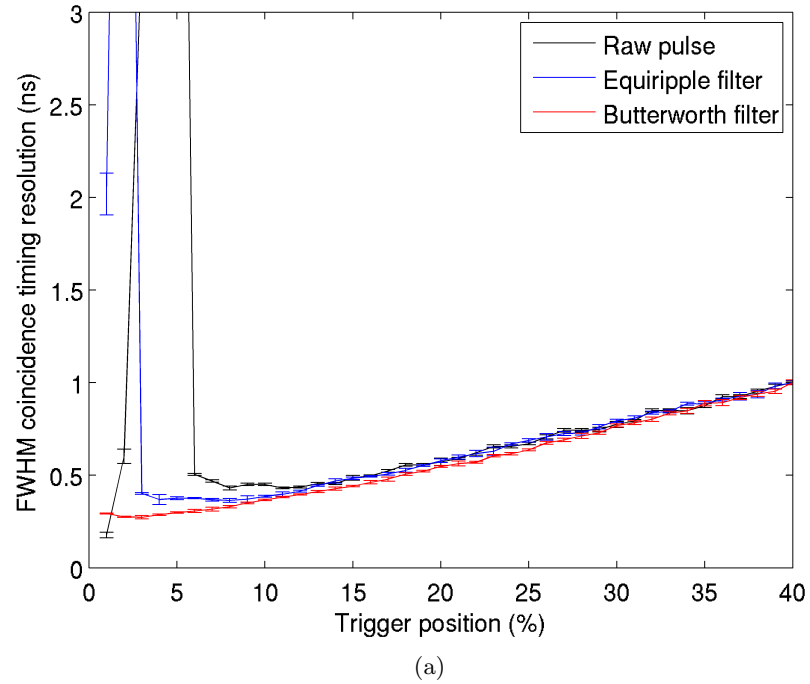


Figure 8.4: Timing resolution as a function of leading edge discriminator position for a coincident system of $3 \times 3 \times 5$ mm LYSO crystals, painted with a reflective TiO_2 paint and read out by Hamamatsu S10362-33-050C SiPMs. The three colour distributions define the processing techniques applied to the recorded pulses before triggers were applied. (a) Simulated system response (b) Experimentally measured system response.

experimental data sets, as measured at a 3% trigger position of the Butterworth filtered data-sets, were calculated as: $\text{CTR}_{Exp} = 290 \pm 10$ ps, $\text{CTR}_{Sim} = 270 \pm 10$ ps, equivalent to within 1.4 error bars. It should be noted here again that the quoted simulation uncertainty does not include systematic effects, which are evaluated in what follows, increasing the total uncertainty. Moreover, the simulation is also shown to recreate all of the features observed in the experimental results, including the correlation of the trigger position and the CTR over a range of 40% of the total pulse height.

The combination of the well reproduced CTR features and the gain characteristics described by the energy and pulse shape comparisons suggests that the 52% Hamamatsu quoted PDE is a good approximation of the system response, including photon activations and cross talk effects, but excluding after pulses. The systematic uncertainties deriving from this approximation and others are detailed below.

8.3 Systematic uncertainties on the timing response

This section presents measurements of systematic contributions to the system CTR introduced through uncertainties on the simulation input parameters. A number of parameters have not been explicitly considered here due to the well defined uncertainties with which they are either quoted in literature, or have been measured experimentally as part of the work presented in Chapter 5. This group includes: the rise time, fall time, gain and jitter as defined in Table 7.3 and the rise time, fall time, energy resolution, scintillation yield and TiO_2 paint reflectivity as given in Table 7.2. The parameters which require further investigation, are: the single pixel dead time, the PDE and the surface roughness of the LYSO crystal. For the measurements described in this section all of energy and timing results were acquired using identical methods to those described in section 8.2.

8.3.1 Dead time

The dead time of individual GM-APD cells is quoted with a 15% uncertainty (Table 7.3) and this was therefore identified as a notable source of uncertainty. By reducing the dead time of the individual pixels, reactivation of pixels by the photon flux becomes more probable. As a result, the contribution of τ_{slow} after-pulses to the total signal gain will be reduced as secondary pixel activations are more likely to occur through photon activation. For these measurements the dead time was varied in the $\pm 3\sigma$ range around the nominal

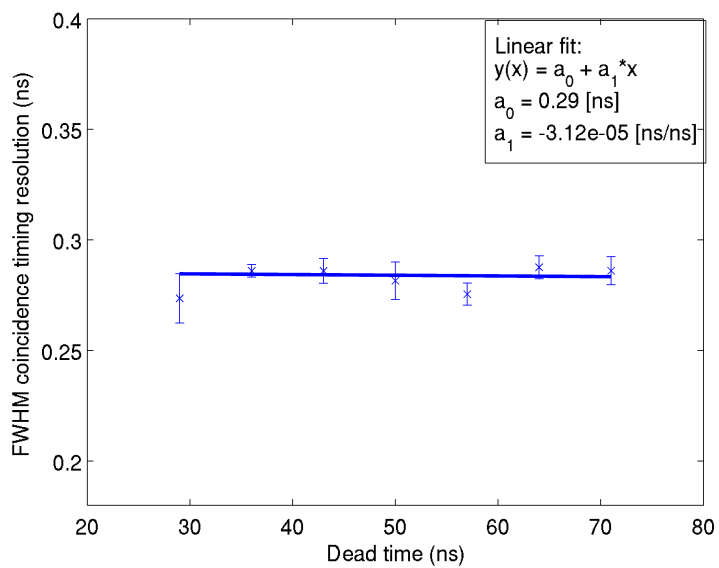
value of 50 ns.

The energy and CTR results for a range of dead time inputs, measured using identical methods to those described in section 8.2, are given in Figure 8.5. Results show negligible effects on the system CRT and energy resolution in the $\pm 3\sigma$ range. This is expected as the dead times in the range 30-70 ns, as applied here, will only affect the shape of the falling edge of the pulse. This is shown explicitly in Figure 8.6 where simulated photopeak pulses have been plotted with some representative values of dead time for comparison. It is shown that the rising edge and maximum pulse height, where the energy and timing measurements are made, are equivalent. The effects of varying this parameter only become visible on the falling edge. It is shown that as the dead time decreases, more pixels are available to fire a second time, increasing the gain of the falling edge.

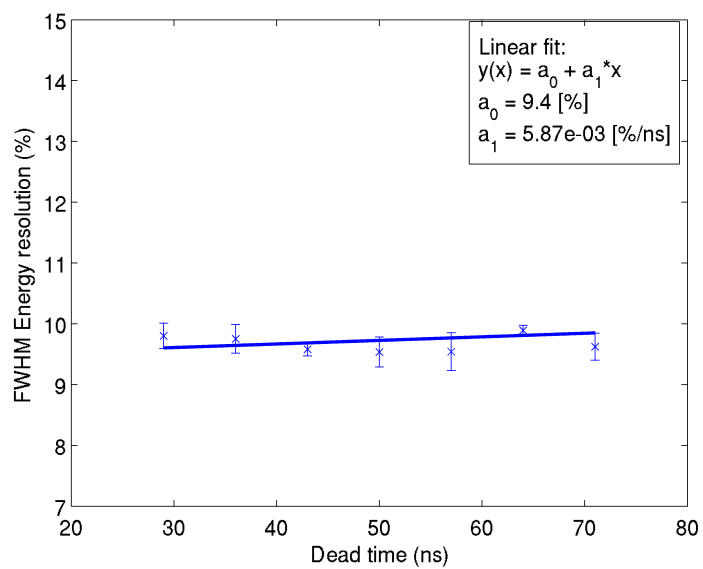
8.3.2 Photon detection efficiency

An uncertainty on the quoted PDE is not available from Hamamatsu and so cannot be applied directly here. However it has been discussed already that Hamamatsu quote data sheet values for the PDE which include the effects from all correlated noise. In this case, by applying the nominal value without properly modelling correlated noise events, the simulation is bound to underestimate the temporal spread of pixel activations. In order to characterise any effect of PDE on the resulting system CTR, the correlation of these two parameters must first be understood.

Again energy and timing results have been measured by applying the techniques described in section 8.2. In this case the PDE has been varied in steps of 5% to show a total spread of $\pm 15\%$ relative to the value quoted by Hamamatsu. Results of the system CTR and the energy resolution as a function of PDE are then given in Figure 8.7. Both the CTR and energy resolution show a clear linear dependence on PDE. The correlation of both parameters can be predicted due to the increased probability that a higher number of pixels will be activated in a given event. In the case of the timing resolution this means that a higher proportion of the early photon flux is detected, these photons arrive with narrower probability density distributions (see Figure 8.1b) and so provide a reduced contribution to the total system timing resolution. In the case of the energy resolution, an increased PDE equates to an increased number of pixels firing and hence an increase in pulse height. The resolution on these pulses is intrinsically improved due to the statistical gains from activating a higher number of cells.



(a)



(b)

Figure 8.5: Selected simulation response parameters plotted as a function of single pixel dead time (a) Coincidence timing resolution (b) Energy resolution.

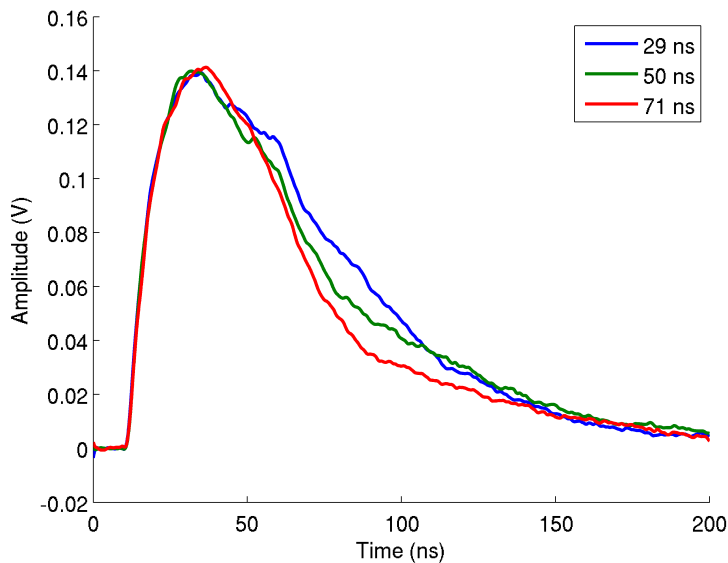
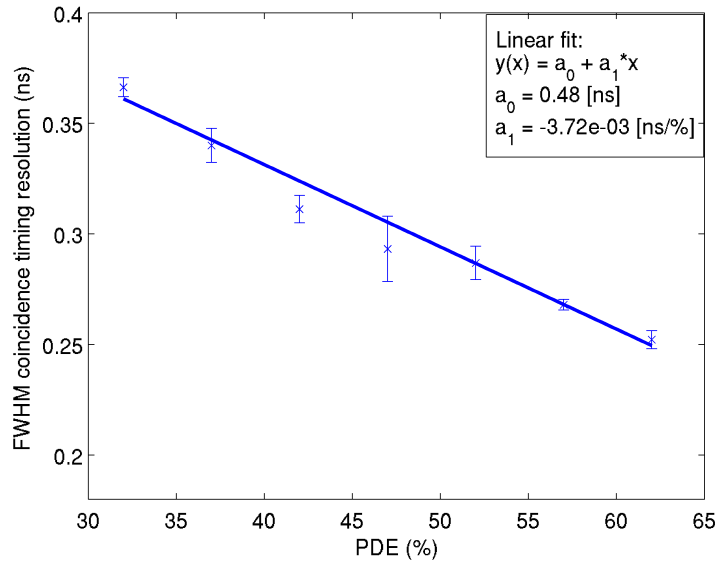
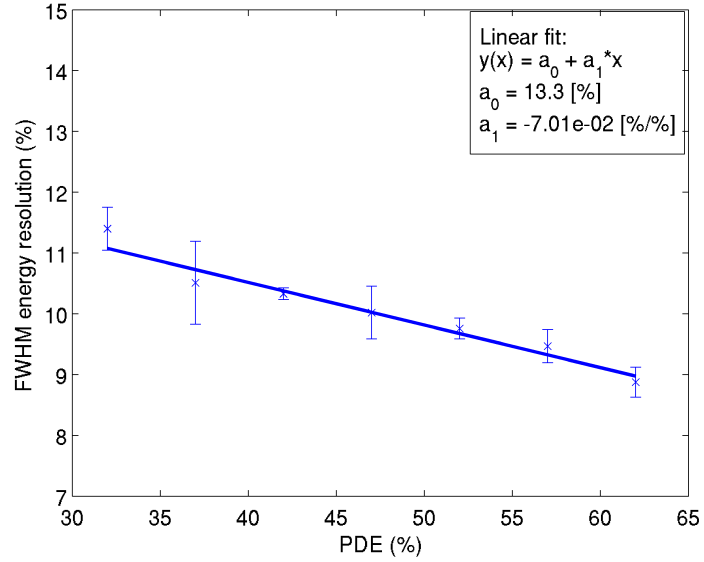


Figure 8.6: Comparison plot showing simulated photopeak pulses with three separate dead times.

In order to extract an uncertainty on the CTR associated with the approximated PDE value, a range of input values must be assumed. The Hamamatsu data sheet PDE is considered here as an upper bound whereby the gain contributions of cross-talk and all after-pulsing effects are compensated for by an inflated PDE. However, it has been shown through comparison of simulated and experimental energy, pulse shape and CTR results that this does not appear to be the case. It is likely then that after pulses may not be fully accounted for in this value. With no information available from Hamamatsu on their measurement technique some assumptions must then be made. If we first consider that due to $\tau_{slow} \approx 4 \times \tau_{fall}$, these after pulse events will often occur after the activated pixel has fully re-charged. These events will therefore be indistinguishable from dark noise events and are hence impossible to correlate to a primary avalanche event on the single event scale. It is likely then that these events were not included in the quoted PDE. As such, in order to estimate a lower bound on this uncertainty it is assumed that all τ_{fast} after pulses were measured with a (over-estimated) gain equivalent to that produced by an avalanche event in a fully re-charged pixel. Hence the quoted PDE is over-estimated by a percentage equivalent to the probability of these events: $\tau_{fast} = 13\%$. The upper bound on the PDE is then $x_{high} = 52\%$ and the estimated lower bound is then $x_{low} = 45.2\%$. By applying the gradient of the straight line fit given in Figure 8.7a, the uncertainty in PDE can be equated to an uncertainty on the CTR of:



(a)



(b)

Figure 8.7: Selected simulation response parameters plotted as a function of PDE (a) Coincidence timing resolution (b) Energy resolution.

$$FWHM_{PDE} = (a_0 + a_1 \cdot x_{low}) - (a_0 + a_1 \cdot x_{high}) = 23 \text{ ps}, \quad (8.3.1)$$

where $a_0 = 0.48 \text{ ns}$ and $a_1 = -3.38 \times 10^{-3} \text{ ns}/\%$.

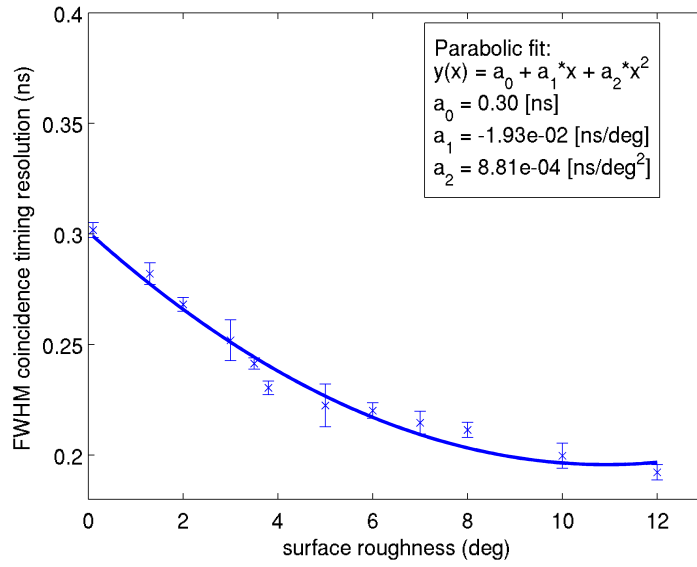
8.3.3 Surface roughness

As discussed previously, modelling the surface roughness of the crystal is one of the largest sources of uncertainty in the input parameters. It has been shown in literature that increasing the roughness of the crystal surface, by applying different surface treatments, will broaden the distribution of photon reflections off that surface. Specifically crystal surfaces which have been mechanically polished, chemically etched and coarsely ground result in an approximately Gaussian distribution of angles of reflection with standard deviations 1.3° , 3.8° and 12° respectively [144]. The crystals used in this work were polished by the manufacturer before delivery, however it is possible that the polishing abrasives/techniques applied were different to those used in the cited work. Crystals could also have been damaged (for example scratched) in transit. In order then to understand the correlation of CTR with surface roughness over all possible surface types, σ_α was varied in the range of 0.1 - 12° .

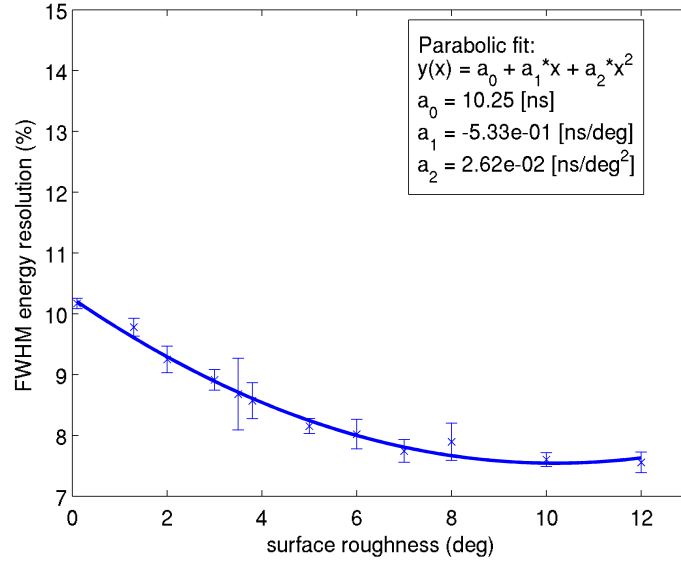
The resulting CTR and energy resolution distributions are given in Figure 8.8. Here both energy and CTR distributions show a quadratic decrease of the resolution as the surface roughness is increased. At larger scattering angles the photon flux is less dependent on the geometry and gamma interaction position in the system, hence reducing the fluctuations in both the temporal and spatial photon distribution at the SiPM surface.

It is possible then to estimate the uncertainty associated with the surface roughness by assuming a $\pm 1.0^\circ$ uncertainty on the 1.3° input parameter. This relates to approximately $\approx 70\%$ of the range difference between the polished and chemically etched crystal surfaces. By considering a $1.3^\circ \pm 1.0^\circ$ one can consider $x_{low} = 0.3^\circ$ and $x_{high} = 2.3^\circ$. By applying the fit equation given in Figure 8.8a an estimated uncertainty due to surface roughness effects can be estimated as:

$$FWHM_{SR} = (a_0 + a_1 \cdot 0.3 + a_2 \cdot x_{low}^2) - (a_0 + a_1 \cdot 2.3 + a_2 \cdot x_{high}^2) = 34 \text{ ps}, \quad (8.3.2)$$



(a)



(b)

Figure 8.8: Selected simulation response parameters plotted as a function of surface roughness (σ_α) (a) Coincidence timing resolution (b) Energy resolution.

8.4 Depth-of-interaction

The depth of interaction experiment as described in Chapter 6 was reproduced in simulation by replacing the $3 \times 3 \times 5 \text{ mm}^3$ crystal in the geometry shown in Figure 7.2 with a $4 \times 4 \times 20 \text{ mm}^3$ crystal painted on the four long edges. A SiPM was optically coupled to each end of the crystal with a $100 \text{ }\mu\text{m}$ layer of optical grease. For each measurement, 662 keV γ -photons were emitted uniformly from within a 2 mm diameter circular source, centred about the quoted offset relative to the crystal surface. This source distribution had been predicted by simulations run by Dr Mukhtar Al Shanqity at the University of Surrey using the Monte Carlo simulation software EGSnrc [149]. In the experimental DOI measurements presented in Chapter 6, no clear distinction between the Compton continuum and the photopeak was observed in data. Hence, Compton scattering events could not be assumed to have a negligible impact on the energy measurements presented in this experiment and the G4ComptonScattering model was turned on. The response characteristics of both the LYSO crystal and SiPM were applied as given in Tables 7.2 and 7.3. Values for the surface roughness have been varied in the range $\sigma_\alpha = 0.1\text{-}12\%$ for comparative analysis and are quoted explicitly in relation to each measurement.

8.4.1 Energy results

For each step position along the length of the simulated crystal 5000 events were used in analysis so as to provide a direct statistical comparison between experiment and simulation. In this case simulated SiPM current pulses were recorded when greater than 10 photons were detected at each of the coincident detectors. During analysis pulses were filtered with a second-order Butterworth filter, $f_c = 350 \text{ MHz}$ and the resulting pulse height values transferred into a histogram with bin widths 0.25 mV .

Unlike the experimental measurements, an exponential component was not observed stretching beyond the photopeak. As a result, simulated photopeaks were fitted with a simple Gaussian distribution between user selected limits. The exponential behaviour seen in the experimental measurements is therefore likely due to source effects resulting from a non-ideal collimator. In order to account for any uncertainty introduced to the fitting routine due to the shape of the Compton distribution about the lower range, the difference between the photopeak mean and the user selected lower range was calculated and fits were re-applied with the lower range varied between 0.5 and 1.5 times the original value. This

range results in fits both with and without the weightings from the Compton shoulder which will be the largest source of uncertainty in the fit. The uncertainty of each of the fit parameters was then approximated as the propagation of the statistical uncertainties and the range of the values measured from these fits. Example gamma spectra for a number of symmetric beam interaction positions are given in Figure 8.9.

The resulting measurements of the photopeak energy for range of σ_α values are given in Figure 8.10. Here each distribution has been normalised relative to the measurement made at the 8 mm beam positions. Applying a normalisation is convenient for comparing results with the equivalent experimentally measured values, also included in Figure 8.10. Both the simulated and experimental photopeak distributions show a common trend whereby the photopeak energy, and therefore the total photon flux reaching the detector, increases as the beam position approaches the SiPM. Clear correlations should also be noted between the surface roughness of the crystal and the gradient of the photopeak energy as a function of position. It is shown that the smoother surfaces show a higher rate of change and therefore a greater dependence of the DOI position. This property can be explained through geometric considerations. If the crystal surface is considered as a perfect specular reflector, then only scintillation photons emitted at a range of extremely well defined angles (see Chapter 3) will escape the crystal to be detected by the SiPM. In this case the amount of light detected is purely a function of the solid angle projected from the point-like emission position of the scintillation light to the end face of the crystal. This effect is therefore expected to scale with r^2 , where r is the radial distance between the crystal face and the scintillation emission position. As the surface roughness increases, reflections at the crystal surface become increasingly randomised and hence the geometric constraints on the range of scintillation emission angles visible to the detector are decreased. The result is then that rough surfaces show a reduced dependence of the light flux intensity as a function of DOI, tending to become increasingly linear as the randomisation of reflection angles is increased. However, the simulation shows that even for the largest applied surface roughness ($\sigma_\alpha = 12^\circ$, relating to the measured angular distribution of a roughly ground crystal surface [144]) some quadratic behaviour is still seen at the positions approaching the SiPM.

The experimentally measured distribution, although showing a comparable change in light response over the length of the crystal, presents a linear dependence. The higher order shaping effects of this distribution could be influenced by a number of systematic uncertainties in the experimental arrangement, notably including: the source collimation and

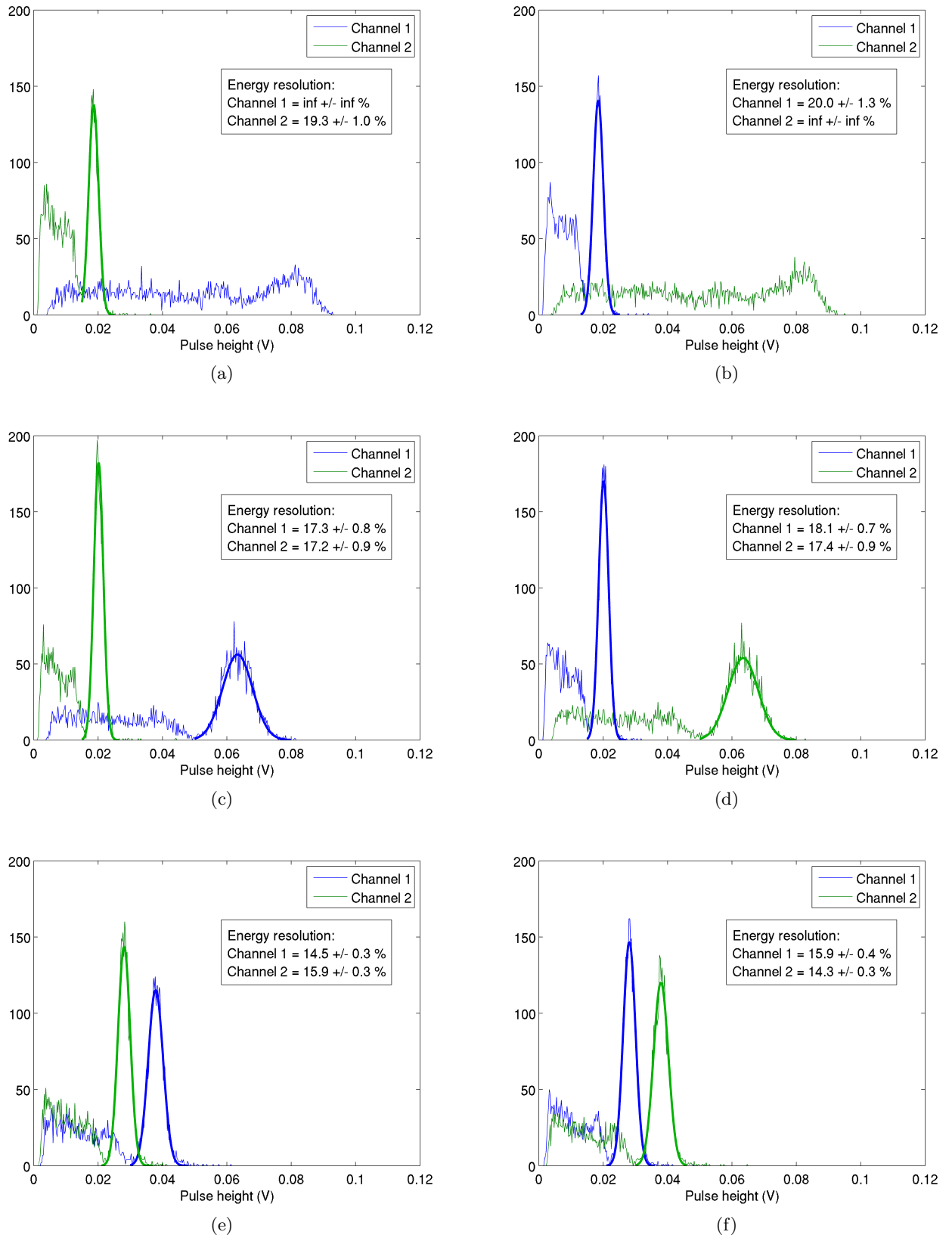


Figure 8.9: Example pulse height spectra ($\alpha = 1.3$) as measured at a number of beam positions along the crystal length (a) -10 mm relative to the crystals centre (b) +10 mm relative to the crystal centre (c) -8 mm relative to the crystal centre (d) +8 mm relative to the crystal centre (e) -2 mm relative to the crystal centre (f) +2 mm relative to the crystal centre. Fits are shown as thick lines coloured relative to the distribution represented.

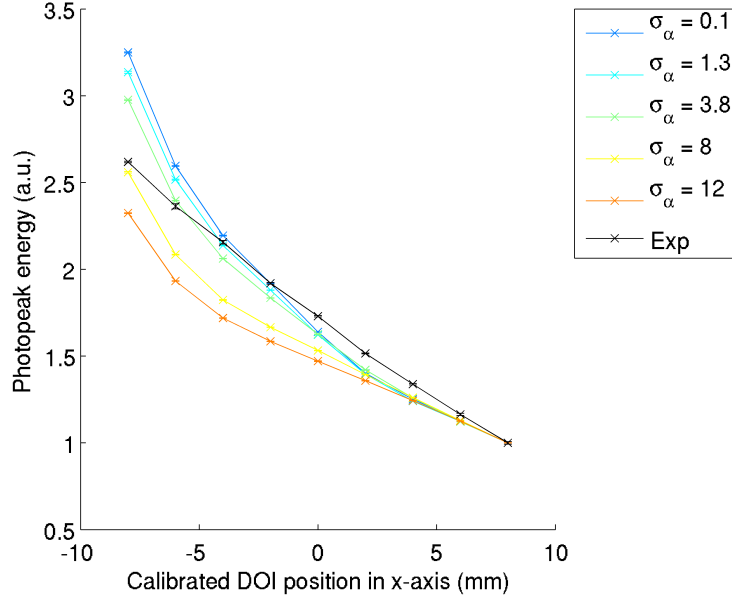


Figure 8.10: Comparison of experimental and simulated photopeak energy. Values of each trace have been normalised relative to the 8 mm beam position for comparison.

distribution, a skewed crystal alignment, and non-uniformities in the crystal surface and paint layers. Without extended characterisation of the experimental apparatus and the potential systematic effects described above, it is difficult to draw specific conclusions on surface roughness of the crystal from the results of these energy measurements. In hope of providing a more detailed conclusion timing measurements have also been analysed for comparison.

8.4.2 Timing results

Timing measurements were performed on simulated data using the same technique described in section 8.2.2, but with triggers applied relative to the crossing point of the photopeak energies. Comparison of the simulated and experimental CTR are then given in Figure 8.11. Here, Figures 8.11a and 8.11b compare the full range of trigger values measured at each of the DOI positions for the experimental and $\sigma_\alpha = 1.3^\circ$ simulation runs. Results show a few significant features. Firstly, the simulated distribution has a reduced dependence on both the DOI position and the trigger level. The spatial dependence is likely due to the higher order discrepancies seen in the energy response of the experiment and simulation as previously presented. The trigger level dependence however is explained by the energy offset seen in the two experimental channels in Figure 6.8a. In the case of the experimental measurements the trigger applied does not relate to a constant fraction

of each pulse in the pulse pair, hence introducing an additional systematic uncertainty. Finally, the timing resolution of the experimental results is offset from the simulated results by approximately 50 ps at the minimum trigger points in the central region.

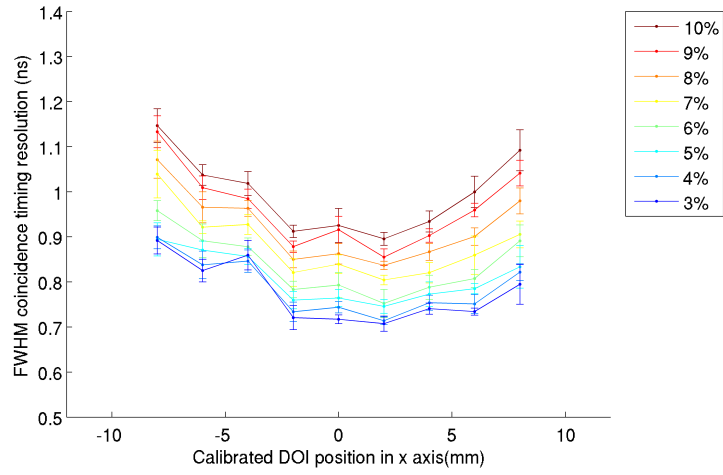
In order to compare results for each of the surface roughness measurements, the 4% trigger results from each are plotted in Figure 8.11c. The simulated results are shown to under predict the experimental results in the range of 30-300 ps, where the closest approximation is shown by the smoother $\sigma_\alpha = 0.1^\circ$ and 1.3° surfaces. By comparing the series directly it is clear that the experimental measurements show anomalous behaviour at the -8 mm to -4 mm positions. A systematic effect at these positions is consistent with the results shown in Figure 8.10 where the parabolic behaviour predicted by the simulation is not reproduced by experiment. Both of these behaviours can be explained by a reduction in the predicted photon flux at these positions. It is possible then that some optical defect in the crystal (i.e. a scratch, or a surface chip) could be causing a systematic reduction in light reaching the SiPM in this region.

In conclusion the depth of interaction experiment and resulting simulations have further validated the base response of the simulation framework by reproducing reasonably well experimental measurements of both energy and CTR effects. However, uncertainties in the experimental results have lead to less than ideal recreation of the higher order effects in both the energy and timing measurements. Therefore, specific, detailed conclusions on the distribution of reflections at the crystal surface cannot be drawn. The estimate of surface roughness, as described in equation 8.3.2, cannot be improved upon with available data, and an extension to DOI measurements would be a natural next step to improve understanding in this area.

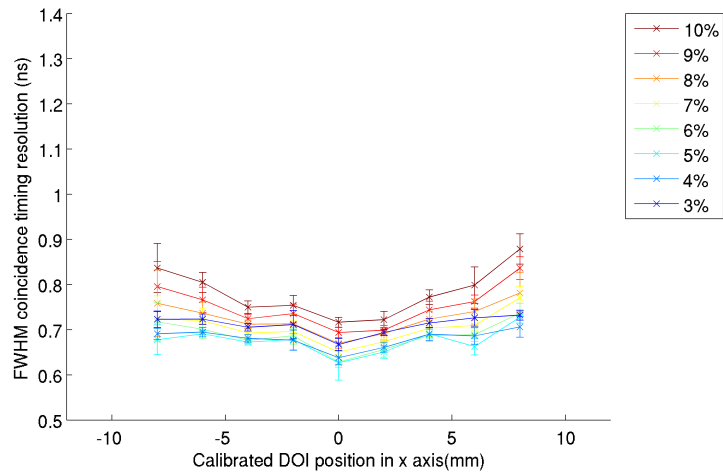
8.5 Comparison of experimental and simulated CTR

With the dominant systematic uncertainties on the simulations input parameters investigated in detail, the uncertainty on the simulated CTR at each trigger point (i) can be estimated as:

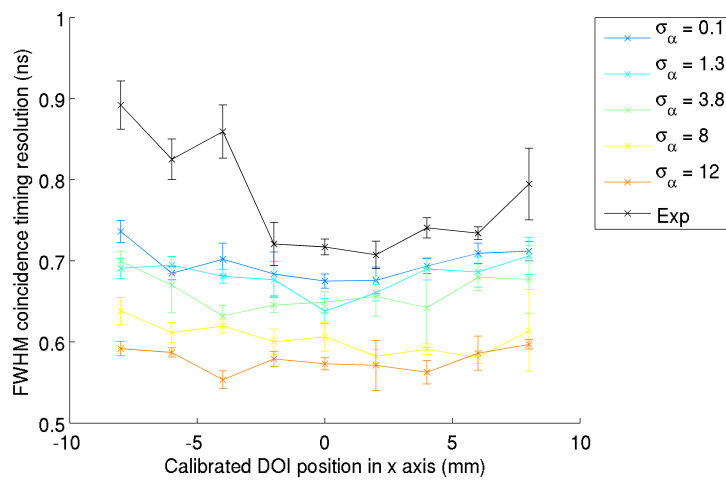
$$\begin{aligned} FWHM_{CTR}^i &= \sqrt{FWHM_{meas.}^i{}^2 + FWHM_{PDE}^2 + FWHM_{SR}^2}, \\ &= \sqrt{FWHM_{meas.}^i{}^2 + 23^2 + 34^2}, \end{aligned} \tag{8.5.1}$$



(a)



(b)



(c)

Figure 8.11: Coincidence timing resolution as a function of absolute position along x-axis (a) Experimental CTR results (b) Simulated CTR ($\sigma_\alpha = 1.3$) (c) Result measured at 4% trigger levels for each simulated surface roughness compared to the equivalent experimental distribution.

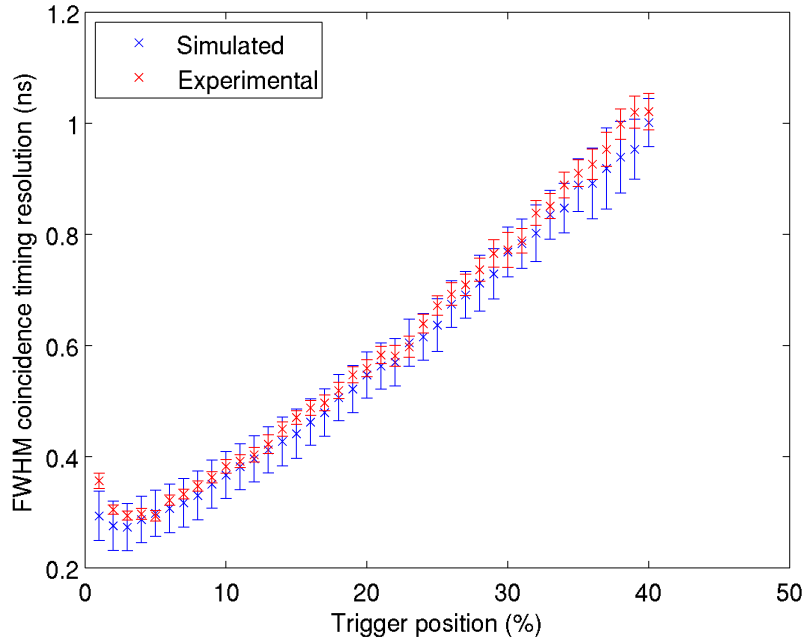


Figure 8.12: Comparison of simulated and experimental CTR distributions as a function of leading edge discriminator position. Coincident pulse pairs for both data sets were filtered with a 2^{nd} order Butterworth filter, $f_c = 350$ MHz. Uncertainties quoted on the simulated result are the propagation of statistical and fitting uncertainties with $FWHM_{PDE}$ and $FWHM_{SR}$.

where $FWHM_{meas.}^i$ includes the statistical and non-Gaussian tail uncertainties as described in all plots to this point. The $FWHM_{PDE}^2$, $FWHM_{SR}^2$ contributions are the input uncertainties deriving from the photon detection efficiency (equation 8.3.1) and surface roughness (equation 8.3.2), respectively. A final comparison of the experimental and simulated CTR distributions as a function of trigger positions is then given in Figure 8.12.

With the inclusion of systematic uncertainties, the simulation is shown to reproduce the experimental measurement to within one sigma at all trigger positions, with the exception of the lower limit at a 1% trigger value. It is possible that additional effects from the experimental electronics may contribute through small baseline fluctuations to the experimental response in this region, the effects of which are not considered in the simulation. If the extreme 1% trigger point is ignored, the simulation is shown to follow the trend of the experimental arrangement extremely well, with a consistent offset of 10-15 ps, well within the uncertainties.

In the following chapter, the simulation will be used to emulate configurations of detector elements within coincident arrays. The ultimate goal of this final exercise will be to provide

design recommendations for a prototype TOF-PET detector system now in construction at RAL. In order to investigate the impact on the performance of various configurations, conclusions will be drawn from central values, in the awareness that systematic uncertainties, estimated including contributions from both $FWHM_{PDE}$ and $FWHM_{SR}$ as in equation 8.5.1, may disguise subtle effects which could be observed in an experimental system.

Chapter 9

Simulation of prototype PET detector systems

The ultimate goal of the body of work presented in this thesis has been to produce a simulation to aid the design of coincident photodetector arrays, to be used as a TOF-PET detector. This chapter presents results from the simulation of coincident arrays consisting of 12×6 individual detector elements, the individual response of which was described in Chapter 8. The performance of different experimental combinations of $3 \times 3 \times 5 \text{ mm}^3$ and $3 \times 3 \times 10 \text{ mm}^3$ LYSO crystals within the coincident arrays are described, to emulate the crystal geometries available to develop a prototype at the Rutherford Appleton Laboratory (RAL). Ultimately, results from the prototype will be used, together with simulations, as a first step towards designing and then realising a scanner for commercial use. The effects of scaling the crystal dimensions to lengths equivalent to clinical scanners (2-3 cm) or bigger have also been investigated as a possible evolution of more conventional designs and the results obtained for the new design are discussed in detail. Finally, an investigation into the use of events where a gamma photon has Compton scattered internally in the detector array is presented. This is a novel idea that, to our knowledge has not been considered before. It is shown that by using such events, gains in detection efficiency of the order upto 60% can be achieved with small cross-section, one-to-one coupled detector elements as proposed here. A signal increase of this magnitude could have significant impact on the efficiency that would be achievable in a clinical environment, and therefore merits further thorough investigation.

9.1 Detector simulations for a TOF-PET prototype

The LYSO crystals available for the realisation of the first TOF-PET prototype under construction at RAL have dimensions $3 \times 3 \times 5 \text{ mm}^3$ and $3 \times 3 \times 10 \text{ mm}^3$, where the third dimension is the length of the crystal. This is significantly shorter than the 20-30 mm crystals typically applied in clinical scanner [29]. Reduced length crystals were chosen for this first prototype is to take advantage of the associated reduction in geometric aspect ratio. Minimising the aspect ratio directly affects the CTR of a system by reducing the average number of reflections undergone by an optical photon detected at the SiPM surface, reducing the effect of σ_{Trans} as defined in Chapter 8. The trade off, however, is a significantly reduced detection efficiency. This limitation can in part be addressed by techniques explored later in this chapter.

Different arrangements for the crystals in the two opposing arrays have been considered and correlations between parameters have been explored systematically in order to optimise the detector geometry based on overall performance.

9.1.1 Array geometries and experimental arrangement

All experimental arrangements simulated in this section consist of coincident arrays of 12 columns by 6 rows of detector elements. With the exception of the crystal length, each detector element in the two arrays are identical, consisting of crystals with a $3 \times 3 \text{ mm}^2$ cross section coupled to a SiPM as described previously in Chapter 8. Experimentally, each of the crystal arrangements chosen for investigation are realisable by arranging crystal elements in a purpose-built mechanical grid, which ensures mechanical stability and reproducibility of coupling between scintillators and SiPMs.

The various array geometries considered are as follows:

- **Full 5 mm.** Both coincident arrays are uniformly populated by 5 mm long crystals (Figure 9.1a).
- **Full 10 mm.** Both arrays are uniformly populated by 10 mm long crystals (Figure 9.1b);
- **Heads.** One array is populated uniformly with 5 mm crystals (Figure 9.1a), the other by 10 mm long crystals (Figure 9.1b).

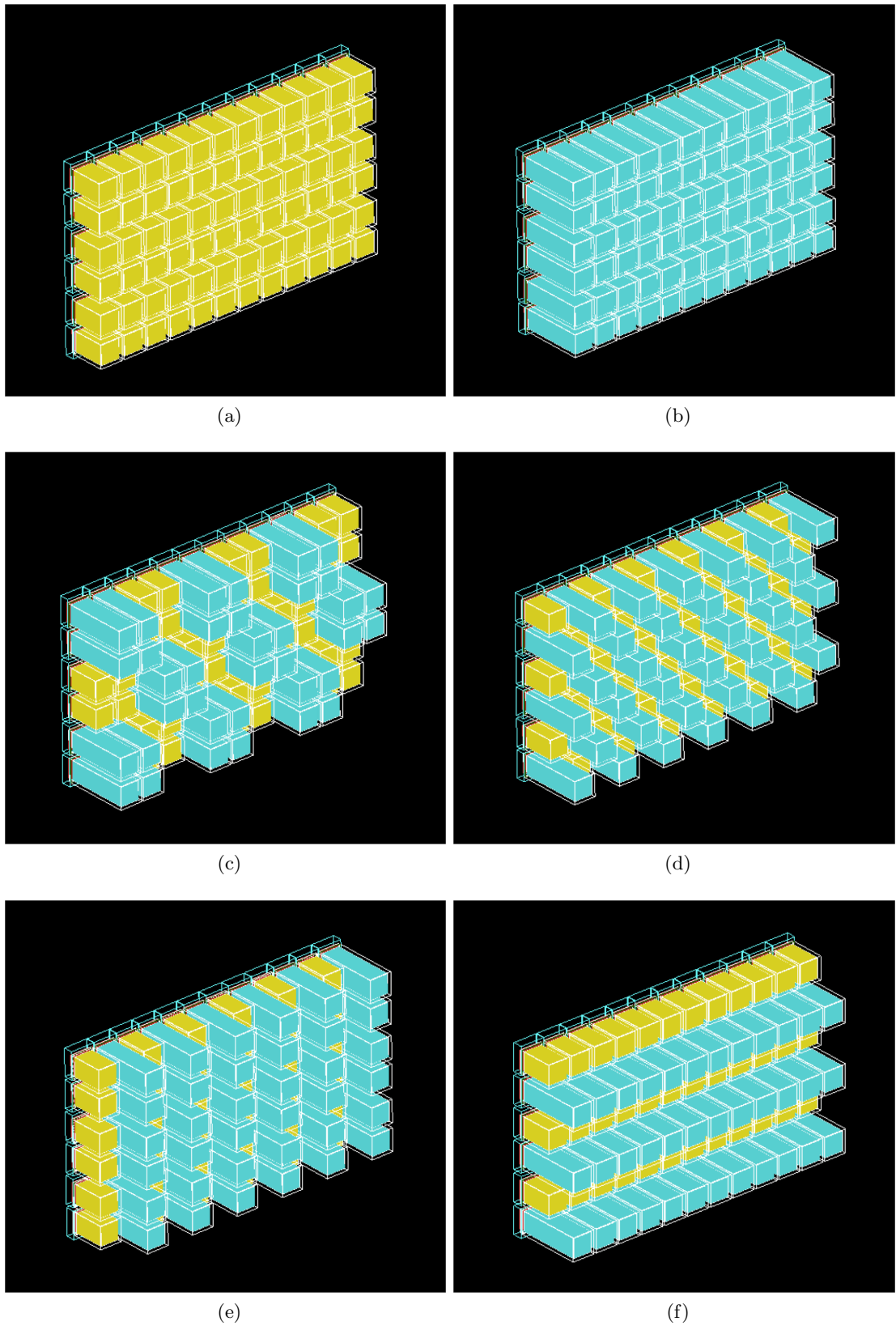


Figure 9.1: GEANT4 visualizations of the geometric crystal arrangements considered for the prototype detector arrays. In these 5 mm and 10 mm crystal are shown in yellow and blue respectively. (a) Full 5 mm (b) Full 10 mm (c) Blocks (d) Mixed (e) Columns (f) Rows.

- **Blocks.** Each array is populated by alternating 4×4 blocks of 5 mm and 10 mm long crystals (Figure 9.1c).
- **Columns.** In each array alternating columns are populated by 5 mm and 10 mm long crystals (Figure 9.1d).
- **Mixed.** In each array 5 mm and 10 mm crystals are alternated along both the vertical and horizontal planes (Figure 9.1e).
- **Rows.** In each array alternating rows were populated by 5 mm and 10 mm crystals (Figure 9.1f).

Arrays are considered in coincidence with respect to a point source emitting collinear 511 keV gamma-ray photons. The source is constructed to emit isotropically with spherical symmetry. However, in order to minimise the total computation time, emissions are restricted to a cone of appropriate angles, illuminating the detector arrays at a radius of 15 cm (see Figure 9.2).

In the case of mixed-length array geometries (i.e. Blocks, Columns, Mixed and Rows), arrays were rotated relative to each other such that a 5 mm crystal in one array is always facing a 10 mm crystal in the array opposite (see Figure 9.2). A notable feature of this symmetry is that, for the case of a point source equidistant between the two arrays, coincidences will activate detector element pairs consisting of either two 5 mm or two 10 mm crystal elements (Figure 9.2). This is in contrast to the Heads arrangement, where a 5 mm crystal will always make a coincident pair with a 10 mm crystal, or the full 5 mm and full 10 mm arrangements, where only coincident pairs of the associated crystal lengths can be made. It should be noted however that this symmetry only holds for the specific source arrangement used for the purpose of the initial simulation results presented here.

For all measurements presented in this section the G4ComptonScatter process was turned on to enable the investigation of effects associated with internal Compton scattering within the two arrays. Although all measurements described in this section, and indeed all measurements made by clinical scanners, only consider events where single detector elements were activated at each opposing array, the advantage of using a Monte Carlo model is that additional physics parameters such as internal Compton scattering within the arrays can be investigated with accuracy. Hence the efficiency of events where all the energy from γ photons is fully deposited in the detector arrays, but one or more Compton scatters have

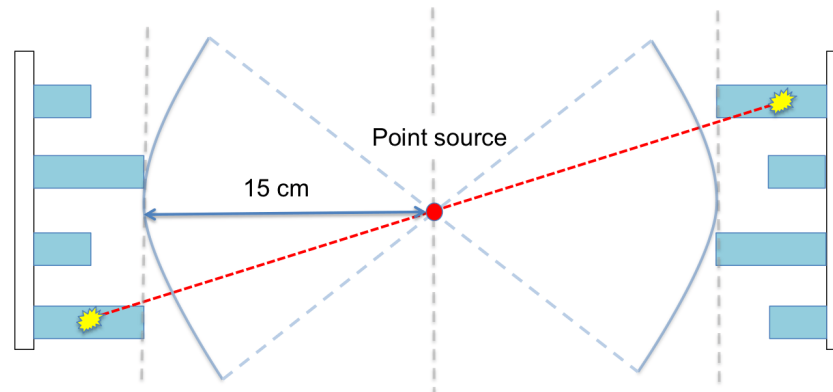


Figure 9.2: Diagram showing the overhead view of a coincident array simulation. A point source with an angular emission distribution restricted to the blue cones is shown at the central position, 15 cm from each array. The crystal arrangement in the coincident arrays is equivalent to Columns as shown in Figure 9.1.

occurred internally in either or both of the arrays, is also considered.

Events were recorded to file when all of the 511 keV energy of each collinear γ photon is deposited in the detector arrays, independent of the number of detector elements that are activated. A technique for the application of these scatter events is explored in Section 9.3.

9.1.2 Energy resolution

In a clinical PET detector system, the pulse height recorded for each detector activation is compared to some pre-set acceptance window (or ‘cut’) in order to reject events whereby a γ photon may have Compton scattered along the path to detection. This is a key step as, if they cannot be identified, such events can lead to an increase in the number of Scatter Coincidence events (as defined in Chapter 2) accepted for processing, ultimately reducing the NECR of the system. The accuracy with which the photopeak can be identified, and therefore Compton events can be tagged and removed, depends on the energy resolution of the system. If the mean energy or the variance (width) of the photopeak is affected by the length of the activated crystal it is important to account for such an effect in order to achieve noise rejection with the highest accuracy in the prototype system.

Therefore, the energy resolution has been investigated for each array geometry as a function of the crystal length for the activated channels. As with energy measurements discussed earlier, the energy resolution has been estimated by filtering the simulated pulses

with a second order Butterworth filter with $f_c = 350$ MHz, and creating a histogram of the resulting pulse heights. Separate histograms have been generated for pulses measured in detector elements using 5 mm and 10 mm long crystals. The energy resolution of the two crystal lengths are then calculated by applying equation 6.1.1, using the mean and FWHM obtained from Gaussian fits to the photopeak.

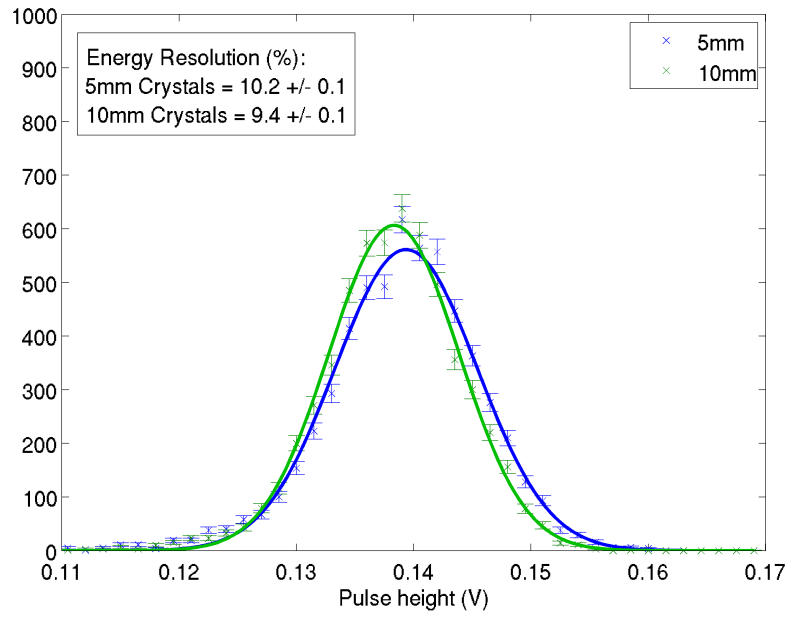
In order to investigate in detail the physics effects which impact on the final recommendations, the systematic uncertainties presented in Chapter 8 are assumed to describe an offset of the simulated and experimental response. As such, inter comparisons of simulated measurements do not consider the full systematic uncertainty associated with the simulations input parameters, but the uncertainties on the specific measurement only. This is true for all results presented in this chapter.

Uncertainties on each of the fit parameters were assumed to be the propagation of the statistical uncertainties and the uncertainty due to non-Gaussian tails in the data set. The contributions due to non-Gaussian tails were estimated by varying the limits of the considered data set between the three to six σ , and re-fitting in steps of $\sigma/2$. The range of measurements for each parameter was then taken as an estimate of the contribution of non-Gaussian tail effects.

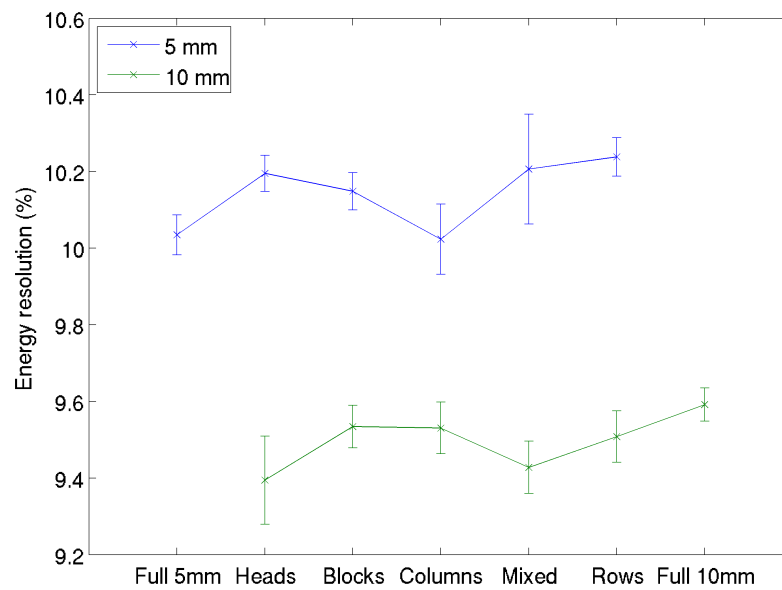
Table 9.1: Weighted mean energy resolutions as calculated from full range of crystal arrangement measurements given in Figure 9.3b. Uncertainties are the standard deviation on the weighted mean.

	Crystal length	
	5 mm	10 mm
Energy Resolution (%)	10.1 ± 0.1	9.5 ± 0.1

A histogram showing example spectra for both 5 mm and 10 mm crystal lengths, measured with the Mixed Crystal arrangement, is given in Figure 9.3a. Measurements of the energy resolution in 5 mm and 10 mm crystal channels, for each of the array arrangements, are then presented in Figure 9.3b. It is shown that, across all arrangements, there is an offset in the response of the different crystal lengths. This is expected as the behaviour of the independent detector element should be independent of the array geometry. The results measured are separated by slightly more than an error bar ($\chi_{nu}^2 = 1.21$), suggesting an underestimation in the quoted uncertainties. A weighted mean of each data series is given in Table 9.1 where it is shown that the 10 mm crystals outperform the 5 mm crystals by 0.5%. This result is not consistent with other measurements available in literature [150],



(a)



(b)

Figure 9.3: Energy results measured using the crystal length channels (a) Example gamma spectra as measured with the mixed array arrangement, fits to the two data sets are shown as a continuous line. (b) Energy resolution of 5 mm and 10 mm detector elements as measured for each crystal arrangement.

where an increased aspect ratio was shown to correlate with a reduction in both light yield and energy resolution. Although a reduced photopeak energy is observed for the longer 10 mm crystals (see Figure 9.3a) the energy resolution does not appear to follow the trend. The correlation between crystal length and energy resolution is investigated further in Section 9.2 where the crystal lengths below 7 mm are observed to present non-typical behaviour. The effect observed here is then discussed and explained in an extended context in the section to follow.

9.1.3 Coincidence timing resolution

In a conventional PET system the time difference (Δt) measured between coincident detector activations is used to correlate a coincident event to a single positron annihilation within the source volume. By only accepting Δt values within a given selection window, coincident timing measurements can be used to discriminate against random coincidences where γ photons from unrelated annihilations happen to activate coincident detector elements. The accuracy to which the time difference between the events can be known is defined by the CTR, typically of the order of 3-12 ns in conventional PET [29].

The CTR of each crystal array arrangement was measured using a similar technique to that introduced in Chapters 6 and 8 whereby only events in which both coincident pulses are within the FWHM of the photopeak are selected for processing. In addition to that, having identified the length of the activated scintillator crystal in this case it was also possible to apply an energy cut to selected events in the photopeak energy range.

A set of timestamps can be recorded for each pulse pair satisfying the initial energy cut, via leading edge discriminators applied at incremental steps along the leading edge, measured relative to the mean photopeak pulse height. For each trigger position, the time difference (Δt) between each pulse pair is calculated and histogrammed using 25 ps bins, equivalent to the 40 GS/s sample rate of the recorded pulses. The final histograms, containing a full sample of Δt values, are then fitted with a Gaussian and the FWHM used to estimate the system CTR. The uncertainty on each FWHM was assumed as the convolution of the statistical uncertainty on the measurement with the range of values returned from independent fits to the histogram applied in the three to six σ range, in steps of $\sigma/2$. It was shown in Chapters 6 and 8 that coincident pulses processed with the Butterworth filter, due to the reduction in σ_{signal} , provide the optimum CTR. All the timing measurements presented in this chapter were calculated after pulses had been

processed with this filter.

The CTR measured as a function of trigger level for all array geometries is shown in Figure 9.4a. A comparison of the CTR as measured at the 2% trigger threshold is presented in Figure 9.4b. Results are additionally listed in Table 9.2.

Table 9.2: Coincident timing resolution as measured at the 2% trigger threshold for each crystal arrangement.

	Full 5 mm	Heads	Blocks	Columns	Mixed	Rows	Full 10 mm
Timing resolution (ps)	262 ± 4	264 ± 5	283 ± 4	286 ± 5	284 ± 3	285 ± 4	270 ± 4

As expected, Figure 9.4b shows the full 5 mm arrangement outperforms the full 10 mm arrangement due to the reduction of the σ_{Trans} contributions. However this effect is small, with approximately a 10 ps offset between the two, a 3% change in relative terms. The Heads arrangement has been measured to perform to within one error bar of the optimally performing full 5 mm arrangement. This behaviour is explained by the observation that in the heads geometry each coincident pair of detector elements must consist of one 5 mm long crystal and one 10 mm long crystal. The response of the system is therefore a convolution of the response of the two types of crystals. This prediction is consistent within the quoted error bars.

All other crystal arrangements consistently show a CTR degradation of approximately 20 ps relative to the Full 5 mm result. This derives directly from how crystals of different lengths are combined in each arrangement when activated in a coincident event. For each of these crystal arrangements it has been discussed previously that, for a point like source, pairs of crystals of the same length are considered in coincidence. As both the photopeak energy and the energy resolution are different for these two channels, the range of pulse heights which pass the energy cuts is increased relative to other arrangements. This effect is shown qualitatively in the pulse height correlation plots given in Figure 9.5 where the correlation between the pulse heights seen in the two channels for different array geometries is shown. In the Mixed Crystal arrangement (Figure 9.5d) the phase space extends from the maximum pulse height shown by the Full 5 mm configuration (Figure 9.5a) to the minimum height defined by the Full 10 mm configuration (Figure 9.5b). This reflects the fact that, for a Mixed Crystal geometry, a greater variance of pulse heights pass the energy cut, in turn leading to a degradation in the CTR response.

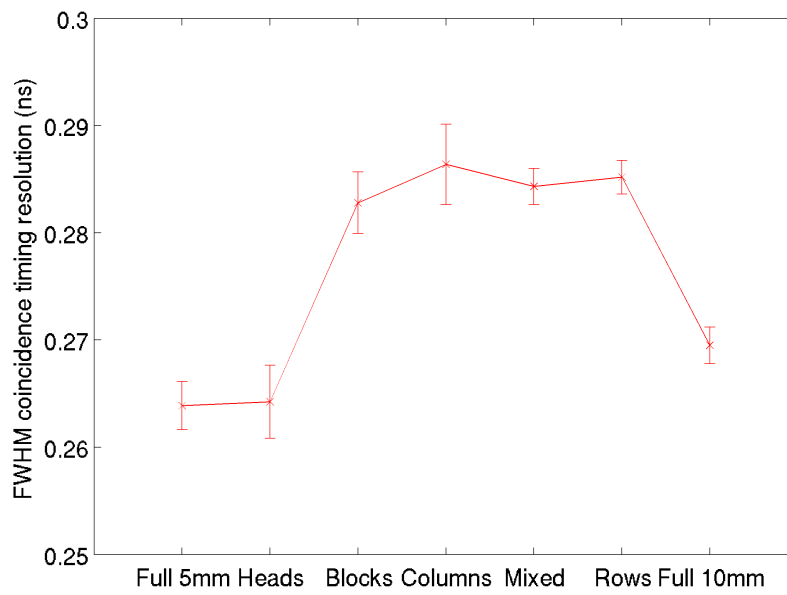
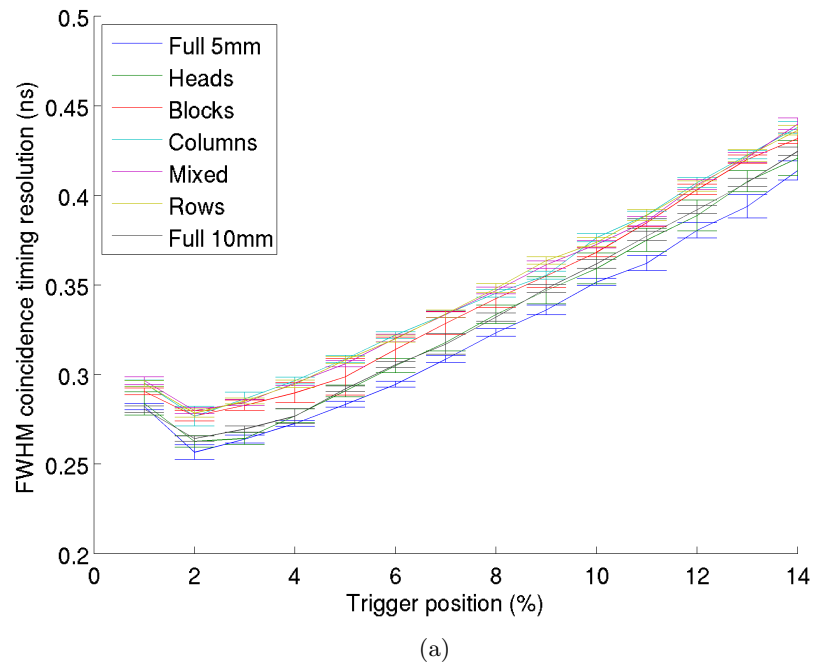


Figure 9.4: Coincidence timing resolution plots (a) Coincidence timing resolution as a function of trigger position on the leading edge. Coloured traces represent the different crystal arrangements. (b) Results measured at the 2% threshold for each of the crystal arrangements.

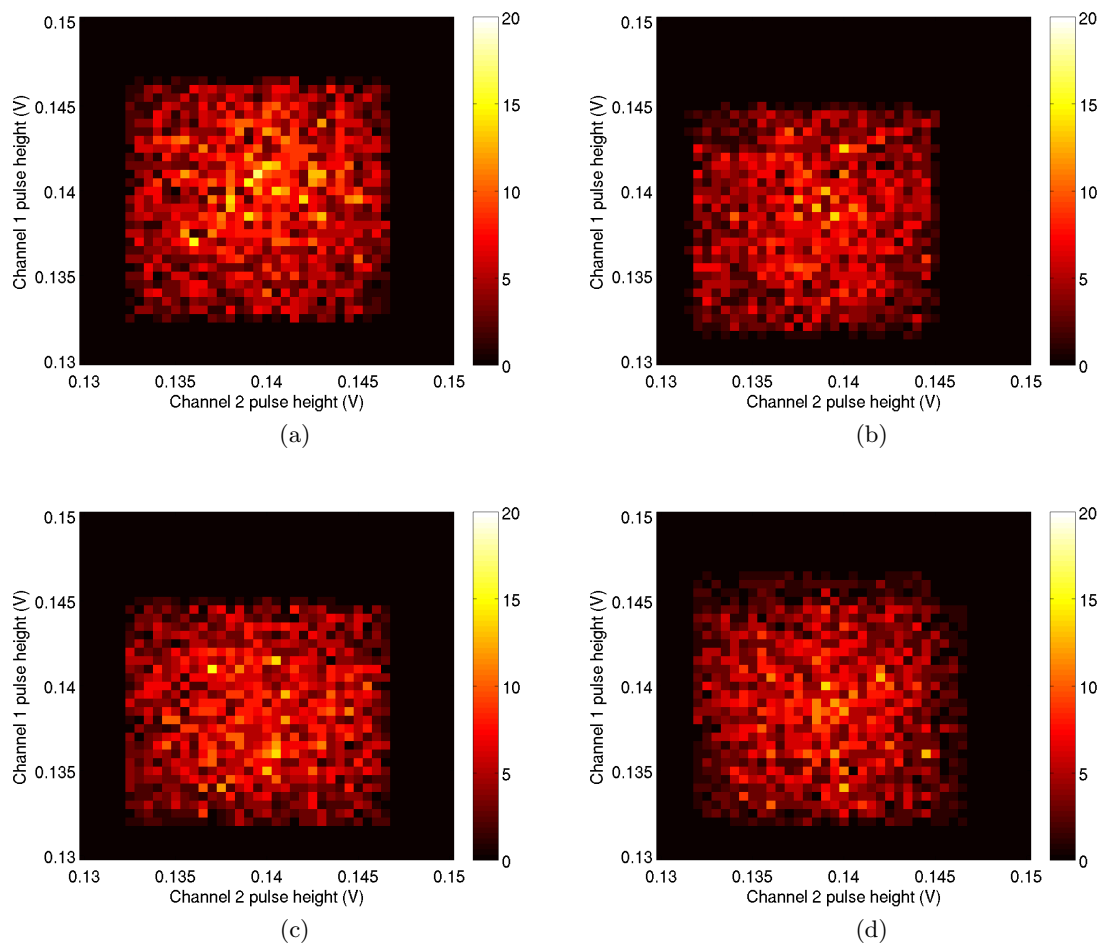


Figure 9.5: Coincident event pulse height correlations for pulse pairs passing initial energy cuts. (a) Full 5 mm (b) Full 10 mm (c) Heads (d) Mixed arrays.

9.1.4 Detection efficiency

Image reconstruction techniques applied to PET typically use statistical and probabilistic methods to recreate the source intensity distribution monitored during a scan. This has proven to be a powerful technique for reconstructing images from a data sets where the annihilation position along the LOR is not known. If the timing resolution of a PET detector system could be as good as to 3 ps or better, the annihilation position could be known to an accuracy of approximately 1 mm. In this ideal case, statistical reconstruction would no longer be necessary as the annihilation position would be known to an accuracy equivalent to the fundamental spatial resolution of PET, defined by the positron emission range effect. However, for a more realistic system, with CTR equivalent to those explored in this work (or available in literature), statistical methods are still required for reconstruction. These however will benefit from a signal-to-noise improved relative to conventional PET. This means the image quality associated with a PET (or TOF-PET) detector system is strongly linked with the number of coincident signals (signal statistics) which can be acquired in a single scan. Due to the side effects of high energy radiation on a patient, the source activity is limited by dose levels which are deemed acceptable for the patient to receive. Typically, for a full body scan, the activity will be 400 MBq at point of administration, falling to ≈ 200 MBq by the time the scan begins (20-60 minutes later). It is therefore of great importance that the detection efficiency of the system is high.

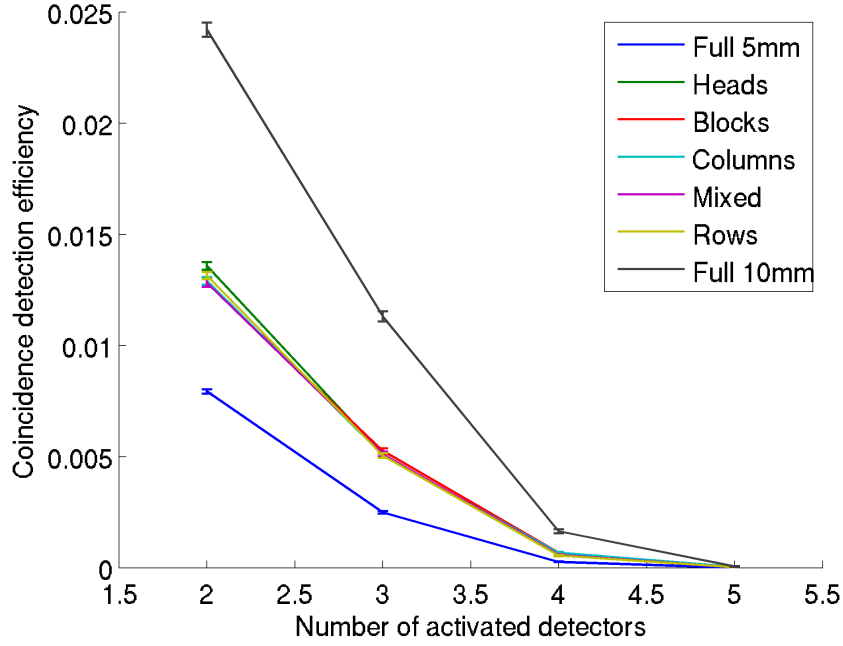
The detection efficiencies (ϵ) is defined as:

$$\epsilon = \frac{m}{N}, \quad (9.1.1)$$

where m is the number of events measured where two or more detectors were activated and N is the number of independent trials. The statistical uncertainty quoted on this value is calculated as [151]:

$$\sigma[\epsilon] = \frac{\sqrt{m(1 - m/N)}}{N}. \quad (9.1.2)$$

Detection efficiencies are shown in Figure 9.6 as a function of the number of activated detectors in the two heads. The Full 10 mm arrangement outperforms Full 5 mm crystal arrangements by approximately a factor of three in the case where two detector elements



(a)

Figure 9.6: Coincident detection efficiency as a function of number of activated detector elements in an full energy deposition.

are activated. This is consistent with expectations, as for two-detector events only interactions via the photoelectric effect influence the results. The attenuation length of LYSO due to purely photoelectric interactions at an interaction energy of 511 keV is 30.4 mm [12], giving estimated detection efficiencies of 0.16 and 0.28 for 5 mm and 10 mm crystal lengths, respectively. This corresponds to coincident detection probabilities of 0.026 and 0.078 respectively. The offset of this result from in the simulated values given in Figure 9.6 is explained by two effects: dead space in the detector arrays and the over estimation of the source projection cone about the two arrays, intentionally defined to ensure full coverage. However, the ratio between the two probabilities, and therefore the relative scaling of the 5 mm and 10 mm crystal efficiencies is preserved.

Crystal array arrangements which implement equal fractions of 5 mm and 10 mm crystals are shown to perform within error of each other at slightly under twice the efficiency measured by the Full 5 mm arrangements. This result is again consistent with expectations based on detection efficiencies of the 5 mm and 10 mm crystals. The estimated efficiency for an equal mixture of two crystal lengths is given by the product of the individual detection efficiencies, namely $0.16 \times 0.28 = 0.045$. The ratio of this result and the detection efficiency estimated for the Full 5 mm arrangement predicts a relative scaling factor of 1.7, equivalent to the scaling observed in Figure 9.6.

It is helpful at this point to again consider the operation of a conventional PET detection system. Following standard techniques, cuts on energy and timing variables are applied only to events whereby single detector element activations have been activated in coincidence. This is for a number of reasons. Firstly, PET reconstruction algorithms use LORs inferred between the two activated elements to produce a final image of the source distribution. Therefore, uncertainties associated with these LORs due to noise effects, systematic contributions of the detector system and the fundamental limitation of the positron emission detection (as explored in Chapter 2) limits the spatial resolution of the final image. As such, events where the energy deposit is spread across multiple detector elements will increase the uncertainty on the projected LOR, in turn reducing the spatial resolution of the data set. Additionally, identifying events where the full 511 keV has been deposited in the array, but distributed across multiple detector elements, is also a more technically demanding task requiring more complex, and therefore more expensive, electronics. However, it is shown in Figure 9.6 that if events where three detector elements have been activated could be recovered, significant gains in signal statistics could be achieved, equivalent to approximately 30% and 45% for the full 5 mm and full 10 mm arrangements respectively. In an application where statistics are key for sensitivity, but the source intensity is limited, these events have been identified for further study.

9.1.5 First design recommendations

The results from the simulation as presented in this section can be used to draw a number of concrete conclusions with impact on the design of the TOF-PET prototype.

- The energy resolution of $3 \times 3 \times 5 \text{ mm}^3$ and $3 \times 3 \times 10 \text{ mm}^3$ have been simulated to be $10.1\% \pm 0.1\%$ and $9.5\% \pm 0.1\%$ respectively. It is to be expected that additional systematic uncertainties associated with the channel to channel gain fluctuations in the experimental arrangement will degrade the accuracy of these measurements. Therefore, the relatively small offset in the resolution for the two geometries does not seem very significant. The energy resolution of 5 mm and 10 mm crystal can therefore be considered of minor consequence in a prototype design.
- The degradation of the timing resolution associated with scaling arrays from a uniform arrangement of 5 mm crystals to a uniform arrangement of 10 mm crystals has been measured to be $8 \text{ ps} \pm 6 \text{ ps}$ where the uncertainty is the propagated uncertainty of the two measurements. This result is consistent with zero. However, for

completeness, if we consider that in PET, TOF information is used to improve the signal-to-noise of a data set, then we can calculate the associated change in signal-to-noise by applying equation ??, where: $D = 0.30$ m, $\Delta t_{5mm} = 262$ ps and $\Delta t_{10mm} = 270$ ps. By increasing the crystal length from 5 mm to 10 mm the signal-to-noise gain factor is therefore reduced from 2.76 to 2.72, a negligible relative change. The CTR associated with the full 5 mm and the full 10 mm arrangements can therefore be considered equivalent and has hence no bearing on design considerations.

- In a ‘Heads’ style crystal arrangement, where one of the collinear 511 keV photons interacts in a 5 mm long crystal and the other in a 10 mm long crystal at the opposing array it is possible to combine the timing response of 5 mm and 10 mm crystals. However, mixing crystal lengths on each of the two arrays results in a relative degradation in CTR of approximately 8%, due to an increase in the total sampling range of coincident pulse height correlations. If two crystal lengths are to be applied to a final system they should therefore be arranged in a Heads arrangement to optimise the timing performance of the detector system.
- The coincidence detection efficiency of the system has been shown to be strongly correlated to the crystal length, but is independent of the arrangement of crystals within an array. The crystal length should therefore be maximised in order to optimise the detection efficiency of the system.

It can be concluded then that for a prototype detector applying 5 mm and 10 mm long LYSO crystals, the largest performance differentials can be seen in the detection efficiency. In fact, all crystal arrangements produced an energy resolution with approximately equivalent uncertainties for both the 5 mm and 10 mm channels. The CTR resolution has then been shown to be equivalent to within uncertainties for all three of the full 5 mm, full 10 mm and Heads arrangements, displaying instead a degradation of approximately 20 ps for all other arrangements discussed earlier. The final selection between these three best performing arrangements will have to be based then on the coincidence detection efficiency. In respect of that, the full 10 mm arrangement is seen to outperform Heads and Full 5 mm by a factor of approximately two or three respectively. It is therefore recommended that the Full 10 mm arrangement is implemented as the baseline in the final prototype.

It is also recommended that, for the purpose of systematic studies, the experimental set up should have the necessary flexibility to enable compositions between 5 mm and 10 mm arrangements, as well as a mixed crystal geometry.

9.2 Crystal length studies

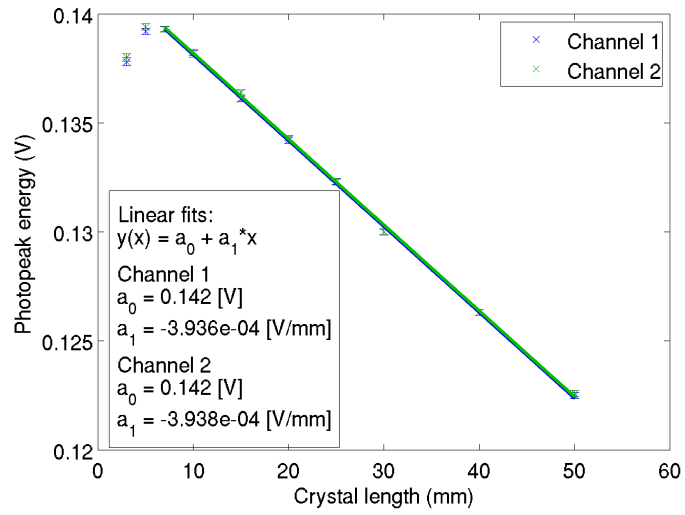
For the first iteration of the TOF-PET prototype, under construction at RAL, crystals have already been acquired, with lengths of 5 mm and 10 mm. Therefore flexibility is limited for the first iteration of measurements. However, in order to explore the potential of future developments for this project, the simulations described in Section 9.1 have been extended to investigate different crystal lengths beyond those available for the first prototype. Lengths have been varied in the range 5-50 mm. The lower value of this interval has been chosen keeping in mind that 5 mm crystals are the shortest which have been considered for ultra-precise timing measurements in PET applications [64]. On the other hand, 50 mm is approximately twice the length of crystals typically applied in clinical PET scanner [29] and has hence been assumed as an upper limit. As no great gains have been observed from using mixed length arrays, for the results presented in this section it was decided to populate arrays uniformly with crystals all of the chosen length. As with previous simulations, all crystals have an identical $3 \times 3 \text{ mm}^2$ cross sectional area.

9.2.1 Energy resolution

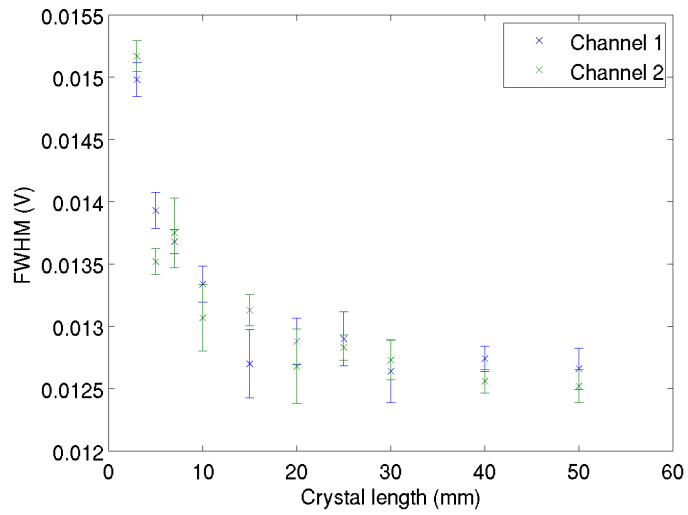
As for other studies, the energy resolution has been evaluated by filtering the simulated pulses with a second order Butterworth filter, $f_c = 350 \text{ MHz}$ and creating a histogram of the resulting pulse heights. For each measurement presented here, arrays were populated with identical crystal lengths and pulse height spectra were produced for the interactions at each of the coincident arrays. The energy resolution of the two channels was then calculated by fitting a Gaussian and applying equation 6.1.1. Uncertainties were calculated as described previously in section 9.1.

Figure 9.7 shows the results of both the measured photopeak energy (Figure 9.7a), FWHM (Figure 9.7b) and energy resolution (Figure 9.7c), calculated as the ratio of the two, as a function of crystal length. In order then to describe the energy resolution of the system both the photopeak energy and FWHM distributions must both be considered.

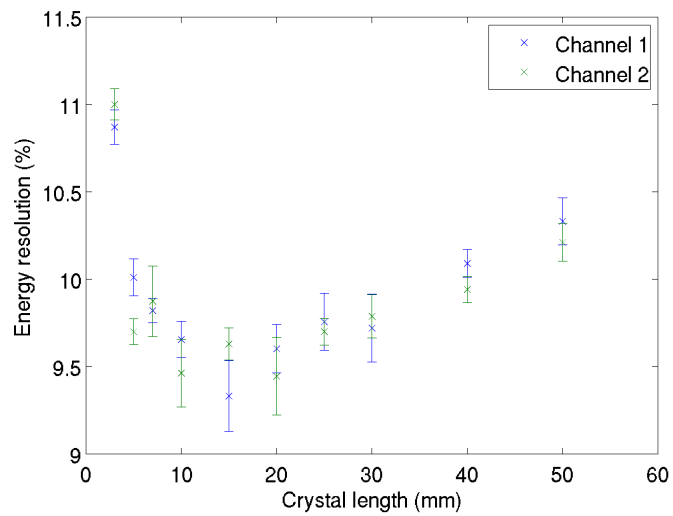
With the exception of very short crystals, a linear behaviour is seen in the photopeak energy measurements given in Figure 9.7. Due to the non-linear behaviour for the shortest crystal lengths, measured originally at the 5 mm point, two additional data points at 3 mm and 7 mm have been simulated for consideration in the energy measurements presented in Figure 9.7. It is shown that for crystals shorter than 7 mm, the photopeak energy no



(a)



(b)



(c)

Figure 9.7: Energy results plotted as a function of crystal length (a) Mean photopeak energy. Linear fits are applied to the 7-50 mm range (b) Photopeak FWHM. (c) Energy resolution. For both (b) and (c) lines are plotted connecting the points in each data series as a guide for the eye.

longer behaves linearly, reducing as the crystal length approaches zero. This behaviour can be explained through purely geometric considerations applied to the positions of γ interaction and the resulting paths of optical photons emitted by the scintillator. The position with the highest interaction probability is the point of entry into the crystal, decaying exponentially for interaction positions reaching through the crystal length. As such, an increase in crystal length is directly correlated with an equivalent increase in the average path length a scintillation photon will travel before reaching the sensitive surface of the SiPM for detection. An increase in path length is directly correlated with an increased attenuation probability, reducing the average number of detected photons and hence yields a shift to lower values of photopeak energy. In the case of the shorter (5 mm and 3 mm) crystals, the non-linear behaviour derives from the attenuation length of 511 keV γ photons in LYSO: $\tau_{Attenuation} = 11.4$ mm. As the crystal length is significantly shorter than the $1/e$ attenuation length of the γ photon, the depth of interaction in the crystal is poorly defined. At this limit, higher order effects relating to non-uniform photon distribution at the SiPMs surface leading to detector saturation become more prominent.

The second system response parameter used to calculate the energy resolution is the variance of the photopeak signal, as measured by the FWHM of the peak. It is shown then in Figure 9.7b that for crystal lengths of 20 mm and above, the variance of the resulting photopeaks is approximately constant, with a significantly increased dependence as the crystal length approaches zero. Again this can be explained through geometric considerations of the γ interaction position in the crystal. As the crystal length increases beyond the 11.4 mm attenuation length of 511 keV γ photons in LYSO, the γ interaction position becomes better defined. As a result the average path of the resulting optical scintillation photons is known more precisely, reducing the variance of the signal.

The weighting of these two effects is then represented in the energy resolution distribution given in Figure 9.7c. It is shown that for crystal lengths below approximately 15 mm the signal variance (Figure 9.7b) is the dominant contribution, limiting the system energy resolution. However, at crystal lengths above 15 mm, as the depth of interaction of the crystal becomes better defined, the attenuation of photons due to the increased path length (Figure 9.7a) becomes the dominant effect, restricting and then degrading the energy resolution of the system.

It can be concluded then from Figure 9.7c, that to optimise the energy resolution of a prototype system, crystals should be selected with lengths in the range 10-20 mm.

9.2.2 Coincidence timing resolution

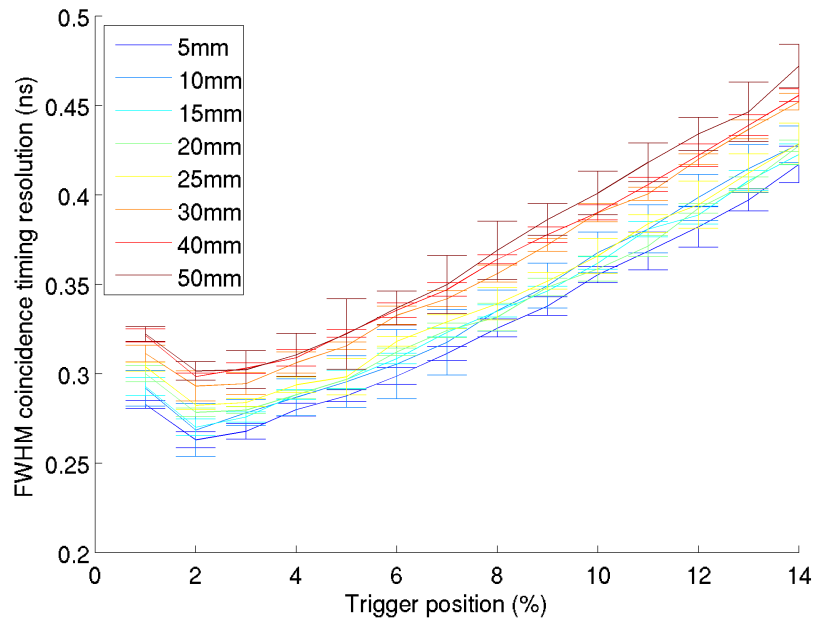
The CTR results presented here were measured with an identical method as described in section 9.1. In this case both coincident arrays were populated with identical crystal lengths, trigger positions were therefore defined relative to the mean photopeak pulse height for the crystal length being applied. Measurements of these values were presented previously in section 9.2.1.

The distributions, for each of the simulated crystal lengths, presenting CTR as a function of trigger position on the leading edge are given in Figure 9.8a. It is shown that increasing the crystal length results in a offset in the measured CTR. This offset is shown in Figure 9.8b to depend linearly on the crystal length with a gradient of ≈ 1 ps/mm. The error bars are shown to have been over-estimated with a $\chi^2_\nu = 0.47$, this is likely due to correlations from systematic effects associated with the variable range of interaction positions for differing crystals lengths. If we consider then that the very fastest photons which reach the SiPM will have undergone little or no reflections at the crystal boundaries, emitted in the solid angle associated with a direct path to the active detector surface, these photons are associated with the early rising edge of the electronic signal, where these thresholds are being applied. As such, this signal region is only minimally influenced by σ_{Trans} which considers the full range of photons paths. The degradation in CTR seen here can then be attributed to σ_{Stats} which is degraded for the longer crystals due to the reduced photon flux as characterised previously in Figure 9.7a.

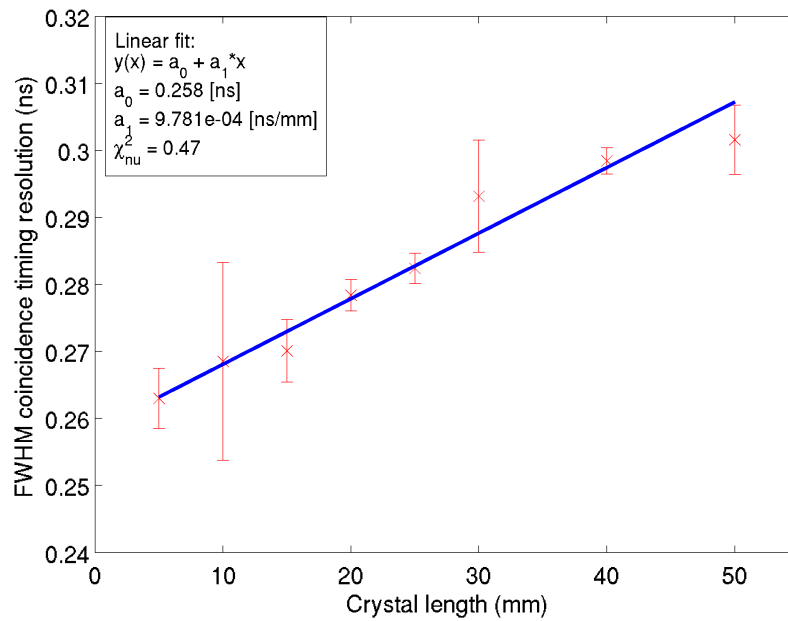
9.2.3 Detection efficiency

The detection efficiencies and associated uncertainties presented here have been calculated using equations 9.1.1 and 9.1.2 given in section 9.1. It was shown in section 9.1 that by considering the 30.4 mm attenuation length associated with photoelectric events of 511 keV γ photons in LYSO, the relative efficiencies of two-detector events could be estimated. Therefore, the increasing coincidence detection efficiency of two-detector events is of interest but could be easily predicted by less involved models.

However, a trend of significant interest is the relative increase in three-detector events as a function of crystal length. The efficiency gain which would result from accepting these events is given as a function of crystal length in Figure 9.9b. An increase in gain of the form $A(1 - \exp(-x/\tau))$ is observed, tending to a limit of 67.7% with an exponential constant



(a)



(b)

Figure 9.8: Coincidence timing resolution plots (a) CTR distributions as a function of trigger position on the leading edge for each crystal arrangement. (b) Results as measured at the 2% threshold for each of the crystal arrangements. Here error bars are given relating to the uncertainty associated with the measurement and the additional convolution of uncertainties related to the simulation input parameters.

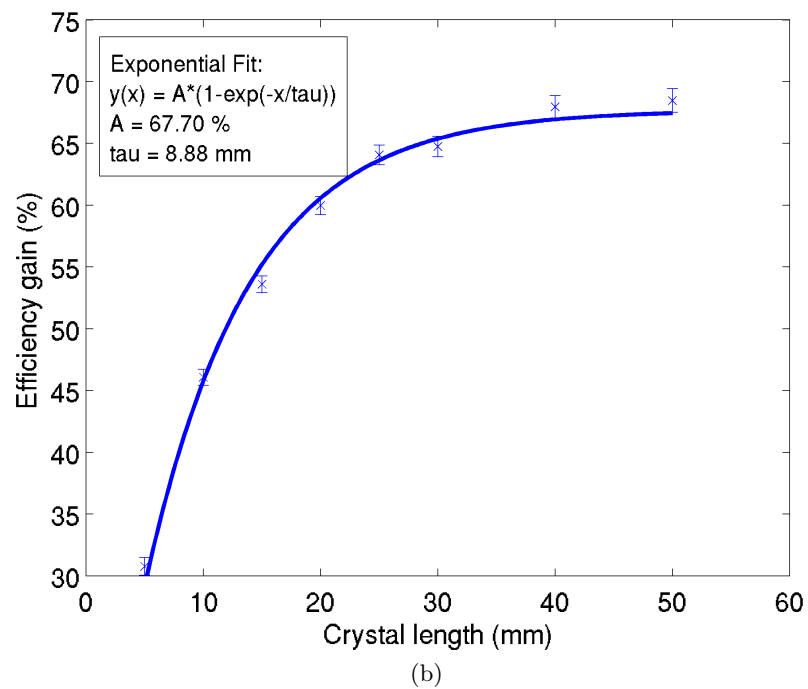
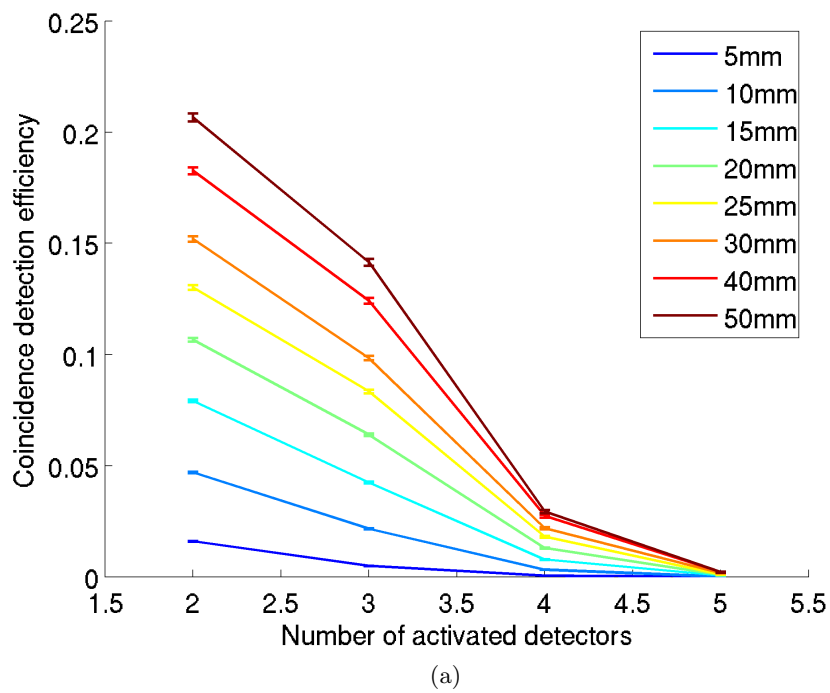


Figure 9.9: Coincident detection efficiency plots (a) Coincidence detection efficiency as a function of number of activated detector elements for each crystal length (b) Efficiency gains associated with application of the three-detector event as a function of crystal length.

(τ) equal to 8.88 mm. It is therefore shown that, for crystal lengths equivalent to those applied to clinical systems (20-30 mm), efficiency gains of 60-65% may be achievable if these events can be identified and applied to the image reconstruction.

This effect cannot be explained simply by attenuation length considerations, as both the angle of the Compton scatter event and the probability of interaction with any further crystals must also be considered. In order to describe this result, the scatter process associated with these events must first be well understood. Figure 9.10a presents a diagram of a scatter event where the 511 keV γ photon energy is shared between two detector elements as a result of a 90° Compton scatter event. By considering the Compton scatter formula as presented in eq 9.2.1 and an *acceptance angle* $\approx 90^\circ$, the energy of the scattered photon can be calculated as:

$$h\nu' |_{\theta=\frac{\pi}{2}} = \frac{h\nu}{1 + h\nu/m_0c^2} = 255.5 \text{ keV}, \quad (9.2.1)$$

where ν is the frequency of the full energy photon, ν' is the frequency of the scattered photon, m_0 is the mass of an electron and h is Planck's constant. Here an acceptance angle refers to an angle through which photon can scatter whereby it is possible a secondary interaction can occur in a neighbouring detector element, as shown in Figure 9.10a. The absolute energy as deposited in each crystal is accessible from the simulation and is shown in Figure 9.10b. This result presents a more detailed investigation of the Compton scatter energies associated with scatter events. Here a clear 511 keV photopeak energy is observed with a distribution of Compton scatter energies centred about the 255.5 keV value, as predicted by equation 9.2.1. The majority of events are shown to scatter with energies in the range 175-325 keV but with a second component of the distribution stretching from 80-420 keV. If we consider that the attenuation length of a 255.5 keV photon in LYSO is 3.9 mm [12], and the average path length of the scattered photon in the original crystal is ≈ 2 mm, then it is likely that these energies correspond to events where a second scatter has occurred in the first crystals. In this case the total energy measured in the initial detector element will be artificially increased with two, indistinguishable, energy deposits. The second scatter then escapes the initial crystal, to be detected by one of the surrounding detector elements with a reduced energy, hence contributing to the low energy tail of the distribution.

With the process well understood, it is then possible to consider the effects introduced by increasing the length of crystals in the detector element arrays as presented in Figure 9.9b.

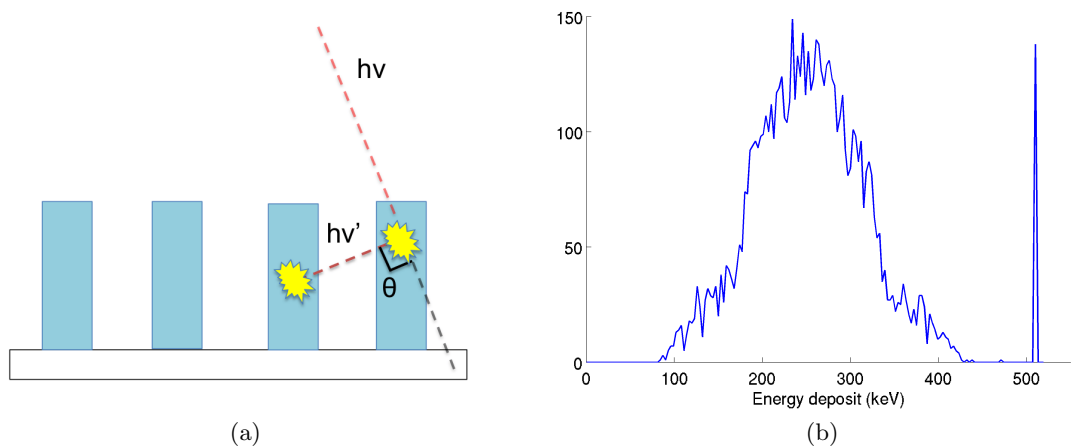


Figure 9.10: (a) Diagram of a typical Compton scatter event (b) Example distribution of absolute energy deposits as recorded in simulated three-detector events with 10 mm crystal arrays.

For a system with infinitely short crystals it can be seen by referring to Figure 9.10a that only photons scattering at a precise angle could be detected by other crystals in the array. As the crystal length is increased the range of angles through which the γ photon can scatter is increased, correlating the crystal length with an increased efficiency of three-detector events. However, for longer crystals, the increased solid angle is associated with Compton scatter angles shallower than 90° (Figure 9.10a). As the scattering angle (θ) reduces the scattered photon must traverse an increased path length through the initial crystal, proportional to $1/\sin(\theta)$. The probability of the scatter photon then re-interacting within the initial crystal is exponential in nature. Hence, the probability of scatter events escaping the original crystal will reduce proportionally with the angular deviation from 90° .

9.3 Three-detector events

In order to make use of the three-detector events, this section considers a technique for identifying and applying such events, based on a spatial acceptance cut which could be applied to an experimental arrangements. Investigations of effects on the detector system's response are then presented with respect to: energy resolution, CTR, angular resolution associated with the reconstructed LOR (identified as the parallax error in Chapter 2) and the gains in detection efficiency as measured after all energy and spatial cuts have been applied.

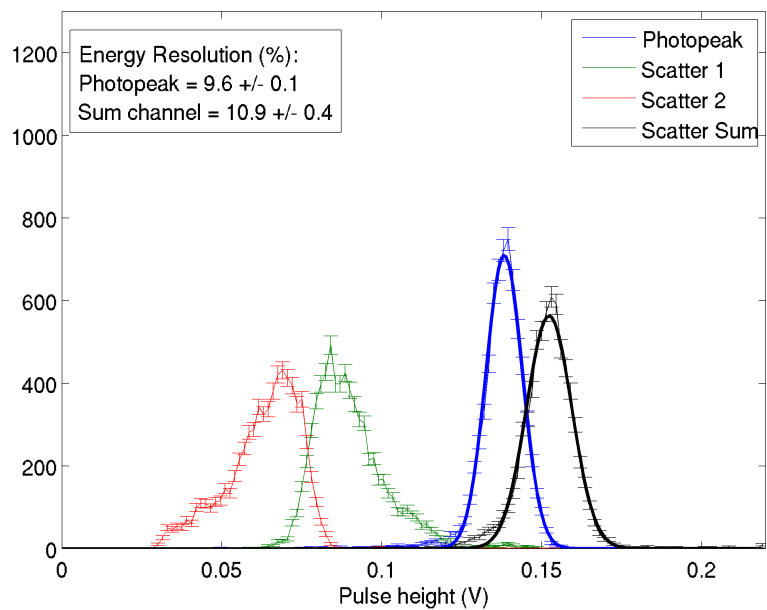
9.3.1 Energy resolution and response

In order to efficiently reject noise events associated with Scatter coincidences (see Chapter 2), it is necessary to select events based on the values of the pulse heights recorded at the detector arrays. Applying cuts for both single and multiple crystal lengths have been discussed previously in sections 9.1 and 9.2 of this chapter. In this section an algorithm is presented that extends the selection criteria to three-detector events.

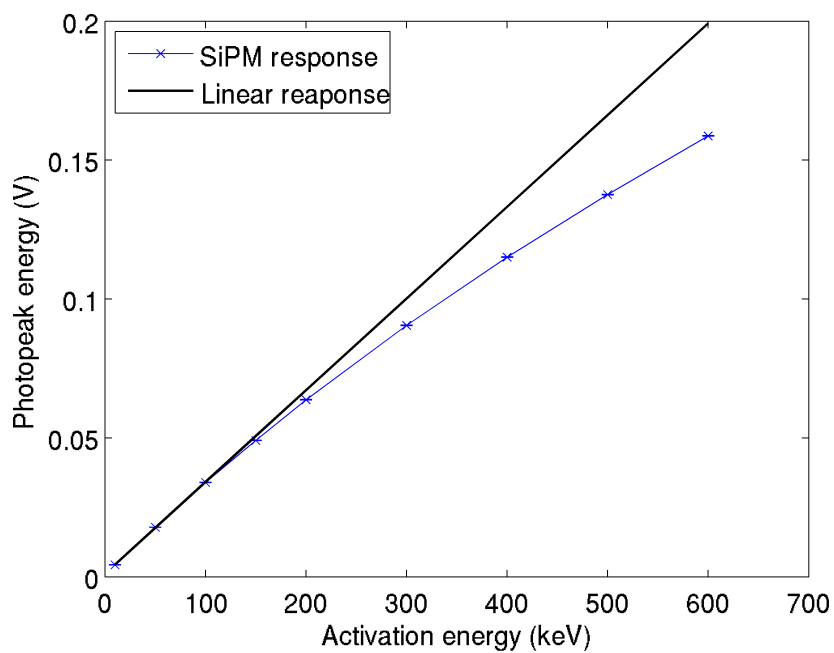
For each three-detector event stored to file, pulse heights are first sorted in height order and the pulses labelled from largest to smallest as: photopeak, scatter 1 and scatter 2 respectively (see Figure 9.11a). With a photopeak and two scatter events identified, the sum of the two scatter pulses was created, mimicking a summing circuit which may be applied experimentally. This is labelled as the scatter sum. Each of the four pulses are filtered with a second order Butterworth filter, f_c 350 MHz and pulse heights measured. The pulse height spectra for each of the four pulse types are presented in Figure 9.11a.

The first feature of note is that the scatter sum distribution has a higher energy than the single photopeak pulse height. This suggests that the SiPM is operating in saturation for the photopeak measurements. This is confirmed by Figure 9.11b. It is shown that for an interaction energy of 511 keV, significant non-linear (saturation) effects are observed. This behaviour derives from the pixellated nature of the simulated SiPM device combined with the 50 ns single pixel dead time, as described in Chapter 8. This renders the device insensitive to multiple photon interactions at a given pixel within the associated dead time. The result is that, for a photon flux where the number of photons is equivalent to, or larger than, the number of detector pixels, the detector response signal will not scale proportionally to the photon flux. Secondly, it is shown in Figure 9.11a that the summed photopeak displays a reduced energy resolution. This effect can be attributed to the distribution of scattering angles, which presents as an asymmetric distribution of the two contributing peaks (i.e. Scatter 1 and Scatter 2 in Figure 9.11a). An high energy tail is visible in Scatter 1 with no low energy equivalent in Scatter 2.

As a result of the offset measured between the photopeak and scatter sum distributions in Figure 9.11a, a separate energy cut would have to be applied for three-detector events. In an experimental environment this is an inconvenience but both online and offline solutions are possible. In the online case a a summing circuit would have to be added to the electronics architecture of a conventional PET system. Including a comparator on the output of the summing system, which can be set with limits independent of those used



(a)



(b)

Figure 9.11: (a) Pulse height spectra for three-detector events including fit results to the photopeak and the summed scatter peak. (b) Linearity response of the simulated 10 mm crystal length detector system.

with the two-detector system, will not be a significant increase in complexity or, as a result, cost. An offline solution would simply store all three-detector events and apply energy cuts before passing to reconstruction. This technique come with the caveat of significantly increasing the storage required for the raw data and likely requiring much faster write speeds to cope with the increased data rate.

9.3.2 Coincidence timing resolution

The CTR results presented here were measured with an identical method as described in section 9.1. In this case the trigger positions have been defined relative to the photopeak pulse height for the crystal length being applied.

The resulting distributions for each of the simulated crystal lengths showing CTR as a function of trigger position on the leading edge are given in Figure 9.12a. As in Figure 9.8a, it is shown that increasing the length of crystals populating the coincident arrays results in a offset in the measured CTR. This offset is shown to be linear with a gradient of ≈ 1 ps/mm in Figure 9.12b. The gradient of this fit is equivalent to the measurements made on the two-detector events (see Figure 9.8b), however an offset of 21 ps is observed between the y-intercept values from 259 ps to 280 ps, a relative change of $8\% \pm 1\%$. This offset is attributed to a combination of the spread in interaction time of the three-detector events, and the reduced photon flux associated with each of the two scatter interactions within these events increasing the contribution of σ_{Stats} . As in Figure 9.8 the error bars are over estimated, returning a $\chi^2_\nu = 0.54$. This is again attributed to correlations from systematic effects associated with the variable range of interaction positions for differing crystals lengths.

It can be concluded that the CTR response of three-detector events is only a minor degradation in comparison to the conventional two-detector coincidences. In an experimental system it is possible that additional degradations could be introduced by non-ideal electronics, however, this effect will likely still be minor compared to the potential 60% gain in signal statistics.

9.3.3 Angular resolution

One of the major contributions to the angular resolution of PET detector systems is the “parallax error”, where an uncertainty on the projected LOR is introduced due to the

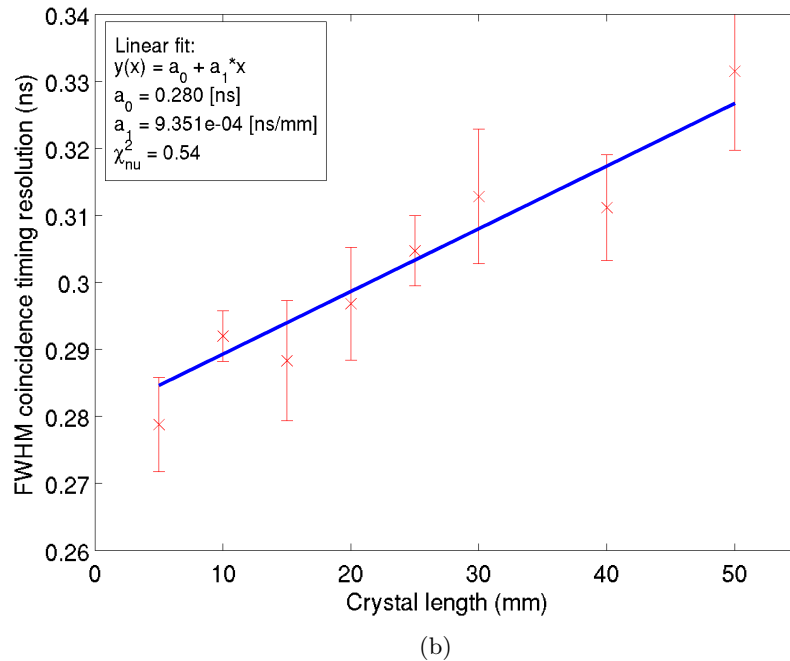
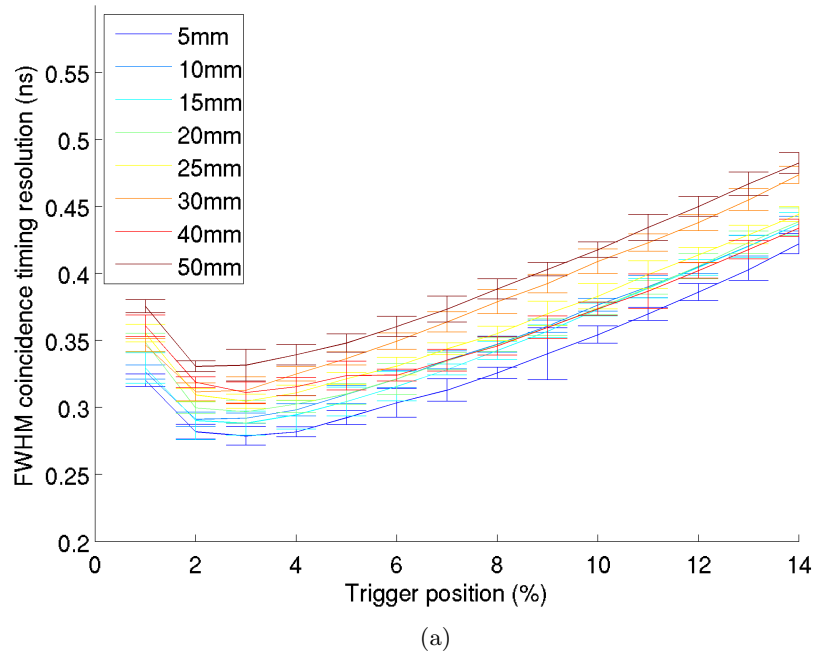


Figure 9.12: Coincidence timing resolution plots (a) CTR as a function of trigger position on the leading edge for each crystal arrangement. (b) Results as measured at the 2% threshold for each of the crystal arrangements. Here error bars are given relating to the uncertainty associated with the measurement and the additional convolution of uncertainties related to the simulation in put parameters.

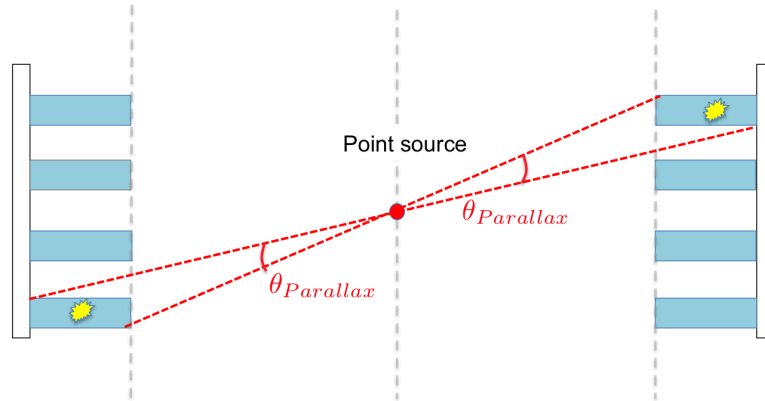


Figure 9.13: Diagram showing the parallax uncertainty introduced by the finite detector dimensions.

finite width of detector elements and the dead space between them. A diagram of this effect is given in Figure 9.13. Due to the nature of scatter events, where the energy deposit is de-localised beyond a single detector element, the parallax error is nominally increased. However, as shown in Figure 9.14a, one of the two scatter activated detectors will always return the correct line of response. If this detector can be identified through either energy or timing considerations, it is possible that three-detector events could be applied without any loss in angular resolution.

Measuring the time difference between activations is extremely difficult, as scatters typically occur over a range of millimetres, corresponding to a time of flight of ~ 10 ps. It has been shown in Figure 9.8b, that the coincident timing resolution of this detector system is in the range 260-300 ps, depending on the length of scintillator crystals applied. By considering CTR as the convolution of two single-channel timing contributions, we can consider the single detector timing resolution to be in the range 180-205 ps. As such, the timing resolution of the system is an order of magnitude too high to identify the time difference of scatter events. Then, the second option for identifying the two events is through energy considerations. The energy deposits of the two scatter events have been discussed in detail in section 9.2.3, where it has been shown in equation 9.2.1 and Figure 9.10b that the energy is shared between the two scatter interactions, with only a small asymmetry. This is an unfortunate result, there is little correlation between the energy deposit of the two scatter events and the order in which those deposits occurred. The order of the scatter events is therefore indistinguishable through either energy or timing considerations. As a result the angular resolution associated with the projected LOR for three-detector events will be degraded relative to the conventional two-detector events. In the paragraphs which

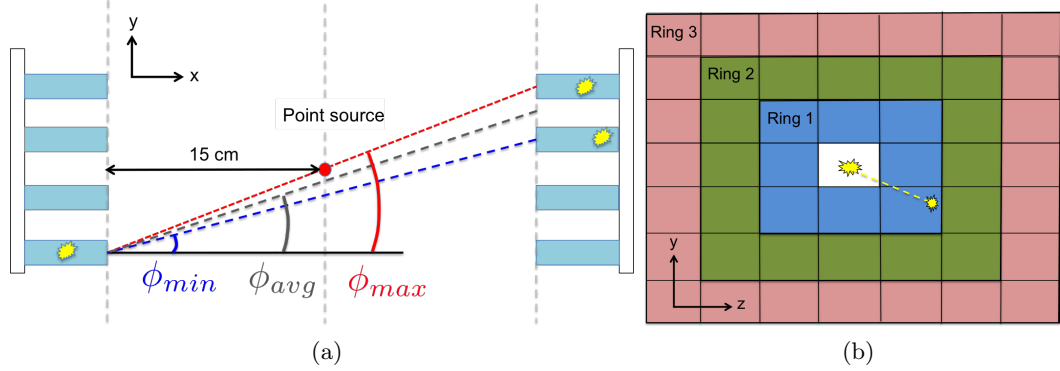


Figure 9.14: (a) Diagram showing reconstructed angles in ϕ as a result of a three-detector event. To calculate ϕ_{avg} , the central y-coordinate between the two activated pixels is considered. (b) Rings of detector elements projected about a scatter event. In this case the scatter has been contained within ring 1.

follow, an averaging technique is described which has been developed in an attempt to minimise this effect.

If we consider the process of reconstructing a LOR, we must first define a coordinate system with which the line can be described. Here the separation of the two detector arrays has been considered as the x -axis, and the columns and rows of the arrays as the y and z axis respectively. The angular resolution as investigated in this section then applies a polar coordinate system where the angle ϕ is the azimuthal angle on the x - y plane and θ is the polar from the positive z -axis. A number of observations can be made from Figure 9.14a. The first thing to notice is that the x coordinate used for each line of response is equivalent, defined as the full 30 cm detector separation. Secondly, the y coordinate defining the angle ϕ is measured relative to the centre of the detector element activated by either a photopeak or scatter event, this is also true for the z coordinate although it is not shown here. Therefore, in a scatter event it is possible to define two ϕ values, one where the angle is at a maximum and one where it is a minimum. As we have shown, no correlation between the two scatter events, and therefore these two angles, is known. As a result, without further consideration, one of these two angles would have to be chosen to define the LOR of this event. The uncertainty associated with this random choice is then the difference between ϕ_{min} and ϕ_{max} . However, if the central y -coordinate between the two detector activations is applied to give ϕ_{avg} (see Figure 9.14a), the range of angles associated with this uncertainty is reduced.

In the scenario presented in Figure 9.14a, detector elements directly adjacent to each other have been activated. Although, due to the exponential attenuation properties of γ photons, this is the most likely scenario, it is possible that scatters will be detected in

elements further away from the original interaction position, yielding a further degradation of the angular resolution associated with that event. In order to investigate the contribution of different scatter ranges a spatial trigger (or ‘cut’) system has been applied here. By projecting rings of detector elements about the scatter positions, as illustrated in Figure 9.14b, it is possible to select events with a defined spatial spread. The effects of angular resolution, and detection efficiency in the section which follows, can therefore be investigated based on events scattering within a spatial range, as defined by the number of detector rings being considered.

Measurements of the angular resolution associated with both two and three-detector events have been made by calculating the residuals of the θ and ϕ angles reconstructed from the detector activations with the precise source emission angles as recorded by the simulation. In the case of three-detector events, residuals were taken using the measured θ_{avg} and ϕ_{avg} for each event. The results are presented in Figure 9.15.

Figures 9.15a, 9.15b, 9.15c and 9.15d show histograms of the calculated residuals in the case of two-detector events and three-detector events with 1-3 ring spatial cuts respectively. The peak structures which are observed in these figures derives from the quantised nature of the reconstructed θ and ϕ angles whereby LORs are always constructed from the central y and z positions of the detector elements. Values of the FWHM and full width tenth maximum (FWTM) measured for each distribution are included in the plots. As the residual distributions do not relate to a standard distribution type these values were not measured using fits, but rather a threshold technique. With this method, thresholds were placed at half and one tenth of the maximum height of the distributions. The width at both positions was estimated as the difference between the first and last bins above each of these thresholds. Uncertainties were then measured by varying the thresholds in within $\pm 1/\sqrt{N}$ where N is the number of entries in the first bin found above threshold.

The lower bound FWTM angular resolution of the system in both θ and ϕ is presented in Figure 9.15a as $1.5^\circ \pm 0.1^\circ$ and $1.3^\circ \pm 0.1^\circ$ respectively. These values represent the parallax error as illustrated in Figure 9.13 for each of the two polar angles. The parallax uncertainty is shown to increase through Figures 9.15b-9.15d as the window on the spatial acceptance range increases. This effect is presented for a range of crystal lengths in Figures 9.16a and 9.16b where it is shown that the FWTM angular resolution associated with three-detector events in both θ (Figure 9.16a) and ϕ (Figure 9.16b) is degraded by equivalent offsets for all crystal lengths.

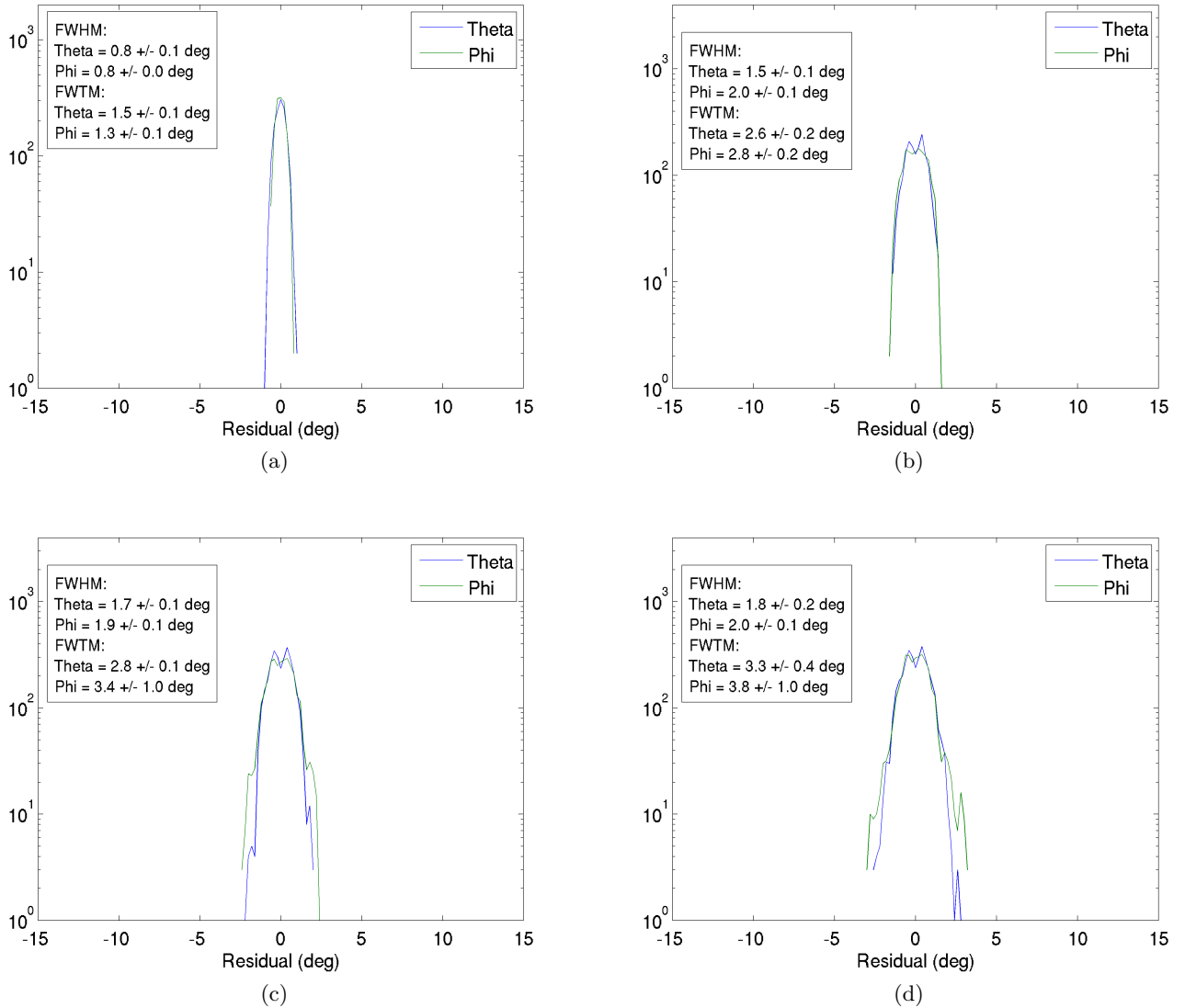


Figure 9.15: Histograms showing residuals of real and reconstructed emission angles (a) Angular resolution in both θ and ϕ for two-detector events for a system populated with 10 mm crystals. This defines the ultimate angular resolution of the system for this crystal length. (b) Angular resolution in θ and ϕ for a system populated with 10 mm crystals. One ring spatial acceptance window. (c) Angular resolution in θ and ϕ for a system populated with 10 mm crystals. Two ring spatial acceptance window. (d) Angular resolution in θ and ϕ for a system populated with 10 mm crystals. Three ring spatial acceptance window.

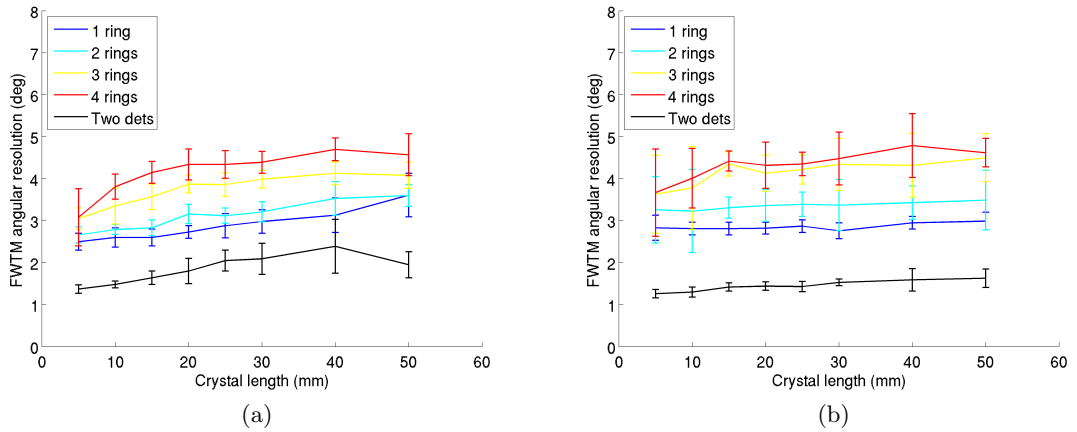


Figure 9.16: (a) FWTM resolution in θ as a function of crystal length. (b) FWTM resolution in ϕ as a function of crystal length.

As a specific example, if we consider the results for 25 mm crystal length arrays, equivalent to detector systems which may be applied in a clinical scanner, then by accepting scatter events within one, two or three detector rings, a degradation in ϕ of 0.83° , 1.07° and 2.17° is measured respectively, a relative degradation in angular resolution of 40%, 52% and 105%. All three of these values show large degradations relative to the lower limit parallax uncertainty of the system with the optimal performance shown with the most constrained spatial cuts, but with a significant jump seen from the 2-3 ring measurements. It is therefore recommended that a spatial cut of no more than two rings is applied to the final system.

9.3.4 Efficiency

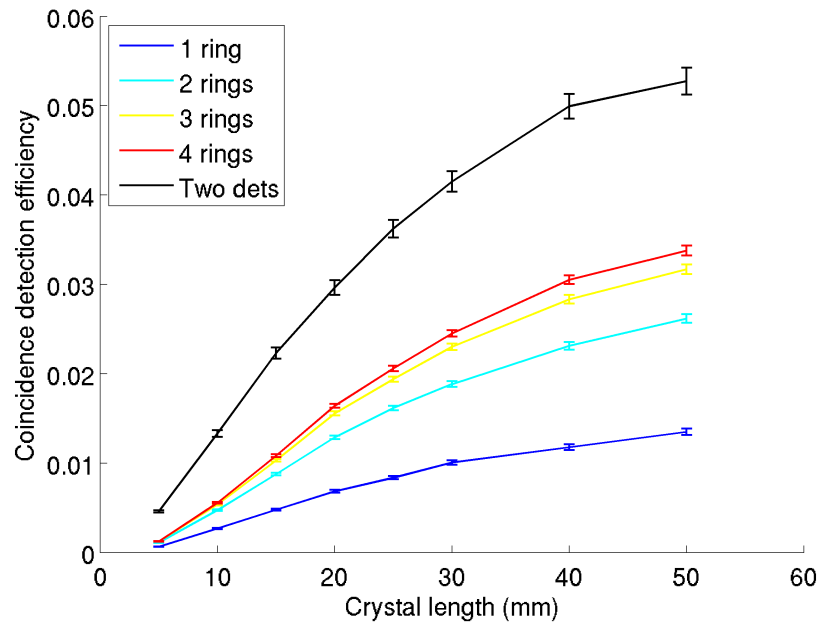
In order to optimise the system response through comparison of the relative gains and degradations associated with both the angular resolution and detection efficiency of three-detector events, the concept of detector rings (Figure 9.14b) is again applied. The efficiency distributions presented up to this point have considered the total number of two and three-detector events recorded by the simulation, whereby the full 511 keV energy of each collinear γ photon emitted in an event has been deposited at the arrays. This is a useful measure of absolute efficiencies of different system arrangements. However, in order to compare the efficiencies of the three-detector events after selection cuts have been applied, here the efficiencies presented for both two and three-detector events are quoted post cuts. In the case of two-detector events, the efficiency is given for pulse pairs where both pulses are within the FWHM of the measured photopeak energy distributions. In the

case of three-detector events the efficiency is given for the scatter events identified within the quoted number of detector rings, where both pulses are within the FWHM of the measured sum peak energy distributions. The results given in Figure 9.17a relate to the absolute efficiency of events which pass the described cuts. Figure 9.17b then presents the relative statistical gains which would result from including scatter events in the data set for reconstruction. The uncertainties quoted in Figure 9.17b are the propagated uncertainties on the two-detector absolute efficiency gain and three-detector absolute efficiency used to calculate the efficiency gains quoted.

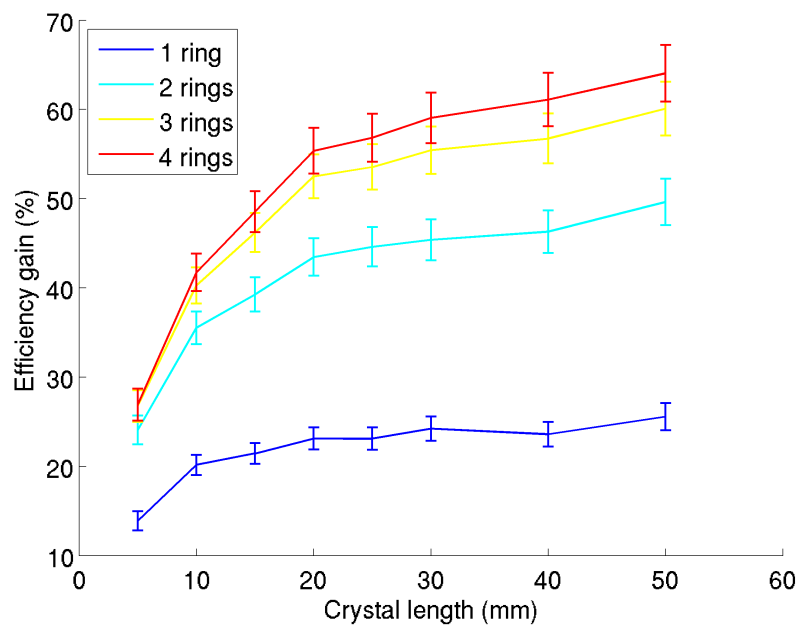
It can be concluded then from Figure 9.17b that for crystal lengths equivalent to those applied to clinical scanners (20-30 mm) statistical signal gains of upto 60% could be achieved, in the case of 3x3 mm² cross section crystals, if three-detector events could be identified and recorded. However, considering the significant reductions in the associated FWTM angular resolutions measured with three or more detector rings given in section 9.3.3, it is shown that a statistical signal gain of 23% ± 1% or 44% ± 2% can be achieved with a one or two detector ring spatial cut respectively. The final choice of one, two or three detector ring cuts is dependent on the contributions which each of the discussed parameters (i.e. energy resolution, CTR, Angular resolution and efficiency) make to the quality of the final, reconstructed image. It is hoped that this work can be extended to investigate the contributions of these effects, possibly with external collaborators, in the near future.

9.3.5 Summary and outlook

To conclude, a method has been presented whereby three-detector events could be identified using a range of spatial scatter triggers. If two scatter signals are measured within a given spatial window, the resulting SiPM response signals could be summed and energy cuts applied to reject noise events where either a non-correlated activation has occurred, or the full 511 keV has not been deposited in the two detectors. With interesting events identified, leading edge discriminator thresholds can be applied to measure timestamps from the summed scatter pulse and the photopeak pulse with a coincidence timing resolution loss of 8% ± 1% with respect to two-detector events. By varying the size of the spatial acceptance window associated with the scatter events it has been shown that a trade-off between angular resolution and the statistical signal gain associated with these events can be considered.



(a)



(b)

Figure 9.17: FWTM efficiency plots. (a) Absolute FWTM detection efficiency after both energy and spatial cuts. (b) Efficiency gains associated with the application of three-detector events as a function of crystal length.

In order to consider the limit of the spatial resolution, and therefore the quality, of the final image, it is useful to redefine the parameters which affect the spatial resolution in a PET system. The relation:

$$FWHM = k_R \cdot \sqrt{R^2 + C^2 + P^2 + B^2}, \quad (9.3.1)$$

was given previously in Chapter 2 where, R, C, P and B represent the contributions of the range effect, the photon non-collinearity, parallax error and the block effect respectively. The constant k_R is associated with the quality of the reconstruction algorithm, accounting for the range of results which may be achieved using a number of iterative or analytic reconstruction techniques [152]. In the prototype system described here, one-to-one coupling of scintillators to photodetectors has been applied, removing any contribution related to the block effect (B). Both the range effect (R) and the photon non-collinearity (C) are physics effects which cannot be removed from the system. The FWHM spatial resolution of the prototype system presented here is therefore limited by the parallax error (angular resolution) of the data set, but can be scaled with the constant k_R by choosing the reconstruction algorithm carefully.

As described previously in Chapter 2, the most common reconstruction techniques applied to modern PET scanners use an iterative method where the full statistical sample of the signal is considered over a number of iterations to converge towards the highest possible resolution image [152] [153] [154]. Here the speed of the convergence is proportional to both the total signal statistics and the signal-to-noise of the data set. With this in mind, a strategy may be to include the additional sample obtained by considering the three-detector events for some number of initial iterations, to aide with fast convergence of a given algorithm. These events could then be removed from the iterative data set for the final iterations, so that image quality can be optimised using only the data with optimum angular resolution. As the inclusion of three-detector events has no impact on the system detection of two-detector events, the image quality would therefore be identical to what can be obtained using conventional techniques, but could be made to converge more quickly and with fewer total iterations.

This scheme could translate to a number of operational advantages while yielding the same quality final signal, including:

- Reduced patient scan times.

- Reduced patient dose.
- Reduced crystal lengths as a cost saving option.

Although not a specific operational advantage the scintillator crystals are typically the most expensive components in a PET detector system. If the total scintillator volume could be reduced and signal statistics achieved equivalent to the current system's costs could be reduced.

An extension to the work presented here would then investigate the possibility of applying such a reconstruction algorithm. If a test algorithm could be developed with a manufacturer of clinical PET machines, optimisations of a prototype system could be investigated in detail with the simulation framework presented here. The full effects of the degraded angular resolution could then be defined in terms directly applicable to a clinical environment and the gains in processing times through the increased statistics quantified.

Chapter 10

Conclusions

The main focus of this thesis is to study the timing performance of a prototype detector system consisting of inorganic scintillating materials, read out by silicon photomultipliers. To this end, the performance of a number of SiPM devices, each with a finite sensitivity to 420 nm light, have been tested. Through comparison of a number of characteristic performance parameters, the Hamamatsu S10362-33-050C SiPM was selected for use in a prototype TOF-PET detection system. It has been shown that, by one-to-one coupling $3 \times 3 \times 5 \text{ mm}^3$ LYSO scintillating crystals to the selected Hamamatsu S10362-33-050C SiPMs, a CTR of $290 \pm 10 \text{ ps}$ can be achieved experimentally with little or no system optimisation. Comparing this result to the $527.5 \pm 4.9 \text{ ps}$ CTR measured with current generation clinical TOF-PET detector systems [3], it is clear that this arrangement can be considered a strong candidate for application in TOF-PET.

The performance of this detector system has been further investigated through the development of a simulation framework which recreates the CTR of coincident detector elements to be $273 \pm 43 \text{ ps}$, equivalent to experimental measurements to within 1.4σ . It has been shown that the simulation provides an accurate model of the extended distribution of CTR as a function of trigger position on the leading edge. The simulation has been scaled to full detector arrays and has hence been used to provide a number of design recommendations to the experimental group at RAL where a prototype system is being developed. Without the results provided here a detector system including only $3 \times 3 \times 5 \text{ mm}^3$ crystals would have been adopted, which is shown to provide little-to-no timing advantage over an identical system with $3 \times 3 \times 10 \text{ mm}^3$ crystals, where detection efficiency is improved by approximately a factor of three. First results from this prototype are expected at the end of summer 2014.

As part of the detector parametrisation studies, it has been identified that significant gains of 20-60% could be achieved in the signal statistics if events where an internal Compton scatter within a detector array can be identified. Although extremely promising, these events can only be measured with a significantly degraded angular resolution. The angular resolution associated with the LORs projected in a coincidence activation is directly proportional to the spatial resolution achievable in the final reconstructed image. It has been shown that by applying cuts on the spatial spread of the Compton scatter interactions, a trade off can be considered between optimising for either additional signal or angular / spatial resolution.

There are therefore a number of extensions to this work which would be explored if more time was available:

- Compare results obtained with the prototype system to simulated predictions. This is an important step in further validating the simulation response. If, in particular, separate data runs can be taken for the two heads, populated by a number of varying crystal lengths, correlations of experimental CTR with crystal length could be produced. This result could be used to further tune the simulation response and further optimise the performance of the prototype.
- Approach an industrial medical imaging partner. Reconstruction algorithms for PET are often extremely complex packages, requiring significant computer resources and very specific input files which describe environmental variables or attenuation properties of the detector system used to acquire the data set. Developing a new algorithm, flexible enough to consider the additional (three detector) inputs, from scratch, requires both expertise in this particular field and a large number of man hours. An industrial partner, with previous experience of developing similar algorithms, would be the most efficient path to move forward. If an algorithm could be developed, then investigations in to the most efficient application of the three detector events could fully quantified.
- Extend experimental and simulated DOI measurements. It has been shown in the work presented here that high aspect ratio crystals are subject to DOI effects which influence σ_{trans} and, more fundamentally for PET applications, also contributes to the parallax uncertainty. Extended experimental DOI measurements could be run using a number of different crystal surface finishes, ideally in partnership with a crystal manufacturer. Results of these experiments could identify correlations

between surface finishes and specific detector system response characteristics (e.g. timing resolution and energy resolution) and be used to further refine the simulation response.

Additionally, if much larger, monolithic scintillators are to be applied, the effects of reflections would be minimised and the spatial distributions of the light reaching the detector array could be calibrated to identify the DOI of a photon in the crystal. The proof of concept for this technique can be investigated with the simulation framework presented here and, if results are promising, experimental validation could be provided by the prototype system at RAL.

In summary, the body of work presented in this thesis has provided a number of design recommendations, each of which have been implemented in a prototype TOF-PET detector system under construction at RAL. With a simulation framework available, extension investigations have been identified which could further refine the recommendations for one-to-one coupled detector arrays, in mind of efficiently applying novel data sets to PET reconstruction.

In the weeks which follow the submission of this thesis, first results from the prototype will become available. These results will be sent to prospective industrial partners in hope that a collaboration can be formed in mind of further extending the impact of the foundation of work presented here.

Bibliography

- [1] P K Spiegel. The first clinical X-ray made in America–100 years. *AJR. American journal of roentgenology*, 164(1):241–3, January 1995. [1](#)
- [2] Valeri Saveliev. Silicon Photomultiplier-New Era of Photon Detection. *cdn.intechopen.com*, 1995(January), 2010. [1](#)
- [3] B W Jakoby, Y Bercier, M Conti, M E Casey, B Bendriem, and D W Townsend. Physical and clinical performance of the mct time-of-flight PET/CT scanner. *Phys. Med. Biol.*, 56(8):2375–2389, Apr 2011. [2](#), [5](#), [191](#)
- [4] Lisa Mosconi, Valentina Berti, Lidia Glodzik, Alberto Pupi, Susan De Santi, and Mony J de Leon. Pre-clinical detection of Alzheimer’s disease using FDG-PET, with or without amyloid imaging. *Journal of Alzheimer’s disease : JAD*, 20(3):843–54, January 2010. [3](#)
- [5] W H Theodore, S Sato, C Kufta, M B Balish, E B Bromfield, and D B Leiderman. Temporal lobectomy for uncontrolled seizures: the role of positron emission tomography. *Annals of neurology*, 32(6):789–94, December 1992. [3](#)
- [6] Thomas H Schindler, Heinrich R Schelbert, Alessandra Quercioli, and Vasken Dilisizian. Cardiac PET imaging for the detection and monitoring of coronary artery disease and microvascular health. *JACC. Cardiovascular imaging*, 3(6):623–40, June 2010. [3](#)
- [7] Yusuf Emre Erdi. The Use of PET for Radiotherapy. *Current Medical Imaging Reviews*, 3(1):3–16, February 2007. [3](#)
- [8] <https://wiki.engr.illinois.edu/display/BI0E414/PET+Scanner+Overview>. [4](#)
- [9] Glenn F Knoll. *Radiation Detection and Measurement*. John Wiley & Sons., 1999. [6](#), [9](#), [11](#), [12](#), [13](#), [31](#), [48](#), [67](#)

- [10] James W Fletcher, Benjamin Djulbegovic, Heloisa P Soares, Barry a Siegel, and Val J et al. Lowe. Recommendations on the use of 18F-FDG PET in oncology. *Journal of nuclear medicine : official publication, Society of Nuclear Medicine*, 49(3):480–508, March 2008. 7
- [11] P Zanzonico. Positron emission tomography: a review of basic principles, scanner design and performance, and current systems. *Seminars in Nuclear Medicine*, 34(2):87–111, April 2004. 7
- [12] <http://physics.nist.gov/PhysRefData/Xcom/html/xcom1.html>. 10, 167, 176
- [13] Kenneth D. Sevier. Atomic electron binding energies. *Atomic Data and Nuclear Data Tables*, 24(4):323–371, October 1979. 11
- [14] Z H Cho and M R Farukhi. Bismuth Germanate as a Potential Scintillation Detector in Positron Cameras. *Journal of nuclear medicine*, 18:840–844, 1977. 14
- [15] B K Lubsandorzhev. On the history of photomultiplier tube invention. *Nucl. Instrum. Meth.*, A567(095):236–238, January 2006. 14, 47
- [16] P Buzhan, B Dolgoshein, and A Ilyin. An advanced study of Silicon Photomultiplier. *ICFA Instrumentation*, 23:28–41, 2001. 14, 54
- [17] P. Buzhan, B. Dolgoshein, L. Filatov, a. Ilyin, V. Kantzerov, V. Kaplin, a. Karakash, F. Kayumov, S. Klemin, E. Popova, and S. Smirnov. Silicon photomultiplier and its possible applications. *Nuclear Instruments and Methods in Physics Research Section A: Accelerators, Spectrometers, Detectors and Associated Equipment*, 504(1-3):48–52, May 2003. 14
- [18] B. Dolgoshein, V. Balagura, P. Buzhan, M. Danilov, L. Filatov, E. Garutti, M. Groll, a. Ilyin, V. Kantserov, V. Kaplin, a. Karakash, F. Kayumov, S. Klemin, V. Korbel, H. Meyer, R. Mizuk, V. Morgunov, E. Novikov, P. Pakhlov, E. Popova, V. Rusinov, F. Sefkow, E. Tarkovsky, and I. Tikhomirov. Status report on silicon photomultiplier development and its applications. *Nuclear Instruments and Methods in Physics Research Section A: Accelerators, Spectrometers, Detectors and Associated Equipment*, 563(2):368–376, July 2006. 14
- [19] Erika Garutti. Silicon Photomultipliers for High Energy Physics Detectors. August 2011. 14

- [20] Tom K Lewellen. Recent developments in PET detector technology. *Physics in medicine and biology*, 53(17):R287–317, September 2008. [14](#)
- [21] Bernd J Pichler, Hans F Wehrl, and Martin S Judenhofer. Latest advances in molecular imaging instrumentation. *Journal of nuclear medicine : official publication, Society of Nuclear Medicine*, 49 Suppl 2:5S–23S, July 2008. [14](#), [15](#), [16](#), [23](#), [101](#)
- [22] Virginia Ch Spanoudaki and Craig S Levin. Photo-detectors for time of flight positron emission tomography (ToF-PET). *Sensors (Basel, Switzerland)*, 10(11):10484–505, January 2010. [xiii](#), [14](#), [56](#)
- [23] JS Lee. Technical advances in current PET and hybrid imaging systems. *Open Nucl Med J*, 2:192–208, 2010. [14](#)
- [24] M E Casey and R Nutt. A Multicrystal Two Dimensional BGO Detector System for Positron Emission Tomography. *IEEE Transactions on Nuclear Science*, 33(1):460–463, 1986. [15](#)
- [25] Todd E Peterson and Lars R Furenlid. SPECT detectors: the Anger Camera and beyond. *Physics in medicine and biology*, 56(17):R145–82, September 2011. [15](#)
- [26] Robert Eisberg and Robert Resnick. *Quantum Physics of Atoms, Molecules, Solids, Nuclei, and Particles*. Wiley, 1985. [16](#), [18](#)
- [27] S. DeBenedetti, C. Cowan, W. Konneker, and H. Primakoff. On the Angular Distribution of Two-Photon Annihilation Radiation. *Physical Review*, 77(2):205–212, January 1950. [16](#)
- [28] W.W. Moses, P.R.G. Virador, S.E. Derenzo, R.H. Huesman, and T.F. Budinger. Design of a high-resolution, high-sensitivity PET camera for human brains and small animals. *IEEE Transactions on Nuclear Science*, 44(4):1487–1491, 1997. [18](#)
- [29] John L Humm, Anatoly Rosenfeld, and Alberto Del Guerra. From PET detectors to PET scanners. *European journal of nuclear medicine and molecular imaging*, 30(11):1574–97, November 2003. [20](#), [49](#), [50](#), [51](#), [101](#), [156](#), [162](#), [170](#)
- [30] D W Townsend. Physical principles and technology of clinical PET imaging. *Annals of the Academy of Medicine, Singapore*, 33(2):133–45, March 2004. [20](#)
- [31] Gabriele Tarantola, Felicia Zito, and Paolo Gerundini. PET instrumentation and

- reconstruction algorithms in whole-body applications. *Journal of nuclear medicine : official publication, Society of Nuclear Medicine*, 44(5):756–69, May 2003. [20](#)
- [32] Maurizio Conti. State of the art and challenges of time-of-flight PET. *Physica medica : PM : an international journal devoted to the applications of physics to medicine and biology : official journal of the Italian Association of Biomedical Physics (AIFB)*, 25(1):1–11, March 2009. [22](#), [23](#)
- [33] P. Geramifar, M.R. Ay, M. Shamsaie Zafarghandi, S. Sarkar, G. Loudos, and a. Rahmim. Investigation of time-of-flight benefits in an LYSO-based PET/CT scanner: A Monte Carlo study using GATE. *Nuclear Instruments and Methods in Physics Research Section A: Accelerators, Spectrometers, Detectors and Associated Equipment*, 641(1):121–127, June 2011. [22](#)
- [34] Dimitri Papathanassiou, Claire Bruna-Muraille, Jean-Claude Liehn, Tan Dat Nguyen, and Hervé Curé. Positron Emission Tomography in oncology: present and future of PET and PET/CT. *Critical reviews in oncology/hematology*, 72(3):239–54, December 2009. [23](#)
- [35] Frederic H Fahey. Data acquisition in PET imaging. *Journal of nuclear medicine technology*, 30(2):39–49, June 2002. [24](#)
- [36] Adam Alessio and Paul Kinahan. PET image reconstruction. *Nuclear Medicine*, 1(figure 1):1–22, 2006. [25](#), [26](#)
- [37] D S Lalush and B M Tsui. Performance of ordered-subset reconstruction algorithms under conditions of extreme attenuation and truncation in myocardial SPECT. *Journal of nuclear medicine : official publication, Society of Nuclear Medicine*, 41(4):737–44, April 2000. [25](#)
- [38] Defrise M. Townsend DW. Image reconstruction methods in positron tomography. Technical report, CERN (European Organization for Nuclear Research) Report 93-0.2, 1993. [27](#)
- [39] AP Dempster, NM Laird, and DB Rubin. Maximum Likelihood from Incomplete Data via the EM Algorithm By. *Journal of the Royal Statistical Society. Series B (Methodological)*, 39(1):1–38, 1977. [27](#)
- [40] Robert E Henkin. *Nuclear Medicine*. Mosby, 2 edition, 2006. [28](#)

- [41] L a Shepp and Y Vardi. Maximum likelihood reconstruction for emission tomography. *IEEE transactions on medical imaging*, 1(2):113–22, January 1982. [28](#)
- [42] H M Hudson and R S Larkin. Accelerated image reconstruction using ordered subsets of projection data. *IEEE transactions on medical imaging*, 13(4):601–9, January 1994. [28](#)
- [43] CWE Van Eijk. Development of inorganic scintillators. *Nuclear Instruments and Methods in Physics Research . . .*, 392:285–290, 1997. [29](#)
- [44] G. Bizarri. Scintillation mechanisms of inorganic materials: From crystal characteristics to scintillation properties. *Journal of Crystal Growth*, 312(8):1213–1215, April 2010. [31](#), [32](#), [33](#)
- [45] W C Barber. Inelastic electron scattering. *Annual Review of Nuclear Science*, 12(1):1,Äì42, Dec 1962. [31](#)
- [46] C Pedrini. Scintillation Mechanisms and Limiting Factors on Each Step of Relaxation of Electronic Excitations. *Physics of the Solid State*, 47(8):1406–1411, 2005. [32](#)
- [47] J.E. Jaffe, D.V. Jordan, and a.J. Peurrung. Energy nonlinearity in radiation detection materials: Causes and consequences. *Nuclear Instruments and Methods in Physics Research Section A: Accelerators, Spectrometers, Detectors and Associated Equipment*, 570(1):72–83, January 2007. [33](#)
- [48] S.E. Derenzo, M.J. Weber, E. Bourret-Courchesne, and M.K. Klintonberg. The quest for the ideal inorganic scintillator. *Nuclear Instruments and Methods in Physics Research Section A: Accelerators, Spectrometers, Detectors and Associated Equipment*, 505(1-2):111–117, June 2003. [33](#)
- [49] Claude a. Klein. Bandgap Dependence and Related Features of Radiation Ionization Energies in Semiconductors. *Journal of Applied Physics*, 39(4):2029, 1968. [33](#)
- [50] William M. Yen. General factors governing the efficiency of luminescence devices. *Optical Materials*, 27(11):1647–1652, October 2005. [35](#)
- [51] Lecoq P. *Inorganic scintillators for detector systems: physical principles and crystal engineering*. Springer, 2006. [35](#), [38](#)
- [52] R. F. Post and L. I. Schiff. Statistical limitations on the resolving time of a scintillation counter. *Physical Review*, (x):5, 1950. [35](#), [41](#), [117](#), [133](#)

- [53] A.L. Lacaita, F. Zappa, S. Bigliardi, and M. Manfredi. Improved timing with NaI(Tl). *Nuclear Science, IEEE Transactions on*, (1):140–147, 1966. [35](#), [42](#), [117](#), [133](#), [134](#)
- [54] S Seifert. Accurate measurements of the rise and decay times of fast scintillators with solid state photon counters. In *Nuclear Science Symposium Conference Record (NSS/MIC)*,, pages 1736–1739, 2010. [36](#), [42](#), [124](#)
- [55] Yiping Shao. A new timing model for calculating the intrinsic timing resolution of a scintillator detector. *Physics in medicine and biology*, 52(4):1103–17, February 2007. [36](#), [42](#), [99](#), [133](#), [134](#)
- [56] P. Dorenbos, J.T.M. de Haas, and C.W.E. van Eijk. Non-proportionality in the scintillation response and the energy resolution obtainable with scintillation crystals. *IEEE Transactions on Nuclear Science*, 42(6):2190–2202, 1995. [37](#), [38](#)
- [57] William W. Moses, Stephen E. Derenzo, and Thomas F. Budinger. PET detector modules based on novel detector technologies. *Nuclear Instruments and Methods in Physics Research Section A: Accelerators, Spectrometers, Detectors and Associated Equipment*, 353(1-3):189–194, December 1994. [38](#)
- [58] WW Moses and SE Derenzo. Scintillators for positron emission tomography. In *LBL - 37720*, 1995. [38](#), [40](#), [101](#)
- [59] M. Kronberger. *Optimization of the light extraction from heavy inorganic scintillators*. PhD thesis, 2008. [xiii](#), [39](#)
- [60] Stefan Seifert, Herman T van Dam, and Dennis R Schaart. The lower bound on the timing resolution of scintillation detectors. *Physics in medicine and biology*, 57(7):1797–1814, March 2012. [40](#), [99](#), [101](#), [117](#)
- [61] Saint-Gobain. Datasheet. <http://www.detectors.saint-gobain.com/PreLude420.aspx>, 2010. [42](#), [97](#), [121](#), [124](#)
- [62] P. Achenbach, C. Ayerbe Gayoso, J. Bernauer, R. Böhm, and M.O. et al. Distler. Measurement of propagation time dispersion in a scintillator. *Nuclear Instruments and Methods in Physics Research Section A: Accelerators, Spectrometers, Detectors and Associated Equipment*, 578(1):253–260, July 2007. [43](#), [99](#)
- [63] Saint-Gobain. Detector assembly materials. goo.gl/jUIueY, 2010. [45](#)
- [64] Stefan Seifert and Ruud Vinke. Ultra precise timing with SiPM-based TOF

- PET scintillation detectors. In *Nuclear Science Symposium Conference Record (NSS/MIC), 2009 IEEE*, pages 2329–2333, 2009. [46](#), [170](#)
- [65] F. Powolny, E. Auffray, S. E. Brunner, E. Garutti, and M. et al. Goettlich. Time-Based Readout of a Silicon Photomultiplier (SiPM) for Time of Flight Positron Emission Tomography (TOF-PET). *IEEE Transactions on Nuclear Science*, 58(3):597–604, June 2011. [46](#), [118](#)
- [66] Martin Janecek and WW Moses. Optical reflectance measurements for commonly used reflectors. *Nuclear Science, IEEE Transactions . . .*, 55(4):2432–2437, 2008. [46](#), [103](#), [104](#)
- [67] Dieter Renker. Properties of avalanche photodiodes for applications in high energy physics, astrophysics and medical imaging. *Nuclear Instruments and Methods in Physics Research Section A: Accelerators, Spectrometers, Detectors and Associated Equipment*, 486(1-2):164–169, June 2002. [52](#)
- [68] D. Wilkinson. The Geiger Discharge. *Physical Review*, 74(10):1417–1429, November 1948. [53](#)
- [69] Junji Haba. Status and perspectives of Pixelated Photon Detector (PPD). *Nuclear Instruments and Methods in Physics Research Section A: Accelerators, Spectrometers, Detectors and Associated Equipment*, 595(1):154–160, September 2008. [53](#), [54](#), [66](#)
- [70] Z. Sadygov. Russian Agency for Patents and Trademarks, #2102820, 1998. [53](#)
- [71] V. Golovin. Russian Agency for Patents and Trademarks, #2142175, 1998. [53](#)
- [72] Claudio Piemonte. A new Silicon Photomultiplier structure for blue light detection. *Nuclear Instruments and Methods in Physics Research Section A: Accelerators, Spectrometers, Detectors and Associated Equipment*, 568(1):224–232, November 2006. [57](#), [63](#)
- [73] R. J. McIntyre. Theory of microplasma instability in silicon. *Journal of Applied Physics*, 32:983–995, 1961. [57](#)
- [74] R. H. Haitz. Model for the electrical behavior of a microplasma. *Journal of Applied Physics*, 35:1370, 1964. [57](#)
- [75] Paola Avella, Antonella De Santo, and Annika Lohstroh. A study of timing properties of Silicon Photomultipliers. *Nuclear Instruments and Methods in Physics Re-*

- search Section A: Accelerators, Spectrometers, Detectors and Associated Equipment*, 2012. [58](#), [59](#), [81](#), [84](#), [90](#), [92](#), [93](#), [109](#)
- [76] F. Corsi, a. Dragone, C. Marzocca, a. Del Guerra, and P. et al. Delizia. Modelling a silicon photomultiplier (SiPM) as a signal source for optimum front-end design. *Nuclear Instruments and Methods in Physics Research Section A: Accelerators, Spectrometers, Detectors and Associated Equipment*, 572(1):416–418, March 2007. [59](#)
- [77] Hamamastu. http://www.hamamatsu.com/resources/pdf/ssd/mppc_kapd0002e.pdf. [59](#), [121](#), [127](#), [129](#), [130](#)
- [78] Hamamastu. MPPC Datasheet. Technical report. [59](#), [70](#)
- [79] V.D. Kovaltchouk, G.J. Lolos, Z. Papandreou, and K. Wolbaum. Comparison of a silicon photomultiplier to a traditional vacuum photomultiplier. *Nuclear Instruments and Methods in Physics Research Section A: Accelerators, Spectrometers, Detectors and Associated Equipment*, 538(1-3):408–415, February 2005. [60](#)
- [80] PK Lightfoot. Characterisation of a silicon photomultiplier device for applications in liquid argon based neutrino physics and dark matter searches. *Journal of Instrumentation*, 44(0), 2008. [60](#)
- [81] Yuri Musienko. Advances in multipixel Geiger-mode avalanche photodiodes (silicon photomultipliers). *Nuclear Instruments and Methods in Physics Research Section A: Accelerators, Spectrometers, Detectors and Associated Equipment*, 598(1):213–216, January 2009. [61](#), [64](#), [67](#)
- [82] Jelena Ninković. Recent developments in silicon photomultipliers. *Nuclear Instruments and Methods in Physics Research Section A: Accelerators, Spectrometers, Detectors and Associated Equipment*, 580(2):1020–1022, October 2007. [61](#)
- [83] WG Oldham. Triggering phenomena in avalanche diodes. *IEEE Transactions on Electron Devices*, 19(9):1056 – 1060, 1972. [62](#)
- [84] W.N. Grant. Electron and hole ionization rates in epitaxial silicon at high electric fields. *Solid-State Electronics*, 16(10):1189–1203, October 1973. [62](#)
- [85] R. Van Overstraeten and H. De Man. MEASUREMENT OF THE IONIZATION RATES IN DIFFUSED SILICON p-n JUNCTIONS. *Solid-State Electronics*, 13:583–608, 1970. [62](#)
- [86] <https://www.hamamatsu.com>. [xiii](#), [64](#)

- [87] <http://www.sensl.com>. xiii, 64
- [88] D. Renker. Geiger-mode avalanche photodiodes, history, properties and problems. *Nuclear Instruments and Methods in Physics Research Section A: Accelerators, Spectrometers, Detectors and Associated Equipment*, 567(1):48–56, November 2006. 64
- [89] P. Buzhan, B. Dolgoshein, L. Filatov, a. Ilyin, and V. et al. Kaplin. Large area silicon photomultipliers: Performance and applications. *Nuclear Instruments and Methods in Physics Research Section A: Accelerators, Spectrometers, Detectors and Associated Equipment*, 567(1):78–82, November 2006. 64
- [90] G. Collazuol, M.G. Bisogni, S. Marcatili, C. Piemonte, and a. Del Guerra. Studies of silicon photomultipliers at cryogenic temperatures. *Nuclear Instruments and Methods in Physics Research Section A: Accelerators, Spectrometers, Detectors and Associated Equipment*, 628(1):389–392, February 2011. 64, 65
- [91] Gerhard Lutz. *Semiconductor Radiation Detectors*. Springer, 1999. 65
- [92] Sergio Cova and A Lacaita. Trapping phenomena in avalanche photodiodes on nanosecond scale. *Electron Device Letters*, 12(12):685–687, 1991. 66
- [93] Y. Du and F. Retière. After-pulsing and cross-talk in multi-pixel photon counters. *Nuclear Instruments and Methods in Physics Research Section A: Accelerators, Spectrometers, Detectors and Associated Equipment*, 596(3):396–401, November 2008. 66, 128, 137
- [94] A.L. Lacaita, F. Zappa, S. Bigliardi, and M. Manfredi. On the bremsstrahlung origin of hot-carrier-induced photons in silicon devices. *IEEE Transactions on Electron Devices*, 40(3):577–582, March 1993. 67
- [95] D. Renker. New developments on photosensors for particle physics. *Nuclear Instruments and Methods in Physics Research Section A: Accelerators, Spectrometers, Detectors and Associated Equipment*, 598(1):207–212, January 2009. 68
- [96] V. Andreev, V. Balagura, B. Bobchenko, P. Buzhan, and J. et al. Cvach. A high-granularity scintillator calorimeter readout with silicon photomultipliers. *Nuclear Instruments and Methods in Physics Research Section A: Accelerators, Spectrometers, Detectors and Associated Equipment*, 540(2-3):368–380, March 2005. 68
- [97] F. Zappa, S. Tisa, a. Tosi, and S. Cova. Principles and features of single-photon

- avalanche diode arrays. *Sensors and Actuators A: Physical*, 140(1):103–112, October 2007. 69
- [98] S. Cova, M. Ghioni, a. Lotito, I. Rech, and F. Zappa. Evolution and prospects for single-photon avalanche diodes and quenching circuits. *Journal of Modern Optics*, 51(9-10):1267–1288, January 2004. 69
- [99] <http://www.ecnmag.com/articles/2012/05/choose-right-daq-board>. 73
- [100] Les Thede. *Practical analogue and digital filter design*. Artech House, 2004. 74
- [101] Schilling R. Heinzl G., Rudiger A. Spectrum and spectral density estimation by the discrete fourier transform (dft), including a comprehensive list of window functions and some new flat-top windows. <http://edoc.mpg.de/395068>, 2002. 76, 84
- [102] *Discrete-Time Signal Processing*. Prentice Hall, 2nd edition, 1999. 76, 77
- [103] MATLAB and Statistics Toolbox Release 2012b, The MathWorks, Inc., Natick, Massachusetts, United States. 78
- [104] ENVISION. <http://envision.web.cern.ch/ENVISION/>. 79, 80
- [105] K Parodi, W Enghardt, and T Haberer. In-beam PET measurements of β + radioactivity induced by proton beams. *Physics in Medicine and Biology*, 47(1):21–36, January 2002. 80
- [106] Photonique. http://www.photonique.ch/Prod_AMP_0600.html. 81, 83, 84
- [107] PicoQuant. Pls series datasheet. http://www.picoquant.com/images/uploads/downloads/pls_series.pdf, 2010. 81
- [108] Private communications with Prof. Boris Vojnovic. The Gray Institute for Radiation Oncology and Biology at the University of Oxford. 82, 83
- [109] Patrick Eckert, Hans-Christian Schultz-Coulon, Wei Shen, Rainer Stamen, and Alexander Tadday. Characterisation studies of silicon photomultipliers. *Nuclear Instruments and Methods in Physics Research Section A: Accelerators, Spectrometers, Detectors and Associated Equipment*, 620(2-3):217–226, August 2010. 89, 128
- [110] Stefan Seifert, Herman T Van Dam, Jan Huizenga, Ruud Vinke, Peter Dendooven, Herbert Löhner, and Dennis R Schaart. Simulation of Silicon Photomultiplier Signals. *IEEE Transactions on Nuclear Science*, 56(6):3726–3733, 2009. 90

- [111] Alexis Rochas, A.R. Pauchard, P.-A. Besse, Dragan Pantic, Zoran Prijic, and R.S. Popovic. Low-noise silicon avalanche photodiodes fabricated in conventional CMOS technologies. *IEEE Transactions on Electron Devices*, 49(3):387–394, March 2002. [93](#)
- [112] Koei Yamamoto, Kazuhisa Yamamura, Kenichi Sato, and Shogo Kamakura. Newly developed semiconductor detectors by Hamamatsu. In *Proceedings of Science (PD07)*, 2007. [94](#)
- [113] P Lecoq, E Auffray, S Brunner, H Hillemanns, P Jarron, A Knapitsch, T Meyer, and F Powolny. Factors Influencing Time Resolution of Scintillators and Ways to Improve them. In *IEEE Nuclear Science Symposium Conference Record*, pages 1880–1885, 2009. [99](#), [101](#), [117](#)
- [114] WS Choong. The timing resolution of scintillation-detector systems: Monte Carlo analysis. *Physics in medicine and biology*, 54(21), 2009. [99](#)
- [115] Gerd Muehlehner and Joel S Karp. Positron emission tomography. *Physics in medicine and biology*, 51(13):R117–37, July 2006. [101](#)
- [116] C.S. Levin, L.R. MacDonald, M.P. Tornai, E.J. Hoffman, and J Park. Optimizing light collection from thin scintillators used in a beta-ray camera for surgical use. *IEEE Transactions on Nuclear Science*, 43(3):2053–2060, June 1996. [103](#)
- [117] SensL. http://www.sensl.com/downloads/ds/TN-Crystal_wrapping_TN_v1p2.pdf. [104](#)
- [118] Laboratoire National Henri Becquerel (LNHB) web site resources. http://www.nucleide.org/DDEP_WG/DDEPdata_by_A.htm. [108](#)
- [119] Herman T Van Dam, Stefan Seifert, Ruud Vinke, Peter Dendooven, Herbert Löhner, Freek J Beekman, and Dennis R Schaart. A Comprehensive Model of the Response of Silicon Photomultipliers. *IEEE TRANSACTIONS ON NUCLEAR SCIENCE*, 57(4):2254–2266, 2010. [109](#)
- [120] Niklas Hegemann. *Simulation studies and validation towards a TOF-PET detector*. PhD thesis, 2011. [116](#)
- [121] Patrick Eckert, Rainer Stamen, and H C Schultz-Coulon. Study of the response and photon-counting resolution of silicon photomultipliers using a generic simulation framework. *Journal of Instrumentation*, 7(08):P08011–P08011, August 2012. [116](#)

- [122] Stefan Seifert, Herman T Van Dam, Ruud Vinke, Peter Dendooven, Herbert Löhner, and et al. A Comprehensive Model to Predict the Timing Resolution of SiPM-Based Scintillation Detectors : Theory and Experimental Validation. *IEEE TRANSACTIONS ON NUCLEAR SCIENCE*, 59(1):190–204, 2012. [116](#)
- [123] J Pulko, F R Schneider, a Velroyen, D Renker, and S I Ziegler. A Monte-Carlo model of a SiPM coupled to a scintillating crystal. *Journal of Instrumentation*, 7(02):P02009–P02009, February 2012. [116](#)
- [124] L Archambault, L Beaulieu, J.F. Carrier, F. Castrovillari, and S et al. Chauvie. Overview of Geant4 applications in medical physics. In *2003 IEEE Nuclear Science Symposium. Conference Record (IEEE Cat. No.03CH37515)*, pages 1743–1745 Vol.3. IEEE, 2003. [116](#), [119](#)
- [125] D. Costanzo, a. Dell’Acqua, M. Gallas, a. Rimoldi, J. Boudreau, V. Tsulaia, and a. Di Simone. The Geant4-Based Simulation Software of the ATLAS Detector. *2006 IEEE Nuclear Science Symposium Conference Record*, pages 5–11, 2006. [116](#)
- [126] J Allison, K Amako, J Apostolakis, H Araujo, and P. et al. Arce Dubois. Geant4 developments and applications. *IEEE Transactions on Nuclear Science*, 53(1):270–278, February 2006. [116](#), [119](#)
- [127] Geant4 Collaboration. Geant4 reference manual v10.0. Technical Report December 2013, 2013. [116](#), [122](#), [124](#)
- [128] Stefan Piperov. Geant4 validation with CMS calorimeters test-beam data. *Hadrom Collider Physics Symposium*, pages 3–7, August 2008. [116](#), [119](#)
- [129] NH Clinthorne, NA Petrick, W.L. Rogers, and A.O. Hero. A fundamental limit on timing performance with scintillation detectors. *IEEE Transactions on Nuclear Science*, 37(2):658–663, April 1990. [117](#)
- [130] S. Agostinelli, J. Allison, K. Amako, J. Apostolakis, and H. et al. Araujo. Geant4, a simulation toolkit. *Nuclear Instruments and Methods in Physics Research Section A: Accelerators, Spectrometers, Detectors and Associated Equipment*, 506(3):250–303, July 2003. [119](#), [122](#)
- [131] ShiChao Tang and David M. Smith. Geant4 Simulations of Gamma-Ray Emission From Accelerated Particles in Solar Flares. *The Astrophysical Journal*, 721(2):1174–1183, October 2010. [119](#)

- [132] Tore Ersmark. *Geant4 Monte Carlo Simulations of the International Space Station Radiation Environment*. PhD thesis, KTH Royal Institute of Technology. 119
- [133] D H Wright, D Aston, M L Kocian, H Marsiske, W S Lockman, D C Williams, A. W. Weidemann, J. R. Wilson, T B Moore, and A J Lyon. Using Geant4 in the BaBar Simulation. pages 1–7, May 2003. 119
- [134] L Cosentino and P Finocchiaro. High-resolution Time-Of-Flight PET with Depth-Of-Interaction becomes feasible: a proof of principle. *arXiv preprint arXiv: ...*, 2012. 119
- [135] Yoshiyuki Hirano. Applications to Development of PET / SPECT System by Use of Geant4. In Charles J Mode, editor, *Applications of Monte Carlo Methods in Biology, Medicine and Other Fields of Science*, chapter 5, pages 77–94. InTech, 2011. 119
- [136] D W O Rogers. Fifty years of Monte Carlo simulations for medical physics. *Physics in medicine and biology*, 51(13):R287–301, July 2006. 119
- [137] M. N. Polyanskiy. Refractive index database. <http://refractiveindex.info>. Accessed Feb. 30, 2014. 121
- [138] Martin Janecek and William W. Moses. Measuring Light Reflectance of BGO Crystal Surfaces. *IEEE Transactions on Nuclear Science*, 55(5):2443–2449, October 2008. 121
- [139] J Apostolakis, S Giani, L Urban, M Maire, a.V Bagulya, and V.M Grichine. An implementation of ionisation energy loss in very thin absorbers for the GEANT4 simulation package. *Nuclear Instruments and Methods in Physics Research Section A: Accelerators, Spectrometers, Detectors and Associated Equipment*, 453(3):597–605, October 2000. 122
- [140] Katsuya Amako, Susanna Guatelli, V.N. Ivanchenko, Michel Maire, Barbara Mascialino, Koichi Murakami, Petteri Nieminen, Luciano Pandola, Sandra Parlati, M.G. Pia, Michela Piergentili, Takashi Sasaki, and L. Urban. Comparison of Geant4 electromagnetic physics models against the NIST reference data. *IEEE Transactions on Nuclear Science*, 52(4):910–918, August 2005. 122
- [141] G.a.P. Cirrone, G. Cuttone, F. Di Rosa, L. Pandola, F. Romano, and Q. Zhang. Validation of the Geant4 electromagnetic photon cross-sections for elements and compounds. *Nuclear Instruments and Methods in Physics Research Section A: Ac-*

- celerators, Spectrometers, Detectors and Associated Equipment*, 618(1-3):315–322, June 2010. [122](#)
- [142] C. Moisan, D. Vozza, and M. Loope. Simulating the performances of an LSO based position encoding detector for PET. *IEEE Transactions on Nuclear Science*, 44(6):2450–2458, 1997. [124](#)
- [143] Cecilia O. Steinbach, Ferenc Ujhelyi, Gabor Erdei, and Eموke Lorincz. Optical scattering length of LYSO scintillator crystals. In *2011 IEEE Nuclear Science Symposium Conference Record*, number 2, pages 2653–2656. IEEE, October 2011. [124](#)
- [144] Martin Janecek and WW Moses. Simulating scintillator light collection using measured optical reflectance. *IEEE Transactions on Nuclear Science*, 57(3):964–970, 2010. [124](#), [127](#), [133](#), [145](#), [148](#)
- [145] A Levin and C Moisan. A more physical approach to model the surface treatment of scintillation counters and its implementation into DETECT. In *IEEE Nuclear Science Symposium. Conference Record*, volume 2, pages 702–706. IEEE, 1996. [124](#)
- [146] M Grodzicka and M Moszynski. Effective dead time of APD cells of SiPM. In *(NSS/MIC), 2011*, pages 553–562, 2011. [128](#), [130](#)
- [147] K Yamamoto, K Yamamura, K Sato, S Kamakura, T Ota, H Suzuki, and S Ohsuka. Development of Multi-Pixel Photon Counter (MPPC). In *2007 IEEE Nuclear Science Symposium Conference Record*, pages 1511–1515. IEEE, 2007. [128](#)
- [148] D. Henseler, R. Grazioso, and M. Schmand. SiPM performance in PET applications: An experimental and theoretical analysis. In *2009 IEEE Nuclear Science Symposium Conference Record (NSS/MIC)*, pages 1941–1948. Ieee, October 2009. [137](#)
- [149] Roberto Capote, Francisco SaÁnchez-Doblado, Antonio Leal, Juan Ignacio Lagares, Rafael ArraÁns, and GuÁnther H. Hartmann. An EGSnrc Monte Carlo study of the microionization chamber for reference dosimetry of narrow irregular IMRT beamlets. *Medical Physics*, 31(9):2416, 2004. [147](#)
- [150] C.M. Pepin, P. Berard, A.-L. Perrot, C. Pepin, and Daniel et al. Houde. Properties of LYSO and recent LSO scintillators for phoswich PET detectors. *IEEE Transactions on Nuclear Science*, 51(3):789–795, June 2004. [160](#)
- [151] Glen Cowan. Error analysis for efficiency. <http://www.pp.rhul.ac.uk/~cowan/stat/notes/efferr.pdf>, July 2008. [166](#)

- [152] Andrew J. Reader and Habib Zaidi. Advances in PET Image Reconstruction. *PET Clinics*, 2(2):173–190, April 2007. [189](#)
- [153] J L Herraiz, S España, J J Vaquero, M Desco, and J M Udías. FIRST: Fast Iterative Reconstruction Software for (PET) tomography. *Physics in medicine and biology*, 51(18):4547–65, September 2006. [189](#)
- [154] Debashish Pal, Joseph a O’sullivan, Heyu Wu, Martin Janecek, and Yuan-Chuan Tai. 2D linear and iterative reconstruction algorithms for a PET-insert scanner. *Physics in medicine and biology*, 52(14):4293–310, July 2007. [189](#)